l'université nantes angers le mans

PÔLE DE RECHERCHE ET D'ENSEIGNEMENT SUPÉRIEUR

UNIVERSITÉ DE NANTES

Thèse de Doctorat

David LE HARDY

Mémoire présenté en vue de l'obtention du
grade de Docteur de l'Université de Nantes
sous le label de l'Université Nantes Angers Le Mans

École doctorale : SPIGA

Discipline : Sciences Pour l'Ingénieur
Spécialité : Mécanique des solides, des matériaux, des structures et des surfaces
Unité de recherche : Laboratoire de Thermocinétique de Nantes, UMR CNRS 6607

Thèse soutenue le 31 janvier 2017

Traitement des conditions aux limites spéculaires pour l'étude du transport radiatif dans des matériaux à géométrie complexe

Jury

Rapporteurs :	**François BAY**, Professeur École des Mines de Paris Sophia Antipolis
	Mouna EL HAFI, Maître assistante titulaire de l'HDR, École des Mines d'Albi
Examinateurs :	**Christophe BERTHON**, Professeur, Université de Nantes
	Pascal BOULET, Professeur, Université de Lorraine
	Nicolas CROUSEILLES, Chargé de recherche titulaire de l'HDR, Inria Rennes
	Denis ROCHAIS, Ingénieur de recherche titulaire de l'HDR, CEA le Ripault
Directeur de Thèse :	**Benoit ROUSSEAU**, Directeur de recherche CNRS, Université de Nantes
Co-encadrant de Thèse :	**Yann FAVENNEC**, Maître de Conférence, Université de Nantes

"Tout obstacle renforce la détermination.
Celui qui s'est fixé un but n'en change pas."
Léonard de Vinci

Remerciements

Une thèse est loin d'être un long fleuve tranquille. Que ce soit directement ou indirectement, beaucoup de personnes ont contribué à l'achèvement de cette thèse. C'est pour cela que je tiens sincèrement à les remercier.

Tout d'abord, un grand merci à Mouna El Hafi et le professeur François Bay qui ont bien accepté de rapporter ma thèse et de m'avoir autorisé à soutenir. Merci aussi aux membres du jury – Christophe Berthon, Pascal Boulet, Nicolas Crouseilles et Denis Rochais – pour leur présence et leurs connaissances ayant permis un très bon échange lors de la soutenance.

Je tiens aussi à remercier mes encadrants : Benoît Rousseau qui a été mon directeur de thèse, et Yann Favennec. De nombreuses discussions fructueuses ont été échangées, que ce soit d'un point de vue professionnel que d'un point de vu personnel. Sans eux, cette thèse ne se serait jamais déroulée aussi bien. Je remercie aussi le Ministère de l'Enseignement Supérieur et de la Recherche qui a financé cette thèse et sans qui cette thèse n'aurait jamais vu le jour.

Merci aussi aux membres de l'équipe $\mathbb{C}$é$f_{\mathrm{o}}{}^{\mathrm{p}}\mathcal{R}$am– Benoît, Yann, Gilberto, Fabien, Simon, Violaine, Aubin, Afeef et moi-même – qui ont permis de faire avancer la recherche avec des discussions de groupe fructueuses.

Je remercie tout le personnel du LTeN : Cathy Castelain, directrice du laboratoire pour sa très bonne gestion du laboratoire, l'administration qui écoute et qui n'hésite pas à nous aider pour gérer les avant et les après conférences, et les autres membres du laboratoire pour des déjeuners dynamiques.

Je remercie aussi le personnel enseignant, notamment Yann, Nadège et Bruno, ainsi que les étudiants de "Thermique, Énergetique" qui m'ont permis d'enseigner des TD dans le calme et la bonne humeur.

Ensuite, je tiens à remercier ma famille. Étant loin du sujet, ils ont été mes cobayes pour me permettre de vulgariser mes travaux, afin qu'ils puissent un minimum comprendre, même si ça n'a pas vraiment fonctionné sur tout le monde. Je remercie ceux qui se sont déplacés pour ma soutenance, même s'ils ont seulement retenu avoir vu des "boules de Noël" et des "chaussettes", notamment ma sœur qui est venue de loin. Je les remercie aussi de m'avoir aidé à préparer mon pot de thèse qui a eu un grand succès au sein du laboratoire.

Je remercie aussi mes amis, doctorants et autres, avec qui j'ai passé de bons moments

en dehors de la recherche.

Enfin, je voulais dire un grand merci à Maëva, ma chère et tendre, qui a bien voulu de moi durant la fin de cette thèse, qui s'est doublement motivée à corriger les coquilles en relisant cette thèse, et qui m'a permis de parcourir la dernière ligne droite sereinement. Je m'excuse auprès d'elle de lui avoir causé du stress les jours précédents ma soutenance.

Table des matières

Introduction générale

Introduite par Chandrasekhar en 1950 en astrophysique [1], l'équation du transfert radiatif permet de modéliser, entre autres, le comportement des photons dans un milieu semi-transparent où coexistent des processus émissifs, absorbants et diffusants. Cette équation phéménologique s'est popularisée au sein d'autres communautés ayant des préoccupations similaires telles que la neutronique, l'optique ou la thermique. En neutronique par exemple, elle est utilisée pour l'étude des neutrons dans les réacteurs nucléaires, ou en radiothérapie [2, 3]. Il convient alors de supposer que les neutrons n'interagissent pas entre eux.

L'équation du transfert radiatif est une équation intégro-différentielle dépendante de plusieurs variables : trois dimensions en espace, deux dimensions en angulaire, une dimension temporelle et une dimension fréquentielle, soit un total de sept dimensions. Ceci constitue l'une des grandes difficultés de résolution, en plus du fait qu'elle contienne un terme intégral et qu'il s'agisse d'une équation de transport.

En transfert radiatif, l'équation de transport est à considérer pour l'étude, entre autre, de la propagation des photons dans les matériaux semi-transparents, comme par exemple les verres, les milieux fibreux ou encore les mousses céramiques. Cependant, au vu du grand nombre de dimensions inhérent à cette équation, des approches de réduction sont souvent considérées. Pour la détermination des propriétés radiatives, les matériaux caractérisés sont généralement pris sous la forme d'échantillons minces. Dans ce cas une réduction de modèle en espace est opérante, et il suffit de se ramener à un problème 1D dans la mesure où le matériau considéré s'y prête. Or, souvent, il est nécessaire de redimensionner par usinage les échantillons, ou de demander aux élaborateurs de fournir des échantillons à façon, ce qui peut être fastidieux. Ailleurs, en optique et plus particulièrement en tomographie optique pour la biologie, au vu du fort caractère diffusif des tissus considérés, c'est le modèle qui peut être simplifié. Dans ce sens, l'approximation de diffusion est l'équation la plus répandue au vu de sa simplicité de résolution, par rapport à l'équation du transfet rafiatif, et donnant des résultats similaires [4]. Une autre forme de simplification/réduction peut être mise en œuvre en supposant que le milieu considéré est "gris". Ceci peut être justifié lorsque les propriétés radiatives ne varient pas dans une gamme de longueur d'onde étudiée. L'équation de transport devient alors indépendante de la longueur d'onde [5, 6].

Dans certains procédés industriels, comme la mise en forme par rayonnement infrarouge, ou la production d'électricité par énergie solaire concentré par exemple, une connaissance fine des transferts radiatifs peut être souhaitée pour, par exemple, dimensionner une installation, voire même pour l'optimiser. La résolution du transfert radiatf est le plus souvent abordé en considérant les géométries des matériaux insolés

comme uni-dimensionnelles alors que les évolutions technologiques amènent de plus en plus à considérer des systèmes à géométries complexes où la résolution de l'équation du transfert radiatif requiert une approche tri-dimensionnelle.

Lorsque l'équation de transport radiatif est considérée, notamment en trois dimensions d'espace, il est rare que les conditions aux limites effectivement appliquées soient représentatives de la physique modélisée. La raison en est qu'il est extrêmement délicat d'appliquer certaines conditions aux limites, tout particulièrement la condition de spécularité.

L'objectif de cette thèse est donc la résolution numérique de l'équation de transport radiatif, en géométrie tri-dimensionnelle, avec une fine prise en compte des conditions à appliquer aux bord, notamment pour la condition de spécularité. Ce travail constitue le premier pas vers la caractérisation avancée de matériaux réels à géométrie complexe menée au sein de l'équipe "Caractérisation et Fonctionnalisation des Propriétés Radiatives des Matériaux" du LTN, dans laquelle j'ai effectué mes travaux. Notons que d'autres domaines ont vu ces dernières années de larges avancées sur la résolution numérique de l'équation de transport radiatif : par exemple en astrophysique [7], en neutronique [8], en tomographie optique [9] ou en transfert radiatif [10].

Cette thèse, articulée autour de quatre articles publiés, soumis, ou en cours de soumission, a permis de construire, étape par étape, un outil numérique permettant de résoudre l'équation du transfert radiatif, en 3 dimensions et avec des conditions de réflexion spéculaire. D'un point de vue général, les trois premiers chapitres décrivent les grandes étapes de construction de l'outil numérique ; le dernier chapitre en présente quelques applications.

Le premier chapitre introductif présente la construction du modèle à résoudre, les principales quantités d'intérêt, ainsi qu'une revue des méthodes numériques les plus courantes pour la résolution du problème considéré. Cette revue sur les méthodes numériques nous a permis de nous orienter sur les méthodes de type éléments finis.

Le chapitre deux présente une comparaison, en deux dimensions d'espace, entre des méthodes de type Galerkin continue et Galerkin discontinue. Ces deux notions sont d'abord présentées en début de chapitre. Les principaux résultats de cette étude ont fait l'objet d'un article publié dans "Journal of Quantitative Spectroscopy and Radiative Transfer" [11]. Parmi les conclusions importantes, il en ressort que, pour les cas qui nous intéressent, la méthode SUPG est un choix pertinent. C'est donc ce schéma qui sera retenu par la suite pour les cas tri-dimensionnels.

Le chapitre trois, qui constitue le cœur de cette thèse, présente la résolution numérique de l'ETR en trois dimensions d'espace, avec un schéma numérique de type SUPG couplé aux ordonnées discrètes, avec prise en compte de la condition de spécularité appliquée aux bords. C'est cette dernière notion qui est la plus novatrice. Nous proposons en effet de nous affranchir des quadratures numériques habituellement utilisées pour la diffusion, et d'utiliser plutôt une discrétisation angulaire. Un calcul de partition de flux entre angles solides permet ensuite une prise en compte fine de la condition de spécularité. Les principaux résultats de cette étude font l'objet d'un article soumis dans "Journal of Computational Physics" [12].

Le dernier chapitre présente quelques résultats complémentaires et applications. Tout d'abord, les réflectances et transmittances normales hémisphériques calculées sur un cube, absorbant et diffusant, à partir des solutions éléments finis sont comparées à celles provenant de modèles bien plus courants : un modèle à deux flux unidimensionnel d'une part, et un modèle basique de type Monte Carlo à une, deux, et trois dimensions d'autre part. Ces modèles ont été développés par deux étudiants de Master 2 dont j'ai co-encadré le stage. Une application portant sur le couplage conducto-radiatif au sein d'une paraboloïde est ensuite considérée. La géométrie est tri-dimensionnelle, et il s' agit de coupler la résolution numérique du transport radiatif avec l'équation de la chaleur. Cette étude a fait l'objet d'un article publié dans "Journal of Applied Mathematics and Physics" [13] suite à la "International Conference on Theoretical and Computational Physics " qui s'est tenue à Xi'an, en Chine, en août 2016 . Enfin, la résolution numérique du transport radiatif en situation réelle est présentée. Le matériau caractérisé est un brin submillilimétrique issu d'une mousse céramique telle qu'utilisée dans des applications de récepteur solaire. La géométrie considérée est fournie par micro-tomographie X et les propriétés radiatives de la phase solide ont été modulées virtuellement de manière à conférer au brin un caractère soit semi-transparent, soit opaque. Les effets de paramètres matériaux (alumine, zircone, carbure de silicium) sur les intensités transmises et réfléchies sont étudiés. Cette étude, qui finalise cette thèse, fait l'objet d'un article en cours de finalisation pour soumission prochaine dans "Journal of Quantitative Spectroscopy and Radiative Transfer" [14].

Une conclusion est ensuite présentée, complétée par des perspectives d'études à court, moyen, et plus long termes. Une annexe vient également compléter certaines notions abordées rapidement, notamment concernant la méthode à deux flux modifiée, et la modélisation Monte Carlo, telles que mises en œuvre.

Références

[1] S. Chandrasekhar, Radiative Transfer, Courier Corporation, 2013. vii

[2] K. Case, P. Zweifel, Linear Transport Theory, Addison-Wesley Pub. Co., 1967. vii

[3] E. Lewis, W. Miller, Computational Methods of Neutron Transport. vii

[4] S. Arridge, Optical Tomography in Medical Imaging, Inverse problems 15 (2) (1999) R41. vii

[5] J. Howell, M. Menguc, R. Siegel, Thermal Radiation Heat Transfer, CRC Press, 2010. vii

[6] M. Modest, Radiative Heat Transfer, Academic Press, 2013. vii

[7] G. Kanschat, E. Meinköhn, R. Rannacher, R. Wehrse, Numerical Methods in Multidimensional Radiative Transfer, Springer, 2009. viii

[8] J. Briesmeister, et al., MCNP–A general Monte Carlo code for neutron and photon transport, Los Alamos National Laboratory, 1986. viii

[9] O. Lehtikangas, T. Tarvainen, A. Kim, S. Arridge, Finite element approximation of the radiative transport equation in a medium with piece-wise constant refractive index, Journal of Computational Physics 282 (2015) 345–359. viii

[10] R. Castro, J. Trelles, Spatial and angular finite element method for radiative transfer in participating media, Journal of Quantitative Spectroscopy and Radiative Transfer 157 (2015) 81–105. viii

[11] D. Le Hardy, Y. Favennec, B. Rousseau, Solution of the 2-D steady-state radiative transfer equation in participating media with specular reflections using SUPG and DG finite elements, Journal of Quantitative Spectroscopy and Radiative Transfer 179 (2016) 149–164. viii

[12] D. Le Hardy, Y. Favennec, B. Rousseau, Specular reflection treatment for the 3D radiative transfer equation solved with the discrete ordinates method, Journal of Computational Physics. viii

[13] D. Le Hardy, Y. Favennec, B. Rousseau, 3D radiative transfer equation coupled with heat conduction equation with realistic boundary conditions applied on complex geometries, Journal of Applied Mathematics and Physics ISSN 2327-4352. ix

[14] D. Le Hardy, Y. Favennec, B. Rousseau, 3d numerical modelling of the propagation of radiative intensity through a real X-ray tomographied ligament, Journal of Quantitative Spectroscopy and Radiative TransferEn cours de soumissions. ix

Nomenclature

Radiatif et optique

α	coefficient de répartition diffus/spéculaire
β	coefficient d'extinction
Φ	fonction de phase
ρ	densité
ρ_d	coefficient de réflexion diffuse
ρ_s	coefficient de réflexion spéculaire
σ_s	coefficient d'absorption
σ_s	coefficient de diffusion
θ_i	angle d'incidence
θ_r	angle de réfraction
$\tilde{n}$	indice de réfraction complexe
c	vitesse des photons dans le milieu
C_p	chaleur spécifique
D	densité radiative
D_T	diffusivité thermique
E	éclairement
E_b	pouvoir émissif du corps noir
I	luminance ou intensité radiative
I_b	émission du corps noir
k	conductivité thermique
Q_r	vecteur flux radiatif
Q_r^+	flux vers l'avant
Q_r^-	flux vers l'arrière
R_{NH}	réflectance normale-hémisphérique
T	température
T_{NH}	transmittance normale- hémisphérique
n	indice de réfraction

Angles et espace

$\boldsymbol{e}_k$	sommet d'un angle solide discret
$\boldsymbol{n}$	normale externe
$\boldsymbol{s}$	direction de propagation
$\boldsymbol{s}'$	direction réfléchie
$\boldsymbol{s}''$	direction réfractée
$\boldsymbol{s}_m$	direction discrète
$\boldsymbol{x}$	coordonnées spatiales
λ	longueur d'onde
$\mathbb{P}_k$	espace des polynômes de degrés k
$\mathbb{R}$	corps des réels
$\mathcal{D}$	domaine
$\mu\ \eta\ \xi$	cosinus directeurs
Ω	angle solide
$\partial\mathcal{D}$	bord du domaine
ϕ	fonction de base éléments finis
$\mathcal{S}^{n-1}$	cercle unité en 2D ($n = 2$) ou sphère unité en 3D ($n = 3$)
$a(\cdot,\cdot)$	forme bilinéaire éléments finis
$l(\cdot)$	forme linéaire éléments finis
N_d	nombre de directions discrètes
t	temps
u_h/v_h	fonctions de l'espace V_h
V_h	espace fonctionnel éléments finis

Constantes

c_0	célérité $\simeq 2,99792\ 10^8$ [m s^{-1}]
C_3	constante de Wien = 2898 μmK
h	constante de Planck $\simeq 6,626068\ 10^{-34}$ [Js]
k	constante de Bolzmann $\simeq\ 1,38065\ 10^{-23}$ [J K^{-1}]

Chapitre 1

ETR : construction, propriétés et résolution

Avant-propos

Ce chapitre se découpe en deux parties. La première partie développe les différents phénomènes physiques en vue de construire l'équation de transfert radiatif (ETR). Les conditions aux limites sont aussi introduites, ainsi que quelques grandeurs d'intérêt. La seconde partie résume les méthodes numériques les plus utilisées permettant de résoudre l'ETR. Ce 1er chapitre permettra de situer nos travaux par rapport à la littérature.

1.1 Du photon à l'ETR

Cette section a été inspirée du cours de G. Jeandel et de D. Lacroix lors de l'école thématique à Odeillo en 2014 [1], de l'ouvrage "Thermal Radiation Heat Transfer" rédigé par JR. Howell, MP. Mengüç et R. Siegel [2], ainsi que les thèses de F. Dubot et de S. Guevelou, toutes deux effectuées au laboratoire. Ces références sont à la fois synthétiques et pédagogiques, permettant de bien comprendre les différentes variables physiques utilisées en rayonnement thermique.

1.1.1 Du photon à la luminance

Tout d'abord, définissons le photon à l'échelle corpusculaire, c'est-à-dire au niveau même des atomes constituant la matière. Un photon est émis ou absorbé par une particule élémentaire, dont les énergies de transition sont quantifiées (phonons, plasmons, etc). Ces particules, qui peuvent être couplées, vont être à l'origine de la production de rayonnement thermique sur un domaine spectral allant de 0,8 micron à 200 microns. Ce sont leurs poids spectraux qui vont conférer, à la matière, sa nature semi-transparente ou opaque [3]. Illustrons notre propos au travers l'exemple des transitions électroniques. Pour exciter un électron, celui-ci a besoin d'énergie et absorbe le photon provenant d'une source extérieure. Lorsque l'énergie accumulée est suffisante, l'électron se déplace vers les couches extérieures. Lorsque l'électron n'est plus excité par une source extérieure, il émet des photons pour libérer l'énergie et retourne dans son état fondamental. Pour une couche fixée, l'électron possède une énergie potentielle E_p qui croît lorsque l'électron s'éloigne du noyau. L'énergie émise ou absorbée est donc la différence de potentiel entre la couche de départ et la couche d'arrivée de l'électron. Cette différence est notée $\Delta E_p = h\nu$, où $h \simeq 6,626068\ 10^{-34}$ [Js] est la constante de Planck et ν est la fréquence associée au photon absorbé ou émis. Lors de son retour à son état fondamental, l'électron peut émettre des photons de fréquences différentes et dans des directions aléatoires.

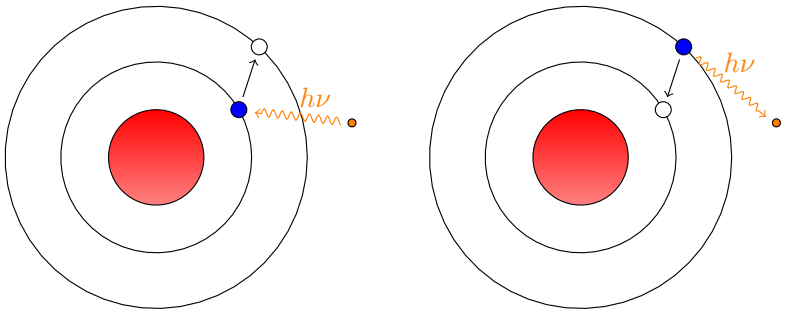

Figure 1.1 – Représentation schématique des phénomènes d'absorption et d'émission d'un photon par un électron

À plus grande échelle, l'émission des photons par le milieu s'homogénéise. Cette énergie émise $E_{b\lambda}(T)$, appelée communément pouvoir émissif du corps noir, est gouvernée par la loi de Planck, dépendante de la température T du milieu, en Kelvin, et de sa longueur d'onde dans le milieu, en micromètre :

$$E_{b\lambda}(T) = \frac{2\pi h c_0^2}{n^2 \lambda^5} \left[e^{\frac{hc_0}{n\lambda kT}} - 1 \right]^{-1} \tag{1.1}$$

où $c_0 \simeq 2,99792458\ 10^8$ [m s^{-1}] est la vitesse de la lumière dans le vide, $n = c_0/c$ est l'indice de réfraction du milieu, c est la vitesse de la lumière dans le milieu, $\lambda = c/\nu$ est la longueur d'onde dans le milieu et $k \simeq 1,3806503\ 10^{-23}$ [J K^{-1}] est la constante de Boltzmann.

Les photons possèdent une vitesse et une direction propre. De plus, les photons n'interagissent pas entre eux. Un paquet de photons, transporté dans une direction $\boldsymbol{s}$, peut être assimilé à un vecteur flux radiatif spectral $Q_{r\lambda}(\boldsymbol{x}, \boldsymbol{s}, t)$, qui représente le transport d'une intensité dans la direction $\boldsymbol{s}$, à la position $\boldsymbol{x}$, à un temps t, et pour la longueur d'onde λ. On définit la luminance I_λ comme l'intensité du vecteur flux passant au travers d'une surface élémentaire dS, munie de sa normale $\boldsymbol{n}$, autour de $\boldsymbol{x}$ à un instant t dans un angle solide élémentaire dΩ porté par la direction $\boldsymbol{s}$, dans un intervalle longueur d'onde dλ centré autour de λ et au temps t :

$$I_\lambda(\boldsymbol{x}, \boldsymbol{s}, t) = \frac{\mathrm{d}Q_{r\lambda} \cdot \boldsymbol{n}}{\boldsymbol{s} \cdot \boldsymbol{n}\ \mathrm{d}S\ \mathrm{d}\Omega\ \mathrm{d}\lambda} \tag{1.2}$$

Comme le montre la figure 1.2, la luminance est l'intensité radiative que l'on "perçoit".

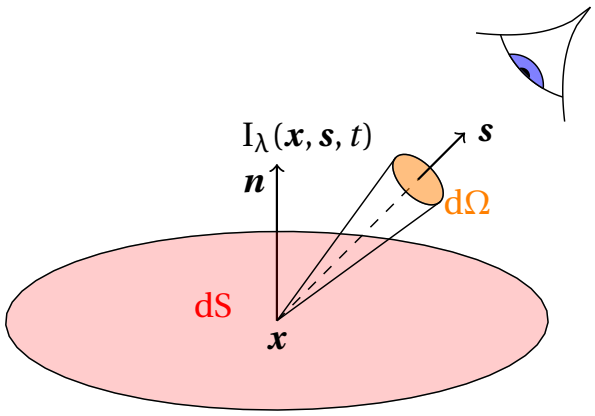

FIGURE 1.2 – Représentation schématique de la luminance pour un élément de surface élémentaire dS et un angle solide élémentaire dΩ

Les photons, émis par le corps noir, sont répartis uniformément dans toutes les directions $\boldsymbol{s}$. L'émittance du corps noir $E_{b\lambda}(T)$ est alors l'intégrale du flux radiatif traversant une surface élémentaire :

$$E_{b\lambda}(T) = \int_{\boldsymbol{s}\cdot\boldsymbol{n}>0} I_{b\lambda}(T)\boldsymbol{s} \cdot \boldsymbol{n}\ \mathrm{d}\boldsymbol{s} \tag{1.3}$$

Comme la répartition des photons est supposée uniforme, la luminance est invariante selon la direction $\boldsymbol{s}$. L'intégrale de l'égalité (1.3) vaut par conséquent π. Ainsi, la luminance du corps noir peut s'exprimer de la manière suivante :

$$I_{b\lambda}(T) = \frac{E_{b\lambda}(T)}{\pi} \tag{1.4}$$

La figure 1.3 présente la luminance du corps noir en fonction de la longueur d'onde λ pour différentes températures. Plus T augmente, plus le maximum d'énergie rayonnée

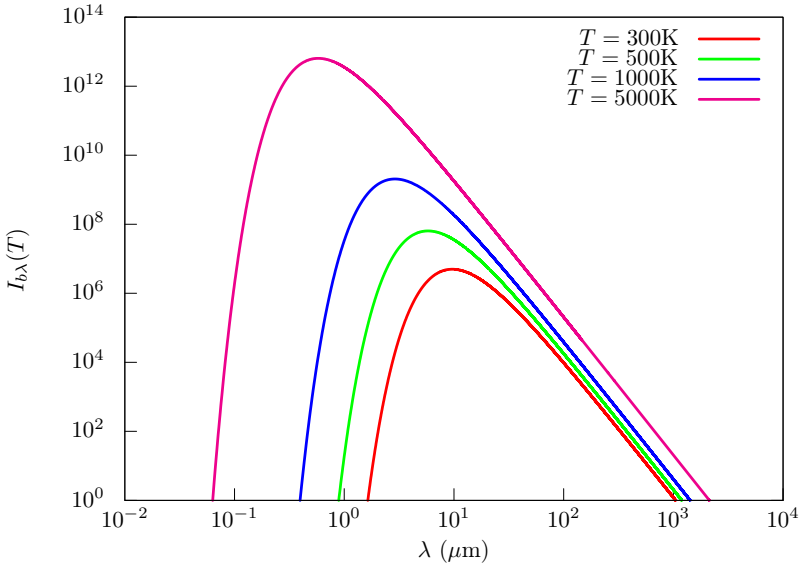

FIGURE 1.3 – Loi de Planck : luminance du corps noir $I_{b\lambda}$ en fonction de la longueur d'onde λ, pour différentes températures

se déplace vers les courtes longueurs d'onde. Ce maximum est déterminé par la loi de Wien. Pour un indice de réfraction n et une température donnée, $\lambda = C_3/(nT)$ est la longueur d'onde où le maximum d'énergie rayonnée est atteint ($C_3 = 2898\mu$mK).

Par la suite, les faisceaux lumineux étudiés sont monochromatiques. Pour des raisons de clarté, l'indice λ est alors omis dans la suite du manuscrit.

1.1.2 Comportement de la luminance dans un volume : l'ETR

Le comportement de l'évolution de la luminance dans un matériau hétérogène dépend intrinsèquement des propriétés radiatives de celui-ci. Un matériau peut être caractérisé par plusieurs paramètres effectifs, qui seront considérés comme homogène dans ce manuscrit : le coefficient d'absorption κ, le coefficient de diffusion σ_s (où l'indice s dérive de l'anglais "scattering"), le coefficient d'extinction $\beta = \kappa + \sigma_s$ et la fonction de phase de diffusion Φ. Chacun de ces paramètres peut être expliqué par des bilans énergétiques dans des volumes élémentaires.

Extinction de la luminance

Dans une direction donnée $\boldsymbol{s}$, un photon parcourt une certaine distance avant d'être soit dévié de sa trajectoire par un mécanisme de diffusion élastique, soit absorbé au sein du volume élémentaire. La moyenne de ces distances parcourues s'appelle le libre parcours moyen d'extinction et se définit par $1/\beta$. Plus le libre parcours moyen est grand par rapport à l'épaisseur du volume traversé, plus le matériau est transparent. Et inversement, plus le libre parcours moyen est petit, plus le matériau est opaque. Le long de la direction $\boldsymbol{s}$, la luminance subit une atténuation. Cette atténuation décrit une

décroissance exponentielle, selon la loi de Beer-Lambert :

$$\mathrm{d}I(\boldsymbol{x} + \mathrm{d}_{\boldsymbol{s}}\boldsymbol{x}, \boldsymbol{s}, t) = -\beta I(\boldsymbol{x}, \boldsymbol{s}, t)\ \mathrm{d}\boldsymbol{x} \tag{1.5}$$

où $\mathrm{d}_{\boldsymbol{s}}\boldsymbol{x} = [(\boldsymbol{s})_x x, (\boldsymbol{s})_y y, (\boldsymbol{s})_z z]^t$ représente la propagation le long de la direction $\boldsymbol{s}$.

Remarque : Lors d'une extinction, l'albedo $\alpha = \sigma_s/\beta$ représente la proportion moyenne de la luminance déviée. Si α est proche de 1, alors le matériau est plus diffusant qu'absorbant. Inversement, si α est proche de 0, alors le matériau est plus absorbant que diffusant.

Gain par diffusion

Lorsqu'un photon dans la direction $\boldsymbol{s}'$ est dévié de sa trajectoire, il est redirigé aléatoirement vers une autre direction $\boldsymbol{s}$. La fonction de phase de diffusion $\Phi(\boldsymbol{s}' \to \boldsymbol{s})$ représente la répartition de la luminance dans la direction $\boldsymbol{s}'$ vers une autre direction $\boldsymbol{s} \in \mathcal{S}^{n-1}$, $\mathcal{S}^{n-1}$ étant l'espace angulaire. Le cercle unité est défini par $\mathcal{S}^1$ et la sphère unité est définie par $\mathcal{S}^2$. Par définition, la fonction de phase Φ vérifie :

$$\oint_{\mathcal{S}^{n-1}} \Phi(\boldsymbol{s}' \to \boldsymbol{s})\ \mathrm{d}\Omega(\boldsymbol{s}) = 1 \tag{1.6}$$

La fonction de phase étant généralement invariante autour de l'axe azimutal, elle s'exprime en fonction du cosinus entre les directions $\boldsymbol{s}'$ et $\boldsymbol{s}$. La fonction de phase est difficile à représenter réellement. Elle est souvent approchée de deux façons : soit par décomposition dans une base polynomiale, comme la base polynomiale de Legendre, soit par la fonction d'Henyey-Greenstein (HG). Dans ce manuscrit, seule la fontion d'Henyey-Greenstein est implémentée. La fonction d'HG est décrite par :

$$\Phi_{HG}(\boldsymbol{s}' \cdot \boldsymbol{s}) = \begin{cases} \dfrac{1 - g^2}{2\pi(1 + g^2 - 2g\boldsymbol{s}' \cdot \boldsymbol{s})} & \text{en 2D} \\ \dfrac{1 - g^2}{4\pi(1 + g^2 - 2g\boldsymbol{s}' \cdot \boldsymbol{s})^{3/2}} & \text{en 3D} \end{cases} \tag{1.7}$$

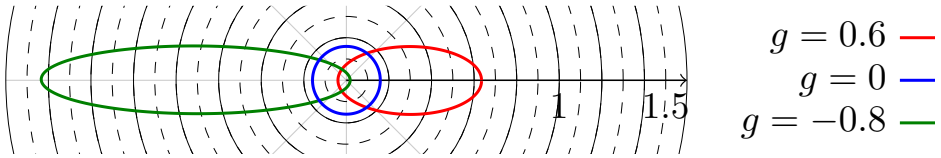

FIGURE 1.4 – Fonctions d'HG normalisées respectivement pour $g = 0.6$, $g = 0$ et $g = -0.8$

$g \in]-1, 1[$ est le paramètre d'anisotropie. Comme le montre la figure 1.4, si $g > 0$ la diffusion de luminance est préférentiellement vers l'avant ; si $g = 0$ alors la distribution est uniforme (on parlera de diffusion isotrope) et si $g < 0$, alors la diffusion est préférentiellement vers l'arrière (on parlera de rétro-diffusion). Le gain dans la direction $\boldsymbol{s}$, apporté par toutes les directions $\boldsymbol{s}' \in \mathcal{S}^{n-1}$ est décrit par l'équation suivante :

$$\mathrm{d}I(\boldsymbol{x} + \mathrm{d}_{\boldsymbol{s}}\boldsymbol{x}, \boldsymbol{s}, t) = \sigma_s \oint_{\mathcal{S}^{n-1}} \Phi(\boldsymbol{s}' \to \boldsymbol{s}) I(\boldsymbol{x}, \boldsymbol{s}', t)\ \mathrm{d}\Omega(\boldsymbol{s}')\ \mathrm{d}\boldsymbol{x} \tag{1.8}$$

Gain par émission

Si un paquet de photons est émis localement dans toutes les directions, cela signifie que le matériau a absorbé localement un paquet de photons lors d'une extinction. Cette émission suit la loi de Planck (1.1) et est modélisée par :

$$\mathrm{d}I(\boldsymbol{x}+\mathrm{d}_s\boldsymbol{x},\boldsymbol{s},t)=\kappa I_b(T)\ \mathrm{d}\boldsymbol{x} \tag{1.9}$$

Bilan d'énergie : l'ETR

Tous les comportements possibles ont été définis localement dans un volume donné. Le bilan local d'énergie est le suivant :

$$\begin{aligned}\text{Évolution de la luminance} = \text{Gain par émission} - \text{Perte par extinction}\\ + \text{Gain par diffusion}\end{aligned}$$

Par conséquent, l'évolution de la luminance pour un volume élémentaire $\mathrm{d}V$ peut se modéliser de la manière suivante :

$$\begin{aligned}I(\boldsymbol{x}+\mathrm{d}_s\boldsymbol{x},\boldsymbol{s},t+c\mathrm{d}t)-I(\boldsymbol{x},\boldsymbol{s},t)=-\beta I(\boldsymbol{x},\boldsymbol{x},t)\ \mathrm{d}\boldsymbol{x}\\ +\kappa I_b(T)\ \mathrm{d}\boldsymbol{x}+\sigma_s\oint_{\mathcal{S}^{n-1}}\Phi(\boldsymbol{s}'\cdot\boldsymbol{s})I(\boldsymbol{x},\boldsymbol{s}',t)\ \mathrm{d}\Omega(\boldsymbol{s}')\ \mathrm{d}\boldsymbol{x}\end{aligned} \tag{1.10}$$

Visuellement, le bilan d'énergie peut être représenté localement par le schéma de la figure 1.5.

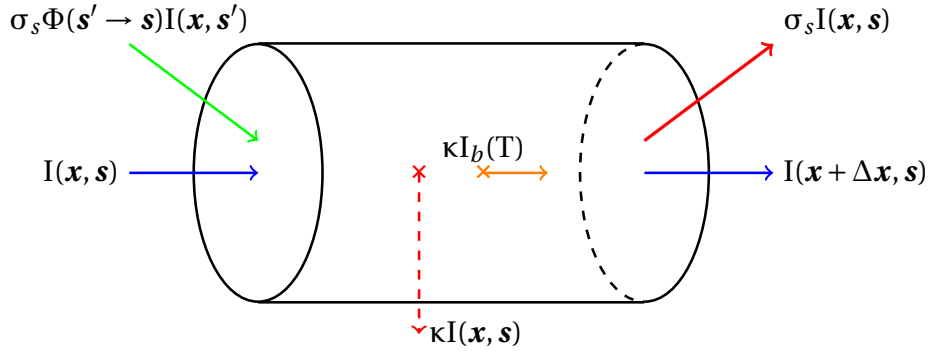

FIGURE 1.5 – Bilan d'énergie dans un élément de volume dV

La figure 1.5 présente un schéma décrivant le comportement de la luminance au sein d'un élément de volume dV. Les flèches bleues correspondent à l'évolution de la luminance dans la direction $\boldsymbol{s}$. Les flèches rouges correspondent à la perte par extinction (absorption en pointillés, diffusion en trait plein). En vert, la flèche représente le gain par diffusion de la direction $\boldsymbol{s}'$ vers la direction $\boldsymbol{s}$, et la flèche orange correspond à l'émission propre.

Dans un domaine $\mathcal{D}$, l'équation (1.10) peut s'écrire sous la forme d'une équation intégro-différentielle que l'on appelle équation de transfert radiatif :

$$\frac{I(\boldsymbol{x},\boldsymbol{s},t)}{c\partial t}+\boldsymbol{s}\cdot\nabla I(\boldsymbol{x},\boldsymbol{s},t)=-\beta I+\kappa I_b(T)+\sigma_s\oint_{\mathcal{S}^{n-1}}\Phi(\boldsymbol{s}'\cdot\boldsymbol{s})I(\boldsymbol{x},\boldsymbol{s}',t)\ \mathrm{d}\Omega(\boldsymbol{s}') \tag{1.11}$$

L'équation du transfert radiatif (1.11) est une équation à 6 dimensions : 3 dimensions en espace ($\boldsymbol{x} \in \mathcal{D} \subset \mathbb{R}^3$), 2 dimensions en angulaire ($\boldsymbol{s} \in \mathcal{S}^2$) et 1 dimension en temps ($t \in \mathbb{R}^+$), pour une longueur d'onde λ fixée.

1.1.3 Autres grandeurs physiques

Plusieurs grandeurs physiques, dépendantes de la luminance, sont utiles en science des transferts, ou pour coupler l'ETR avec d'autres physiques :

— La densité radiative $D(\boldsymbol{x})$ (ou $G(\boldsymbol{x})$), appelée aussi rayonnement incident :

$$D(\boldsymbol{x}) = \oint_{\mathcal{S}^{n-1}} I(\boldsymbol{x}, \boldsymbol{s}) \, \mathrm{d}\Omega(\boldsymbol{s}) \tag{1.12}$$

— le vecteur flux radiatif $Q_r(\boldsymbol{x})$:

$$Q_r(\boldsymbol{x}) = \oint_{\mathcal{S}^{n-1}} I(\boldsymbol{x}, \boldsymbol{s}) \boldsymbol{s} \, \mathrm{d}\Omega(\boldsymbol{s}) \tag{1.13}$$

Au niveau d'une surface, définie par sa normale $\boldsymbol{n}$, on peut aussi définir les flux entrant $Q_r^+(\boldsymbol{x})$ et flux sortant $Q_r^-(\boldsymbol{x})$:

$$Q_r^+(\boldsymbol{x}) = \int_{\boldsymbol{s}\cdot\boldsymbol{n}<0} I(\boldsymbol{x}, \boldsymbol{s}) |\boldsymbol{s} \cdot \boldsymbol{n}| \, \mathrm{d}\boldsymbol{s} \quad , \quad Q_r^-(\boldsymbol{x}) = \int_{\boldsymbol{s}\cdot\boldsymbol{n}>0} I(\boldsymbol{x}, \boldsymbol{s}) |\boldsymbol{s} \cdot \boldsymbol{n}| \, \mathrm{d}\boldsymbol{s} \tag{1.14}$$

— l'éclairement $E(\boldsymbol{x})$ au niveau d'une surface est défini comme le flux entrant :

$$E(\boldsymbol{x}) = Q_r^+(\boldsymbol{x}) \tag{1.15}$$

1.2 Comportement de la luminance en surface : Conditions aux limites

Le comportement des photons à la traversée d'une interface séparant deux matériaux joue un rôle très important dans le comportement global de la luminance. Ce comportement varie selon plusieurs paramètres : d'une part les propriétés radiatives effectives des deux matériaux et, d'autre part, la rugosité de surface. Lorsqu'un paquet de photons entre en contact avec une surface, la rugosité en surface définit le type de réflexion. Deux principales réflexions sont décrites ici :

— la réflexion spéculaire, où la surface est supposée optiquement lisse,

— la réflexion diffuse, où la surface est supposée optiquement rugueuse.

L'étude des deux réflexions se fait sur un élément de surface $\mathrm{d}S$, muni de sa normale $\boldsymbol{n}$.

1.2.1 Réflexion spéculaire

Pour un matériau semi-transparent, dans le cas de la réflexion spéculaire, la luminance incidente $I(\boldsymbol{x}, \boldsymbol{s})$ est divisée dans au plus deux directions : la direction réfléchie $\boldsymbol{s}'$

et la direction réfractée $\boldsymbol{s}''$. La figure 1.6 résume les différentes étapes de la réflexion spéculaire pour la luminance incidente $I(\boldsymbol{x}, \boldsymbol{s})$. Pour déterminer ces directions, définissons $\tilde{n}_1$ et $\tilde{n}_2$ les indices de réfraction complexe des deux différents matériaux :

$$\begin{cases} \tilde{n}_1 = n_1 + ik_1 \\ \tilde{n}_2 = n_2 + ik_2 \end{cases} \tag{1.16}$$

où n_1 et n_2 représentent l'indice de réfraction, et k_1 et k_2 représentent l'indice d'absorption. Définissons aussi l'angle incident $\theta_i \in [-\pi/2, \pi/2]$, vérifiant $\cos(\theta_i) = -\boldsymbol{s}\cdot\boldsymbol{n} = \boldsymbol{s}'\cdot\boldsymbol{n}$ et l'angle de réfraction complexe $\tilde{\theta}_r = \theta_r + i\varphi_r$.

La direction réfléchie est le symétrique de la direction incidente par rapport à la normale $\boldsymbol{n}$. Elle vérifie l'équation :

$$\boldsymbol{s}' = \zeta(\boldsymbol{s}) = \boldsymbol{s} - 2\cos(\theta_i)\boldsymbol{n} \tag{1.17}$$

Comme $\boldsymbol{s}$ et $\boldsymbol{n}$ sont connues, le calcul de la direction $\boldsymbol{s}'$ par l'équation (1.17) ne représente aucune difficulté. Pour déterminer la direction réfractée $\boldsymbol{s}''$, il faut d'abord déterminer l'angle de réfraction complexe $\tilde{\theta}_r$ qui se calcule par la loi de Snell-Descartes généralisée (1.18) :

$$\tilde{n}_1 \sin\theta_i = \tilde{n}_2 \sin\tilde{\theta}_r \tag{1.18}$$

Dans la suite de ce manuscrit, on supposera k_1, $k_2 \ll 1$, et par conséquent négligeable. Avec ses hypothèses, la loi de Snell-Descartes généralisée (1.18) devient :

$$n_1 \sin\theta_i = n_2 \sin\theta_r \tag{1.19}$$

Dans le cas où $n_1 > n_2$, on peut avoir $n_1/n_2 \sin\theta_i > 1$. Dans ce cas, l'angle θ_r n'est pas défini. On dit alors que la réflexion est totale. Toujours dans le cas où $n_1 > n_2$, définissons $\theta_c = \arcsin\frac{n_2}{n_1}$ comme l'angle l'angle critique incident. Cet angle vérifie l'équation (1.19) pour $\theta_r = \pi/2$. Il est l'angle incident à la limite de la réflexion totale. Pour le cas où $n_1 \leq n_2$ l'angle de réfraction θ_r est toujours bien défini. Quand l'angle de réfraction θ_r existe, la direction réfractée $\boldsymbol{s}''$ s'écrit [4] :

$$\boldsymbol{s}'' = \frac{n_1}{n_2}\boldsymbol{s} + \left[\cos(\theta_r) - \frac{n_1}{n_2}\cos(\theta_i)\right]\boldsymbol{n} \tag{1.20}$$

La répartition de la luminance est, quant à elle, décrite par la loi de Fresnel (1.21) :

$$\rho_s = \begin{cases} \left(\dfrac{n_1 - n_2}{n_1 + n_2}\right)^2 & \text{si } \theta_i = 0 \\ \dfrac{1}{2}\left(\dfrac{\sin(\theta_i - \theta_r)^2}{\sin(\theta_i + \theta_r)^2} + \dfrac{\tan(\theta_i - \theta_r)^2}{\tan(\theta_i + \theta_r)^2}\right) & \text{si } \theta_i \in]0, \theta_c[\\ 1 & \text{si } \theta_i \in [\theta_c, \pi/2] \end{cases} \tag{1.21}$$

où ρ_s est le coefficient de réflectivité. Par construction $\rho_s \in [0, 1]$. Il dépend des indices de réfraction $n_1$et n_2, de la direction $\boldsymbol{s}$ et de la normale $\boldsymbol{n}$ (pour plus de clarté, cette dépendance est omise). ρ_s correspond à la proportion réfléchie de la luminance incidente. Par analogie $1 - \rho_s$ correspond à la proportion réfractée :

$$\begin{cases} I(\boldsymbol{x}, \boldsymbol{s}') = \rho_s I(\boldsymbol{x}, \boldsymbol{s}) \\ I(\boldsymbol{x}, \boldsymbol{s}'') = (1 - \rho_s) I(\boldsymbol{x}, \boldsymbol{s}) \end{cases} \tag{1.22}$$

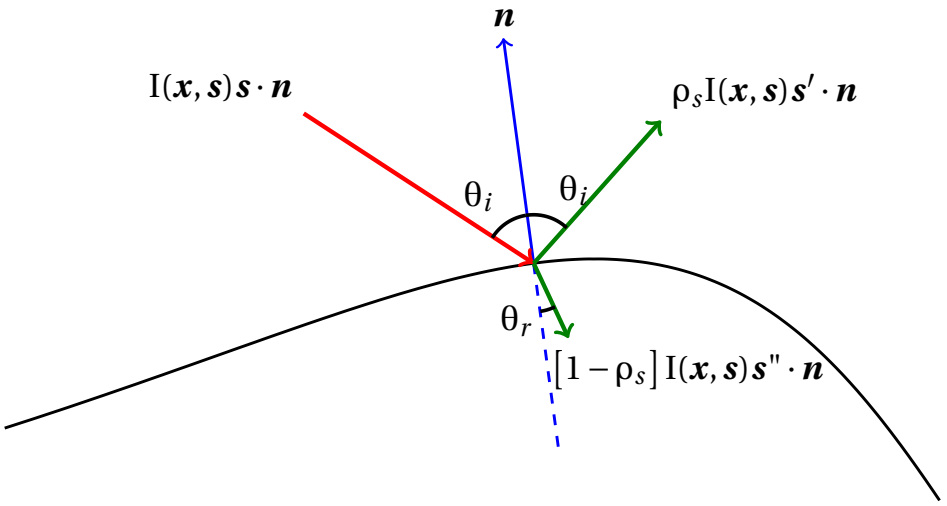

FIGURE 1.6 – Réflexion spéculaire

1.2.2 Réflexion diffuse

La réflexion diffuse apparaît lorsque le matériau est optiquement rugueux. Quand un paquet de photons impacte une surface rugueuse, celui-ci est supposé se disperser dans toutes les directions. D'après la littérature, de ce comportement résulte deux égalités de flux, une pour le flux réfléchi, et une autre pour le flux réfracté :

$$\begin{aligned} \rho_d I(\boldsymbol{x}, \boldsymbol{s})|\boldsymbol{s} \cdot \boldsymbol{n}| &= \int_{\boldsymbol{s}' \cdot \boldsymbol{n} > 0} I(\boldsymbol{x}, \boldsymbol{s}')|\boldsymbol{s}' \cdot \boldsymbol{n}| \, \mathrm{d}\boldsymbol{s}' \\ (1 - \rho_d) I(\boldsymbol{x}, \boldsymbol{s})|\boldsymbol{s} \cdot \boldsymbol{n}| &= \int_{\boldsymbol{s}'' \cdot \boldsymbol{n} < 0} I(\boldsymbol{x}, \boldsymbol{s}'')|\boldsymbol{s}'' \cdot \boldsymbol{n}| \, \mathrm{d}\boldsymbol{s}'' \end{aligned} \tag{1.23}$$

avec ρ_d le coefficient de réflexion diffuse. La réflexion diffuse suppose que la luminance est redistribuée uniformément. La luminance réfléchie $I(\boldsymbol{x}, \boldsymbol{s}')$ et la luminance réfractée $I(\boldsymbol{x}, \boldsymbol{s}'')$ sont alors respectivement indépendantes des directions $\boldsymbol{s}'$ et $\boldsymbol{s}''$. Avec ces hypothèses, les équations (1.23) deviennent :

$$\begin{aligned} \frac{\rho_d}{\pi} I(\boldsymbol{x}, \boldsymbol{s})|\boldsymbol{s} \cdot \boldsymbol{n}| &= I(\boldsymbol{x}, \boldsymbol{s}') \\ \frac{1 - \rho_d}{\pi} I(\boldsymbol{x}, \boldsymbol{s})|\boldsymbol{s} \cdot \boldsymbol{n}| &= I(\boldsymbol{x}, \boldsymbol{s}'') \end{aligned} \tag{1.24}$$

Quand un paquet de photons incident arrive dans toutes les directions $\boldsymbol{s}$, la luminance dans chaque direction incidente $\boldsymbol{s}$ vérifie les équations (1.24). La luminance réfléchie pour la direction $\boldsymbol{s}'$ est donc la somme des luminances dans toutes les directions $\boldsymbol{s}$. Il en est de même pour la luminance réfractée $\boldsymbol{s}''$:

$$\begin{aligned} \frac{\rho_d}{\pi} \int_{\boldsymbol{s} \cdot \boldsymbol{n} < 0} I(\boldsymbol{x}, \boldsymbol{s})|\boldsymbol{s} \cdot \boldsymbol{n}| \, \mathrm{d}\boldsymbol{s} &= I(\boldsymbol{x}, \boldsymbol{s}') \\ \frac{1 - \rho_d}{\pi} \int_{\boldsymbol{s} \cdot \boldsymbol{n} < 0} I(\boldsymbol{x}, \boldsymbol{s})|\boldsymbol{s} \cdot \boldsymbol{n}| \, \mathrm{d}\boldsymbol{s} &= I(\boldsymbol{x}, \boldsymbol{s}'') \end{aligned} \tag{1.25}$$

Notons que pour les réflexions diffuses internes, c'est-à-dire dans les directions $\boldsymbol{s}$ vérifiant $\boldsymbol{s} \cdot \boldsymbol{n} > 0$, les équations (1.25) sont aussi valables. La figure (1.7) décrit le comportement d'une luminance incidente dans la direction $\boldsymbol{s}$ lors d'une réflexion diffuse.

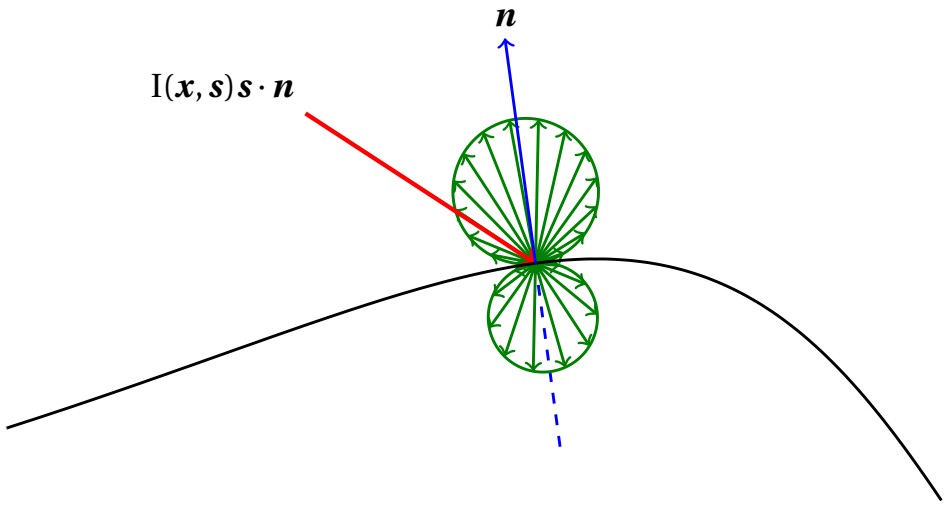

FIGURE 1.7 – Réflexion diffuse pour un flux incident dans la direction $\boldsymbol{s}$

1.2.3 Réflexion mixte

Dans les cas intermédiaires, combinants réflexion spéculaire et réflexion diffuse, une interpolation linéaire peut être utilisée. Cette réflexion mixte dépend d'un paramètre $\alpha \in [0,1]$ qui régit le taux de luminance réfléchi par réflexion spéculaire par rapport à la réflexion diffuse. Les équations (1.22) et (1.25) sont alors combinées. Pour un faisceau incident entrant, la reflexion mixte peut s'écrire :

$$\begin{cases} I(\boldsymbol{x},\boldsymbol{s}') = \alpha\rho_s I(\boldsymbol{x},\boldsymbol{s}) + (1-\alpha)\dfrac{\rho_d}{\pi}\displaystyle\int_{\boldsymbol{s}\cdot\boldsymbol{n}<0} I(\boldsymbol{x},\boldsymbol{s})|\boldsymbol{s}\cdot\boldsymbol{n}|\ \mathrm{d}\boldsymbol{s} \\ I(\boldsymbol{x},\boldsymbol{s}'') = \alpha(1-\rho_s)I(\boldsymbol{x},\boldsymbol{s}) + (1-\alpha)\dfrac{1-\rho_d}{\pi}\displaystyle\int_{\boldsymbol{s}\cdot\boldsymbol{n}<0} I(\boldsymbol{x},\boldsymbol{s})|\boldsymbol{s}\cdot\boldsymbol{n}|\ \mathrm{d}\boldsymbol{s} \end{cases} \tag{1.26}$$

Quand $\alpha = 1$ alors la réflexion est totalement spéculaire, quand $\alpha = 0$ alors la réflexion est totalement diffuse. Pour les autres cas $\alpha \in]0,1[$ la réflexion est dite mixte.

1.3 Modélisation

Dans cette section, la direction $\boldsymbol{s}$ est définie comme la direction principale d'étude pour construire notre modèle. De plus, au niveau du domaine $\mathcal{D}$, toute la surface possède ses différentes normales $\boldsymbol{n}$ dirigées vers l'extérieur du domaine. Cela permet de différencier une direction sortante $\boldsymbol{s}$ (vérifiant $\boldsymbol{s}\cdot\boldsymbol{n} > 0$) d'une direction entrante $\boldsymbol{s}$ (vérifiant $\boldsymbol{s}\cdot\boldsymbol{n} < 0$).

1.3.1 Équation stationnaire

Nos études portent sur l'équation stationnaire. C'est-à-dire que l'on suppose que $\frac{\partial I}{\partial t}(\boldsymbol{x},\boldsymbol{s},t) = 0$. L'équation principale de notre modèle est :

$$\boldsymbol{s}\cdot\nabla I(\boldsymbol{x},\boldsymbol{s}) + \beta I(\boldsymbol{x},\boldsymbol{s}) = \sigma_s \oint_{\mathcal{S}^{n-1}} \Phi(\boldsymbol{s}'\cdot\boldsymbol{s}) I(\boldsymbol{x},\boldsymbol{s}')\ \mathrm{d}\Omega(\boldsymbol{s}') + \kappa I_b(T) \tag{1.27}$$

L'équation stationnaire peut être utilisée pour le calcul de transmittance et de réflectance. De plus, l'ETR stationnaire peut être couplée avec des équations instationnaires, en partant du principe que le temps caractéristique du phénomène physique couplé est beaucoup grand que celui de l'ETR.

1.3.2 Conditions aux limites

Pour compléter le modèle, les conditions aux limites doivent aussi être déterminées. Pour commencer, supposons une luminance incidente connue et collimatée dans la direction $\boldsymbol{s}_0$, notée $\tilde{I}(\boldsymbol{x}, \boldsymbol{s}_0)$. Quand les photons associés entrent dans le domaine $\mathcal{D}$, ceux-ci sont en partie réfractés vers la direction $\xi(\boldsymbol{s}_0)$ et diffusés dans toutes les directions entrantes. La luminance $\tilde{I}(\boldsymbol{x}, \boldsymbol{s})$, où $\boldsymbol{s}$ est une direction entrante quelconque, est définie par :

$$\tilde{I}(\boldsymbol{x}, \boldsymbol{s}) = \left[\alpha(1-\rho_s)\mathbb{1}_{[\boldsymbol{s}=\xi(\boldsymbol{s}_0)]} + (1-\alpha)\frac{1-\rho_d}{\pi}|\boldsymbol{s}_0 \cdot \boldsymbol{n}|\right] \tilde{I}(\boldsymbol{x}, \boldsymbol{s}_0) \quad \forall \boldsymbol{s} : \boldsymbol{s} \cdot \boldsymbol{n} < 0 \tag{1.28}$$

La luminance $\tilde{I}(\boldsymbol{x}, \boldsymbol{s})$ de l'équation (1.28) est une des conditions aux limites, la conditions de Dirichlet. La condition de Dirichlet (1.28) seule ne suffit pas. Les réflexions internes sont aussi à prendre en compte. Similairement aux réflexions externes (1.26), les conditions de réflexion interne sont définies comme suivant :

$$I_{\text{Int}}(\boldsymbol{x}, \boldsymbol{s}) = \alpha\rho_s I(\boldsymbol{x}, \zeta(\boldsymbol{s})) + (1-\alpha)\frac{\rho_d}{\pi}\int_{\boldsymbol{s}'\cdot\boldsymbol{n}>0} I(\boldsymbol{x}, \boldsymbol{s}')|\boldsymbol{s}' \cdot \boldsymbol{n}| \, \mathrm{d}\boldsymbol{s}' \quad \forall \boldsymbol{s} : \boldsymbol{s} \cdot \boldsymbol{n} < 0 \tag{1.29}$$

où $\zeta(\boldsymbol{s})$ est la direction incidente et $\boldsymbol{s}$ la direction réfléchie. Les conditions aux limites utilisées sont la somme des conditions de Dirichlet (1.28) et des conditions de réflexions internes :

$$I(\boldsymbol{x}, \boldsymbol{s}) = \tilde{I}(\boldsymbol{x}, \boldsymbol{s}) + I_{\text{Int}}(\boldsymbol{x}, \boldsymbol{s}) \quad \forall \boldsymbol{s} : \boldsymbol{s} \cdot \boldsymbol{n} < 0 \tag{1.30}$$

1.4 Méthodes numériques

Que ce soit dans la communauté radiative [2, 5, 6, 7, 8, 9, 10, 11, 12], en tomographie optique [13, 14, 15, 16, 17] ou en neutronique [18, 19, 20, 21, 22, 23, 24] par exemple, de nombreuses avancées peuvent être recensées, notamment sur les différents schémas numériques. Durant ces dernières années, l'évolution des capacités de calcul numérique a aussi permis de débloquer quelques verrous scientifiques, notamment sur les limitations de problèmes de mémoire. En parallèle, les méthodes de résolutions numériques de l'ETR se sont aussi développées. Deux grandes familles de méthodes se distinguent : les méthodes statistiques et les méthodes déterministes. Une revue des méthodes les plus utilisées est présentée dans cette section.

1.4.1 Méthodes Monte Carlo

Les méthodes Monte-Carlo sont des méthodes statistiques [18, 20, 25, 26, 27, 28, 29, 30]. Elles convergent vers la solution à l'aide de la description des phénomènes stochastiques décrivant le comportement des photons. Deux approches principales :

— l'approche analogue [31]. Cette méthode, qui se base sur des densités de probabilité et le suivi des photons, est plus accessible au premier abord.

— l'approche intégrale [32] qui, comme le nom l'indique, décrit les phénomènes physiques à l'aide d'intégrales multiples. Elle est plus compliquée théoriquement, mais permet de construire des programmes plus optimisés, donc plus rapides. De plus, elle est aussi très adaptée pour le calcul de sensibilité des paramètres.

Les méthodes Monte-Carlo sont peu coûteuses en capacité mémoire et sont très rapides pour des cas simples (comme par exemple, un cube homogénéisé). Mais dès lors que la géométrie se complexifie, que le milieu devient hétérogène ou que l'on veut calculer certaines propriétés comme la densité volumique, elles deviennent alors complexes à implémenter. À titre d'information, il existe des logiciels utilisant les méthodes Monte-Carlo dans des géométries complexes et à grandes précisions comme les codes EDStar, SERPENT ou MCNP [33, 34, 35].

1.4.2 Discrétisations angulaires

Les méthodes déterministes consistent à approcher les opérateurs différentiels ou les espaces fonctionnels dans lesquels on cherche la solution. Deux étapes : discrétisation angulaire et discrétisation spatiale. L'intégrale dans l'ETR (1.27), due au gain par diffusion, peut être approché par une discrétisation angulaire. Il existe des revues des différentes méthodes existantes [2, 12] mais seules les méthodes les plus utilisées sont présentées dans cette section.

Méthode des harmoniques sphériques (P_N)

La méthode des harmoniques sphériques a été introduite pour l'étude d'étoiles gazeuses en 1917 pas Jeans [36]. Elle consiste à décomposer l'espace des directions dans une base d'harmoniques sphériques [37, 38, 39] :

$$I(\boldsymbol{x}, \boldsymbol{s}) = \sum_{l=0}^{\infty} \sum_{m=-l}^{l} I_l^m(\boldsymbol{x}) Y_l^m(\boldsymbol{s}) \tag{1.31}$$

avec la base des harmoniques sphériques suivante :

$$Y_l^m(\boldsymbol{s}) = (-1)^{(m+|m|)/2} \left[\frac{(l-|m|)!}{(l+|m|)!}\right]^{0.5} e^{im\phi} P_l^{|m|}(\cos\theta) \tag{1.32}$$

Dans l'équation (1.32), ϕ correspond à l'angle azimutal et θ à l'angle polaire, pour la direction $\boldsymbol{s}$. $P_l^{|m|}$ est un polynôme de Legendre. La méthode P_N consiste à tronquer la base en $2N+1$ fonctions harmoniques $Y_l^m(\boldsymbol{s})$. La méthode P_1 est la plus souvent utilisée

car il n'en ressort que 3 équations à résoudre. Le désavantage de cette méthode est la prise en compte des conditions aux limites qui suppose une luminance entrante isotrope. De plus, la diffusion est aussi supposée isotrope. Cette méthode est très bien décrite dans les ouvrages [2, 12]. Une simplification de la méthode, appelée SP_N est aussi utilisée pour améliorer la méthode P_N originale, que ce soit en ordre de convergence que en temps de calcul [2, 40, 41, 42, 43]. Récemment, la méthode P_N originale a été revisitée et très améliorée, comme l'ajout de filtres sur les harmoniques sphériques. [44, 45].

Méthode à deux-flux

Comme le nom de la méthode laisse sous-entendre, la méthode à deux-flux utilise seulement deux directions opposées qui propagent respectivement un hémisphère dans ces deux directions. On note $I^+(\boldsymbol{x})$ la luminance se propageant vers l'avant et $I^-(\boldsymbol{x})$ la luminance se propageant vers l'arrière. L'ETR (1.27) est alors décomposée en un système de deux équations à deux inconnues. Cette méthode étant utilisée pour des tests à une dimension, l'ETR (1.27) devient :

$$\begin{cases} \mu \dfrac{\partial}{\partial x} I^+(x) + \beta I^+(x) = \sigma_s \left(B^+ I^+(x) + B^- I^-(x) \right) \\ -\mu \dfrac{\partial}{\partial x} I^-(x) + \beta I^-(x) = \sigma_s \left(B^+ I^+(x) + B^- I^-(x) \right) \end{cases} \tag{1.33}$$

avec $B^{\pm} = \int_{\mathcal{S}^{0\pm}} \Phi(\mu)\, \mathrm{d}\mu$ représentant l'anisotropie du domaine.

Cette méthode a l'avantage de fournir une solution analytique en 1D de la transmittance T_{NH} et réflétance R_{NH} rapidement, dû à son faible nombre d'équations. De plus, l'erreur est souvent faible pour une épaisseur optique mince [2, 46, 47, 48]. Il existe aussi des méthodes à 4-flux et 6-flux [49, 50]. On note que les effets visant à réduire les effets de diffusion ont été étudiés [51].

Méthode des ordonnées discrètes

La méthode des ordonnées discrètes, que l'on appelera DOM par la suite, est une extension de la méthode à deux-flux. Le principe consiste à discrétiser l'espace angulaire $\mathcal{S}^{n-1}$ en N_d angles solides se propageant dans N_d directions $\boldsymbol{s}_m$, $m = 1, \cdots, N_d$. L'ETR (1.27) devient alors un système semi-discret à N_d équations à N_d inconnues, continues en espace [52, 53, 54, 55, 56, 57, 58, 59] :

$$\boldsymbol{s}_m \cdot \nabla I_m(\boldsymbol{x}) + \beta I_m(\boldsymbol{x}) = \sigma_s \sum_{j=1}^{N_d} \omega_j \Phi_{m,j} I_j(\boldsymbol{x}) + \kappa I_b(T) \quad \forall m = 1, \ldots, N_d \tag{1.34}$$

où $I_m(\boldsymbol{x}) = I(\boldsymbol{x}, \boldsymbol{s}_m)$. Les poids ω_j associés aux directions $\boldsymbol{s}_j$ correspondent à l'importance de ces directions. Les couples $(\boldsymbol{s}_j, \omega_j)$ peuvent se déterminer de plusieurs façons : par l'utilisation de quadratures [60, 61, 62], par éléments finis [63] ou par calcul d'aire de l'angle solide [9, 64, 65, 66, 67, 68, 69]. Quelques méthodes de discrétisations sont détaillées dans le chapitre 3.

1.4.3 Discrétisations spatiales

L'ETR (1.27) combinée avec les conditions aux limites (1.30) devient rapidement compliquée à résoudre analytiquement. Le besoin de discrétiser spatialement le domaine d'étude devient alors nécessaire. Une fois le domaine maillé, des méthodes d'approximation peuvent être alors utilisées. Les méthodes les plus courantes citées dans ce chapitre sont : les méthodes de différences finies, de volumes finis et de Galerkin. D'autres méthodes de résolution peuvent être trouvées dans la littérature [2, 70, 71].

Méthodes des différences finies

Les méthodes des différences finies sont faciles à implémenter. Elles consistent à approcher les opérateurs différentiels par une différence divisée entre mailles voisines. Cette méthode est lente en convergence et est difficile à implémenter pour des géométries complexes [15, 72, 73, 74].

Méthodes de volumes finis

Les méthodes de volumes finis sont basées sur la conservation des flux. Couplées généralement avec les ordonnées discrètes, elles sont alors adaptées pour approcher le terme de transport $\boldsymbol{s}_m \cdot \nabla I_m(\boldsymbol{x})$. Ces méthodes supposent que la solution numérique est constante par maille. L'ETR est intégrée sur chaque maille puis un bilan de flux est alors appliqué pour effectuer une connexion entre les mailles. Cette méthode est applicable pour des géométries complexes et des maillages non structurés [53, 75, 76, 77, 78, 79, 80, 81, 82, 83, 84, 85]. En complément, la revue de Coelho [86] donne de nombreuses versions de méthodes de volumes finis.

Méthodes de Galerkin Continues

Les méthodes de Galerkin continues, appelées aussi communément "les méthodes éléments finis", consistent à créer une base de fonctions continues et polynomiales par maille. La solution continue est alors approchée par une fonction générée par cette base. Utilisées pour la première fois en géométrie 1D [87], elles sont depuis étendues pour des géométries complexes [63, 88]. La méthode des éléments finis classiques approche difficilement le terme de transport $\boldsymbol{s}_m \cdot \nabla I_m(\boldsymbol{x})$ [89, 90]. Cependant, des méthodes de décentrement ou des méthodes de transformation de l'ETR ont permis de mieux approcher ce terme [4, 9, 91, 92, 93]. Les méthodes de Galerkin continues sont adaptées pour approcher la solution dans des géométries complexes ainsi que pour la prise en compte des différentes conditions aux limites. Ces méthodes sont plus amplement détaillées dans le chapitre 2.

Méthodes de Galerkin discontinues

Les méthodes de Galerkin discontinues sont en quelque sorte un mélange de méthodes de volumes finis et d'éléments finis. Elles consistent à créer des fonctions de base polynomiales sur chacune des mailles, puis de faire des bilans de flux entre chacune des mailles (comme dans les méthodes de volumes finis) [6, 7, 94, 95, 96, 97, 98]. C'est une méthode efficace mais complexe à implémenter car elle utilise des outils d'éléments finis ainsi que des outils de volumes finis. Cette méthode est aussi plus détaillée dans le chapitre 2.

1.4.4 Choix de la méthode numérique

L'objectif étant de travailler en géométrie complexe, les outils de Galerkin sont adaptés et plus facile à prendre en mains selon mon opinion. Par conséquent, on choisit les méthodes Galerkin en spatial. De plus, le besoin de connaître la solution de la luminance dans un volume, pour coupler à d'autres physiques, nous incite à privilégier les méthodes déterministes par rapport aux méthodes Monte-Carlo. Ensuite, l'étude utilise un faisceau collimaté. La méthode des ordonnées discrètes est alors préférable par rapport à la méthode des harmoniques sphériques. Par conséquent, nous avons choisi la méthode des ordonnées discrètes combiné à une méthode Galerkin. Le chapitre 2 est l'étude entre une méthode Galerkin continue et une méthode Galerkin discontinue. Cette étude permet de raffiner le choix de la méthode de discrétisation spatiale.

Références

[1] G. Jeandel and D. Lacroix. Notions de base en rayonnement thermique. *Four Solaire d'Odeillo*, 2014. 3

[2] JR Howell, R. Siegel, and MP Menguc. *Thermal Radiation Heat Transfer*. CRC press, 2011. 3, 12, 13, 14, 15

[3] B. Rousseau. Rayonnement thermique en milieux semi- transparents. *Four Solaire d'Odeillo*, 2014. 3

[4] O. Lehtikangas, T. Tarvainen, AD Kim, and SR Arridge. Finite element approximation of the radiative transport equation in a medium with piece-wise constant refractive index. *Journal of Computational Physics*, 282 :345–359, 2015. 9, 15

[5] S. Richling, E. Meinköhn, N Kryzhevoi, and G Kanschat. Radiative transfer with finite elements-I. basic method and tests. *Astronomy & Astrophysics*, 380(02) :776–788, 2001. 12

[6] LH Liu and LJ Liu. Discontinuous finite element method for radiative heat transfer in semitransparent graded index medium. *Journal of Quantitative Spectroscopy and Radiative Transfer*, 105(3) :377–387, 2007. 12, 16

[7] H. Gao and H. Zhao. A fast-forward solver of radiative transfer equation. *Transport Theory and Statistical Physics*, 38(3) :149–192, 2009. 12, 16

[8] E. Meinköhn. A general-purpose finite element method for 3d radiative transfer problems. pages 99–173, 2009. 12

[9] G. Kanschat, E. Meinköhn, R. Rannacher, and R. Wehrse. *Numerical Methods in Multidimensional Radiative Transfer*. Springer, 2009. 12, 14, 15

[10] V. Le Dez and H. Sadat. On the radiative heat transfer in a semi-transparent medium enclosed in a cylindrical annulus of infinite length with specularly reflecting lateral surfaces. *Applied Mathematical Modelling*, 40(1) :150–168, 2016. 12

[11] M. Roger, C. Caliot, N. Crouseilles, and PJ Coelho. A hybrid transport-diffusion model for radiative transfer in absorbing and scattering media. *Journal of Computational Physics*, 275 :346–362, 2014. 12

[12] MF Modest. *Radiative Heat Transfer*. Academic press, New York, 3rd ed. edition, 2013. 12, 13, 14

[13] GS Abdoulaev and AH Hielscher. Three-dimensional optical tomography with the equation of radiative transfer. *Journal of Electronic Imaging*, 12(4) :594–601, 2003. 12

[14] T. Tarvainen, M. Vauhkonen, and SR Arridge. Gauss–Newton reconstruction method for optical tomography using the finite element solution of the radiative transfer equation. *Journal of Quantitative Spectroscopy and Radiative Transfer*, 109(17) :2767–2778, 2008. 12

[15] AD Klose and AH Hielscher. Quasi-Newton methods in optical tomographic image reconstruction. *Inverse Problems*, 19(2) :387, 2003. 12, 15

[16] F. Dubot, Y. Favennec, B. Rousseau, and DR Rousse. A wavelet multi-scale method for the inverse problem of diffuse optical tomography. *Journal of Computational and Applied Mathematics*, 289 :267–281, 2015. 12

[17] HK Kim and A. Charette. Frequency domain optical tomography using a conjugate gradient method without line search. *Journal of Quantitative Spectroscopy and Radiative Transfer*, 104(2) :248–256, 2007. 12

[18] J. Spanier and EM Gelbard. Monte Carlo principles and neutron transport problems. *Reading, Mass., USA*, 1969. 12, 13

[19] EE Lewis and WF Miller. *Computational Methods of Neutron Transport*. John Wiley and Sons, Inc., New York, NY, 1984. 12

[20] I. Lux and L. Koblinger. *Monte Carlo particle transport methods : neutron and photon calculations*, volume 102. Citeseer, 1991. 12, 13

[21] J. Wood and MMR Williams. Recent progress in the application of the finite element method to the neutron transport equation. *Progress in Nuclear Energy*, 14(1) :21–40, 1984. 12

[22] CRE De Oliveira. An arbitrary geometry finite element method for multigroup neutron transport with anisotropic scattering. *Progress in Nuclear Energy*, 18(1-2) :227–236, 1986. 12

[23] J. Hansen, J. Peterson, J. Morel, J. Ragusa, and Y. Wang. A least-squares transport equation compatible with voids. *Journal of Computational and Theoretical Transport*, 43(1-7) :374–401, 2014. 12

[24] VM Laboure, RG McClarren, and Y. Wang. Globally Conservative, Hybrid Self-Adjoint Angular Flux and Least-Squares Method Compatible with Void. *arXiv preprint arXiv :1605.05388*, 2016. 12

[25] J. Willert and H. Park. Residual Monte Carlo high-order solver for Moment-Based Accelerated Thermal Radiative Transfer equations. *Journal of Computational Physics*, 276 :405–421, 2014. 13

[26] JD Densmore, KG Thompson, and TJ Urbatsch. A hybrid transport-diffusion Monte Carlo method for frequency-dependent radiative-transfer simulations. *Journal of Computational Physics*, 231(20) :6924–6934, 2012. 13

[27] JR Howell. The Monte Carlo method in radiative heat transfer. *Journal of Heat Transfer*, 120(3) :547–560, 1998. 13

[28] M. Cherkaoui, J-L Dufresne, R. Fournier, J-Y Grandpeix, and A. Lahellec. Monte Carlo simulation of radiation in gases with a narrow-band model and a net-exchange formulation. *Journal of Heat Transfer*, 118(2) :401–407, 1996. 13

[29] MF Modest. Backward Monte Carlo simulations in radiative heat transfer. *Journal of Heat Transfer*, 125(1) :57–62, 2003. 13

[30] R. Fournier, S. Blanco, V. Eymet, M. El Hafi, and C. Spiesser. Radiative, conductive and convective heat-transfers in a single Monte Carlo algorithm. In *Journal of Physics : Conference Series*, volume 676, page 012007. IOP Publishing, 2016. 13

[31] SA Prahl, M. Keijzer, SL Jacques, and AJ Welch. A Monte Carlo model of light propagation in tissue. *Dosimetry of laser radiation in medicine and biology*, 5 :102–111, 1989. 13

[32] J. Dauchet, S. Blanco, J-F Cornet, M. El Hafi, V. Eymet, and R. Fournier. The practice of recent radiative transfer Monte Carlo advances and its contribution to the field of microorganisms cultivation in photobioreactors. *Journal of Quantitative Spectroscopy and Radiative Transfer*, 128 :52–59, 2013. 13

[33] http://www.starwest.ups-tlse.fr/edstar. 13

[34] J. Leppänen. SERPENT –a continuous-energy Monte Carlo reactor physics burnup calculation code. *VTT Technical Research Centre of Finland*, 4, 2013. 13

[35] JF Briesmeister and et al. MCNPTM – a general Monte Carlo N-Particle transport code. *Version 4C, LA-13709-M, Los Alamos National Laboratory*, 2000. 13

[36] JH Jeans. The equations of radiative transfer of energy. *Monthly Notices of the Royal Astronomical Society*, 78(1) :28–36, 1917. 13

[37] KF Evans. The spherical harmonics discrete ordinate method for three-dimensional atmospheric radiative transfer. *Journal of the Atmospheric Sciences*, 55(3) :429–446, 1998. 13

[38] W. Ge, R. Marquez, MF Modest, and SP Roy. Implementation of high-order spherical harmonics methods for radiative heat transfer on OpenFOAM. *Journal of Heat Transfer*, 137(5) :052701, 2015. 13

[39] M. Benassi, RDM Garcia, AH Karp, and CE Siewert. A high-order spherical harmonics solution to the standard problem in radiative transfer. *The Astrophysical Journal*, 280 :853–864, 1984. 13

[40] EM Gelbard. Simplified spherical harmonics equations and their use in shielding problems. Technical report, Westinghouse Electric Corp. Bettis Atomic Power Lab., Pittsburgh, 1961. 14

[41] EW Larsen, JE Morel, and JM McGhee. Asymptotic derivation of the multigroup P 1 and simplified P N equations with anisotropic scattering. *Nuclear science and engineering*, 123(3) :328–342, 1996. 14

[42] PS Brantley and EW Larsen. The simplified P 3 approximation. *Nuclear Science and Engineering*, 134(1) :1–21, 2000. 14

[43] EW Larsen, G. Thömmes, A. Klar, M. Seaıd, and T. Götz. Simplified P N approximations to the equations of radiative heat transfer and applications. *Journal of Computational Physics*, 183(2) :652–675, 2002. 14

[44] D. Radice, E. Abdikamalov, L. Rezzolla, and CD Ott. A new spherical harmonics scheme for multi-dimensional radiation transport I. static matter configurations. *Journal of Computational Physics*, 242 :648–669, 2013. 14

[45] W. Ge, MF Modest, and R. Marquez. Two-dimensional axisymmetric formulation of high order spherical harmonics methods for radiative heat transfer. *Journal of Quantitative Spectroscopy and Radiative Transfer*, 156 :58–66, 2015. 14

[46] LK Matthews, R Viskanta, and FP Incropera. Combined conduction and radiation heat transfer in porous materials heated by intense solar radiation. *Journal of Solar Energy Engineering*, 107(1) :29–34, 1985. 14

[47] CJ Cornelison and JT Howe. Analytic solution of the transient behavior of radiation-backscattering heat shields. *Journal of thermophysics and heat transfer*, 6(4) :612–617, 1992. 14

[48] CM Spuckler and R Siegel. Two-flux and diffusion methods for radiative transfer in composite layers. *Journal of Heat Transfer*, 118(1) :218–222, 1996. 14

[49] AG De Marco and FC Lockwood. A new flux model for the calculation of radiation in furnaces. *La rivista dei Combustibili*, 29 :184–196, 1975. 14

[50] GD Stefanidis, B. Merci, GJ Heynderickx, and GB Marin. CFD simulations of steam cracking furnaces using detailed combustion mechanisms. *Computers & Chemical Engineering*, 30(4) :635–649, 2006. 14

[51] L. Dombrovsky, J. Randrianalisoa, and D. Baillis. Modified two-flux approximation for identification of radiative properties of absorbing and scattering media from directional-hemispherical measurements. *Optical Society of America A*, 23(1) :91–98, 2006. 14

[52] S. Jendoubi, HS Lee, and R-K Kim. Discrete ordinates solutions for radiatively participating media in a cylindrical enclosure. *Journal of Thermophysics and Heat Transfer*, 7(2) :213–219, 1993. 14

[53] R. Vaillon, M. Lallemand, and D. Lemonnier. Radiative heat transfer in orthogonal curvilinear coordinates using the discrete ordinates method. *Journal of Quantitative Spectroscopy and Radiative Transfer*, 55(1) :7–17, 1996. 14, 15

[54] D. Balsara. Fast and accurate discrete ordinates methods for multidimensional radiative transfer. part I, basic methods. *Journal of Quantitative Spectroscopy and Radiative Transfer*, 69(6) :671–707, 2001. 14

[55] R. Koch and R. Becker. Evaluation of quadrature schemes for the discrete ordinates method. *Journal of Quantitative Spectroscopy and Radiative Transfer*, 84(4) :423–435, 2004. 14

[56] D. Joseph, M. El Hafi, R. Fournier, and B. Cuenot. Comparison of three spatial differencing schemes in discrete ordinates method using three-dimensional unstructured meshes. *International Journal of Thermal Sciences*, 44(9) :851–864, 2005. 14

[57] SC Mishra, HK Roy, and N. Misra. Discrete ordinate method with a new and a simple quadrature scheme. *Journal of Quantitative Spectroscopy and Radiative Transfer*, 101(2) :249–262, 2006. 14

[58] L. Trovalet, G. Jeandel, PJ Coelho, and F. Asllanaj. Modified finite-volume method based on a cell vertex scheme for the solution of radiative transfer problems in complex 3D geometries. *Journal of Quantitative Spectroscopy and Radiative Transfer*, 112(17) :2661–2675, 2011. 14

[59] PJ Coelho. Advances in the discrete ordinates and finite volume methods for the solution of radiative heat transfer problems in participating media. *Journal of Quantitative Spectroscopy and Radiative Transfer*, 145 :121–146, 2014. 14

[60] WA Fiveland. Three-dimensional radiative heat-transfer solutions by the discrete-ordinates method. *Journal of Thermophysics and Heat Transfer*, 2(4) :309–316, 1988. 14

[61] WA Fiveland. The selection of discrete ordinate quadrature sets for anisotropic scattering. *Fundamentals of Radiation Heat Transfer*, 160 :89–96, 1991. 14

[62] VI Lebedev. Quadratures on a sphere. *USSR Computational Mathematics and Mathematical Physics*, 16(2) :10–24, 1976. 14

[63] RO Castro and JP Trelles. Spatial and angular finite element method for radiative transfer in participating media. *Journal of Quantitative Spectroscopy and Radiative Transfer*, 157 :81–105, 2015. 14, 15

[64] CE Lee. The discrete Sn approximation to transport theory. Technical report, Los Alamos Scientific Lab., N. Mex., 1961. 14

[65] CP Thurgood, A. Pollard, and HA Becker. The TN quadrature set for the discrete ordinates method. *Journal of Heat Transfer*, 117(4) :1068–1070, 1995. 14

[66] SH Kim and KY Huh. Assessment of the finite-volume method and the discrete ordinate method for radiative heat transfer in a three-dimensional rectangular enclosure. *Numerical Heat Transfer : Part B : Fundamentals*, 35(1) :85–112, 1999. 14

[67] SH Kim and KY Huh. A new angular discretization scheme of the finite volume method for 3-D radiative heat transfer in absorbing, emitting and anisotropically scattering media. *International Journal of Heat and Mass Transfer*, 43(7) :1233–1242, 2000. 14

[68] GN Lygidakis and IK Nikolos. Using the finite-volume method and hybrid unstructured meshes to compute radiative heat transfer in 3-D geometries. *Numerical Heat Transfer, Part B : Fundamentals*, 62(5) :289–314, 2012. 14

[69] T Yin, J-P Gastellu-Etchegorry, N. Lauret, E. Grau, and J. Rubio. A new approach of direction discretization and oversampling for 3D anisotropic radiative transfer modeling. *Remote Sensing of Environment*, 135 :213–223, 2013. 14

[70] LH Liu and JY Tan. Meshless local Petrov–Galerkin approach for coupled radiative and conductive heat transfer. *International Journal of Thermal Sciences*, 46(7) :672–681, 2007. 15

[71] H. Sadat, C-A Wang, and V. Le Dez. Meshless method for solving coupled radiative and conductive heat transfer in complex multi-dimensional geometries. *Applied Mathematics and Computation*, 218(20) :10211–10225, 2012. 15

[72] LG Stenholm, H. Störzer, and R. Wehrse. An efficient method for the solution of 3-D radiative transfer problems. *Journal of Quantitative Spectroscopy and Radiative Transfer*, 45(1) :47–56, 1991. 15

[73] AH Hielscher, RE Alcouffe, and RL Barbour. Comparison of finite-difference transport and diffusion calculations for photon migration in homogeneous and heterogeneous tissues. *Physics in Medicine and Biology*, 43(5) :1285, 1998. 15

[74] Y. Qiao, H. Qi, Q. Chen, L. Ruan, and H Tan. Multi-start iterative reconstruction of the radiative parameter distributions in participating media based on the transient radiative transfer equation. *Optics Communications*, 351 :75–84, 2015. 15

[75] JC Chai, HS Lee, and SV Patankar. Finite volume method for radiation heat transfer. *Journal of Thermophysics and Heat Transfer*, 8(3) :419–425, 1994. 15

[76] D. Lacroix, N. Berour, P. Boulet, and G. Jeandel. Transient radiative and conductive heat transfer in non-gray semitransparent two-dimensional media with mixed boundary conditions. *Heat and Mass Transfer*, 42(4) :322–337, 2006. 15

[77] VA Fiveland and JP Jessee. Acceleration schemes for the discrete ordinates method. *Journal of Thermophysics and Heat Transfer*, 10(3) :445–451, 1996. 15

[78] P. Boulet, A. Collin, and JL Consalvi. On the finite volume method and the discrete ordinates method regarding radiative heat transfer in acute forward anisotropic scattering media. *Journal of Quantitative Spectroscopy and Radiative Transfer*, 104(3) :460–473, 2007. 15

[79] H. Grissa, F Askri, MB Salah, and SB Nasrallah. Three-dimensional radiative transfer modeling using the control volume finite element method. *Journal of Quantitative Spectroscopy and Radiative Transfer*, 105(3) :388–404, 2007. 15

[80] M. Gazdallah, V. Feldheim, K. Claramunt, and C. Hirsch. Finite volume method for radiative heat transfer in an unstructured flow solver for emitting, absorbing and scattering media. In *Journal of Physics : Conference Series*, volume 369, page 012020. IOP Publishing, 2012. 15

[81] B. Ramamoorthy, GC Cheng, RP Koomullil, and RK Rahmani. Finite volume method for non-equilibrium radiative heat transfer. *International Journal of Heat and Mass Transfer*, 65 :670–681, 2013. 15

[82] M. Marin, F. Asllanaj, and D. Maillet. Sensitivity analysis to optical properties of biological tissues subjected to a short-pulsed laser using the time-dependent radiative transfer equation. *Journal of Quantitative Spectroscopy and Radiative Transfer*, 133 :117–127, 2014. 15

[83] F. Asllanaj, A. Addoum, and S. Contassot-Vivier. Detection of tumor-like inclusions embedded within human liver tissue using a short-pulsed near-infrared laser beam : Parallel simulations with radiative transfer equation. *Journal of Quantitative Spectroscopy and Radiative Transfer*, 165 :1–11, 2015. 15

[84] PJ Coelho, N. Crouseilles, P. Pereira, and M. Roger. Multi-scale methods for the solution of the radiative transfer equation. *Journal of Quantitative Spectroscopy and Radiative Transfer*, 2015. 15

[85] H Amiri and PJ Coelho. A parametric study of optimal number and location of radiant heaters in enclosures with participating media. *Scientia Iranica. Transaction B, Mechanical Engineering*, 23(1) :206, 2016. 15

[86] PJ Coelho. Advances in the discrete ordinates and finite volume methods for the solution of radiative heat transfer problems in participating media. *Journal of Quantitative Spectroscopy and Radiative Transfer*, 145 :121–146, 2014. 15

[87] JN Reddy and VD Murty. Finite-Element Solution of Integral Equations Arising in Radiative Heat Transfer and Laminar Boundary-Layer Theory. *Numerical Heat Transfer, Part B : Fundamentals*, 1(3) :389–401, 1978. 15

[88] W. An, LM Ruan, H Qi, and LH Liu. Finite element method for radiative heat transfer in absorbing and anisotropic scattering media. *Journal of Quantitative Spectroscopy and Radiative Transfer*, 96(3) :409–422, 2005. 15

[89] LH Liu. Least-squares finite element method for radiation heat transfer in graded index medium. *Journal of Quantitative Spectroscopy and Radiative Transfer*, 103(3) :536–544, 2007. 15

[90] JM Zhao, JY Tan, and LH Liu. A deficiency problem of the least squares finite element method for solving radiative transfer in strongly inhomogeneous media. *Journal of Quantitative Spectroscopy and Radiative Transfer*, 113(12) :1488–1502, 2012. 15

[91] JE Morel and JM McGhee. A self-adjoint angular flux equation. *Nuclear Science and Engineering*, 132(3) :312–325, 1999. 15

[92] R Becker, R Koch, H-J Bauer, and MF Modest. A finite element treatment of the angular dependency of the even-parity equation of radiative transfer. *Journal of Heat Transfer*, 132(2) :023404, 2010. 15

[93] O. Balima, T. Pierre, A. Charette, and D. Marceau. A least square finite element formulation of the collimated irradiation in frequency domain for optical tomography applications. *Journal of Quantitative Spectroscopy and Radiative Transfer*, 111(2) :280–286, 2010. 15

[94] JC Ragusa and Y. Wang. A two-mesh adaptive mesh refinement technique for SN neutral-particle transport using a higher-order DGFEM. *Journal of Computational and Applied Mathematics*, 233(12) :3178–3188, 2010. 16

[95] X. Cui and B.Q Li. Discontinuous finite element solution of 2-d radiative transfer with and without axisymmetry. *Journal of Quantitative Spectroscopy and Radiative Transfer*, 96(3) :383–407, 2005. 16

[96] X Cui and Ben Q Li. A discontinuous finite-element formulation for multidimensional radiative transfer in absorbing, emitting, and scattering media. *Numerical Heat Transfer, Part B : Fundamentals*, 46(5) :399–428, 2004. 16

[97] X. He, E. Lee, L. Wilcox, R. Munipalli, and L. Pilon. A High-Order-Accurate GPU-Based Radiative Transfer Equation Solver for Combustion and Propulsion Applications. *Numerical Heat Transfer, Part B : Fundamentals*, 63(6) :457–484, 2013. 16

[98] O. Balima, Y. Favennec, J. Boulanger, and A. Charette. Optical tomography with the discontinuous Galerkin formulation of the radiative transfer equation in frequency domain. *Journal of Quantitative Spectroscopy and Radiative Transfer*, 113(10) :805–814, 2012. 16

Chapitre 2

Discrétisation spatiale : méthodes de Galerkin

Sommaire

Avant-propos

Ce chapitre présente, en deux dimensions d'espace, une comparaison entre des méthodes SUPG et Garlerkin discontinues pour la résolution de l'équation de transport radiatif. Ce chapitre commence par une présentation très générale de ces deux méthodes, notamment lors de la construction de la base éléments finis. Une comparaison détaillée est ensuite effectuée entre les deux schémas, pour la résolution de problèmes radiatifs. De plus, des conditions aux limites spéculaires ont été intégrées à la modélisation mathématique. Cette deuxième partie, qui constitue le cœur du chapitre, a été publié dans le "Journal of Quantitative Spectroscopy and Radiative Transfer" (JQSRT) en août 2016 [1].

2.1 Quelques généralités sur les méthodes de Galerkin

Avant d'appliquer une méthode de Galerkin, il est nécessaire d'approcher le domaine d'étude $\mathcal{D}$ par un domaine polyédrique qui est "maillé". Soit donc un maillage, noté $\mathcal{M}_h$, constitué d'un ensemble de mailles $\mathcal{C}_i$, $i = 1, \cdots, N_e$. La figure 2.1 présente schématiquement un maillage possible pour un ouvert régulier $\mathcal{D}$.

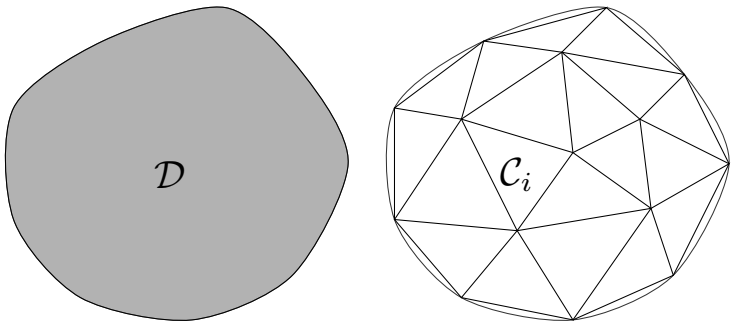

FIGURE 2.1 – Gauche : Domaine $\mathcal{D}$ – Droite : Maillage associé à $\mathcal{D}$

De prime abord, dans chaque maille $\mathcal{C}_i$, il peut être utilisé une infinité de fonctions. Les méthodes éléments finis consistent alors à créer une base locale, libre et génératrice et de **dimension finie** $\mathcal{B}_{\text{loc}} = \{\hat{\sigma}_1, \cdots, \hat{\sigma}_{n_f}\}$. Un grand nombre de bases possibles existe dans la littérature [2], mais seules les bases d'éléments finis lagrangiennes sont abordées dans cette section. Les bases éléments finis lagrangiennes sont construites à partir des bases polynomiales $\mathbb{P}_k$. Définissons $\boldsymbol{x}_i$, les n_f degrés de liberté sur lesquels est créée la base éléments finis. Selon la méthode lagrangienne, la base $\mathcal{B}_{\text{loc}}$ est construite de telle sorte que les fonctions de base vérifient $\hat{\sigma}_i(\boldsymbol{x}_j) = \mathbb{1}_{[i=j]}$. La figure 2.2 présente, à titre d'exemple, les trois fonctions de base lagrangiennes $\mathbb{P}_1$ pour une maille triangulaire $\mathcal{C}_i$.

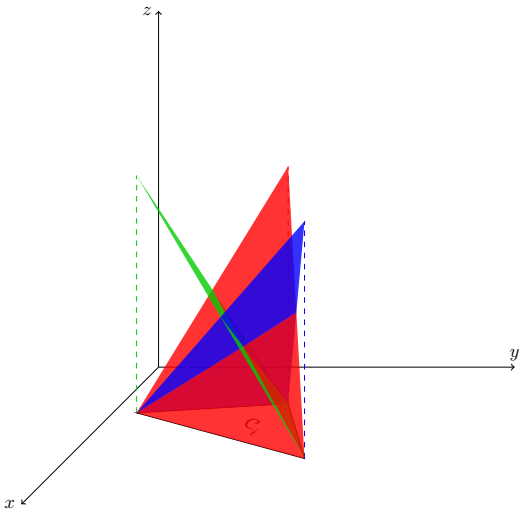

FIGURE 2.2 – Les 3 fonctions de base dans $\mathbb{P}_1$ pour une maille triangulaire $\mathcal{C}_i$

Dans le cas de la base $\mathbb{P}_2$ en 2 dimensions, on a besoin de 6 degrés de liberté correspondant généralement aux sommets ainsi qu'aux milieux de chaque coté du triangle associé. Dans la base $\mathbb{P}_0$, l'orthocentre du triangle est le plus souvent utilisé comme

unique degré de liberté. Une fois la base créée sur chaque maille, on peut alors créer une base éléments finis globale pour le maillage $\mathcal{M}_h$, appelée $\mathcal{B} = \{\varphi_1, \cdots, \varphi_{N_{\text{dof}}}\}$. Entre les méthodes Galerkin continues et Galerkin discontinues, la création de cette base diffère.

Remarque : Pour déterminer facilement le nombre de degrés de liberté nécessaire à la construction d'une base locale, génératrice et lagrangienne, il suffit de compter le nombre de fonctions de base $\mathbb{P}_k$ dans sa base **usuelle**. À titre d'exemple, la base usuelle de $\mathbb{P}_2$ en 2 dimensions est $\{1, x, y, x^2, y^2, xy\}$. Il y a bien 6 degrés de liberté.

2.1.1 Méthodes Galerkin continues

Les méthodes de Galerkin continues s'appuient sur des fonctions de base **continues** en espace, dans $\mathcal{M}_h$. En s'aidant des fonctions de la base lagrangienne par maille, les fonctions de base du maillage se déterminent facilement. En effet, la fonction de base φ_i associée à $\boldsymbol{x}_i$ est la réunion des fonctions de base locales $\hat{\sigma}_j$ associées à ce degré de liberté. Ces fonctions de base vérifient également $\varphi_i(\boldsymbol{x}_j) = \mathbb{1}_{[i=j]}$. La figure 2.3 montre à gauche un exemple de fonctions $\varphi_i(\boldsymbol{x})$ de base $\mathbb{P}_1$ pour un des degrés de liberté du maillage $\mathcal{M}_h$. Ces fonctions sont surnommées les fonctions "chapeaux" vis-à-vis de leur forme pointue. La figure 2.3 de droite présente les degrés de liberté $\boldsymbol{x}_i$ nécessaires pour créer une base lagrangienne $\mathbb{P}_1$, libre, génératrice et continue.

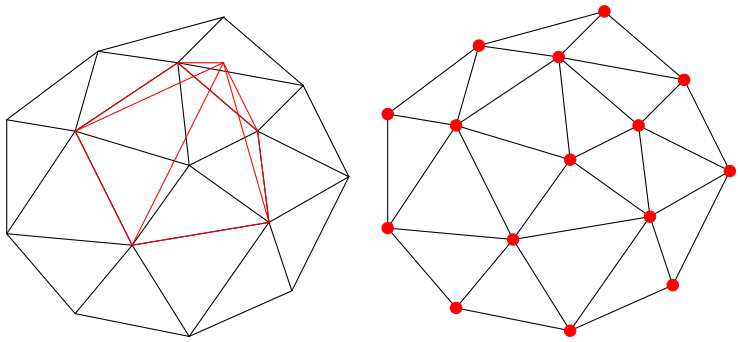

FIGURE 2.3 – Une fonction de base φ_i de V_h – Degrés de liberté de $\mathbb{P}_1$

Une fois la base lagrangienne du maillage construite, définissons V_h l'espace des fonctions générées par cette base. Cet espace fonctionnel peut être défini par :

$$V_h = \{v_h \in C^0(\mathcal{D}) \text{ telle que } v_{h|\mathcal{C}_i} \in \mathbb{P}_k(\mathcal{C}_i),\ i = 1, \cdots, N_e, +CL\} \tag{2.1}$$

Toute fonction $v_h \in V_h$ est générée par la base $\{\varphi\}_{i=1,\cdots,N_{\text{dof}}}$. La fonction v_h peut alors s'écrire comme une somme pondérée des fonctions de base :

$$v_h(\boldsymbol{x}) = \sum_{i=0}^{N_{\text{dof}}} \alpha_i\ \varphi_i(\boldsymbol{x})\ , \forall v \in V_h\ ,\ \alpha_i \in \mathbb{R} \tag{2.2}$$

En parallèle, supposons l'équation linéaire $E(u) = 0$, avec $u \in \mathcal{H}^m$, où $\mathcal{H}^m$ est un espace de Sobolev. Si u n'est pas déterminable analytiquement, alors le passage par la formulation "faible" de l'équation $E(u) = 0$ permet de générer une solution approchée de u par les éléments finis. Pour construire la formulation faible, multiplions l'équation

$E(u) = 0$ par une fonction linéaire $f(v)$, où $v \in V$ est appelé couramment fonction "test", puis intégrons sur le domaine d'étude $\mathcal{D}$:

$$\int_{\mathcal{D}} E(u)f(v)\ \mathrm{d}\boldsymbol{x} = 0\ , \forall v \in V \tag{2.3}$$

Ensuite, après intégrations par parties par la méthode de Green, en vue d'exhiber explicitement les conditions à appliquer aux bord, l'équation (2.3) s'écrit sous sa forme faible :

$$a(u, v) = l(v)\ , \forall v \in V \tag{2.4}$$

Comme u n'est pas explicite dans V et comme par construction $V_h \subset V$, cherchons alors une estimation de la solution dans V_h, où les fonctions sont générées pas des fonctions de base **explicites**. Définissons $u_h \in V_h$ le projeté de u dans V_h. Comme $V_h \subset V$ alors la formulation faible $a(u_h, v) = l(v)$ est bien définie, quelque soit $v \in V$. Définissons $v_h \in V_h$ comme une des fonctions "test". La formulation faible peut se réécrire de cette façon :

$$a(u_h, v_h) = l(v_h)\ , \forall v_h \in V_h \tag{2.5}$$

Chercher la solution u_h, solution de (2.5) revient à chercher les constantes α_i. En choisissant $v_h = \varphi_i$, avec l'équation (2.2) et avec la bi-linéarité de l'opérateur $a(\cdot, \cdot)$, la formulation faible devient :

$$\sum_{j=1}^{N_{\text{dof}}} a(\varphi_j, \varphi_i)\alpha_j = l(\varphi_i)\ , i = 1, \cdots, N_{\text{dof}} \tag{2.6}$$

On a alors un système linéaire à N_{dof} équations à N_{dof} inconnues à résoudre. Celui-ci peut s'écrire formellement $A\boldsymbol{\alpha} = b$, avec $\boldsymbol{\alpha} = [\alpha_1, \cdots, \alpha_{N_{\text{dof}}}]$, $A = (a(\varphi_i, \varphi_j))_{0 \leq i,j \leq N_{\text{dof}}}$ et $b = (l(\varphi_i))_{0 \leq i \leq N_{\text{dof}}}$. La fonction $u_h \in V_h$ solution approchée de u, solution de $E(u) = 0$, est alors déterminée par résolution de ce système linéaire.

Remarque : Comme les fonctions de bases sont continues en espace, la base $\mathbb{P}_0$ n'est pas applicable pour les méthodes de Galerkin continues.

2.1.2 Méthodes de Galerkin Discontinues

Les méthodes de Galerkin discontinues s'appuient sur des fonctions de base **discontinues** en espace sur $\mathcal{M}_h$. La base de fonctions discontinues et lagrangiennes $\{\varphi_i\}$ du maillage $\mathcal{M}_h$ est alors le cumul de toutes les bases lagrangiennes de chacune des mailles. La figure 2.4 montre une des fonctions de base $\mathbb{P}_1$ discontinues du maillage ainsi que les degrés de liberté nécessaires à la construction de cette base. On peut constater qu'il peut y avoir plusieurs degrés de libertés en un même point de l'espace.

La base lagrangienne discontinue $\{\varphi_1, \cdots, \varphi_{N_{\text{dof}}}\}$ est construite pour être libre et génératrice. Définissons $\tilde{V}_h$ l'espace des fonctions générées par cette base. Il peut être défini par :

$$\tilde{V}_h = \{v_h \in L_2(\mathcal{D}) \text{ telle que } v_{h|\mathcal{C}_i} \in \mathbb{P}_k(\mathcal{C}_i),\ i = 1, \cdots, N_e, +CL\} \tag{2.7}$$

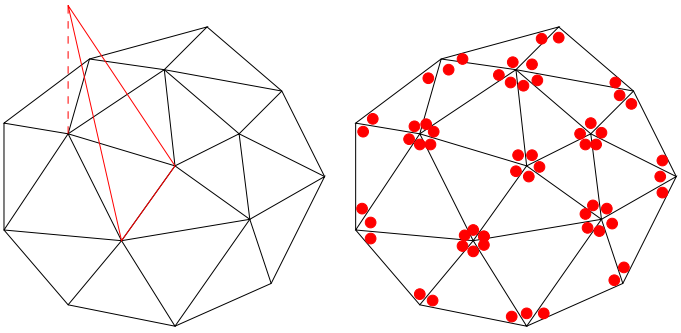

FIGURE 2.4 – Une fonction de base de $\tilde{V}_h$ – Degrés de liberté de $\mathbb{P}_1$

Pour trouver une solution $u \in V$ de l'équation $E(u) = 0$, il faut aussi se ramener à une forme variationnelle, du même type que pour (2.4). Pour cela, on multiplie l'équation par une fonction linéaire $f(v)$ avec $v \in V$ sur **chacune des mailles** $\mathcal{C}_i$:

$$\int_{\mathcal{C}_i} E(u) f(v) \, \mathrm{d}\boldsymbol{x} = 0 \ , \forall v \in V \ , \forall i = 1, \cdots, N_e \tag{2.8}$$

Après intégration par partie en utilisant le théorème de Green, en vue d'exhiber les conditions aux limites sur chaque maille, il apparaît N_e formulations faibles locales que l'on somme pour avoir une formulation faible globale de la forme $a(u, v) = l(v)$. Le système linéaire $A\boldsymbol{\alpha} = b$ est alors créé, puis résolu pour la détermination de la solution $u_h \in \tilde{V}_h$.

Solution of the 2-D steady-state radiative transfer equation in participating media with specular reflections using SUPG and DG finite elements

D. Le Hardy* , Y. Favennec* , B. Rousseau*

LTN UMR CNRS 6607, Université de Nantes, France

Abstract

The 2D radiative transfer equation coupled with specular reflection boundary conditions is solved using finite element schemes. Both Discontinuous Galerkin and Streamline-Upwind Petrov–Galerkin variational formulations are fully developped. These two schemes are validated step-by-step for all involved operators (transport, scattering, reflection) using analytical formulations. Numerical comparisons of the two schemes, in terms of convergence rate, reveal that the quadratic SUPG scheme proves efficient for solving such problems. This comparison constitutes the main issue of the paper. Moreover, the solution process is accelerated using block SOR-type iterative methods, for which the determination of the optimal parameter is found in a very cheap way.

Keywords : *Steady Radiative Transfer Equation, Specular Reflection, Discontinuous Galerkin, Streamline-Upwind Petrov–Galerkin, Jacobi, Gauss-Seidel, Successive Over-Relaxation*

2.2 Introduction

Thermal radiation is a heat transfer mode important to take into account in many practical high temperature engineering applications such as, in modelling industrial furnaces, combustion chambers, or forming processes, to cite but a few [3, 4]. The forward model commonly used to model the propagation of thermal radiation within semi-transparent participating media is the so-called radiative transfer equation (RTE). This equation is integro-differential, so that its solution is far from being given straightforwardly, especially when the geometry of the bounded domain cannot be considered as mono-dimensional. In such cases, the use of numerical and physical approximation methods is mandatory to access the solution of the RTE.

In the field of numerical methods, for the solution of radiative transfer problems in participating media, the finite volume method (FVM) for the space discretization, coupled with the discrete ordinated method (DOM) or other methods, are among the most widely used. Indeed, they can provide good accuracy in a wide range of practical problems with moderate computational requirements [5, 6, 7, 8]. The review paper [9] lists recent advances in such numerical methods for the solution of the RTE with FVM.

Nomenclature

β	extinction coefficient
κ	absorption coefficient
Φ	scattering phase function
ρ	reflectivity coefficient
σ_s	scattering coefficient
$\tilde{n}_i$	refraction index
$\tilde{L}$	incoming radiance
G	incident radiation
L	radiance
L_b	emitting radiance of blackbody

Angle and space

$\boldsymbol{n}$	outward unit normal vector of a boundary
$\boldsymbol{s}$	direction
ω_i	quadrature weight
$\boldsymbol{x}$	space coordinates
δ, γ	proportion of solide angle
$\Delta\theta$	angle between two nearby discrete directions
$\mathcal{C}_i$	cell i
$\mathcal{D}$	space of medium
Ω	Solide angle
$\partial\mathcal{D}_*$	part of boundary of medium
$\mathcal{S}^{n-1}$	unit disk
h	maximal size of triangles of a mesh
N_d	number of discrete directions
N_e	number of mesh elements
r	relaxation parameter
v	test function

Subscripts and superscripts

$+$	boundary for outgoing radiance
$-$	boundary for incoming radiance
inc	incident direction
in	input radiance
out	output radiance
ς	permutation function
m, j, k	discrete direction of radiation
N	number of the iteration

Other methods that have been used to solve the RTE include, the zonal method [10], natural element and meshless methods [11, 12], or the finite difference method [13].

Besides above cited methods, the finite element method (FEM) has a growing attention mainly because it is based on the variational formulation, thus allowing theoretical studies such as existence, uniqueness and stability of the solution. Also, very complex geometries can be dealt with, and FEM can be versatile as soon as the variational formulation is written down in a general framework. For instance, using appropriate finite element libraries such as those in [14], for a given variational formulation, the theoretical development of the code with quadratic Lagrange functions is not more expensive than with linear Lagrange functions. In the same spirit, the change of boundary condition location or sources can be performed in a very straightforward way, as well as the modification of physical properties and so on, because, basically, one of the main effort resides in writing down the variational formulation in a general framework. This has been used many times in the last decade for the RTE, for instance in [15, 16, 17].

The RTE being an equation in which the advection operator plays a central role, it might sometimes be inappropriate to employ ordinary FEM due to the presence of oscillations, especially when the albedo gets high. In order to cope up with such a difficulty, decentered schemes such as the Least-Squares (LS) or Streamline Upwind Petrov–Galerkin (SUPG) allows to drastically avoid oscillations, but at the price of adding artificial numerical diffusion. Recently, the LS-FEM and related SUPG schemes

have been used in [18, 19, 20, 21, 22, 23] mostly in view of optical tomography applications. Note that in most of these papers the free output bondary condition was considered, not the one allowing reflections. Also, another difficulty arising with pure LS-FEM is that the number of terms in the variational formulation can become very high, especially when considering the specular boundary condition as it is the case in this study. That is the reason why the SUPG scheme, which is a purely decentered finite element scheme is the subject of this study.

Another possibility for the solution of the RTE based on variational formulations is to use a Discontinuous Galerkin (DG) formulation. The DG method, firstly developped in the field of neutron transport [24], has then been used for solving the transport problem of radiation [25, 26, 27, 28, 29, 30]. This method is very attractive because it has all the advantages of the FEM and, moreover, it is also elementwise conservative, such as the FVM.

Based on the above-cited methods, several extensions have been developped for instance the Multi-Scale Finite Element Method [31] with mesh adaptation or the use of vector radiative transfer equation to adjust atmosphere and surface properties [32].

As far as we are concerned, the numerical developments are performed in view of radiative characterization of multi-dimensional materials such as open-cell foams for instance [33]. Such characterization relies on solving an inverse problem that demands numerous iterations of "forward" model while changing the physical properties. As a consequence, the numerical tools must lead to a simulation that is i) accurate in the sense that the approximated numerical solution must be close enough to the solution of the continuous problem, ii) robust in the sense that the solution is of equal quality in various situations (physical properties, boundary conditions, etc.), and iii) effective in the sense that the solution is robust and accurate in a reasonnable CPU time.

The physical model of concern is now precised. At a given temperature, the RTE problem consists in searching the radiance $L(\boldsymbol{x}, \boldsymbol{s})$ in a medium $\mathcal{D}$ such that :

$$(\boldsymbol{s} \cdot \nabla + \kappa + \sigma_s)\, L(\boldsymbol{x}, \boldsymbol{s}) - \sigma_s \oint_{\mathcal{S}^{n-1}} L(\boldsymbol{x}, \boldsymbol{s}')\Phi(\boldsymbol{s}, \boldsymbol{s}')\, \mathrm{d}\boldsymbol{s}' = \kappa L_b \quad \forall \boldsymbol{s} \in \mathcal{S}^{n-1} \tag{2.9}$$

where $\boldsymbol{s} \in \mathcal{S}^{n-1}$ is the direction of propagation of L at the location $\boldsymbol{x}$ ($\mathcal{S}^{n-1}$ is the unit circle in 2D), κ and σ_s are the homogeneized absorption and scattering coefficients, respectively, and $\Phi(\boldsymbol{s}, \boldsymbol{s}')$ is the scattering phase function. The spectral dependance of physical properties (and thus of the radiance) is omitted for clarity considerations.

In applications considered here, the medium is illuminated with a collimated beam (i.e. with $\boldsymbol{s} = \boldsymbol{s}_{\text{in}}$ and $\boldsymbol{s} \cdot \boldsymbol{n} < 0$ on the surface boundary $\boldsymbol{x} \in \partial\mathcal{D}_0$) such that the incoming part of the boundary condition can be written as $L(\boldsymbol{x}, \boldsymbol{s}) = \tilde{L}_{\text{in}} \times \mathbb{1}_{[\boldsymbol{s}=\boldsymbol{s}_{\text{in}}]} \times \mathbb{1}_{[\boldsymbol{x}\in\partial\mathcal{D}_0]}$. Added to this Dirichlet-type condition, specular reflection is also considered. Such external boundary condition has been dealt with using FVM [34]. Also, [35, 36] used such internal boundary condition coupled with refraction phenomenon with the frequency version of the RTE using FEM for modeling light propagation in biological tissues in view of optical tomography.

The specular reflection phenomenon specifies that the outcoming radiance $L(\boldsymbol{x}, \boldsymbol{s}_{\text{out}})$ is partially reflected on a direction $\boldsymbol{s}$ (with $\boldsymbol{s}_{\text{out}} \cdot \boldsymbol{n} > 0$ and $\boldsymbol{s} \cdot \boldsymbol{n} < 0$) according to the Fresnel law at the rate $\rho(\boldsymbol{s}_{\text{out}} \cdot \boldsymbol{n})L(\boldsymbol{x}, \boldsymbol{s}_{\text{out}})$ where $\rho(\boldsymbol{s}_{\text{out}} \cdot \boldsymbol{n})$ is the reflectivity. This

function depends on both the angle between the impact direction and the normal of the boundary and on the complex refraction index $\tilde{n}_{\text{in}}$ and $\tilde{n}_{\text{out}}$ of both the medium and its surrounding. The reflected part is thus $L(\boldsymbol{x}, \boldsymbol{s}) = \rho(\boldsymbol{s}_{\text{out}} \cdot \boldsymbol{n}) L(\boldsymbol{x}, \boldsymbol{s}_{\text{out}}) \times \mathbb{1}_{[\boldsymbol{x} \in \partial\mathcal{D}]}$. Combining the two physical phenomena, the boundary condition including Dirichlet and specular reflection is written as :

$$L(\boldsymbol{x}, \boldsymbol{s}) = \tilde{L}_{in} \times \mathbb{1}_{[\boldsymbol{s}=\boldsymbol{s}_{in}]} \times \mathbb{1}_{[\boldsymbol{x} \in \partial\mathcal{D}_0]} + \rho(\boldsymbol{s}_{out} \cdot \boldsymbol{n}) L(\boldsymbol{x}, \boldsymbol{s}_{out}) \times \mathbb{1}_{[\boldsymbol{x} \in \partial\mathcal{D}]} \tag{2.10}$$

The problem dealt with in this paper concerns the solution of the radiative transfer equation (2.9) coupled with the specific boundary condition (2.10) that accounts for specular reflections. From a material point of view, this concerns radiative transfer in semitransparent materials with optically polished surfaces.

The well-known DOM is the first used ingredient in order to semi-discretize the continuous equations. Such an approximation is given in Section 2.3. Next, spatial discretization schemes are considered in Section 2.4 : firstly, the DG scheme is presented, and the complete variational formulation is written down in a general framework, the SUPG scheme being considered in a second step with the same completeness. Though the development of the variational formulation for such mathematical problem can be found in other forms elsewhere (e.g. in [35, 37]), we believe the one presented in this paper is very detailed and complete, especially for the contribution of the specular reflection at outer boundaries, so that it can be easily understood and extended. Section 2.5 is then dedicated to numerical validations and scheme comparisons. Involved operators are validated one by one using extensively analytical solutions taken from literature or created for the purpose. The developped methodology is, to the best knowledge of the authors, very novel separating appart all terms of the RTE (transport and absorption, scattering, reflection), for both validation and convergence rate studies. It will be seen that both the DG and SUPG schemes behave very well in terms of convergence, but with a greater convergence to number-of-degrees of freedom rate for the SUPG scheme. Finally, a proposed strategy for enhancing the speed-up of the solution using block SOR-type iterative methods is presented in Section 2.6. It is also shown that the optimal relaxation parameter is numerically found to be indepedent of the space mesh, thus allowing a very cheap way to determine it on a highly coarse mesh. The paper then ends in Section 2.7 with concluding remarks and extensions of this work.

2.3 Semi-discretization of continuous equations with the DOM

In most situations, the system of equations (2.9)-(2.10) cannot be analytically solved due to the integral term $\oint_{\mathcal{S}^{n-1}} \cdot \, \mathrm{d}\boldsymbol{s}$ on one hand, and reflections $\rho L(\cdot)$ on the other hand. To cope up with this first difficulty, the Discrete Ordinates Method (DOM) approximates the integral by a quadrature of the kind $\oint_{\mathcal{S}^{n-1}} u(\boldsymbol{s}) \, \mathrm{d}\boldsymbol{s} = \lim_{N_d \to \infty} \sum_{j=1}^{N_d} \omega_j u_j$ where we used the notations $u_j = u(\boldsymbol{s}_j)$. Among the numerous quadrature methods that can be used, the simplest, though effective, is the uniform one. It is schematically depicted in Figure 2.5.

With the DOM, the continuous RTE (2.9) becomes the system of semi-discrete

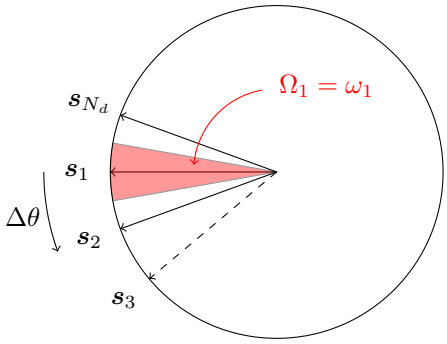

FIGURE 2.5 – Uniform quadrature of solid angle Ω_m with the main direction $\boldsymbol{s}_m$ and the weight ω_m

equations (SDE) :

$$\begin{aligned} &\forall m = 1, \cdots, N_d : \\ &(\boldsymbol{s}_m \cdot \nabla + \kappa + \sigma_s)\, L_m - \sigma_s \textstyle\sum_{j=1}^{N_d} \omega_j L_j \Phi_{m,j} = \kappa L_b \quad \forall \boldsymbol{x} \in \mathcal{D} \end{aligned} \tag{2.11}$$

where we used $L_m = L(\boldsymbol{x}, \boldsymbol{s}_m)$ and $\Phi_{m,j} = \Phi(\boldsymbol{s}_m, \boldsymbol{s}_j)$.

The continuous boundary condition (2.10) is also to be discretized with respect to angles. For a uniform quadrature, the entering radiance $\tilde{L}_{\text{in}}$ is divided proportionally between the two nearby directions, as it is schematically presented in Figure 2.6. The first part of equation (2.10) becomes :

$$\tilde{L}_m = \delta_m \tilde{L}_{\text{in}} \mathbb{1}_{[\boldsymbol{s}_{\text{in}} \in [\boldsymbol{s}_m, \boldsymbol{s}_{m+1}]]} \ , \ \tilde{L}_{m+1} = (1 - \delta_m) \tilde{L}_{\text{in}} \mathbb{1}_{[\boldsymbol{s}_{\text{in}} \in [\boldsymbol{s}_m, \boldsymbol{s}_{m+1}]]} \tag{2.12}$$

with the sharing coefficient being calculated by :

$$\delta_m = \frac{\arccos(\boldsymbol{s}_{\text{in}} \cdot \boldsymbol{s}_{m+1})}{\arccos(\boldsymbol{s}_{\text{in}} \cdot \boldsymbol{s}_m) + \arccos(\boldsymbol{s}_{\text{in}} \cdot \boldsymbol{s}_{m+1})} \in [0, 1] \tag{2.13}$$

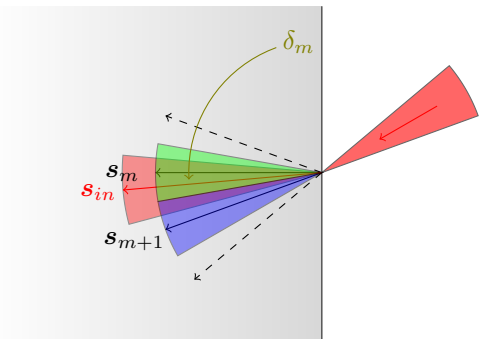

FIGURE 2.6 – Repartition of $\boldsymbol{s}_{\text{in}}$ in $\boldsymbol{s}_m$ and $\boldsymbol{s}_{m+1}$.

For the second part of the boundary condition, we define $\varsigma(\boldsymbol{x}, \boldsymbol{s}_m)$ the index of one incident angle of the reflected angle $\boldsymbol{s}_m$. For a uniform quadrature, as depicted schematically in Figure 2.7, the specular part of the condition (2.10) becomes :

$$L_m = \gamma_m \rho(\boldsymbol{s}_{\varsigma(\boldsymbol{x},\boldsymbol{s}_m)} \cdot \boldsymbol{n}) L_{\varsigma(\boldsymbol{x},\boldsymbol{s}_m)} + (1 - \gamma_m) \rho(\boldsymbol{s}_{\varsigma(\boldsymbol{x},\boldsymbol{s}_m)+1} \cdot \boldsymbol{n}) L_{\varsigma(\boldsymbol{x},\boldsymbol{s}_m)+1} \tag{2.14}$$

with the sharing coefficient being this time calculated by :

$$\gamma_m = \frac{\arccos(\boldsymbol{s}_m \cdot \boldsymbol{s}_{m+1'})}{\arccos(\boldsymbol{s}_m \cdot \boldsymbol{s}_{m'}) + \arccos(\boldsymbol{s}_m \cdot \boldsymbol{s}_{m+1'})} \in [0, 1] \tag{2.15}$$

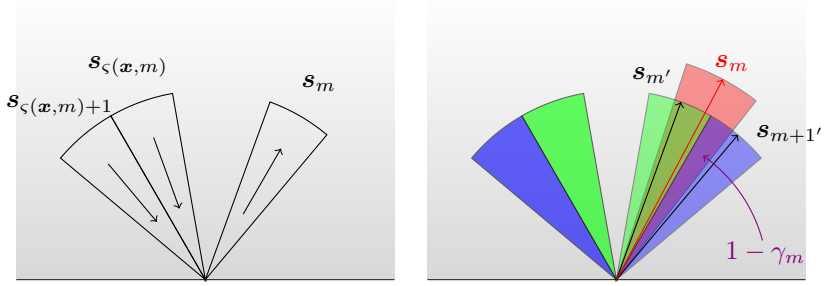

FIGURE 2.7 – Repartition of reflected direction $\boldsymbol{s}_m$ between the incident directions $\boldsymbol{s}_{\varsigma(\boldsymbol{x},m)}$ and $\boldsymbol{s}_{\varsigma(\boldsymbol{x},m)+1}$.

Finally, the discrete boundary condition is the combination of the equations (2.12) and (2.14) :

$$\begin{aligned} L_m = {} & \delta_m \tilde{L}_{\text{in}} \mathbb{1}_{[\boldsymbol{s}_{\text{in}} \in [\boldsymbol{s}_m, \boldsymbol{s}_{m+1}]]} + (1-\delta_{m-1}) \tilde{L}_{\text{in}} \mathbb{1}_{[\boldsymbol{s}_{\text{in}} \in [\boldsymbol{s}_{m-1}, \boldsymbol{s}_m]]} \\ & + \gamma_m \rho(\boldsymbol{s}_{\varsigma(\boldsymbol{x},\boldsymbol{s}_m)} \cdot \boldsymbol{n}) L_{\varsigma(\boldsymbol{x},\boldsymbol{s}_m)} + (1-\gamma_m) \rho(\boldsymbol{s}_{\varsigma(\boldsymbol{x},\boldsymbol{s}_m)+1} \cdot \boldsymbol{n}) L_{\varsigma(\boldsymbol{x},\boldsymbol{s}_m)+1} \end{aligned} \quad \text{on } \partial\mathcal{D} \tag{2.16}$$

2.4 Spatial discretization with FEM

After applying the DOM on the continuous set of equations (2.9)-(2.10), the radiative problem consists in searching $L(\boldsymbol{x}, \boldsymbol{s}_m)$, $\forall m = 1, \cdots, N_d$, for $\boldsymbol{x} \in \mathcal{D}$ that satisfies (2.11) and (2.16), the sharing coefficients δ_m and γ_m being given by (2.13) and (2.15), respectively. This semi-continuous problem is then discretized in space in order to deal with a completely finite problem that can be written down in matrix form. In the following, two distinct FEM-type methods are given, namely the DG method first, and the SUPG method next.

For the sake of simplicity and clarity, it is assumed that the directional entering beam propagates along a given discrete direction, and that it is also the case for the reflected beams. Note that these two conditions can be available at the same time considering for instance a square medium and a uniform angular quadrature.

Before writing down variational formulations for both DG and SUPG schemes, let us define the mesh $\mathcal{M}$ of the domain $\mathcal{D}$ as a finite collection of disjoint polyhedra $\mathcal{M} = \{\mathcal{C}_i\}$, $i = 1, \cdots, N_e$ forming a partition of $\mathcal{D}$, and for which each $\mathcal{C}_i \in \mathcal{M}$ is called a mesh element. Further, let $h_{\mathcal{C}_i}$ denotes the diameter of $\mathcal{C}_i$, and let the meshsize be defined as the real number :

$$h = \max_{i=1,\cdots,N_e} h_{\mathcal{C}_i} \tag{2.17}$$

2.4.1 DG variational formulation

Discontinuous Galerkin schemes may be seen as hybrid methods between FEM and FVM because, on one hand, the variational formulation is the starting point of

mathematical developments and, on the other hand, because the conservation property is preserved. The functional space in which the solution is searched is first to be defined. Let it be :

$$V_h^{\mathrm{DG}} = \left\{ v \in \mathbb{P}_k(\mathcal{C}_i),\ k \in \mathbb{N}^+,\ i = 1, \cdots, N_e \right\} \tag{2.18}$$

which means that a polynom of order k is used within all elements $\mathcal{C}_i$, but there is no continuity prescription between elements. Next, in order to build the DG variational formulation, the integration is performed on each cell $\mathcal{C}_i$ of the mesh, and the cells are then connected by an exchange of flux on the boundary of nearby upstream cells.

The m^{th} equation of the system of semi-discrete equations (2.11) – in short (SDE$_m$) – is multiplied by a test function v before being integrated over each cell $\mathcal{C}_i$:

$$\int_{\mathcal{C}_i} (\boldsymbol{s}_m \cdot \nabla + \beta)\, L_m v \ \mathrm{d}\boldsymbol{x} - \sum_{j=1}^{N_d} \omega_j \Phi_{m,j} \int_{\mathcal{C}_i} \sigma_s L_j v \ \mathrm{d}\boldsymbol{x} = \int_{\mathcal{C}_i} \kappa L_b v \ \mathrm{d}\boldsymbol{x} \tag{2.19}$$

Green's theorem is applied on the first term $\boldsymbol{s}_m.\nabla L_m v$ in order to exhibit flux connexions as well as boundary conditions :

$$\int_{\mathcal{C}_i} \boldsymbol{s}_m \cdot \nabla L_m v \ \mathrm{d}\boldsymbol{x} = -\int_{\mathcal{C}_i} L_m \boldsymbol{s}_m \cdot \nabla v \ \mathrm{d}\boldsymbol{x} + \int_{\partial\mathcal{C}_i} L_m v \boldsymbol{s}_m \cdot \boldsymbol{n} \ \mathrm{d}\boldsymbol{\zeta} \tag{2.20}$$

In order to exhibit the flux connexion in the particular direction $\boldsymbol{s}_m$, the cell border $\partial\mathcal{C}_i$ is split into two parts : $\partial\mathcal{C}_i^{m+} = \{\boldsymbol{\zeta} \in \partial\mathcal{C}_i \mid \boldsymbol{s}_m \cdot \boldsymbol{n} \geq 0\}$ and $\partial\mathcal{C}_i^{m-} = \{\boldsymbol{\zeta} \in \partial\mathcal{C}_i \mid \boldsymbol{s}_m \cdot \boldsymbol{n} < 0\}$. The radiance value on $\partial\mathcal{C}_i^{m+}$ is the radiance of the cell $\mathcal{C}_i$ and the radiance on $\partial\mathcal{C}_i^{m-}$ is chosen to be the one of the upstream nearby cell. This latter radiance is denoted $\hat{L}_m$. With this partition, one has :

$$\int_{\partial\mathcal{C}_i} L_m v \boldsymbol{s}_m \cdot \boldsymbol{n} \ \mathrm{d}\boldsymbol{\zeta} = \int_{\partial\mathcal{C}_i^{m+}} L_m v \boldsymbol{s}_m \cdot \boldsymbol{n} \ \mathrm{d}\boldsymbol{\zeta} + \int_{\partial\mathcal{C}_i^{m-}} \hat{L}_m v \boldsymbol{s}_m \cdot \boldsymbol{n} \ \mathrm{d}\boldsymbol{\zeta} \tag{2.21}$$

At this stage, the essential boundary condition as well as reflections can be expressed on $\partial\mathcal{C}_i^{m-} \cap \partial\mathcal{D}$, i.e. on the condition that the cell is located on physical boundaries :

$$\begin{aligned} \int_{\partial\mathcal{C}_i^{m-}\cap\partial\mathcal{D}} \hat{L}_m v \boldsymbol{s}_m \cdot \boldsymbol{n} \ \mathrm{d}\boldsymbol{\zeta} = &\int_{\partial\mathcal{C}_i^{m-}\cap\partial\mathcal{D}_0} \tilde{L}_{\mathrm{in}} \mathbb{1}_{[\boldsymbol{s}_m = \boldsymbol{s}_{\mathrm{in}}]} v \boldsymbol{s}_m \cdot \boldsymbol{n} \ \mathrm{d}\boldsymbol{\zeta} \\ &+ \int_{\partial\mathcal{C}_i^{m-}\cap\partial\mathcal{D}} \rho(\boldsymbol{s}_{\varsigma(\boldsymbol{x},\boldsymbol{s}_m)} \cdot \boldsymbol{n}) L_{\varsigma(\boldsymbol{x},\boldsymbol{s}_m)} v \boldsymbol{s}_m \cdot \boldsymbol{n} \ \mathrm{d}\boldsymbol{\zeta} \end{aligned} \tag{2.22}$$

Defining $\partial\mathcal{D}_{mj} = \{\boldsymbol{\zeta} \in \partial\mathcal{D} \mid \varsigma(\boldsymbol{x}, \boldsymbol{s}_m) = j\}$, the last integral in the equation (2.22) is split into N_d parts :

$$\int_{\partial\mathcal{C}_i^{m-}\cap\partial\mathcal{D}} \rho(\boldsymbol{s}_{\varsigma(\boldsymbol{x},\boldsymbol{s}_m)}\cdot\boldsymbol{n}) L_{\varsigma(\boldsymbol{x},\boldsymbol{s}_m)} v \boldsymbol{s}_m \cdot \boldsymbol{n} \ \mathrm{d}\boldsymbol{\zeta} = \sum_{j=1}^{N_d} \int_{\partial\mathcal{C}_i^{m-}\cap\partial\mathcal{D}_{mj}} \rho(\boldsymbol{s}_j \cdot \boldsymbol{n}) L_j v \boldsymbol{s}_m \cdot \boldsymbol{n} \ \mathrm{d}\boldsymbol{\zeta} \tag{2.23}$$

Let us denote as $\mathcal{T}(L_m)$, $\mathcal{S}(\boldsymbol{L})$, $\mathcal{R}(\boldsymbol{L})$, $\mathcal{D}(\tilde{L}_{in})$ and $\mathcal{E}(L_b)$ the five parts of the variational formulations related to "transport", "scattering", "reflection", "Dirichlet" and "emission" physics, respectively.

The DG variationnal formulation is formed combining equations (2.19), (2.20), (2.21) and (2.23) and performing a summation on all cells $\mathcal{C}_i$:

$$\mathcal{T}^{\mathrm{DG}}(L_m) + \mathcal{S}^{\mathrm{DG}}(\boldsymbol{L}) + \mathcal{R}^{\mathrm{DG}}(\boldsymbol{L}) = \mathcal{D}^{\mathrm{DG}}(\tilde{L}_{\mathrm{in}}) + \mathcal{E}^{\mathrm{DG}}(L_b) \tag{2.24}$$

with

$$\begin{cases} \mathcal{T}^{\mathrm{DG}}(L_m) = \displaystyle\int_{\mathcal{D}} \beta L_m v \ \mathrm{d}\boldsymbol{x} - \int_{\mathcal{D}} L_m \boldsymbol{s}_m \cdot \nabla v \ \mathrm{d}\boldsymbol{x} \\ \qquad\qquad + \displaystyle\sum_{i=1}^{N_e} \left[\int_{\partial \mathcal{C}_i^{m+}} L_m v \boldsymbol{s}_m \cdot \boldsymbol{n} \ \mathrm{d}\boldsymbol{\zeta} + \int_{\partial \mathcal{C}_i^{m-} \setminus \partial \mathcal{D}} \hat{L}_m v \boldsymbol{s}_m \cdot \boldsymbol{n} \ \mathrm{d}\boldsymbol{\zeta} \right] \\ \mathcal{S}^{\mathrm{DG}}(\boldsymbol{L}) = -\displaystyle\sum_{j=1}^{N_d} \omega_j \Phi_{m,j} \int_{\mathcal{D}} \sigma_s L_j v \ \mathrm{d}\boldsymbol{x} \\ \mathcal{R}^{\mathrm{DG}}(\boldsymbol{L}) = \displaystyle\sum_{j=1}^{N_d} \int_{\partial \mathcal{D}_{mj}} \rho(\boldsymbol{s}_j \cdot \boldsymbol{n}) L_j v \boldsymbol{s}_m \cdot \boldsymbol{n} \ \mathrm{d}\boldsymbol{\zeta} \\ \mathcal{D}^{\mathrm{DG}}(\tilde{L}_{\mathrm{in}}) = -\displaystyle\int_{\partial \mathcal{D}_0} \tilde{L}_{\mathrm{in}} \mathbb{1}_{[\boldsymbol{s}_m = \boldsymbol{s}_{\mathrm{in}}]} v \boldsymbol{s}_m \cdot \boldsymbol{n} \ \mathrm{d}\boldsymbol{\zeta} \\ \mathcal{E}^{\mathrm{DG}}(L_b) = \displaystyle\int_{\mathcal{D}} \kappa L_b v \ \mathrm{d}\boldsymbol{x} \end{cases} \tag{2.25}$$

Let us remark that for most j, $\partial \mathcal{D}_{mj} = \emptyset$ because the incident direction $\boldsymbol{s}_j$ needs to check $\boldsymbol{s}_j \cdot \boldsymbol{n} > 0$ and the reflection direction $\boldsymbol{s}_m$ needs to check $\boldsymbol{s}_m \cdot \boldsymbol{n} < 0$. So the number of non-null components depends on the geometry of the medium. For instance, for a uniform angular quadrature, a square medium has at most two $\partial \mathcal{D}_{mj} \neq \emptyset$ per $\boldsymbol{s}_m$. Also, still for a uniform angular quadrature, a circle has around one half of $\partial \mathcal{D}_{mj} \neq \emptyset$ per $\boldsymbol{s}_m$.

2.4.2 SUPG

The Streamline-Upwind Petrov–Galerkin (SUPG) scheme [38] uses the lagrangian $\mathbb{P}_k$ basis to build the variational formulation. The functional space in which the solution is searched is the ordinary one when using finite elements :

$$V_h^{\mathrm{SUPG}} = \left\{ v \in C^0(\mathcal{D}),\ v \in \mathbb{P}_k(\mathcal{C}_i),\ k \in \mathbb{N}^+,\ i = 1, \cdots, N_e \right\} \tag{2.26}$$

In order to build the SUPG variational formulation, (SDE_m) is multiplied by a test function $\boldsymbol{s}_m \cdot \nabla v$ before integration on $\mathcal{D}$

$$\begin{aligned} \int_{\mathcal{D}} \left(\boldsymbol{s}_m \cdot \nabla + \beta \right) L_m \ \boldsymbol{s}_m \cdot \nabla v \ \mathrm{d}\boldsymbol{x} = & \sum_{j=1}^{N_d} \omega_j \Phi_{m,j} \int_{\mathcal{D}} \sigma_s L_j \ \boldsymbol{s}_m \cdot \nabla v \ \mathrm{d}\boldsymbol{x} \\ & + \int_{\mathcal{D}} \kappa L_b \ \boldsymbol{s}_m \cdot \nabla v \ \mathrm{d}\boldsymbol{x} \end{aligned} \tag{2.27}$$

The SUPG scheme is similar to the Least-Squares scheme (LS) [39]. For LS, the (SDE_m) is multiplied by a test function $v + h\boldsymbol{s}_m \cdot \nabla v$ before integration on $\mathcal{D}$. Usually, the value $h >> 1$ depends of the mesh refinement : the finer the mesh, the higher the

value of h. The SUPG scheme amounts to omit the term v in the LS test function. The LS scheme is supposed to be slightly more accurate than the SUPG scheme, but only for suitable value h. Moreover, SUPG schemes are much faster than LS schemes owing to the fact that less terms are to be computed.

As for the DG scheme, Green's theorem is applied on advection terms $L_*\ \boldsymbol{s}\cdot\nabla v$ in order to exhibit boundary conditions :

$$\begin{cases} \displaystyle\int_{\mathcal{D}} \beta L_m\ \boldsymbol{s}_m\cdot\nabla v\ \ \mathrm{d}\boldsymbol{x} = -\int_{\mathcal{D}} \beta\ \boldsymbol{s}_m\cdot\nabla L_m\ v\ \mathrm{d}\boldsymbol{x} + \int_{\partial\mathcal{D}} \beta L_m v\ \boldsymbol{s}_m\cdot\boldsymbol{n}\ \ \mathrm{d}\boldsymbol{\zeta} \\ \displaystyle\int_{\mathcal{D}} \sigma_s L_j\ \boldsymbol{s}_m\cdot\nabla v\ \ \mathrm{d}\boldsymbol{x} = -\int_{\mathcal{D}} \sigma_s\ \boldsymbol{s}_m\cdot\nabla L_j\ v\ \mathrm{d}\boldsymbol{x} + \underbrace{\displaystyle\int_{\partial\mathcal{D}} \sigma_s L_j v\ \boldsymbol{s}_m\cdot\boldsymbol{n}\ \ \mathrm{d}\boldsymbol{\zeta}}_{(2.28^\star)} \end{cases} \tag{2.28}$$

The integrals on $\partial\mathcal{D}$ allow to express the boundary condition. For the first integral on $\partial\mathcal{D}$ involved in (2.28), the boundary condition is expressed in the same manner as that of the DG scheme. For other integrals, some tricks allow to simplify the variational problem in order to get an appropriate variational formulation : these integrals are splitted into an integral on $\partial\mathcal{D}^{j+} = \{\boldsymbol{\zeta}\in\partial\mathcal{D} \mid \boldsymbol{s}_j\cdot\boldsymbol{n}\geq 0\}$ and into an integral on $\partial\mathcal{D}^{j-} = \{\boldsymbol{\zeta}\in\partial\mathcal{D} \mid \boldsymbol{s}_j\cdot\boldsymbol{n} < 0\}$. We have :

$$(2.28^\star) = \int_{\partial\mathcal{D}^{j+}} \sigma_s L_j v\ \boldsymbol{s}_m\cdot\boldsymbol{n}\ \ \mathrm{d}\boldsymbol{\zeta} + \underbrace{\int_{\partial\mathcal{D}^{j-}} \sigma_s L_j v\ \boldsymbol{s}_m\cdot\boldsymbol{n}\ \ \mathrm{d}\boldsymbol{\zeta}}_{(2.29^\star)} \tag{2.29}$$

The boundary condition is expressed in the last term of (2.29) :

$$\begin{aligned} (2.29^\star) = &\int_{\partial\mathcal{D}_0^{j-}} \sigma_s \tilde{L}_{\mathrm{in}} \mathbb{1}_{[\boldsymbol{s}_j=\boldsymbol{s}_{\mathrm{in}}]} v\ \boldsymbol{s}_m\cdot\boldsymbol{n}\ \ \mathrm{d}\boldsymbol{\zeta} \\ &+ \underbrace{\int_{\partial\mathcal{D}^{j-}} \sigma_s \rho(\boldsymbol{s}_{\varsigma(\boldsymbol{x},\boldsymbol{s}_j)}\cdot\boldsymbol{n}) L_{\varsigma(\boldsymbol{x},\boldsymbol{s}_j)} v\ \boldsymbol{s}_m\cdot\boldsymbol{n}\ \ \mathrm{d}\boldsymbol{\zeta}}_{(2.30^\star)} \end{aligned} \tag{2.30}$$

As for the DG scheme, the integral related to specular reflection is splitted into integrals on $\partial\mathcal{D}_{jk}$:

$$(2.30^\star) = \sum_{k=1}^{N_d} \int_{\partial\mathcal{D}_{jk}} \sigma_s \rho(\boldsymbol{s}_k\cdot\boldsymbol{n}) L_k v\ \boldsymbol{s}_m\cdot\boldsymbol{n}\ \ \mathrm{d}\boldsymbol{\zeta} \tag{2.31}$$

The sum of the N_d integrals in (2.31) is to be multiplied by the weight $w_j\Phi_{m,j}$ as this term comes from (2.27). One has the equations :

$$\begin{aligned} \sum_{j=1}^{N_d} \omega_j\Phi_{m,j} \int_{\partial\mathcal{D}^{j-}} \sigma_s \rho(\boldsymbol{s}_{\varsigma(\boldsymbol{x},\boldsymbol{s}_j)}\cdot\boldsymbol{n}) L_{\varsigma(\boldsymbol{x},\boldsymbol{s}_j)} v\ \boldsymbol{s}_m\cdot\boldsymbol{n}\ \ \mathrm{d}\boldsymbol{\zeta} = \\ \sum_{j=1}^{N_d} \omega_j\Phi_{m,j} \sum_{k=1}^{N_d} \int_{\partial\mathcal{D}_{jk}} \sigma_s \rho(\boldsymbol{s}_k\cdot\boldsymbol{n}) L_k v\ \boldsymbol{s}_m\cdot\boldsymbol{n}\ \ \mathrm{d}\boldsymbol{\zeta} = \\ \sum_{j=1}^{N_d}\sum_{k=1}^{N_d} \int_{\partial\mathcal{D}_{jk}} \sigma_s \omega_j\Phi_{m,j} \rho(\boldsymbol{s}_k\cdot\boldsymbol{n}) L_k v\ \boldsymbol{s}_m\cdot\boldsymbol{n}\ \ \mathrm{d}\boldsymbol{\zeta} \end{aligned} \tag{2.32}$$

Defining the function $\tilde{\rho}_{m,k} = \sum_{l=1}^{N_d} \omega_l \Phi_{m,l} \rho(\boldsymbol{s}_k \cdot \boldsymbol{n}) \mathbb{1}_{[\zeta \in \partial \mathcal{D}_{lk}]}$, for each j involving the integral $\int_{\partial \mathcal{D}_{jk}} \cdot \, \mathrm{d}\boldsymbol{\zeta}$, all terms $\omega_l \Phi_{m,l} \rho(\boldsymbol{s}_k \cdot \boldsymbol{n}) \mathbb{1}_{[\zeta \in \partial \mathcal{D}_{lk}]}$ equal zero except the one for $l = j$. So, let us add this sum of terms into (2.32) and use the definition for $\tilde{\rho}_{m,k}$:

$$(2.32) = \sum_{j=1}^{N_d} \sum_{k=1}^{N_d} \int_{\partial \mathcal{D}_{jk}} \sigma_s \sum_{l=1}^{N_d} \omega_l \Phi_{m,l} \rho(\boldsymbol{s}_k \cdot \boldsymbol{n}) \mathbb{1}_{[\zeta \in \partial \mathcal{D}_{lk}]} L_k v \ \boldsymbol{s}_m \cdot \boldsymbol{n} \ \ \mathrm{d}\boldsymbol{\zeta} =$$
$$\sum_{j=1}^{N_d} \sum_{k=1}^{N_d} \int_{\partial \mathcal{D}_{jk}} \sigma_s \tilde{\rho}_{m,k} L_k v \ \boldsymbol{s}_m \cdot \boldsymbol{n} \ \ \mathrm{d}\boldsymbol{\zeta} \quad (2.33)$$

The purpose of the use of the function $\tilde{\rho}_{m,k}$ was the elimination of the index j in the equation (2.33), so that at this stage, the integrals $\int_{\partial \mathcal{D}_{jk}} \cdot \, \mathrm{d}\boldsymbol{\zeta}$ for $j = 1, \cdots, N_d$ are joined together. It is also pointed out that the boundary $\bigcup_j \partial \mathcal{D}_{jk}$ means the part such as the direction $\boldsymbol{s}_k$ is an incident direction. Also, if $\boldsymbol{s}_k$ is an incident direction, then $\boldsymbol{s}_k \cdot \boldsymbol{n} > 0$. So one can write :

$$\bigcup_j \partial \mathcal{D}_{jk} = \partial \mathcal{D}^{k+} \quad (2.34)$$

The two sums in the equation (2.33) are swap and the integral terms $\int_{\partial \mathcal{D}_{jk}} \cdot \, \mathrm{d}\boldsymbol{\zeta}$ for $j = 1, \cdots, N_d$ are joined together.

$$(2.33) = \sum_{k=1}^{N_d} \sum_{j=1}^{N_d} \int_{\partial \mathcal{D}_{jk}} \sigma_s \tilde{\rho}_{m,k} L_k v \ \boldsymbol{s}_m \cdot \boldsymbol{n} \ \ \mathrm{d}\boldsymbol{\zeta}$$
$$= \sum_{k=1}^{N_d} \int_{\partial \mathcal{D}^{k+}} \sigma_s \tilde{\rho}_{m,k} L_k v \ \boldsymbol{s}_m \cdot \boldsymbol{n} \ \ \mathrm{d}\boldsymbol{\zeta} \quad (2.35)$$

All parts of the variational formulation of SUPG scheme being defined, the variationl formulation is the gathering of the (2.27), (2.28) and (2.35) :

$$\mathcal{T}^{\mathrm{SUPG}}(L_m) + \mathcal{S}^{\mathrm{SUPG}}(\boldsymbol{L}) + \mathcal{R}^{\mathrm{SUPG}}(\boldsymbol{L}) = \mathcal{D}^{\mathrm{SUPG}}(\tilde{L}_{\mathrm{in}}) + \mathcal{E}^{\mathrm{SUPG}}(L_b) \quad (2.36)$$

with

$$\begin{cases} \mathcal{T}^{\mathrm{SUPG}}(L_m) = \displaystyle\int_{\mathcal{D}} \boldsymbol{s}_m \cdot \nabla L_m \ \ \boldsymbol{s}_m \cdot \nabla v \ \ \mathrm{d}\boldsymbol{x} - \int_{\mathcal{D}} \beta \ \boldsymbol{s}_m \cdot \nabla L_m \ v \ \mathrm{d}\boldsymbol{x} \\ \qquad\qquad + \displaystyle\int_{\partial\mathcal{D}^{m+}} \beta L_m v \ \boldsymbol{s}_m \cdot \boldsymbol{n} \ \ \mathrm{d}\boldsymbol{\zeta} \\ \mathcal{S}^{\mathrm{SUPG}}(\boldsymbol{L}) = -\displaystyle\sum_{j=1}^{N_d} \omega_j \Phi_{m,j} \left[-\int_{\mathcal{D}} \sigma_s \ \boldsymbol{s}_m \cdot \nabla L_j \ v \ \mathrm{d}\boldsymbol{x} + \int_{\partial\mathcal{D}^{j+}} \sigma_s L_j v \ \boldsymbol{s}_m \cdot \boldsymbol{n} \ \ \mathrm{d}\boldsymbol{\zeta} \right] \\ \mathcal{R}^{\mathrm{SUPG}}(\boldsymbol{L}) = \displaystyle\sum_{j=1}^{N_d} \int_{\partial\mathcal{D}_{mj}} \beta\rho(\boldsymbol{s}_j \cdot \boldsymbol{n}) L_j v \ \boldsymbol{s}_m \cdot \boldsymbol{n} \ \ \mathrm{d}\boldsymbol{\zeta} \\ \qquad\qquad - \displaystyle\sum_{j=1}^{N_d} \int_{\partial\mathcal{D}^{j+}} \sigma_s \tilde{\rho}_{m,j} L_j v \ \boldsymbol{s}_m \cdot \boldsymbol{n} \ \ \mathrm{d}\boldsymbol{\zeta} \\ \mathcal{D}^{\mathrm{SUPG}}(\tilde{L}_{\mathrm{in}}) = -\displaystyle\int_{\partial\mathcal{D}_0} \beta \tilde{L}_{\mathrm{in}} \mathbb{1}_{[\boldsymbol{s}_m = \boldsymbol{s}_{\mathrm{in}}]} v \ \boldsymbol{s}_m \cdot \boldsymbol{n} \ \ \mathrm{d}\boldsymbol{\zeta} \\ \qquad\qquad + \displaystyle\sum_{j=1}^{N_d} \omega_j \Phi_{m,j} \int_{\partial\mathcal{D}_0} \sigma_s \tilde{L}_{\mathrm{in}} \mathbb{1}_{[\boldsymbol{s}_j = \boldsymbol{s}_{\mathrm{in}}]} v \ \boldsymbol{s}_m \cdot \boldsymbol{n} \ \ \mathrm{d}\boldsymbol{\zeta} \\ \mathcal{E}^{\mathrm{SUPG}}(L_b) = \displaystyle\int_{\mathcal{D}} \kappa L_b \ \boldsymbol{s}_m \cdot \nabla v \ \ \mathrm{d}\boldsymbol{x} \end{cases} \tag{2.37}$$

2.5 Validation

The numerical schemes developped in previous sections need to be validated. Usually, the validation process relies either on analytical solutions if available, or on experimental measurements, or otherwise based on Monte–Carlo-type numerically integrated data [4].

In this study, a strategy relying on the decomposition of variational formulations validating groups of operators is proposed. It means here all operators are validated independently one from the other, using analytical formulations. This is made possible because numerical schemes are based on variational formulations.

1. As a first step, one assumes that the medium under consideration has its index of refraction equal to unity. With $\tilde{n}_{\mathrm{in}} = 1$, one has $\rho = 0$, which means there is no reflection. With this hypothesis, the reflection operator $\mathcal{R}(\boldsymbol{L})$ can be removed from equations (2.24) and (2.36), for which the generic formulation can be simplified to :

$$\mathcal{T}(L_m) + \mathcal{S}(\boldsymbol{L}) = \mathcal{D}(\tilde{L}_{\mathrm{in}}) + \mathcal{E}(L_b) \tag{2.38}$$

   In certain specific circumstances, the equation (2.38) can be solved with analytical solutions [37] : an appropriate choice of the power entering beams $\tilde{L}_{\mathrm{in}}$ along with a non-uniform distribution of the radiance allows to find the blackbody radiance L_b.

2. As a second step, one assumes there exists specular reflections on boundaries but it is a non-scattering medium, so $\sigma_s = 0$, the scattering operator $\mathcal{S}(\boldsymbol{L})$ can be

removed from equations (2.24) and (2.36), for which the generic formulation can be simplified to :

$$\mathcal{T}(L_m) + \mathcal{R}(\boldsymbol{L}) = \mathcal{D}(\tilde{L}_{\text{in}}) + \mathcal{E}(L_b) \tag{2.39}$$

In this case some analytical solutions have been developped, the exponential attenuation being based on the Beer-Lambert formulation, coupled with the Fresnel law in a square medium and for an entering collimated beam.

3. As a third step, one reduces one dimension in space such that, even though the whole code is solved using two dimensional integrations, the physics can be explained and expressed in a single dimension in space. Analytical solutions are used, all operator from (2.24) and (2.36) are involved.

In the validation process, simulations are performed on a 4 cm^2 square semi-transparent medium with edge locations $(-1,-1)$, $(-1,1)$, $(1,-1)$, and $(1,1)$. The mesh convergence is performed for both DG and SUPG schemes. More specifically, orders $\mathbb{P}_0$ and $\mathbb{P}_1$ are considered for the DG scheme, and orders $\mathbb{P}_1$ and $\mathbb{P}_2$ are considered for the SUPG scheme. The four meshes given in Figure 2.8 are used for the calculation of the quality of the solutions based on the $\mathcal{L}_2(\mathcal{D})$-norm error defined as

$$e(u) = \frac{\|u - u_{\text{ex}}\|_{\mathcal{L}_2(\mathcal{D})}}{\|u\|_{\mathcal{L}_2(\mathcal{D})}} \quad \text{with} \quad \|u\|_{\mathcal{L}_2(\mathcal{D})} = \left(\int_{\mathcal{D}} u^2(\boldsymbol{x}) \, \mathrm{d}\boldsymbol{x} \right)^{\frac{1}{2}} \tag{2.40}$$

This relative error is computed to determine the quality of the DG and the SUPG schemes. Table 2.1 summarizes the main characteristics of meshes $\mathcal{M}_i$, $i = 1, \cdots, 4$, and related dimensions of functional spaces for DG and SUPG schemes. Let us also remark that a finer mesh called $\mathcal{M}_5$ is used to project both numerical and analytical solutions before computing the relative errors. The finer mesh $\mathcal{M}_5$ has a number of element per side $n_e = 300$, $N_v = 108,165$ vertices and $N_e = 215,128$ elements.

–	$\mathcal{M}_1$	$\mathcal{M}_2$	$\mathcal{M}_3$	$\mathcal{M}_4$
n_e	11	41	81	151
N_e	276	3,888	15,464	54,668
N_v	161	2,027	7,895	27,637
h	0.302	0.0845	0.0436	0.0263
$n_{\text{dof}}^{\text{DG-}\mathbb{P}_0}$	276	3,888	15,464	54,668
$n_{\text{dof}}^{\text{DG-}\mathbb{P}_1}$	828	11,664	46,392	164,004
$n_{\text{dof}}^{\text{SUPG-}\mathbb{P}_1}$	161	2,027	7,895	27,637
$n_{\text{dof}}^{\text{SUPG-}\mathbb{P}_2}$	597	7,941	31,253	109,941

Tableau 2.1 – Mesh characteristics : name $\mathcal{M}_i$, number of elements per side n_e, number of elements N_e, number of vertices N_v, mesh size h, number of degrees of freedom for DG-$\mathbb{P}_0$ $n_{\text{dof}}^{\text{DG-}\mathbb{P}_0}$, number of degrees of freedom for DG-$\mathbb{P}_1$ $n_{\text{dof}}^{\text{DG-}\mathbb{P}_1}$, number of degrees of freedom for SUPG-$\mathbb{P}_1$ $n_{\text{dof}}^{\text{SUPG-}\mathbb{P}_1}$, number of degrees of freedom for SUPG-$\mathbb{P}_2$ $n_{\text{dof}}^{\text{SUPG-}\mathbb{P}_2}$.

2.5.1 $\mathcal{T} + \mathcal{S} = \mathcal{D} + \mathcal{E}$

As explained above, the RTE problem is first validated letting apart the reflection operator. An analytical expression is built in order to validate (2.38) for both DG and

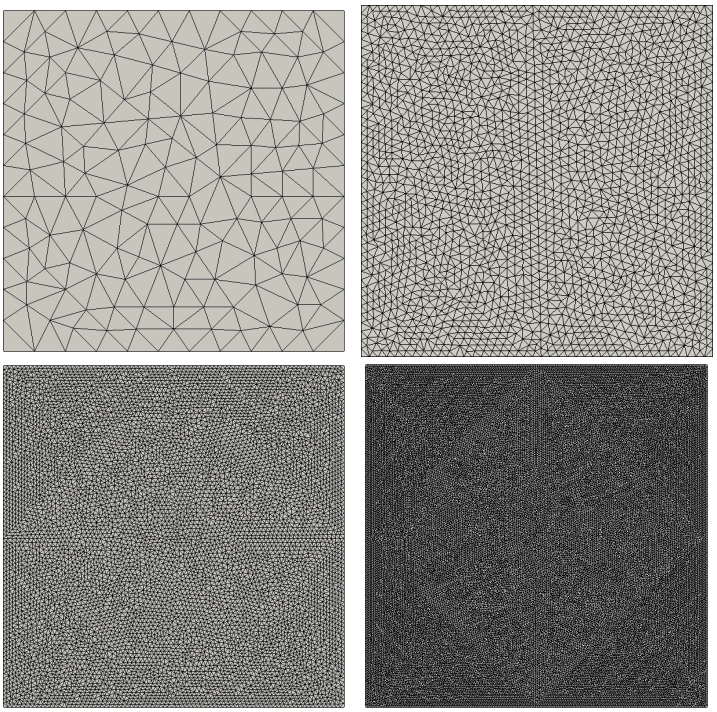

FIGURE 2.8 – The four meshes used in the validation process. From top-left to bottom-right : $\mathcal{M}_1$, $\mathcal{M}_2$, $\mathcal{M}_3$ and $\mathcal{M}_4$.

SUPG schemes. The quality of the solution is calculated integrating the error on the angular integrated variable $G(\boldsymbol{x}) = \int_{\mathcal{S}^{n-1}} L(\boldsymbol{x}, \boldsymbol{s})\ \mathrm{d}\boldsymbol{s} \simeq \sum_{j=1}^{N_d} \omega_j L_j(\boldsymbol{x})$, as in [37]. G is the fluence.

The analytical solution is determinated for a given radiance $L(\boldsymbol{x}, \boldsymbol{s})$, chosen in the current study to be independent of the direction $\boldsymbol{s}$. To be specific, one chooses :

$$L(\boldsymbol{x}, \boldsymbol{s}) = \hat{L}(\boldsymbol{x}) = e^{-\kappa x - \sigma_s y} \tag{2.41}$$

such that its angular integration, the fluence, is

$$G(\boldsymbol{x}) = 2\pi e^{-\kappa x - \sigma_s y} \tag{2.42}$$

The blackbody radiance is then calculated such that the equation (2.38) holds. The radiance intensity (2.41) being independent of the direction $\boldsymbol{s}$, the integral term $\sigma_s \oint_{\mathcal{S}^{n-1}} L(\boldsymbol{x}, \boldsymbol{s}')\Phi(\boldsymbol{s}, \boldsymbol{s}')\ \mathrm{d}\boldsymbol{s}' = \sigma_s \hat{L}(\boldsymbol{x}) \oint_{\mathcal{S}^{n-1}} \Phi(\boldsymbol{s}, \boldsymbol{s}')\ \mathrm{d}\boldsymbol{s}' = \sigma_s \hat{L}(\boldsymbol{x})$. After basic calculation, one finds :

$$\kappa L_b(\boldsymbol{x}, \boldsymbol{s}) = \boldsymbol{s} \cdot \nabla e^{-\kappa x - \sigma_s y} + \kappa e^{-\kappa x - \sigma_s y} \tag{2.43}$$

Numerical tests have been performed with the Henyey-Greenstein phase fonction, the anisotropy coefficient g being taken equal to 0.5. Simulations have been performed with four sets of coefficients $\kappa = \{0.1, 5\}$ cm^{-1} and $\sigma_s = \{0.1, 5\}$ cm^{-1} in order to test the robustness of developped algorithms.

Figure 2.9 presents the solutions $G(\boldsymbol{x})$ for the four sets of radiative properties. Figure 2.10 presents the mesh convergence studies for the four sets of radiative properties. It is seen that for all tests and all meshes, $\mathcal{L}_2(\mathcal{D})$ errors on $G(\boldsymbol{x})$ are small ; thus numerical

schemes are accurate. Moreover, errors are quite similar for the DG-$\mathbb{P}_1$ and SUPG-$\mathbb{P}_1$ schemes, for a number of degrees of freedom much less for the SUPG-$\mathbb{P}_1$ than for the DG-$\mathbb{P}_1$. Also, the DG-$\mathbb{P}_0$ scheme is much less accurate than other schemes, while, on the other side, the SUPG-$\mathbb{P}_2$ scheme is much more accurate. For this specific numerical test, the orders of convergence for the DG-$\mathbb{P}_0$, DG-$\mathbb{P}_1$, SUPG-$\mathbb{P}_1$ and SUPG-$\mathbb{P}_2$ have been found to be roughly equal to 1, 1.7, 1.9 and 2.7, respectively. Ending, adding the fact that the number of degrees of freedom for the SUPG-$\mathbb{P}_2$ scheme is less than the number of degrees of freedom for the DG-$\mathbb{P}1$, the conclusion arising is that the SUP-P2 is more interesting for this first test.

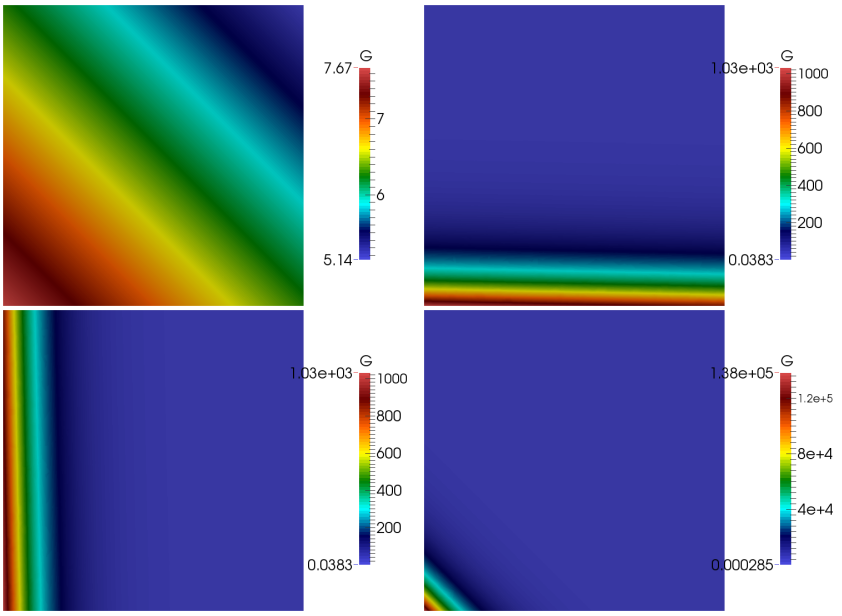

FIGURE 2.9 – Representation of the analytical fluence $G(\boldsymbol{x})$ constructed from (2.42) for different radiative properties, in the square $[-1,+1]^2$. Up-left : $\kappa = 0.1$ cm^{-1}, $\sigma_s = 0.1$ cm^{-1} ; up-right : $\kappa = 0.1$ cm^{-1}, $\sigma_s = 5$ cm^{-1} ; down-left : $\kappa = 5$ cm^{-1}, $\sigma_s = 0.1$ cm^{-1} ; down-right : $\kappa = 5$ cm^{-1}, $\sigma_s = 5$ cm^{-1}. The mesh $\mathcal{M}_5$ is used for these constructions.

Another test deals with the radiance which is, as in [37], a function of both the space and the direction. One supposes the scattering phase function equal to $\Phi(\boldsymbol{s},\boldsymbol{s}') = \frac{1}{2\pi}\frac{2+\boldsymbol{s}\cdot\boldsymbol{s}'}{2}$ and the radiance intensity equals to $L(\boldsymbol{x},\boldsymbol{s}) = e^{-\kappa x-\sigma_s y}(1+(\boldsymbol{s})_x)$. With these conditions, the integral term $\sigma_s \oint_{\mathcal{S}^{n-1}} L(\boldsymbol{x},\boldsymbol{s}')\Phi(\boldsymbol{s},\boldsymbol{s}')\,\mathrm{d}\boldsymbol{s}'$ becomes $\sigma_s e^{-\kappa x-\sigma_s y}\oint_{\mathcal{S}^{n-1}}\frac{1}{2\pi}\times\frac{2+\boldsymbol{s}\cdot\boldsymbol{s}'}{2}(1+(\boldsymbol{s}')_x)\,\mathrm{d}\boldsymbol{s}' = \sigma_s e^{-\kappa x-\sigma_s y}(1+\frac{1}{4}(\boldsymbol{s})_x)$. After calculations, applying (2.38), one finds the blackbody radiance to be :

$$\kappa L_b(\boldsymbol{x},\boldsymbol{s}) = \left[(\kappa-\kappa(\boldsymbol{s})_x-\sigma_s(\boldsymbol{s})_y)\left((1+(\boldsymbol{s})_x)+\frac{3}{4}\sigma_s(\boldsymbol{s})_x\right]e^{-\kappa x-\sigma_s y}\right. \tag{2.44}$$

The angular integration of $L(\boldsymbol{x},\boldsymbol{s})$ is $G(\boldsymbol{x}) = 2\pi e^{-\kappa x-\sigma_s y}$. Table 2.2 represents the order of convergence of the different schemes for this second numerical test case. Conclusions were found to be similar than with the previous presented test case, with orders of convergence much bigger for the SUPG-$\mathbb{P}_2$ scheme than for other schemes.

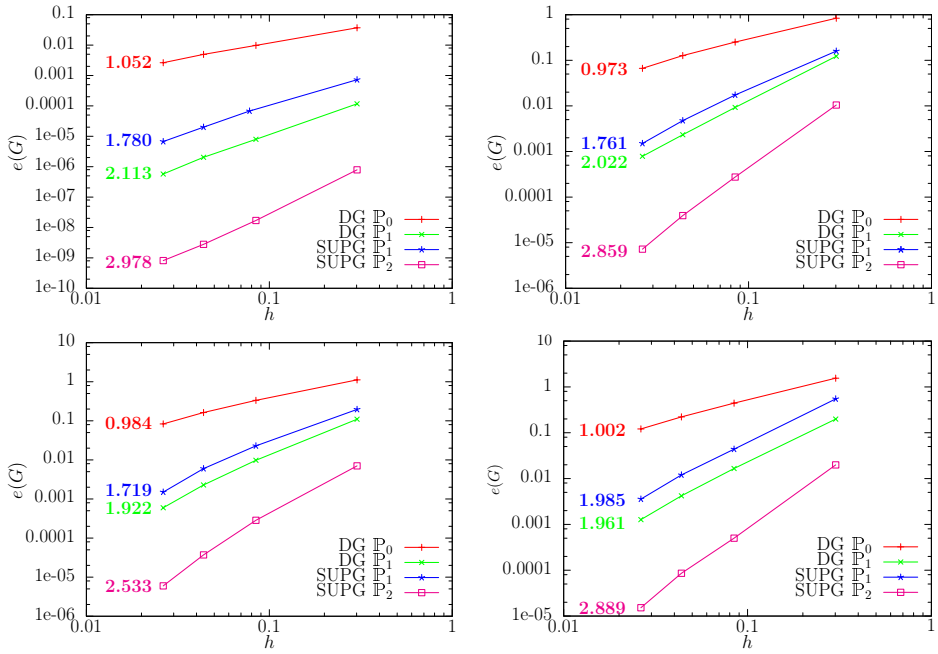

FIGURE 2.10 – Errors $e(G)$ as a function of h. Up-left : $\kappa = 0.1$ cm^{-1}, $\sigma_s = 0.1$ cm^{-1} ; up-right : $\kappa = 0.1$ cm^{-1}, $\sigma_s = 5$ cm^{-1} ; bottom-left : $\kappa = 5$ cm^{-1}, $\sigma_s = 0.1$ cm^{-1} ; bottom-right : $\kappa = 5$ cm^{-1}, $\sigma_s = 5$ cm^{-1}.

$\kappa - \sigma_s$	0.1 – 0.1	0.1 – 5	5 – 0.1	5 – 5
DG-$\mathbb{P}_0$	1.054	0.9691	0.9654	0.9920
DG-$\mathbb{P}_1$	2.104	2.026	1.893	1.929
SUPG-$\mathbb{P}_1$	1.749	1.662	1.877	1.836
SUPG-$\mathbb{P}_2$	2.974	2.848	2.601	2.859

TABLEAU 2.2 – Order of convergence for the second test

2.5.2 $\mathcal{T} + \mathcal{R} = \mathcal{D} + \mathcal{E}$

As a second step, the RTE problem is validated letting apart the scattering operator. An analytical expression is built in order to validate (2.39) for both DG and SUPG schemes. The quality of the solution is calculated integrating the error on the angular integrated density function $D(\boldsymbol{x}) = \sum_{l=0}^{+\infty} L_l(\boldsymbol{x}) \simeq \sum_{j=1}^{N_d} L_j(\boldsymbol{x})$.

As depicted in Figure 2.11-Left, a collimated beam is entering through the left boundary, in the middle, with an incidence angle equal to $\theta_{\text{inc}} = \arcsin(n \sin(\frac{\pi}{4}))$. In this case, the refracted angle θ_{in} is equal to $\frac{\pi}{4}$. The photons do loop within the medium until their extinction.

For such a case, after mathematical calculations, the analytical density is found to

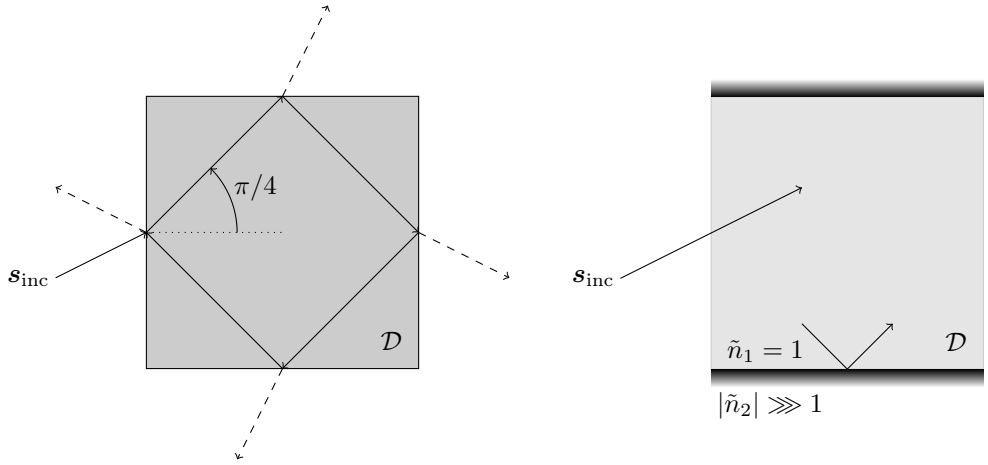

FIGURE 2.11 – Sketch of the test cases for the validation of the equation (2.39) (Left) and the equations (2.24) – (2.36) (Right)

be equal to :

$$\begin{aligned} D_{ex} = (1-\rho_{12}) \sum_{i=0}^{\infty} \Big[& \rho_{21}^{4i} \tilde{L}_{\text{in}}(-1, y)\ e^{-\kappa\sqrt{2}(x+1)-\kappa\sqrt{8}(2i)} \mathbb{1}_{y-(x+1)\in[-1,1]} \\ & + \rho_{21}^{4i+1} \tilde{L}_{\text{in}}(-1, 2-y)\ e^{-\kappa\sqrt{2}(x+1)-\kappa\sqrt{8}(2i)} \mathbb{1}_{y+(x+1)\in[-1,1]} \\ & + \rho_{21}^{4i+2} \tilde{L}_{\text{in}}(1, -y)\ e^{-\kappa\sqrt{2}(1-x)-\kappa\sqrt{8}(2i+1)} \mathbb{1}_{y+(1-x)\in[-1,1]} \\ & + \rho_{21}^{4i+3} \tilde{L}_{\text{in}}(1, y-2)\ e^{-\kappa\sqrt{2}(1-x)-\kappa\sqrt{8}(2i+1)} \mathbb{1}_{y-(1-x)\in[-1,1]} \Big] \end{aligned} \tag{2.45}$$

where ρ_{12} is the reflectivity for the incoming radiance propagating towards $\theta_{\text{inc}} = \arcsin\left(\tilde{n} \sin \frac{\pi}{4}\right)$, and ρ_{21} is the reflectivity for the outgoing radiance propagating towards $\theta_{\text{inc}} = \frac{\pi}{4}$. The relationship (2.45) has been constructed using geometrical symmetries coupled with the Beer–Lambert extinction law, since scattering is not considered. Each i in the summation symbol represents one full loop of a ray. The first term within the summation symbol represents the path from the west border to the north border ; the second term reprents the path from the north to the east, the third term represents the path from the east to the south and, finally, the fourth term represents the path from the south to the west.

At first, a gaussian colimated beam is dealt with. The prescribed entering radiance is chosen to be such that :

$$\tilde{L}_{\text{in}}(\boldsymbol{x}) = 10^5 e^{\frac{10}{(y-1.1)^2}}\ \mathbb{1}_{y\in[-0.8,0.8]} \tag{2.46}$$

Figure 2.12 presents the space-dependent density function and the convergence results. As for the previous test, the convergence order for the SUPG-$\mathbb{P}_2$ scheme is found to be greater than for the DG-$\mathbb{P}_1$ scheme but the error is greater for the coarsest mesh. Also, both DG-$\mathbb{P}_0$ and SUPG-$\mathbb{P}_1$ schemes exhibit inferior convergence.

Next, a door-shaped colimated beam is dealt with. This test is highly challenging because, on one hand, the exact solution presents a discontinuity and, on the other hand, the solution is searched in $V_h^{\text{SUPG}} \subset H^1(\mathcal{D})$ for the SUPG schemes. Moreover the mesh is not built on the solution so that a discontinuity can arise within mesh elements.

The prescribed entering radiance is chosen to be such that :

$$\tilde{L}_{\text{in}}(\boldsymbol{x}) = \mathbb{1}_{y\in[-0.4,0.4]} \tag{2.47}$$

Figures 2.13 and 2.14 present the space-dependent density function for the analytical solution, the DG-$\mathbb{P}_1$ scheme and the SUPG-$\mathbb{P}_2$ scheme. It can be seen that the solutions present discontinuities for the DG schemes, as expected, while solutions are smooth for the SUPG schemes. Moreover, only the DG-$\mathbb{P}_0$ scheme has the order-preserving mapping.

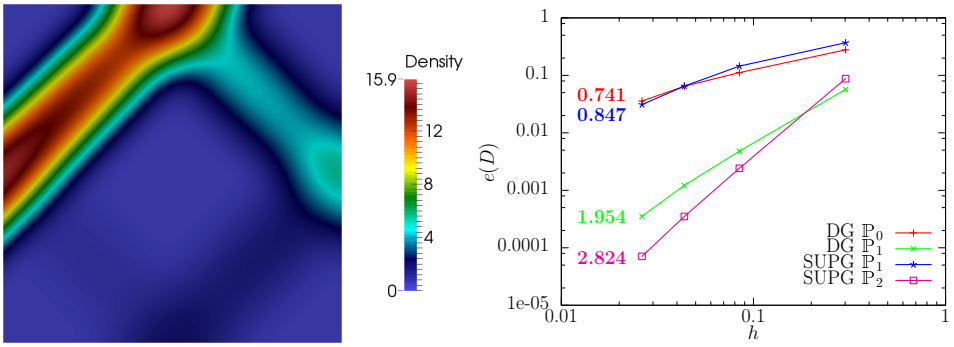

FIGURE 2.12 – Gaussian beam – Left : Exact solution , Right : L2 error.

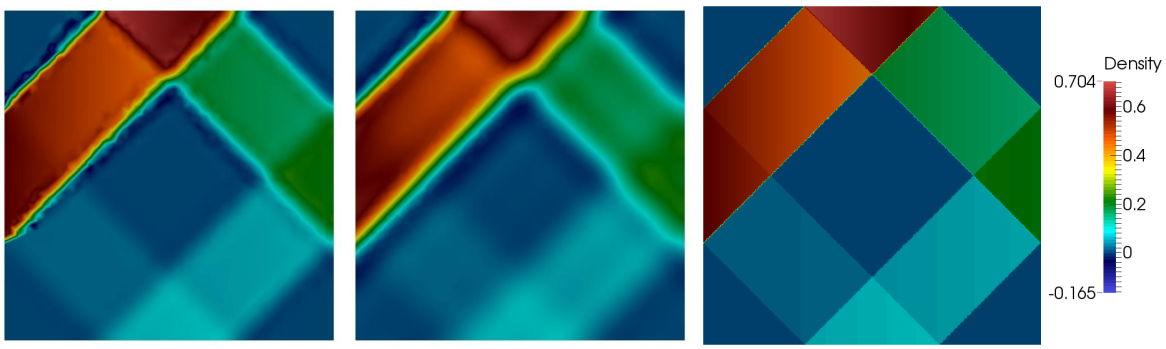

FIGURE 2.13 – Door beam. From left to right : DG-$\mathbb{P}_1$ solution, SUPG-$\mathbb{P}_2$ solution, and Exact solution on the mesh $\mathcal{M}_5$. The mesh $\mathcal{M}_2$ is used for these constructions.

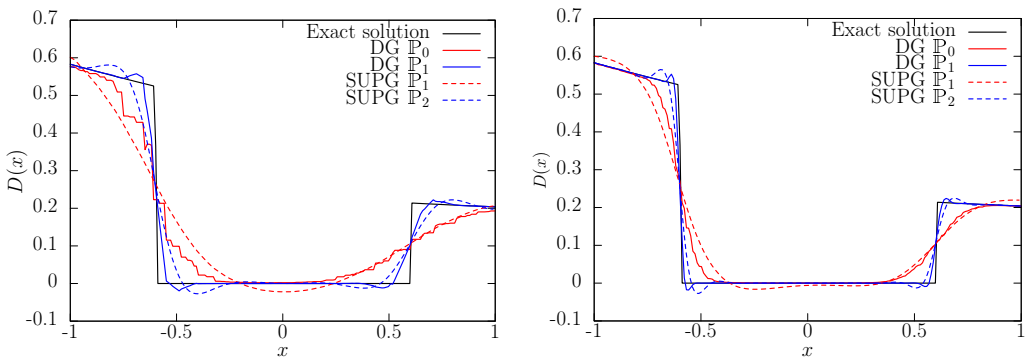

FIGURE 2.14 – Door beam – 1D horizontal cut of the density D, at $y = 0$. Left : on the mesh $\mathcal{M}_2$ – Right : on the mesh $\mathcal{M}_4$

2.5.3 $\mathcal{T} + \mathcal{S} + \mathcal{R} = \mathcal{D} + \mathcal{E}$

As a third step, the RTE is validated considering together all operators involved in variational formulations. The geometry is considered to be monodimensional, though the two-dimensional computation is performed. Figure 2.11-Right schematically depicts the test. The medium is placed between two opaque media. The absorption coefficient and the scattering coefficient of the isotropic studied medium are $\kappa = 1\ \mathrm{cm}^{-1}$ and $\sigma_s = 0.2\ \mathrm{cm}^{-1}$. The refractive index of the studied medium is $\tilde{n}_1 = 1$ to avoid the Fresnel boundary condition on the left and the right side. The refractive index of the opaque media is chosen big, $|\tilde{n}_2| \gg 1$, so that the whole incident radiance is reflected.

To get a 1D analytial solution, suppose the radiance independent of y and independent of $\boldsymbol{s}$. For example, one assumes $L(\boldsymbol{x}, \boldsymbol{s}) = \arctan(\pi x)\cos(2\pi x) + 3$. This analytical radiance is then integrated into the RTE (2.9) and the analytical blackbody radiance L_b is given by :

$$\begin{aligned} \kappa L_b(\boldsymbol{x}, \boldsymbol{s}) =& (\boldsymbol{s})_x \, \mathrm{d}_x L(\boldsymbol{x}, \boldsymbol{s}) + \kappa L(\boldsymbol{x}, \boldsymbol{s}) \\ =& (\boldsymbol{s})_x \left[\frac{\pi \cos(2\pi x)}{1 + (\pi x)^2} - 2\pi \sin(2\pi x) \arctan(\pi x) \right] \\ &+ \kappa \left(\arctan(\pi x) \cos(2\pi x) + 3 \right) \end{aligned} \tag{2.48}$$

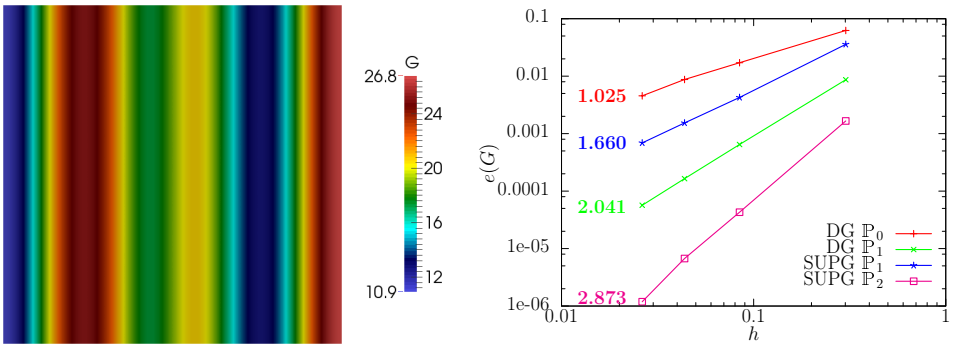

FIGURE 2.15 – Left : Exact Solution of $G(\boldsymbol{x})$, Right : $e(G)$ error

As in Section 2.5.1, the numerical fluence $G(\boldsymbol{x})$ is computed to plot the solution and compare it with the analytical solution. Once more, it is seen that the order of convergence for the SUPG-$\mathbb{P}_2$ is far greater than other orders of convergence.

Another much steeper test is performed with the function $L(\boldsymbol{x}, \boldsymbol{s}) = \arctan(30\pi x)\cos(\pi x) + 3$. This exemple is chosen to test the limits of the SUPG and the DG schemes with a sharp solution at the middle of the medium. Figure 2.16 presents the analytical solution as well as numerical solutions with the mesh $\mathcal{M}_2$ and DG-$\mathbb{P}_1$ and SUPG-$\mathbb{P}_2$ schemes. Both schemes give accurate solution even if there exist some variations close to the steep variation of the solution.

2.6 Iterative solvers

In practice the variational formulations are written down in a more condensed way such that the stiffness matrix related to the bilinear form and the second hand-side

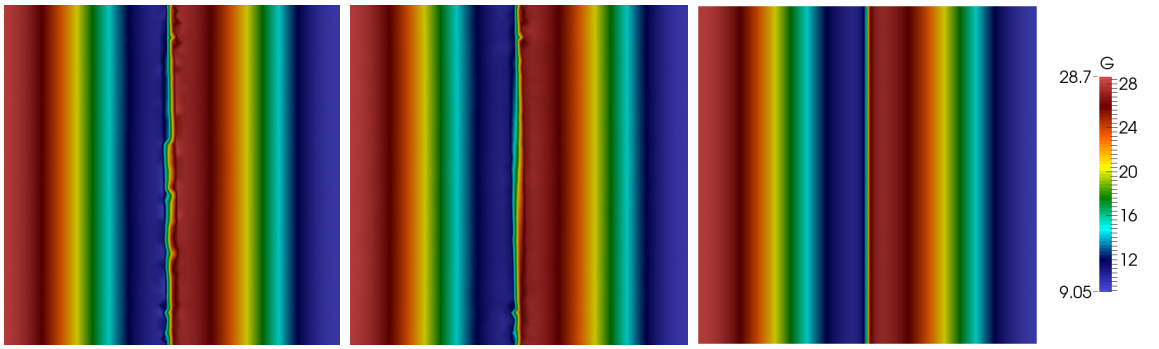

FIGURE 2.16 – Steep ridge. From left to right : DG-$\mathbb{P}_1$ solution, SUPG-$\mathbb{P}_2$ solution, and Exact solution on the mesh $\mathcal{M}_5$. The mesh $\mathcal{M}_2$ is used for these constructions.

vector related to the linear form are explicitely expressed.

Denoting $\mathbf{L}$ as the vector gathering the radiance for all directions, i.e. $\mathbf{L} = \{L_i\}$, $i = 1, \cdots, N_d$, the problem is thus to find $\mathbf{L}$ such that :

$$\mathbf{a}(\mathbf{L}, \mathbf{v}) = \mathbf{l}(\mathbf{v}) \tag{2.49}$$

2.6.1 Iterative methods

Iterative methods considered here consist in decomposing the matrix system (2.49) in blocks of matrices, each block corresponding to a given direction. Thus, for a given direction, say m, the problem consists in finding L_m such that

$$a_{m,m}(L_m, v) + \sum_{j=1,\cdots,N_d; j\neq m} a_{m,j}(L_j, v) = l_m(v) \tag{2.50}$$

Let us introduce the notation $L_j^{(n)}$ as the radiance vector for the direction j and at the iteration n. Also, let us introduce three distinct iterative solvers based on block-matrix decomposition.

1. The method of Jacobi uses the radiance at the n^{th} iteration in all directions but m to compute the next iterate L_m^{n+1} :

$$a_{m,m}(L_m^{(n+1)}, v) = -\sum_{j=1,\cdots,N_d; j\neq m} a_{m,j}(L_j^{(n)}, v) + l_m(v) \tag{2.51}$$

   This method, often called the Source-Iteration method [40] is popular mainly because of its simplicity.

2. The method of Gauss-Seidel uses the radiance at the n^{th} iteration in all directions $j > m$, and the radiance computed at the curent $(n+1)^{\text{th}}$ iteration for $j < m$ to compute the next iterate L_m^{n+1} :

$$a_{m,m}(L_m^{(n+1)}, v) + \sum_{j=1,\cdots,m-1} a_{m,j}(L_j^{(n+1)}, v) = - \sum_{j=m+1,\cdots,N_d} a_{m,j}(L_j^{(n)}, v) + l_m(v) \tag{2.52}$$

This Gauss-Seidel methodology has been used elsewhere with similar boundary conditions [37].

3. The successive over relaxation (SOR) method uses both the radiance at the n^{th} iteration for $j \geq m$, and the radiance computed at the current $(n+1)^{\text{th}}$ iteration $j < m$ to compute the next iterate L_m^{n+1} :

$$a_{m,m}(L_m^{(n+1)}, v) + \sum_{j=1,\cdots,m-1} r a_{m,j}(L_j^{(n+1)}, v) = (1-r)a_{m,m}(L_m^{(n)}, v) - \sum_{j=m+1,\cdots,N_d} r a_{m,j}(L_j^{(n)}, v) + r l_m(v) \quad (2.53)$$

where $r \in]0, 2[$ is the relaxation parameter.
The SOR method is an extension of the GS method. If the relaxation parameter $r = 1$, the SOR method is exactly the GS method. If $r < 1$, the SOR method is under-relaxed, and if $r > 1$, the SOR method is over-relaxed. Note that the SOR method has been applied elsewhere for other boundary conditions [41, 42].

2.6.2 Numerical convergence and acceleration

In order to compare the efficiency of the above-presented iterative methods, let us define the error for the global radiance at iteration n :

$$e^n(\boldsymbol{L}) = \sqrt{\frac{|\mathcal{D}|}{N_d \times n_{\text{dof}}}} \|\boldsymbol{L}^n - \boldsymbol{L}^{n-1}\|_2 \quad (2.54)$$

This error decreases along iterations following $an^{-\alpha}$, i.e. α is the order of convergence of the iterative method. The order of convergence is, after erratic evolution in the first few iterations, stable, as presented afterwards in Figures 2.18 and 2.20. So, to get the averaged order of convergence $\bar{\alpha}$, one computes the mean value of the slope of e^n in log scale, following :

$$\alpha^n = \ln\left(\frac{e^n(\boldsymbol{L})}{e^{n+1}(\boldsymbol{L})}\right) \quad ; \quad \bar{\alpha} = -\frac{1}{N-6}\sum_{n=6}^{N} \alpha^n \quad (2.55)$$

Two different geometries are presented afterwards. The first one is a square, such as the shape remains unchanged regardless the mesh refinement. The second one is a part of a parabola whose shape depends on the mesh refinement. For the two geometries, the isotropic medium properties are defined by $\kappa = 0.1$ cm^{-1}, $\sigma_s = 3$ cm^{-1}, and $\tilde{n} = 1.4$.

Square geometry

For this first geometry, one uses two different meshes : a very coarse one denoted $\mathcal{M}_0$, and the mesh $\mathcal{M}_2$ presented before in section 2.5. Dirichlet condition is prescribed on the left boundary with a gaussian shaped intensity.

Solutions are presented for both meshes on Figure 2.17. It can be seen from this figure that the solution for the mesh $\mathcal{M}_0$ is far away from the solution for the mesh

$\mathcal{M}_2$. Actually, the solution for the former mesh is far from being accurate, but the computation time for this coarse mesh is absolutely negligible, the number of degrees of freedom being very low.

Added to this, Figure 2.18 depicts 3 complementary results.

1. The first sub-figure presents the evolution of the error $e^n(\boldsymbol{L})$ along iterations, the coarse mesh $\mathcal{M}_0$ being used, for the Jacobi and Gauss-Seidel methods as well as for the SOR method, an appropriate relaxation parameter $r = 1.3$ being chosen. It is shown that, for this particular case, the SOR method outperforms the Gauss-Seidel that itself outperforms the Jacobi method. Still in this figure, it is seen that the error 10^{-10} needs, for being reached, a bit more than 100 iterations for Jacobi, almost 60 for Gauss-Seidel, and only 25 for SOR.
2. Next, the second sub-figure corroborates previous results since it presents the order of convergence α^n along iterations. It is seen that for Jacobi and GS methods, α^n stabilizes rapidly to a quite low value, while for the SOR α^n is much greater even if there exists some small oscillations.
3. To end, the third subfigure presents the averaged order of convergence, α, for the fine mesh $\mathcal{M}_2$ as well as for the very coarse mesh $\mathcal{M}_0$, for both the Jacobi and the GS methods, and also the SOR method, the relaxation parameter ranging from 0.9 to 1.6. From this subfigure, one concludes that, for this particular case, the averaged order of convergence α is almost independent of the mesh refinement and, consequently, the optimal relaxation parameter, defined as the one that gives the highest α is independent of the mesh refinement.

Parabolic geometry

The second geometry represents a parabola with a lenght bewteen the focus and the vertex equal to $\frac{1}{3}$ cm. 3 different meshes, denoted $\mathcal{F}_0$, $\mathcal{F}_1$ and $\mathcal{F}_2$, are studied. The $\mathcal{F}_0$ is a coarsest mesh, $\mathcal{F}_2$ is the finest mesh, and $\mathcal{F}_1$ is in between. These meshes are presented in Figure 2.19. On this figure 2.19, it can be verified that the shape of the medium depends on the mesh refinement, because the curved domain is approximated by sets of triangles in the triangulation process, so that the coarsest mesh does not yield a perfect parabolic domain. Also, the entering beam being of constant intensity on the left boundary, solutions on the different meshes are not that different, even though the finest mesh gives, naturally, the finest and smoothest numerical solutions.

Figure 2.20 present the convergence results. The conclusion are, roughly speaking, the same as for the square geometry : the SOR method with an appropriate relaxation parameter outperforms other block-based iterative methods. However, in this case, because the curved domain cannot be accurately covered by coarsest mesh, the optimal relaxation parameter depends on mesh refinement. However, the range of optimality is very narrow ($[1.20 : 1.25]$) when compared to the whole search range ($[0.9 : 1.6]$).

From such behaviors, the conclusion is that the block-based iterative SOR method is a good alternative to the usual ordinary Jacobi method also known as the source iteration method. Further, the optimal relaxation parameter whose search is usually highly time consuming, can be found using a very coarse mesh, making finally this search very inexpensive.

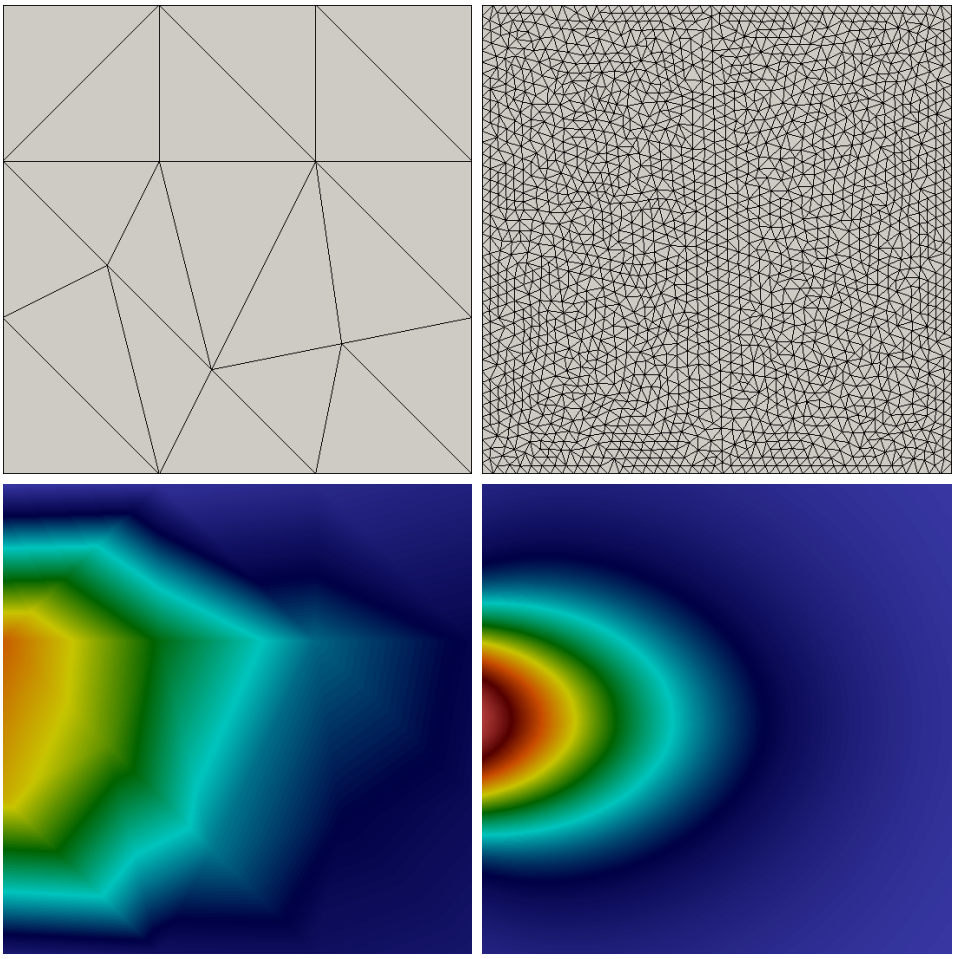

FIGURE 2.17 – Top : Meshes $\mathcal{M}_0$ and $\mathcal{M}_2$ – Down : Density solution in meshes $\mathcal{M}_0$ and $\mathcal{M}_2$.

2.7 Conclusion

This paper presented numerical schemes based on finite elements for solving the RTE, with specular reflection boundary conditions.

Two weak formulations have been fully developped : the Discontinuous Galerkin formulation and the Streamline Upwind Petrov-Galerkin formulation, the latter being somehow a slightly simplified version of the full Least-Square formulation. The different finite element methods have been validated step by step making the operators involved seperately one from another : transport and absorption, scattering, reflectivity, Dirichlet input, and emission.

Convergence studies allowed us to validate variationnal formulations as well as developped algorithms. We could also bring to light the fact that the SUPG method at order $\mathbb{P}_2$ has a rate of convergence much higher than the DG method at orders $\mathbb{P}_0$ and $\mathbb{P}_1$. So, because the associated number of degrees of freedom is not that large, this SUPG method is a goàod choice when the solution is in $H_1(\mathcal{D})$. Otherwise, when the solution is not in $H_1(\mathcal{D})$, i.e. the solution presents discontinuities, then the DG method is to be considered.

To end, when solving the linear matrix system built by weak formulations, three

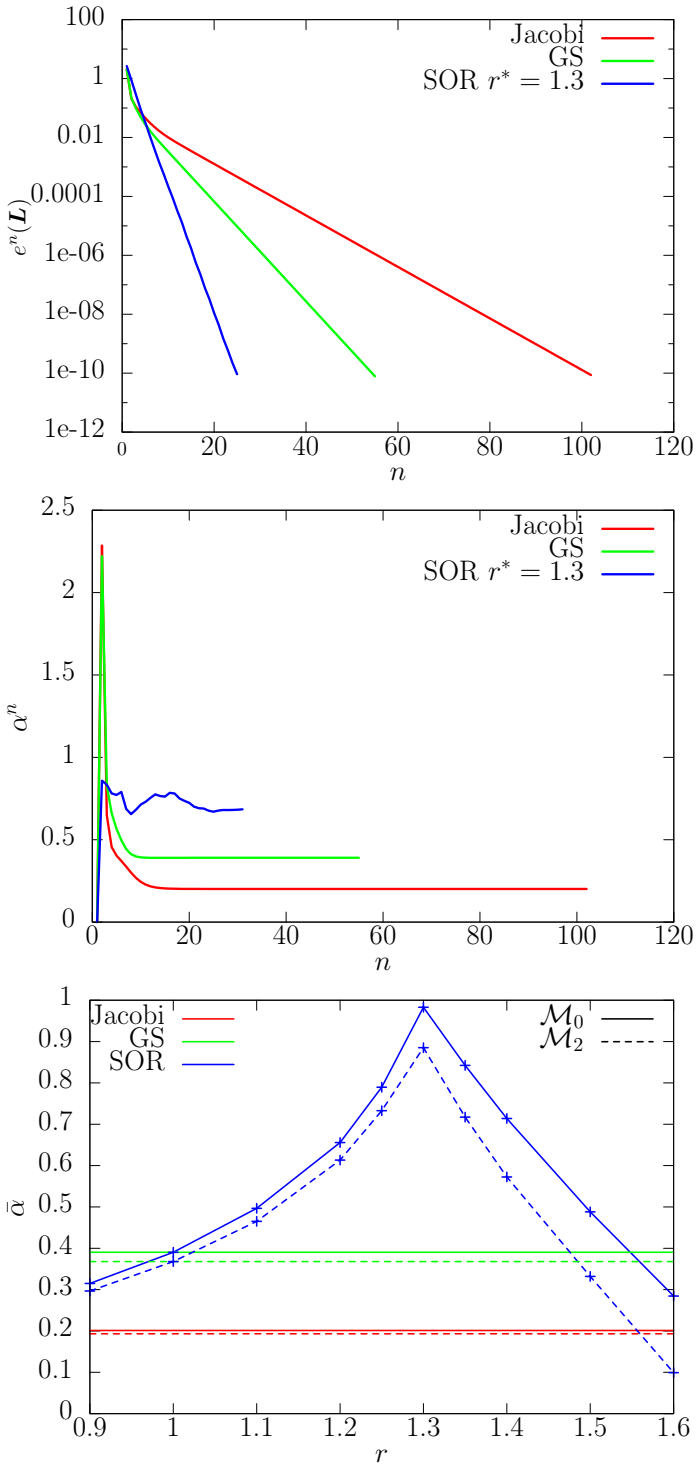

FIGURE 2.18 – Square geometry. From top to bottom : evolution of errors with respect to iterations, convergence order with respect to iterations, average convergence order with respect to relaxation parameter. The mesh $\mathcal{M}_0$ is used to build the two first figures.

block-based iterative methods have been presented : the Jacobi method, the most commonly used and also knowm as the source iteration method, the Gauss-Seidel, and the Successive-Over Relaxation. Convergence studies could show the efficiency of the SOR methods when the relaxation parameter is chosen adequately.

Moreover, The SOR optimal parameter has been found to be independent of the

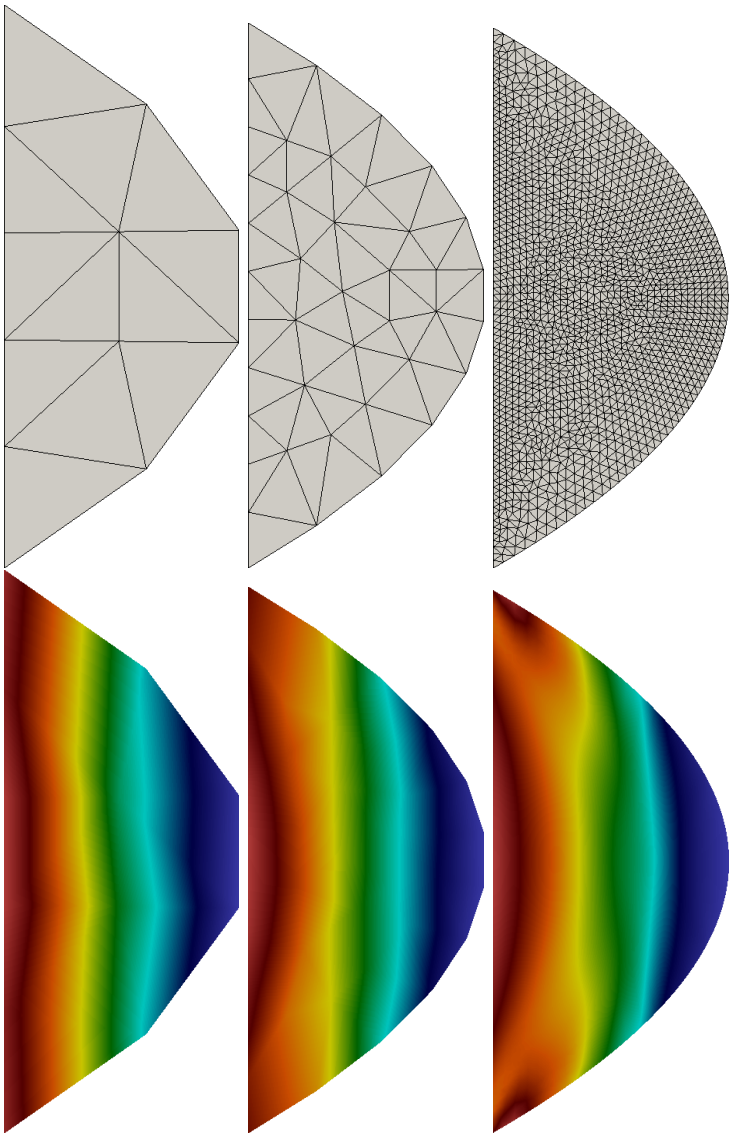

FIGURE 2.19 – Top : Meshes from $\mathcal{F}_0$ to $\mathcal{F}_2$. Bottom : numerical solutions for the density for the three meshes.

mesh refinement. This parameter can thus be searched on a coarse mesh, as a pre-processing work, before being used on the refined working mesh, allowing to save a tremendous amount of computation time.

2.8 Acknowledgements

The authors would like to thank developers of the FreeFem++ environment which was extensively used in this study. The author also thank the French Ministry of Higher Education and Research for funding this research. Finally, the authors would like to sincerely thank the reviewers for their constructive and relevant comments formulated on the first version that significantly enhanced the quality of this paper.

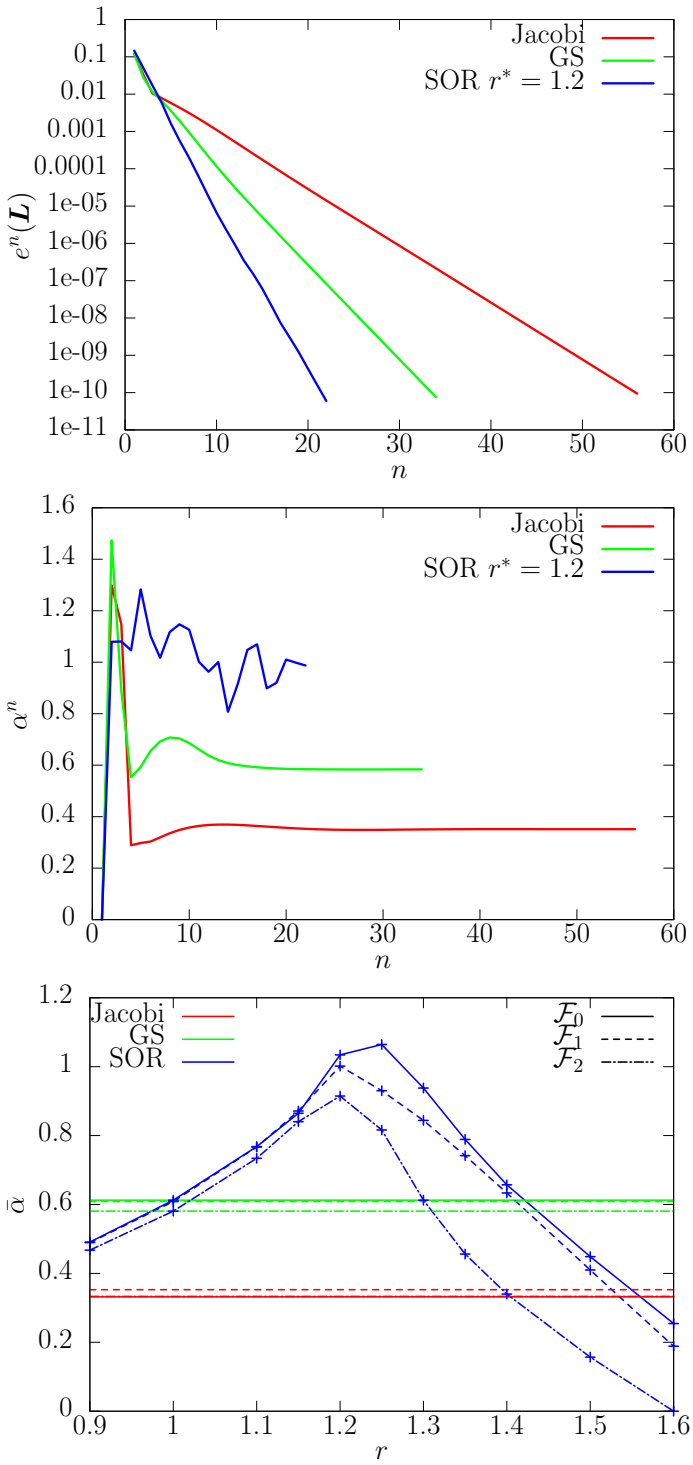

FIGURE 2.20 – Parabolic geometry. From top to bottom : evolution of errors with respect to iterations, convergence order with respect to iterations, average convergence order with respect to relaxation parameter. The mesh $\mathcal{F}_1$ is used to build the two first figures.

Références

[1] D Le Hardy, Y Favennec, and B Rousseau. Solution of the 2-D steady-state radiative transfer equation in participating media with specular reflections using supg and dg finite elements. *Journal of Quantitative Spectroscopy and Radiative Transfer*, 179 :149–164, 2016. 26

[2] Alexandre Ern and Jean-Luc Guermond. *Eléments finis : théorie, applications, mise en oeuvre*, volume 36. Springer Science & Business Media, 2002. 27

[3] M.F. Modest. *Radiative heat transfer*. Academic press, New York, 3rd ed. edition, 2013. 31

[4] John R Howell, Robert Siegel, and M Pinar Mengüç. *Thermal Radiation Heat Transfer*. CRC press, 2011. 31, 41

[5] WA Fiveland. Discrete-ordinates solutions of the radiative transport equation for rectangular enclosures. *Journal of Heat Transfer*, 106(4) :699–706, 1984. 31

[6] John C Chai, HaeOk S Lee, and Suhas V Patankar. Finite volume method for radiation heat transfer. *Journal of Thermophysics and Heat Transfer*, 8(3) :419–425, 1994. 31

[7] Pedro J Coelho. A hybrid finite volume/finite element discretization method for the solution of the radiative heat transfer equation. *Journal of Quantitative Spectroscopy and Radiative Transfer*, 93(1) :89–101, 2005. 31

[8] MRJ Charest, CPT Groth, and ÖL Gülder. Solution of the equation of radiative transfer using a newton–krylov approach and adaptive mesh refinement. *Journal of Computational Physics*, 231(8) :3023–3040, 2012. 31

[9] Pedro J Coelho. Advances in the discrete ordinates and finite volume methods for the solution of radiative heat transfer problems in participating media. *Journal of Quantitative Spectroscopy and Radiative Transfer*, 145 :121–146, 2014. 31

[10] Z Altaç and M Tekkalmaz. Benchmark solutions of radiative transfer equation for three-dimensional rectangular homogeneous media. *Journal of Quantitative Spectroscopy and Radiative Transfer*, 109(4) :587 – 607, 2008. 32

[11] Yong Zhang, Hong-Liang Yi, and He-Ping Tan. Natural element method for radiative heat transfer in a semitransparent medium with irregular geometries. *Journal of Computational Physics*, 241 :18–34, 2013. 32

[12] JM Zhao, JY Tan, and LH Liu. A second order radiative transfer equation and its solution by meshless method with application to strongly inhomogeneous media. *Journal of Computational Physics*, 232(1) :431–455, 2013. 32

[13] Yaobin Qiao, Hong Qi, Qin Chen, Liming Ruan, and Heping Tan. Multi-start iterative reconstruction of the radiative parameter distributions in participating media based on the transient radiative transfer equation. *Optics Communications*, 351 :75–84, 2015. 32

[14] F Hecht. New development in freefem++. *Journal of Numerical Mathematics*, 20(3-4) :251–266, 2012. 32

[15] LM Ruan, M Xie, H Qi, W An, and HP Tan. Development of a finite element model for coupled radiative and conductive heat transfer in participating media. *Journal of Quantitative Spectroscopy and Radiative Transfer*, 102(2) :190–202, 2006. 32

[16] W An, LM Ruan, H Qi, and LH Liu. Finite element method for radiative heat transfer in absorbing and anisotropic scattering media. *Journal of Quantitative Spectroscopy and Radiative Transfer*, 96(3) :409–422, 2005. 32

[17] Dimitris Gorpas, Dido Yova, and Konstantinos Politopoulos. A three-dimensional finite elements approach for the coupled radiative transfer equation and diffusion approximation modeling in fluorescence imaging. *Journal of Quantitative Spectroscopy and Radiative Transfer*, 111(4) :553–568, 2010. 32

[18] LH Liu. Least-squares finite element method for radiation heat transfer in graded index medium. *Journal of Quantitative Spectroscopy and Radiative Transfer*, 103(3) :536–544, 2007. 33

[19] T Tarvainen, M Vauhkonen, and SR Arridge. Gauss–newton reconstruction method for optical tomography using the finite element solution of the radiative transfer equation. *Journal of Quantitative Spectroscopy and Radiative Transfer*, 109(17) :2767–2778, 2008. 33

[20] Tanja Tarvainen, Marko Vauhkonen, and Simon R Arridge. Image reconstruction in optical tomography using the finite element solution of the radiative transfer equation. In *Biomedical Optics*, page BSuD17. Optical Society of America, 2010. 33

[21] O Balima, A Charette, and D Marceau. Comparison of light transport models based on finite element and the discrete ordinates methods in view of optical tomography applications. *Journal of Computational and Applied Mathematics*, 234(7) :2259–2271, 2010. 33

[22] JM Zhao, JY Tan, and LH Liu. A deficiency problem of the least squares finite element method for solving radiative transfer in strongly inhomogeneous media. *Journal of Quantitative Spectroscopy and Radiative Transfer*, 113(12) :1488–1502, 2012. 33

[23] Aki Pulkkinen and Tanja Tarvainen. Truncated fourier-series approximation of the time-domain radiative transfer equation using finite elements. *Optical Society of America A*, 30(3) :470–478, 2013. 33

[24] Wm H Reed and TR Hill. Triangular mesh methods for the neutron transport equation. *Los Alamos Report LA-UR-73-479*, 1973. 33

[25] X Cui and Ben Q Li. A discontinuous finite-element formulation for multidimensional radiative transfer in absorbing, emitting, and scattering media. *Numerical Heat Transfer, Part B : Fundamentals*, 46(5) :399–428, 2004. 33

[26] LH Liu and LJ Liu. Discontinuous finite element method for radiative heat transfer in semitransparent graded index medium. *Journal of Quantitative Spectroscopy and Radiative Transfer*, 105(3) :377–387, 2007. 33

[27] JC Ragusa and Y Wang. A two-mesh adaptive mesh refinement technique for SN neutral-particle transport using a higher-order DGFEM. *Journal of Computational and Applied Mathematics*, 233(12) :3178–3188, 2010. 33

[28] O Balima, Y Favennec, J Boulanger, and A Charette. Optical tomography with the discontinuous galerkin formulation of the radiative transfer equation in frequency domain. *Journal of Quantitative Spectroscopy and Radiative Transfer*, 113(10) :805–814, 2012. 33

[29] Xing He, Euntaek Lee, Lucas Wilcox, Ramakanth Munipalli, and Laurent Pilon. A high-order-accurate gpu-based radiative transfer equation solver for combustion and propulsion applications. *Numerical Heat Transfer, Part B : Fundamentals*, 63(6) :457–484, 2013. 33

[30] O. Balima, Y. Favennec, and D. Rousse. Optical tomography reconstruction algorithm with the finite element method : An optimal approach with regularization tools. *Journal of Computational Physics*, 25(1) :461–479, 2013. 33

[31] Rafael O Castro and Juan Pablo Trelles. Spatial and angular finite element method for radiative transfer in participating media. *Journal of Quantitative Spectroscopy and Radiative Transfer*, 157 :81–105, 2015. 33

[32] William Martin, Brian Cairns, and Guillaume Bal. Adjoint methods for adjusting three-dimensional atmosphere and surface properties to fit multi-angle/multi-pixel polarimetric measurements. *Journal of Quantitative Spectroscopy and Radiative Transfer*, 144 :68–85, 2014. 33

[33] S Guévelou, B Rousseau, G Domingues, J Vicente, C Caliot, and G Flamant. Identification of the radiative properties of α-sic foams realistically designed with a numerical generator. *Proceedings of the 15th International Heat Transfer Conference*, 2014. 33

[34] David Lacroix, Nacer Berour, Pascal Boulet, and Gérard Jeandel. Transient radiative and conductive heat transfer in non-gray semitransparent two-dimensional media with mixed boundary conditions. *Heat and Mass Transfer*, 42(4) :322–337, 2006. 33

[35] O Lehtikangas, T Tarvainen, AD Kim, and SR Arridge. Finite element approximation of the radiative transport equation in a medium with piece-wise constant refractive index. *Journal of Computational Physics*, 282 :345–359, 2015. 33, 34

[36] O Lehtikangas. *Approximations and Hybrid Models for Modeling Light Propagation in Biological Tissues*. PhD thesis, University of Eastern Finland, 2014. 33

[37] H Gao and H Zhao. A fast-forward solver of radiative transfer equation. *Transport Theory and Statistical Physics*, 38(3) :149–192, 2009. 34, 41, 43, 44, 50

[38] Pavel B Bochev, Max D Gunzburger, and John N Shadid. Stability of the SUPG finite element method for transient advection–diffusion problems. *Computer Methods in Applied Mechanics and Engineering*, 193(23) :2301–2323, 2004. 38

[39] O Balima, T Pierre, A Charette, and D Marceau. A least square finite element formulation of the collimated irradiation in frequency domain for optical tomography applications. *Journal of Quantitative Spectroscopy and Radiative Transfer*, 111(2) :280–286, 2010. 38

[40] Elmer E Lewis and Warren F Miller Jr. Computational methods of neutron transport. 1984. 49

[41] L Léger, L Chevallier, and F Paletou. Fast 2D non–LTE radiative modelling of prominences-numerical methods and benchmark results. *Astronomy & Astrophysics*, 470(1) :1–9, 2007. 50

[42] Hyun Keol Kim and André Charette. Frequency domain optical tomography using a conjugate gradient method without line search. *Journal of Quantitative Spectroscopy and Radiative Transfer*, 104(2) :248–256, 2007. 50

Chapitre 3

Discrétisation angulaire : méthodes de partitionnement et traitement des conditions de réflexion spéculaire

Sommaire

Avant-propos

Dans le chapitre précédent, deux méthodes Galerkin continues et discontinues ont été comparées en 2 dimensions afin de choisir un schéma spatial adéquat pour la dimension 3. Nous avons pu voir que la méthode SUPG est satisfaisante pour l'étude d'un faisceau collimaté gaussien entrant dans un milieu à bords réfléchissants. Cependant, au cours du passage du 2D à la 3D, il s'est avéré que la méthode SUPG du chapitre 2 pouvait présenter des instabilités pour des milieux transparents. Une méthode SUPG plus stable a alors été implémentée, préservant la même efficacité en milieu opaque et fournissant une bonne solution pour les milieux plus transparents. De plus, lors de la construction de la formulation variationnelle, l'intégration par parties ne se fait plus que sur le terme de transport.

L'article dans ce chapitre a été accepté le 12 janvier 2017 dans "Journal of Computational Physics". L'objectif principal est d'approcher au mieux les conditions spéculaires à l'échelle 3D. Dans un premier temps, une méthode de partitionnement d'angles solides est présentée pour les conditions de réflexion spéculaire. Ensuite, la nouvelle formulation faible SUPG est développée, puis a été validée par comparaison des solutions numériques avec des solutions analytiques. Enfin, des comparaisons entre la méthode de partitionnement, la méthode de projection à 1 direction et la méthode de projection à 3 directions sont présentées, afin de montrer la robustesse et l'efficacité de la méthode de partitionnement.

En complément de l'article, quatre discrétisations sont détaillées : la discrétisation $\mathrm{SqT}_{p,n}$, utilisée dans certaines comparaisons dans l'article ; la discrétisation S_n, utilisée également dans des comparaisons dans cet article ; la discrétisation T_n, qui a servi à construire la discrétisation $\mathrm{SqT}_{p,n}$; et enfin la discrétisation uniforme à base icosaédrique, utilisée dans le chapitre 4, dans l'étude de la propagation d'un faisceau laser dans un brin de mousse céramique.

Specular reflection treatment for the 3D radiative transfer equation solved with the discrete ordinates method

D. Le Hardy , Y. Favennec , B. Rousseau

LTN UMR CNRS 6607, Université de Nantes, France

F. Hecht

Sorbonne Universités, UPMC Université Paris 06, UMR 7598, inria de Paris, Laboratoire Jacques-Louis Lions, F-75005, Paris, France

Abstract

The contribution of this paper relies in the development of numerical algorithms for the mathematical treatment of specular reflection on borders when dealing with the numerical solution of radiative transfer problems. The radiative transfer equation being integro-differential, the discrete ordinates method allows to write down a set of semi-discrete equations in which weights are to be calculated. The calculation of these weights is well known to be based on either a quadrature or on angular discretization, making the use of such method straightforward for the state equation. Also, the diffuse contribution of reflection on borders is usually well taken into account. However, the calculation of accurate partition ratio coefficients is much more tricky for the specular condition applied on arbitrary geometrical borders. This paper presents algorithms that calculate analytically partition ratio coefficients needed in numerical treatments. The developed algorithms, combined with a decentered finite element scheme, are validated with the help of comparisons with analytical solutions before being applied on complex geometries.

Keywords : *Radiative Transfer Equation, Specular Reflection, Discrete Ordinates Methods, Finite Elements, Streamline-Upwind Petrov–Galerkin (SUPG)*

3.1 Introduction

The modelling of radiative transport problems has received growing attention during the last decades for many scientific and engineering applications, such as in neutron transport [1], in heat transfer [2, 3], or in bio-medical optics [4]. As far as this paper is concerned, the developments are performed in order to characterize and design radiative properties of participating media such as industrial ceramic foams used in concentrated solar power technologies [5, 6]. The equation of concern, which models the propagation of photons in absorbing, scattering and emitting media, is the so-called Radiative Transfer Equation (RTE). This equation contains a differential operator corresponding to advection and an angular integration term corresponding to positive gains by scattering. This transport equation being therefore integro-differential, its solution is far

from being given straightforwardly, especially for three-dimensional geometries.

Numerical methods that have been developed to solve the RTE can be divided into statistical and deterministic methods. The former, based on Monte Carlo methods [7], uses sampling and randoms to model the average transport of photons. Such approach is used extensively in modelling radiation (see e.g. [8, 9, 10, 11, 12, 13, 14] from the heat transfer community, and [15, 16] from the neutronic community, to cite but a few). The main advantage of Monte Carlo methods is that they are based on physical processes, and can converge to the physical solutions if : i) the physical process is accurately modeled, ii) the model does not contain any inherited biases and, iii) the physical data used by these algorithms, such as scattering probability, are well known. Highly complex geometries can be dealt with, but high accuracy needs high computational expense [17].

On the other hand, in the field of deterministic methods, Finite Volume Methods (FVM) used for the space discretization of the RTE is probably the most common. It is well accepted that they can provide accurate results within a reasonable computational time [18, 19, 20, 21]. In this field, [22] reviews recent advances for the numerical solution of the RTE with FVM.

Besides FVM, Finite Element Methods (FEM) are interesting alternatives, essentially because of versatility : complex geometries can be dealt with, and degrees of approximation can be chosen almost arbitrarily. Also, generic finite element libraries can be used as general frameworks for the numerical implementation of variational formulations (for example, the presented developments are extensively based on [23]), following the work of [24, 25, 26].

FEM have been used recently for the space discretization on three-dimensional radiative transfer problems using Discontinuous Galerkin (DG) approach [27, 28, 29, 30]. This scheme has been developed mainly because the advection term of the RTE plays a central role : its attractiveness comes from the fact that it has the advantages of versatility from FEM and it has the element-wise conservativity of FVM. Other schemes such as Least-Squares (LS) and Streamline Upwind Petrov–Galerkin (SUPG) allows stable solutions but at the price of adding artificial diffusion. A recent comparison between DG and SUPG [26, 31] showed, in terms of convergence rate and number of degrees of freedom, and in two-dimensional geometries, that SUPG methods were effective when continuous solutions were to be found, or in conjunction with sub-grid scale models. Physical cases considered in the present paper involve three spatial dimensions and continuous external sources, henceforth SUPG schemes have been chosen for the proposed algorithmic developments.

Formally, the steady radiative transfer equation can be written as, for a monochromatic wavelength λ :

$$\boldsymbol{s} \cdot \nabla I(\boldsymbol{x}, \boldsymbol{s}) + \beta I(\boldsymbol{x}, \boldsymbol{s}) = \sigma_s \int_{4\pi} \Phi(\boldsymbol{s}, \boldsymbol{s}') I(\boldsymbol{x}, \boldsymbol{s}') \, \mathrm{d}\Omega(\boldsymbol{s}') + \kappa I_b(T) \tag{3.1}$$

where I is the radiative intensity for all directions $\boldsymbol{s}$ of the unit sphere, and for all $\boldsymbol{x}$ in the open bounded domain $\mathcal{D}$. Also, σ_s is the scattering coefficient, κ is absorption coefficient, $\beta = \kappa + \sigma_s$ is the so-called extinction coefficient, and the function Φ under the integral sign is the phase scattering function. Further, I_b is the black body emissivity

function that depends explicitly on temperature T. the wavelength symbol λ is omited for clearer equations.

In order to complete the physical problem statement, boundary conditions are to be specified. In the field of radiative transfer, this is written as, for $\boldsymbol{s} \cdot \boldsymbol{n} < 0$:

$$I(\boldsymbol{x}, \boldsymbol{s}) = \tilde{I}(\boldsymbol{x}, \boldsymbol{s}) + (1 - \alpha) I^{\Cup}(\boldsymbol{x}, \boldsymbol{s}) + \alpha I^{\Vee}(\boldsymbol{x}, \boldsymbol{s}) \tag{3.2}$$

The first term on the right-hand-side of (3.2) is the Dirichlet contribution which may explain external sources for example, as well as diffuse emission. The second term is the diffuse contribution of the reflection, and the third term is the specular contribution of the reflection. In order to gauge each reflection contribution, a balance is applied thanks to the coefficient α. Though the diffuse reflection is often treated in literature, the specular reflection is less often treated, maybe because its numerical treatment is more tricky. Diffuse and specular reflections are given by (3.3) and (3.4), respectively :

$$I^{\Cup}(\boldsymbol{x}, \boldsymbol{s}) = \frac{\rho_d}{\pi} \int_{\boldsymbol{s}' \cdot \boldsymbol{n} > 0} I(\boldsymbol{x}, \boldsymbol{s}') \boldsymbol{s}' \cdot \boldsymbol{n} \, \mathrm{d}\boldsymbol{s}' \tag{3.3}$$

$$I^{\Vee}(\boldsymbol{x}, \boldsymbol{s}) = \rho_s (\boldsymbol{s} \cdot \boldsymbol{n}) I(\boldsymbol{x}, \zeta(\boldsymbol{s})) \tag{3.4}$$

with ρ_d and ρ_s the reflectivity coefficients for the diffuse and specular contributions, respectively, and $\zeta(\boldsymbol{s}) = \boldsymbol{s} - 2(\boldsymbol{s} \cdot \boldsymbol{n})\boldsymbol{n}$ is the out-going direction of $\boldsymbol{s}$.

At this stage, the knowledge of physical properties $\kappa(\boldsymbol{x})$, $\sigma_s(\boldsymbol{x})$, $\Phi(\boldsymbol{s}, \boldsymbol{s}')$, ρ_d, ρ_s, α, incident external source $\tilde{I}$, temperature T and geometry $\mathcal{D}$, forms the input for solving the radiative transfer problem. The radiative problem therefore consists in finding $I(\boldsymbol{x}, \boldsymbol{s}) \in \mathcal{D} \times \mathcal{B} \mapsto \mathbb{R}^+$ that satisfies both the continuous state equation (3.1) and the condition on the border (3.2), with the open bounded space domain $\mathcal{D} \subset \mathbb{R}^3$ and the unit sphere $\mathcal{B} = [0, 2\pi] \times [0, \pi] \subset \mathbb{R}^2$.

The main objective of this paper is to give general algorithms needed to solve accurately the radiative transfer equation along with the above-mentioned diffuse and specular reflections.

This paper is organized as follows. Section 3.2 presents the angular discretization of the unit-sphere in order to semi-discretize the radiative transfer equation, and emphasizes the differences between numerical quadrature and angular discretization. In fact, the discretization that is chosen in this study corresponds to $P0$ angular finite elements (AFEM) (i.e. based on a variational formulation) as defined for example in [32]. Next, Section 3.3 deals with the discretization of the specular reflection boundary condition. This section, which constitutes the core of the paper, details very precisely the derivation of partition ratio coefficients. Section 3.4 details the variational formulation related to the full strong radiative transfer problem. To add more, the bilinear and linear forms are built. Validations of all algorithms then come in Section 3.5 through a comparison bewteen 3 specular methods and a convergence analysis for both space and angles. Before conclusions and perspectives being drawn, Section 3.6 finally presents applications of the radiative transfer coupled with specular reflection on complex geometries.

3.2 RTE semi-discretization

In most situations, the continuous equations (3.1)-(3.2) governing radiative transfer in semi-transparent media cannot be used as it is, they need to be discretized, both in space and angle. The ordinary way is to first discretize angles. To do so, the discrete ordinate method is performed on the unit sphere. The result of this is a set of directions $\boldsymbol{s}_m$, $m = 1, \dots N_d$ along with associated weights ω_m.

The application of this discrete ordinate method on the fully continuous radiative transfer equation yields the semi-discretized version of the RTE :

$$\boldsymbol{s}_m \cdot \nabla I_m(\boldsymbol{x}) + \beta I_m(\boldsymbol{x}) = \sigma_s \sum_{j=1}^{N_d} \omega_j \Phi_{m,j} I_j(\boldsymbol{x}) + \kappa I_b(T) \quad \forall m = 1, \dots, N_d \tag{3.5}$$

Each equation of this system of semi-discrete equations is further to be discretized in space with an appropriate approximation scheme such as the finite volume methods, discontinuous Galerkin methods, decentered finite elements, etc. Based on a survey performed on two dimensional problems, which revealed that SUPG approximations were good challengers for RTE problems [26, 31], the section 3.4 details an appropriate scheme for the space discretization.

Couples of directions/weights, $\{\boldsymbol{s}_m, \omega_m\}_{m=1,\cdots,N_d}$, are determined either discretizing the unit sphere, see for instance [33, 34] or using a quadrature, [35, 36] to cite but a few. Other methods exist, such as using finite elements for angles for the calculation of weights approximating the integral of the phase function [32].

Among the large number of different quadratures, the S_n-based methods, i.e. the level symmetric quadrature, which has been revisited for example by [37] for acceleration purposes, is probably the most famous. Such a quadrature has been applied in a huge number of applications coupled with either finite difference [38], finite elements [39, 40, 41, 42, 43, 44, 45, 46, 47, 48, 49], meshless methods [50, 51] and especially finite volume methods [52, 53, 54, 55, 56, 57, 58, 59, 60, 61]. Note that during the past 40 years, significant progress has been achieved in the development of acceleration that speed up the iterative convergence of such problems, see the review [62]. Moreover, it is well accepted, see e.g. [2, 3, 63], that optimized quadrature converge more quickly to the solution than angular discretizations.

However, on the other hand, the Discrete Ordinates Method based on angular discretization allows accurate treatment of specular reflection when considering arbitrary geometries, say different from rectangular enclosures [18, 64]. This consideration that motivated this study is fully developed in section 3.3. More specifically, the treatment of specular reflection is based on analytical calculation of partition ratio coefficients from any spherical angle to any other spherical angle, based on mathematical considerations as well as on the basic application of the Fresnel law.

Two ordinary angular discretization methods presented schematically in Figure 3.1 will be used in the present study. The T_n methods introduced in [34], and the first S_n method developed by [33]. As schematically presented in this figure, it is suggested to calculate analytically the weight associated to a given direction as the area of the closed solid angle surrounding the direction, i.e. $\omega_m = \text{meas}(\Omega_m)$.

Note that other angular discretizations could have been used, such as the so-called piecewise constant approximation (PCA) scheme which has been used for example by [50, 65] or the $\mathrm{SqT}_{p,n}$ discretization used afterwards for validation and application purposes (see Sections 3.5 and 3.6), this latter angular discretization being explained in detail in 3.9. Note also that, sometimes if not often, practitioners use already-made tables for both the determination of angles and associated weights.

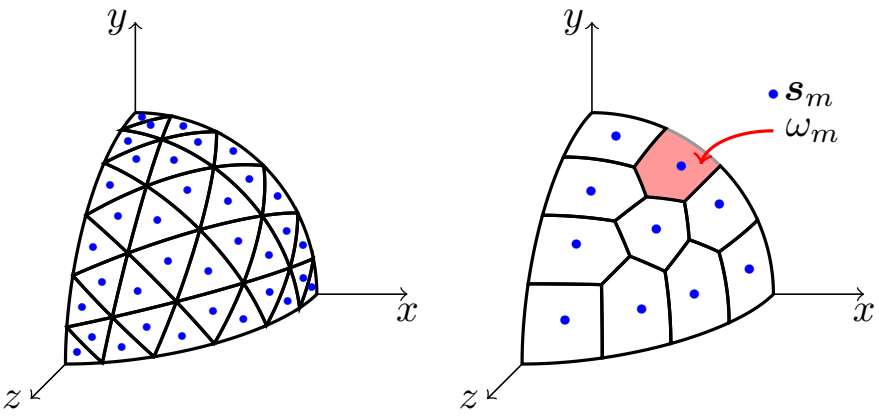

FIGURE 3.1 – Ordinary discretization of an eighth of a unit sphere with the T_n method [34] and the S_n method [33].

3.3 Specular reflection

In the same manner as for the RTE, the continuous equation (3.2) governing reflections on borders $\partial\mathcal{D} \cap (\boldsymbol{s}_m \cdot \boldsymbol{n} < 0)$, $\boldsymbol{n}$ being the outward normal unit vector, is discretized thanks to the discrete ordinate method :

$$I_m(\boldsymbol{x}) = \tilde{I}_m(\boldsymbol{x}) + (1-\alpha) I_m^{\uplus}(\boldsymbol{x}) + \alpha I_m^{\vee}(\boldsymbol{x}) \tag{3.6}$$

We recall that the first two components in the right-hand-side of (3.6) are often treated in the literature, while the last term related to specular reflection needs special treatment. For the diffuse contribution, the discrete version of the boundary condition (3.3) is written as :

$$I_m^{\uplus}(\boldsymbol{x}) = \frac{\rho_d}{\bar{\pi}} \sum_{\boldsymbol{s}_j \cdot \boldsymbol{n} > 0} \omega_j I_j(\boldsymbol{x}) \; \boldsymbol{s}_j \cdot \boldsymbol{n} \tag{3.7}$$

with ρ_d the diffuse reflectivity. Note that the denominator $\bar{\pi}$, approximation of π, is to be evaluated numerically, using $\bar{\pi} = \sum_{\boldsymbol{s}_j \cdot \boldsymbol{n} > 0} \omega_j \; \boldsymbol{s}_j \cdot \boldsymbol{n}$, in order to conserve the energy in diffusive reflection. Besides this ordinary condition, for the continuous condition (3.4) of the specular reflection, one has :

$$I_m^{\vee}(\boldsymbol{x}) = \rho_s(\boldsymbol{s}_m, \boldsymbol{n}) \sum_{\boldsymbol{s}_j \cdot \boldsymbol{n} > 0} \delta_{m,j}(\boldsymbol{n}) I_j(\boldsymbol{x}) \quad \forall m, \boldsymbol{s}_m \cdot \boldsymbol{n} < 0 \tag{3.8}$$

In this relationship, ρ_s is the specular reflectivity, and $\delta_{m,j}(\boldsymbol{n})$, $m, j = 1, \ldots, N_d$ are partition ratio coefficients. The partition ratio coefficient $\delta_{m,j}$ if $m \neq j$ represents the

part of the solid angle of Ω_j which is reflected into the other solid angle Ω_m. Note also that the relationship (3.8) assumes that the solid angle Ω_j respects the partition :

$$\sum_{\boldsymbol{s}_m \cdot \boldsymbol{n} < 0} \delta_{m,j}(\boldsymbol{n}) = 1 \quad \forall j, \boldsymbol{s}_j \cdot \boldsymbol{n} > 0 \tag{3.9}$$

The computation of partition ratio coefficients $\delta_{m,j}(\boldsymbol{n})$, $\forall j \mid \boldsymbol{s}_j \cdot \boldsymbol{n} > 0$ is performed following these three distinct steps :

1. A solid angle is fully reflected on the border (see Figure 3.2, left) or only partially reflected (see Figure 3.2, right). The computation of the amount of the reflected part is presented in section 3.3.1.
2. The reflected solid angle is very unlikely to correspond to any already introduced solid angle (see Figure 3.3). So, the intersections of this solid angle with all others are to be calculated. This calculation is presented in section 3.3.2.
3. Finally, partition ratio coefficients $\delta_{m,j}(\boldsymbol{n})$ are determined with the strategy presented in section 3.3.3.

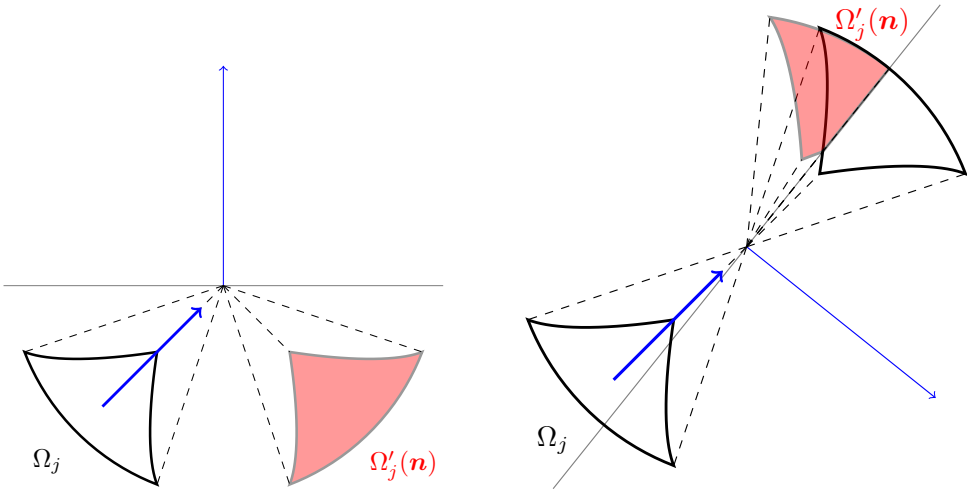

FIGURE 3.2 – Determination of the reflected solid angle $\Omega'_j(\boldsymbol{n})$ – Left : the whole solid angle Ω_j is reflected ; Right : only a part of the solid angle Ω_j is reflected

Note that the calculation of partition ratio coefficients is part of pre-processing. The related computation time is negligible in the context of finite elements : linear system building and solving iteratively.

This partitioning method (in short PM) is compared with two other projection methods. In the first projection method (in short 1-DP), the reflected radiative intensity is projected onto the first closest direction of the angular discretization. In the second projection method (in short 3-DP), the reflected radiative intensity is projected onto the three closest directions of the angular discretization, the three weights being the relative distance between the reflected direction and the three closest angular discretization directions. Note that both the 1-DP and 3-DP methods are explained more in detail in section 3.5.1.

For readability considerations, we attempt to highlight the differences between partitioning method and other projection methods via a simplified non-uniform discretization of the unit circle. Note that such a discretization has been used for two-dimensional

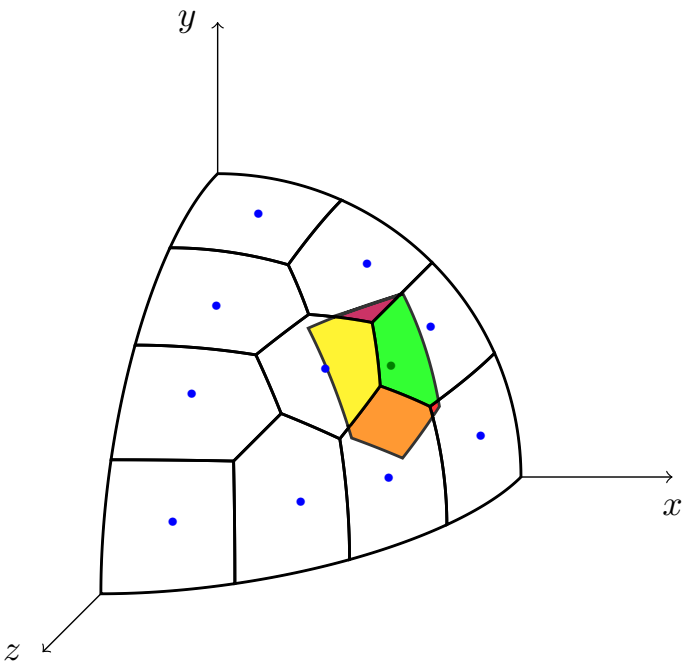

FIGURE 3.3 – Proportional redistribution of a given solid angle.

cases in [26, 27]. For this particular context, one can still consider the PM and 1-DP methods, while the 2-DP method is to be considered instead of the 3-DP method. A schematic representation of these differences are illustrated in Figure 3.4.

In figure 3.4, cases a. and b. on the top represent the 1-DP method, cases c. and d. in the middle represent the 2-DP method, and cases e. and f. on the bottom represent the PM partitioning method. Solid angles painted in blue represent the incident solid angles. Solid angles closed by green lines represent the theoretical reflected solid angles, for a reflectivity coefficient equal to one, and solid angles painted in red represent the reflected solid angles determined by the three different methods.

The angular discretization of the half circle is very coarse on the first quarter (there are only three elements in $[\pi/2 : \pi]$), and fairly fine on the other quarter (there are 20 elements in $[0 : \pi/2]$). Note that such strategy may be used to reduce the number of directions and therefore save computational time, such as in [66] for example. In our applications, such angular refinement may be used to model accurately radiative sensors in Infra-Red spectrometer for example.

What appears from Figure 3.4 is that there is small disparity of results between projection methods and the partition method when a large number of solid angles reflects onto a large solid angle. Computed solutions are close to theoretical ones.

However, errors are highly exacerbated for projection methods when a large solid angle is reflected onto a large number of small solid angles. In this particular case, the partition method is the only method that does not lead to large errors, as indicated in Figure 3.4.

Note that similar conclusions could have been stated for some other cases, but in general the partition method leads to obtain a close approximation of the theoretical solution, as shall be seen later on in the numerical tests section.

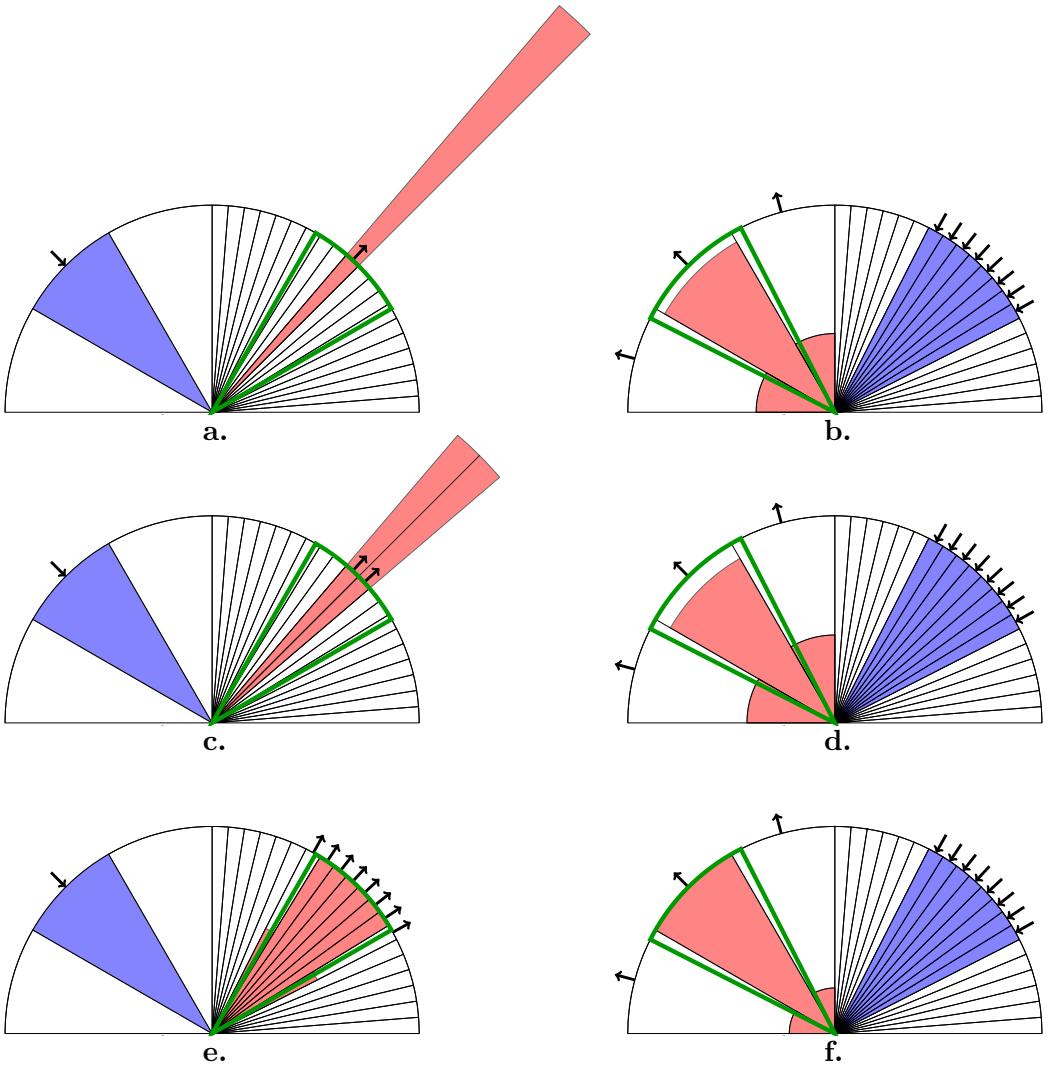

FIGURE 3.4 – 2D examples of specular reflection for two kinds of solid angle intersections – a. b. : 1-DP method – c. d. : 2-DP method – e. f. : partition method (PM).

In order to perform calculations associated to the partition method, necessary tools are given as preliminaries, below.

Preliminary tools

— The specular reflectivity ρ_s follows the Fresnel law. The specular reflectivity calculation is available from the knowledge of both the incident direction $\boldsymbol{s}_m$ and the external normal $\boldsymbol{n}$ satisfying $\boldsymbol{s}_m \cdot \boldsymbol{n} \in [0, 1]$. For a medium with a refraction index n, the specular reflectivity is [2] :

$$\rho(\boldsymbol{s}_m, \boldsymbol{n}) = \begin{cases} 1 & \text{if } \pi/2 > \theta_i > \theta_c \\ \dfrac{1}{2}\left[\left(\dfrac{\sin(\theta_i - \theta_r)}{\sin(\theta_i + \theta_r)}\right)^{1/2} + \left(\dfrac{\tan(\theta_i - \theta_r)}{\tan(\theta_i + \theta_r)}\right)^{1/2}\right] & \text{if } \theta_c > \theta_i > 0 \\ \left(\dfrac{n-1}{n+1}\right)^2 & \text{if } \theta_i = 0 \end{cases} \tag{3.10}$$

where $\theta_r = \arcsin(\sqrt{1-(\boldsymbol{s}_n \cdot \boldsymbol{n})^2}/n)$ is the refracted angle and $\theta_c = \arcsin(1/n)$ is the critical angle. Both angles are obtained by the Snell-Descartes law [3].

— A solid angle Ω is defined as the spherical area between 3 diametrical planes. The intersections between these planes are the edge directions of Ω denoted $\{\boldsymbol{e}_1, \boldsymbol{e}_2, \boldsymbol{e}_3\}$. Such a solid angle is schematically presented in Figure 3.5. Further, with $\alpha_{ik} = \arccos(\boldsymbol{e}_i \cdot \boldsymbol{e}_k)$ the angle between edges $\boldsymbol{e}_i$ and $\boldsymbol{e}_k$, the area $\omega = \text{meas}(\Omega)$ is calculated using Huilier theorem :

$$\omega = 4 \arctan \left[\sqrt{\tan \frac{p}{2} \tan \frac{p-\alpha_{12}}{2} \tan \frac{p-\alpha_{13}}{2} \tan \frac{p-\alpha_{23}}{2}} \right] \tag{3.11}$$

where $p = \frac{1}{2}(\alpha_{12} + \alpha_{13} + \alpha_{23})$ is the half perimeter.

— The spherical curve between $\boldsymbol{e}_i$ and $\boldsymbol{e}_k$ is also needed. Its parametric function is formally expressed, in vector form, as :

$$\mathcal{C}_{ik}(t) = \frac{(1-t)\boldsymbol{e}_i + t\boldsymbol{e}_k}{||(1-t)\boldsymbol{e}_i + t\boldsymbol{e}_k||_2} \quad t \in [0,1] \tag{3.12}$$

— Finally, it is assumed that a polygonal solid angle can always be split into several triangular solid angles yielding to a partition. Such a partition is schematically presented in Figure 3.6.

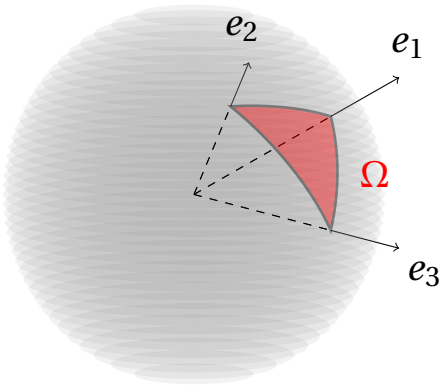

FIGURE 3.5 – Schematic representation of a triangular solid angle.

3.3.1 Step 1 : solid angle reflection

On the border, each direction $\boldsymbol{s}'$ satisfying the condition $\boldsymbol{s}' \cdot \boldsymbol{n} < 0$ is called from now on a reflected direction. It is pointed out that each reflected direction comes from a single and unique incident direction $\boldsymbol{s}$. We recall that the weight associated to a given direction is equal to the area of the spherical polygon associated to the direction, i.e. one has $\omega_i = \text{meas}(\Omega_i)$. The edge $\boldsymbol{e}_i$ of Ω_i is reflected to $\boldsymbol{e}'_i$, edge of Ω'_i, applying $\boldsymbol{e}'_i = -R(\boldsymbol{n})\boldsymbol{e}_i = \boldsymbol{e}_i - 2(\boldsymbol{e}_i \cdot \boldsymbol{n})\boldsymbol{n}$ with $R(\boldsymbol{n})$ the rotational matrix given by

$$R(\boldsymbol{n}) = \begin{pmatrix} 2(\boldsymbol{n})_x^2 - 1 & 2(\boldsymbol{n})_x(\boldsymbol{n})_y & 2(\boldsymbol{n})_x(\boldsymbol{n})_z \\ 2(\boldsymbol{n})_x(\boldsymbol{n})_y & 2(\boldsymbol{n})_y^2 - 1 & 2(\boldsymbol{n})_y(\boldsymbol{n})_z \\ 2(\boldsymbol{n})_x(\boldsymbol{n})_z & 2(\boldsymbol{n})_y(\boldsymbol{n})_z & 2(\boldsymbol{n})_z^2 - 1 \end{pmatrix} \tag{3.13}$$

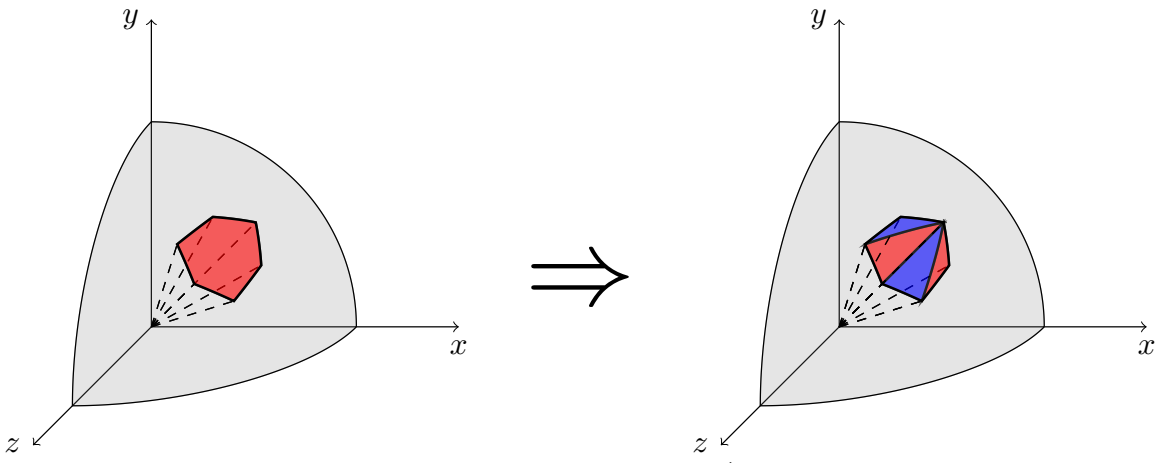

FIGURE 3.6 – Schematic representation of a partition of a polygonal solid angle into triangular solid angles.

After reflection, the shape of the solid angle may change, for example if a part of it is not reflected (see Figure 3.2). So, one has to compute the reflected solid angle in terms of edges to build the reflected polygon. Let us denote $\Omega'_j(\boldsymbol{n})$ the reflected part coming from the solid angle Ω_j, and $\{\boldsymbol{e}_i^j\}_{i=1,\cdots,I}$ the set of edges of the polygon Ω_j. In the following the superscript j is omitted for readability considerations. Two cases are available :

1. if $\boldsymbol{e}_i \cdot \boldsymbol{n} > 0 \ \forall i$, then the solid angle Ω_j is totally reflected. In this first case, the reflected solid angle $\Omega'_j(\boldsymbol{n})$ being the symmetric of Ω_j, one has $\text{meas}(\Omega'_j(\boldsymbol{n})) = \text{meas}(\Omega_j)$.
2. else, $\exists i \mid \boldsymbol{e}_i \cdot \boldsymbol{n} < 0$, then only a part of the solid angle is reflected. In this case, the reflected solid angle $\Omega'_j(\boldsymbol{n})$ is not similar to Ω_j. Thus edges of $\Omega'_j(\boldsymbol{n})$ must be determined. To do so, assume two edges $\boldsymbol{e}_i$ and $\boldsymbol{e}_k$ such that $\boldsymbol{e}_i \cdot \boldsymbol{n} > 0$ and $\boldsymbol{e}_k \cdot \boldsymbol{n} < 0$. Then, there exists a unique edge $\boldsymbol{e}_*$ in between $\boldsymbol{e}_i$ and $\boldsymbol{e}_k$ found to be equal to the vector parametric curve $\mathcal{C}_{ik}(t_*)$, $t_* \in]0,1[$ satisfying $\boldsymbol{e}_* \cdot \boldsymbol{n} = 0$. Hence, t_* is found to be expressed as :

$$t_* = -\frac{\boldsymbol{e}_i \cdot \boldsymbol{n}}{(\boldsymbol{e}_k - \boldsymbol{e}_i) \cdot \boldsymbol{n}} \tag{3.14}$$

The detailed algorithm developed to compute reflected solid angles is given in Algorithm 1, in 3.8.

3.3.2 Step 2 : intersection of solid angles

The reflected solid angle $\Omega'_j(\boldsymbol{n})$ must be compared with all existing solid angles Ω_m of the discretization. Indeed, except in rare cases, the solid angle $\Omega'_j(\boldsymbol{n})$ does not match perfectly with any already existing solid angle of the discretization. Therefore, the reflected solid angle $\Omega'_j(\boldsymbol{n})$ is to be shared proportionally between all solid angles Ω_m that it intersects. Such intersection is presented schematically in Figure 3.3. In order to present the calculation of the shared area, let us work on arbitrary two triangular solid angle Ω_m and $\Omega'_j(\boldsymbol{n})$ as presented arbitrarily on Figure 3.7.

The objective is to determine the intersection area between Ω_m and $\Omega'_j(\boldsymbol{n})$, which is denoted $A_{mj}(\boldsymbol{n})$. To calculate this area, one needs the knowledge of all edges of this

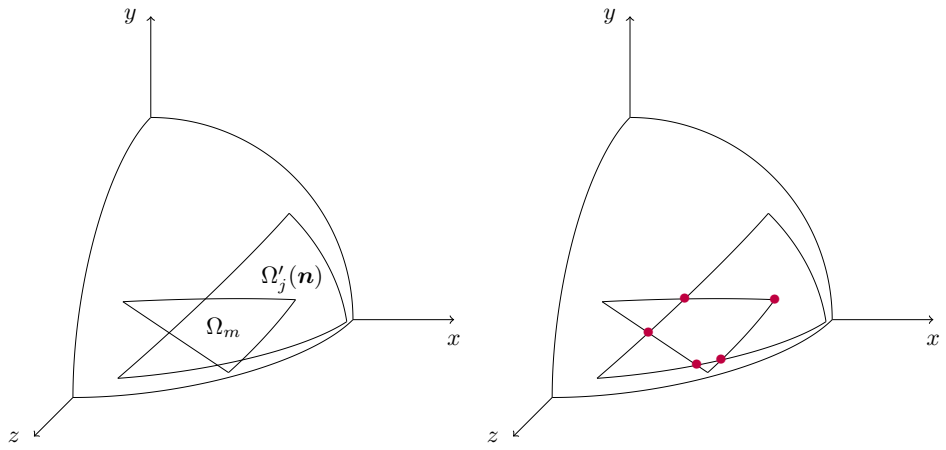

FIGURE 3.7 – Left : presentation of two arbitrary triangular solid angles Ω_m and $\Omega'_j(\boldsymbol{n})$ that intersect. Right : Edges of $\Omega_{mj}(\boldsymbol{n})$

crossed solid angles $\Omega_{mj}(\boldsymbol{n})$. To do so, one has to know if a given edge of Ω_m stands within the solid angle $\Omega'_j(\boldsymbol{n})$ or whether it stands outside. In the former case, this edge is kept. In the latter case, the edge standing at the intersection between the two sides of solid angles Ω_m and $\Omega'_j(\boldsymbol{n})$ is introduced.

Let us introduce P_m the change of basis matrix between the standard basis $\{\boldsymbol{e}_x, \boldsymbol{e}_y, \boldsymbol{e}_z\}$ and the basis $\{\boldsymbol{e}_{m,1}, \boldsymbol{e}_{m,2}, \boldsymbol{e}_{m,3}\}$ based on edges of the solid angle Ω_m, and let us denote this matrix P_m and its inverse as :

$$P_m = (\boldsymbol{e}_{m,1} \quad \boldsymbol{e}_{m,2} \quad \boldsymbol{e}_{m,3}) \quad ; \quad P_m^{-1} = \begin{pmatrix} \boldsymbol{v}_1^t \\ \boldsymbol{v}_2^t \\ \boldsymbol{v}_3^t \end{pmatrix} \tag{3.15}$$

To check whether or not the edge $\boldsymbol{e}_{j,k}$ stands within the solid angle Ω_m, one uses the following property. The edge $\boldsymbol{e}_{j,k}$ stands within the solid angle Ω_m if, and only if :

$$P_m^{-1}\boldsymbol{e}_{j,k} = \begin{pmatrix} \alpha > 0 \\ \beta > 0 \\ \gamma > 0 \end{pmatrix} \tag{3.16}$$

The intersection point $\boldsymbol{e}_* = \mathcal{C}_{ik}^{(j)}(t_*)$ between the side $\mathcal{C}_{ik}^{(j)}(t)$ and the side opposite at $\boldsymbol{e}_{m,1}$ satisfies :

$$P_m^{-1}\mathcal{C}_{ik}^{(j)}(t_*) = \begin{pmatrix} \alpha = 0 \\ \beta > 0 \\ \gamma > 0 \end{pmatrix} \quad t_* \in [0,1] \tag{3.17}$$

The equality $\alpha = 0$ means that the edge $\boldsymbol{e}_*$ does not depend on the edge $\boldsymbol{e}_{m,1}$ in the Ω_m basis, and then this edge $\boldsymbol{e}_*$ is on the plane $(\boldsymbol{e}_{m,2}0\boldsymbol{e}_{m,3})$. For $\boldsymbol{e}_{m,2}$, one has $\beta = 0$ and for $\boldsymbol{e}_{m,3}$, one has $\gamma = 0$. With the notation of P_m^{-1} in the equation (3.15), the edge $\boldsymbol{e}_* = \mathcal{C}_{ik}^{(j)}(t_*)$ is analytically determined for each side of Ω_m opposite to $\boldsymbol{e}_{m,l}$ with the parameter t_* being equal to :

$$t_* = -\frac{\boldsymbol{e}_i \cdot \boldsymbol{v}_l}{(\boldsymbol{e}_k - \boldsymbol{e}_i) \cdot \boldsymbol{v}_l} \tag{3.18}$$

Figure 3.7 shows the edges of $\Omega_{mj}(\boldsymbol{n})$ computed with the equations (3.16), (3.17) and (3.18). However, if edges are not ordered properly, the area $A_{mj}(\boldsymbol{n})$ calculated with the equation (3.11) is wrong. Figure 3.8 shows on the top a wrong calculation area if edges are not properly ordered. To solve this problem, all edges are projected onto the Ω_m basis thanks to the matrix P_m^{-1}. These projections $\boldsymbol{e}'_*$ are now into a positive octant in the Ω_m basis (see step (a) in Figure 3.8). Then, these directions are projected onto the plane $x + y + z = 1$ from the Ω_m basis (see step (b) in Figure 3.8). The projected edges $\bar{e}_*$ on this plane are then easily ordered thanks to the convex envelope method (see step (c) in Figure 3.8). With the same ordering of the edge $\bar{\boldsymbol{e}}_*$, the edges $\boldsymbol{e}_*$ are well ordered (step (d) in Figure 3.8), and the area $A_{mj}(\boldsymbol{n})$ can now be calculated analytically thanks to Huilier equation. We used relationships :

$$\boldsymbol{e}'_* = P_m^{-1}\boldsymbol{e}_* \quad ; \quad \bar{\boldsymbol{e}}_* = \frac{\boldsymbol{e}'_*}{\|\boldsymbol{e}'_*\|_1} \tag{3.19}$$

In practice, the determination of the cross section $\Omega_{mj}(\boldsymbol{n})$ between Ω_m and Ω'_j as detailed in this subsection is the main difficulty of the whole procedure. The global algorithm is split into 3 algorithms. The first one checks if an edge of a solid angle is included in the other solid angles (see Algorithm 2 in 3.8). The second one checks if an intersection between two sides called $\mathcal{C}^{(m)}_{k_1k_2}(t)$ for a side of the solid angle Ω_m and $\mathcal{C}^{(j)}_{i_1i_2}(t)$ for a side of the solid angle $\Omega'_j(\boldsymbol{n})$, exists (see Algorithm 3). Another algorithm then gathers the two other algorithms in order to get all edges of Ω_{mj} (see Algorithm 4). Finally, the algorithm used to order properly edges of reflected polygons in the one given in Algorithm 5 in 3.8.

3.3.3 Step 3 : calculation of partition ratio coefficients $\delta_{m,j}(\boldsymbol{n})$

At this stage, all cross section areas $A_{mj}(\boldsymbol{n})$ between the reflected solid angle Ω_m and the incident solid angle Ω_j are calculated. The partition ratio coefficient $\delta_{m,j}(\boldsymbol{n})$ is finally defined as the normalised ratio between $A_{mj}(\boldsymbol{n})$ and ω_m, the area of the solid angle Ω_m :

$$\delta_{m,j}(\boldsymbol{n}) = \frac{A_{mj}(\boldsymbol{n})}{\omega_j}\frac{1}{\sum_m A_{mj}(\boldsymbol{n})/\omega_j} \qquad \forall j \neq m \tag{3.20}$$

In the general case $\sum_m A_{mj}(\boldsymbol{n})/\omega_j = 1$, except in very special case where $|\boldsymbol{s}_j \cdot \boldsymbol{n}| \ll 1$. In these excepted cases, the solid angle is not fully reflected and a part is reflected to itself.

3.4 SUPG scheme

After applying the DOM on the RTE equation (3.1) and after fully discretizing the boundary condition (3.2), the problem consists at this stage in searching $I(\boldsymbol{x}, \boldsymbol{s}_m)$, $\forall m = 1, \cdots, N_d$, $\boldsymbol{x} \in \mathcal{D}$ that satisfies (3.5) and (3.6).The Streamline Upwind Pretrov-Galerkin finite element (SUPG) is used to get a space approximation of the radiative intensity for each solid angle Ω_m.

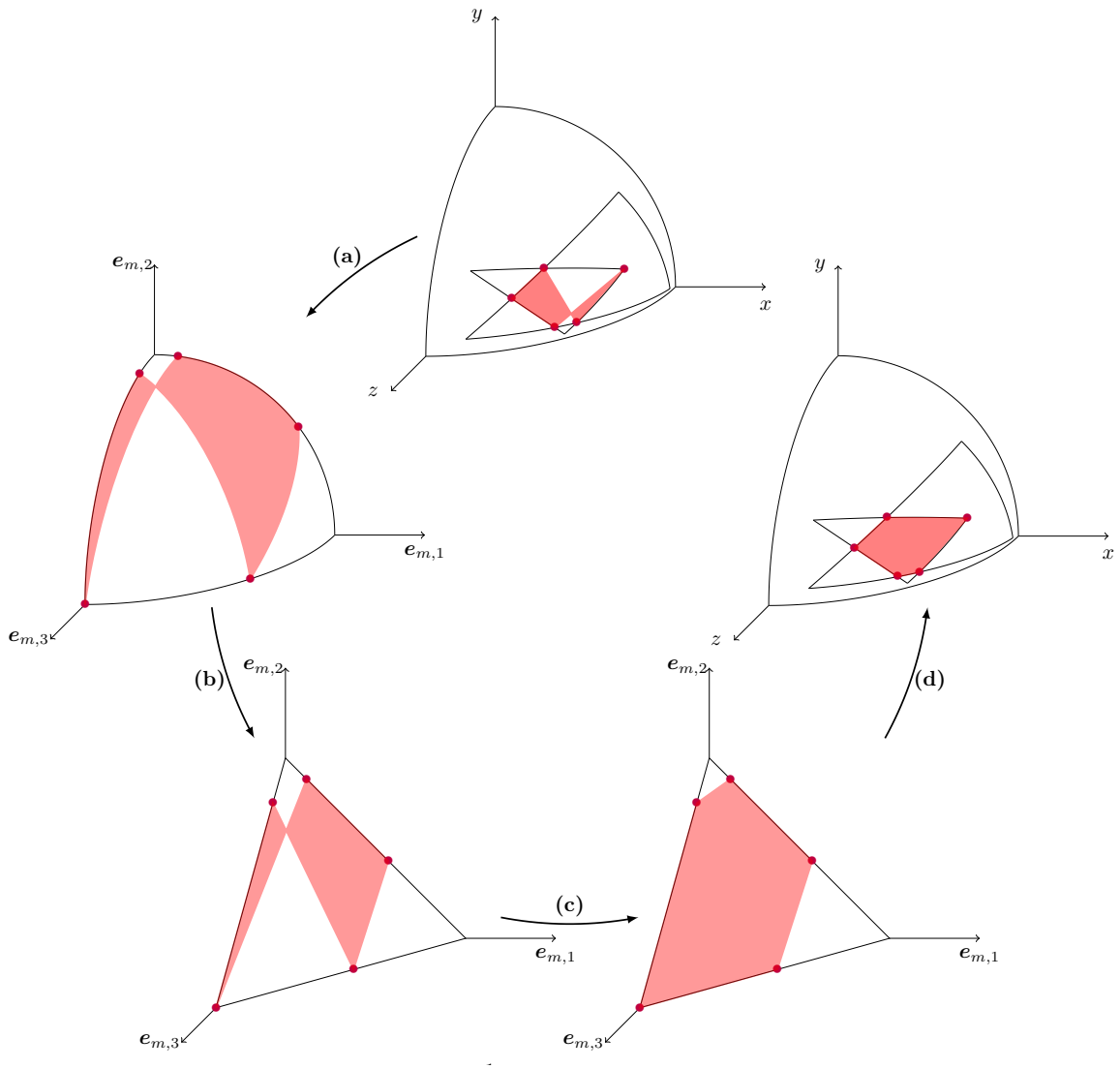

FIGURE 3.8 – Reordering of intersection edges following 4 steps : step (a) : projection of intersection edges onto the Ω_m basis ; step (b) : projection of intersection edges onto the plane $x + y + z = 1$; step (c) : re-ordering of intersection edges in the plane basis ; step (d) : transposition of ordering on the initial basis.

Before writing down variational formulations for the SUPG scheme, let us define the mesh $\mathcal{M}$ of the domain $\mathcal{D}$ as a finite collection of disjoint tetrahedral polyhedron $\mathcal{M} = \{\mathcal{C}_i\}\,,\ i = 1, \cdots, N_e$ forming a partition of $\mathcal{D}$, and for which each $\mathcal{C}_i \in \mathcal{M}$ is called a mesh element.

In order to simplify the presentation and notations, only the specular reflection is dealt with from now on, since this constitutes the most difficult point, and ρ is thus assimilated to ρ_s.

The SUPG scheme, studied for example in [67] on advection-diffusion problems, uses the lagrangian $\mathbb{P}_k$ basis to build the variational formulation. The functional space in which the solution is searched is the ordinary one when using finite elements :

$$\mathcal{V}_h = \left\{v \in C^0(\mathcal{D}),\ v \in \mathbb{P}_k(\mathcal{C}_i),\ k \in \mathbb{N}^+,\ i = 1, \cdots, N_e\right\} \tag{3.21}$$

In order to build the SUPG variational formulation, each semi-discrete equation (SDE_m) is multiplied by a function of the test function $v \in \mathcal{V}$, equal to $f_m(v) = v + \gamma \boldsymbol{s}_m \cdot \nabla v$, before integration on $\mathcal{D}$:

$$\int_{\mathcal{D}} \left[\boldsymbol{s}_m \cdot \nabla I_m + \beta I_m\right] f_m(v)\ \mathrm{d}\boldsymbol{x} = \int_{\mathcal{D}} \left[\sigma_s \sum_{j=1}^{N_d} \omega_j \Phi_{m,j} I_j + \kappa I_b(T)\right] f_m(v)\ \mathrm{d}\boldsymbol{x} \tag{3.22}$$

The m^{th} term under the sum symbol can be written down at the left-hand-side of the equality symbol and, after applying the Green theorem on the term $\boldsymbol{s}_m \cdot \nabla I_m v$, one finds :

$$\begin{aligned}\int_{\mathcal{D}} (\gamma \boldsymbol{s}_m \cdot \nabla I_m - I_m)(\boldsymbol{s}_m \cdot \nabla v) + \tilde{\beta}_m I_m f_m(v)\ \mathrm{d}\boldsymbol{x} \\ + \int_{\partial\mathcal{D}} I_m v \boldsymbol{s}_m \cdot \boldsymbol{n}\ \mathrm{d}\Gamma = \int_{\mathcal{D}} \left[\sigma_s \sum_{j=1, j\neq m}^{N_d} \omega_j \Phi_{m,j} I_j + \kappa I_b(T)\right] f_m(v)\ \mathrm{d}\boldsymbol{x}\end{aligned} \tag{3.23}$$

with $\tilde{\beta}_m = \beta - \sigma_s \omega_m \Phi_{m,m}$.

The integration over the boundary is split into two parts in order to exhibit the boundary conditions :

$$\int_{\partial\mathcal{D}} I_m v \boldsymbol{s}_m \cdot \boldsymbol{n}\ \mathrm{d}\Gamma = \int_{\boldsymbol{s}_m \cdot \boldsymbol{n} > 0} I_m v \boldsymbol{s}_m \cdot \boldsymbol{n}\ \mathrm{d}\Gamma + \int_{\boldsymbol{s}_m \cdot \boldsymbol{n} < 0} I_m v \boldsymbol{s}_m \cdot \boldsymbol{n}\ \mathrm{d}\Gamma \tag{3.24}$$

The boundary condition (3.6) coupled with (3.8) is then prescribed : the last term of the previous equation becomes :

$$\begin{aligned}\int_{\boldsymbol{s}_m \cdot \boldsymbol{n} < 0} I_m v \boldsymbol{s}_m \cdot \boldsymbol{n}\ \mathrm{d}\Gamma \\ = \int_{\boldsymbol{s}_m \cdot \boldsymbol{n} < 0} \left[\tilde{I}_m + \rho(\boldsymbol{s}_m, \boldsymbol{n}) \sum_{\boldsymbol{s}_j \cdot \boldsymbol{n} > 0} \delta_{m,j}(\boldsymbol{n}) I_j(\boldsymbol{x})\right] v \boldsymbol{s}_m \cdot \boldsymbol{n}\ \mathrm{d}\Gamma\end{aligned} \tag{3.25}$$

The SUPG variational formulation is finally written as the combination of equations (3.23), (3.24), and (3.25) for all directions $\boldsymbol{s}_m$. Formally, this results in a system of

variational formulations written as :

$$\sum_{m=1}^{N_d}\sum_{j=1}^{N_d} a_{m,j}(\mathbf{I},\mathbf{v}) = \sum_{m=1}^{N_d} l_m(\mathbf{v}) \tag{3.26}$$

with

$$\begin{cases} a_{m,m}(\mathbf{I},\mathbf{v}) = \displaystyle\int_{\mathcal{D}} (\gamma \boldsymbol{s}_m\cdot\nabla I_m - I_m)(\boldsymbol{s}_m\cdot\nabla v) + \tilde{\beta}_m I_m f_m(v)\ \mathrm{d}\boldsymbol{x} \\ \qquad\qquad + \displaystyle\int_{\boldsymbol{s}_m\cdot\boldsymbol{n}>0} I_m v \boldsymbol{s}_m\cdot\boldsymbol{n}\ \mathrm{d}\Gamma \\ a_{m,j\neq m}(\mathbf{I},\mathbf{v}) = -\displaystyle\int_{\mathcal{D}} \sigma_s\omega_j \Phi_{m,j} I_j f_m(v)\ \mathrm{d}\boldsymbol{x} \\ \qquad\qquad + \displaystyle\int_{\boldsymbol{s}_m\cdot\boldsymbol{n}<0\cap\boldsymbol{s}_j\cdot\boldsymbol{n}>0} \rho(\boldsymbol{s}_m,\boldsymbol{n})\delta_{m,j}(\boldsymbol{n}) I_j(\boldsymbol{x}) v \boldsymbol{s}_m\cdot\boldsymbol{n}\ \mathrm{d}\Gamma \\ l_m(\mathbf{v}) = -\displaystyle\int_{\boldsymbol{s}_m\cdot\boldsymbol{n}<0} \tilde{I}_m v \boldsymbol{s}_m\cdot\boldsymbol{n}\ \mathrm{d}\Gamma + \displaystyle\int_{\mathcal{D}} \kappa I_b(T) f_m(v) \end{cases} \tag{3.27}$$

The choice of the parameter γ may depend on the physical properties as well as on the mesh size. Following [68], a good choice for this so-called streamline parameter is given by :

$$\gamma \approx \begin{cases} 0.3h & \text{if } \beta \ll 1 \\ 0 & \text{if } \beta > 1 \end{cases} \tag{3.28}$$

where h is the mesh size defined later on in Section 3.5. It has been tested that such a choice for this parameter adds enough stability over traditional finite element methods, especially when the extinction parameter is very low.

It is also to be pointed out that for $\gamma = \tilde{\beta}_m$, the weak formulation (3.27) is similar to a Least-Square formulation. Moreover, this weak formulation (3.27) is also similar to the so-called SAAF (self-adjoint angular flux) weak formulation used in the neutronics community, even if the way to build it is different [48, 49].

3.5 Validation of the reflection strategy

The set of variational formulations (3.26) gives us numerical approximations of the radiative intensity I for each direction $\boldsymbol{s}_m$, and for all $\boldsymbol{x} \in \mathcal{D}$. To validate the proposed strategy for the specular reflection treatment coupled with the DOM and SUPG formulation, some comparisons with exact solutions are performed.

At first, the partitioning method approach is compared with projection methods which are simpler and much more straightforward (Section 3.5.1). These comparisons will show that the partitioning approach is accurate and challenging in critical cases, for coarse and fine angular discretizations, and especially for non-uniform angular discretizations. Then, as a second step, a convergence study is performed (see Section 3.5.2) .

In following examples, the block-based Gauss–Seidel iterative algorithm as the one used in [69] is used to solve the linear system arising from the discretization of variational formulations (3.26). The criterion used to ensure stabilization of the solution

is based on the euclidean norm of the difference between two successive solutions of the full radiative intensity vector. At a given iteration k, the stabilization criterion is fulfilled if $\|\mathbf{I}^{(k)} - \mathbf{I}^{(k-1)}\|_2 \leq 10^{-12}$.

3.5.1 Comparison with projection methods

In this section, numerical results obtained by the partitioning strategy are compared with those based on two projection strategies. For the 1-DP method, the radiative intensity relative to a given calculated incident direction is projected onto the single closest existing direction of the angular discretization. One thus uses :

$$I_k(\boldsymbol{x}) = \rho(\boldsymbol{s}_k \cdot \boldsymbol{n}) I_m(\boldsymbol{x}) \tag{3.29}$$

with $m = \arg\max_i \zeta(\boldsymbol{s}_k) \cdot \boldsymbol{s}_i$, i.e. m maximizes the scalar product among all possibilities.

For the 3-DP method, the radiative intensity relative to a given calculated incident direction $\boldsymbol{s}_j$ is shared between the 3 closest existing directions of the angular discretization. For one reflected direction $\boldsymbol{s}_k$, the incoming radiative intensity is the sum of the weighted incident radiations. One thus uses :

$$I_k(\boldsymbol{x}) = \rho(\boldsymbol{s}_k \cdot \boldsymbol{n}) \sum_{j=1}^{N_d} \delta_{k,j}(\boldsymbol{n}) I_j(\boldsymbol{x}) \tag{3.30}$$

Note that for a given incident direction $\boldsymbol{s}_j$, only 3 weights $\delta_{k,j}(\boldsymbol{n})$ are different from zero. Moreover, the weights satisfy $\sum_{k=1}^{N_d} \delta_{k,j}(\boldsymbol{n}) = 1$, $\forall j = 1, \ldots, N_d$.

1st comparison : specularity only with isotropic incident radiative intensity

For this first comparison, the test case is chosen to be totally independent of space, i.e. there is no scattering, no absorption, and no transport. There is only specular reflection on a boundary. In such case, the numerical computation can be compared to the theoretical solution.

Let, on a given point $\boldsymbol{x}_0 \in \partial\mathcal{D}$ on a boundary a given outward unit normal vector $\boldsymbol{n}$. And let the incident radiative intensity be equal to one for all directions : $I(\boldsymbol{x}_0, \boldsymbol{s}) = 1$, $\forall \boldsymbol{s} \cdot \boldsymbol{n} > 0$. For a reflectivity coefficient $\rho = 1$, the reflected radiative intensity is supposed to be given by $I(\boldsymbol{x}_0, \boldsymbol{s}) = 1$, $\forall \boldsymbol{s} \cdot \boldsymbol{n} < 0$, as schematically presented in Figure 3.9. In such case, the reflected density is equal to the incident density, i.e. $D^+(\boldsymbol{x}_0) = \int_{\boldsymbol{s}\cdot\boldsymbol{n}>0} I(\boldsymbol{x}_0, \boldsymbol{s})\ \mathrm{d}\boldsymbol{s} = \int_{\boldsymbol{s}\cdot\boldsymbol{n}<0} I(\boldsymbol{x}_0, \boldsymbol{s})\ \mathrm{d}\boldsymbol{s} = D^-(\boldsymbol{x}_0) = 2\pi$.

Discrete ordinates are used. Each incident direction is associated to the weight equal to the proportion of the related solid angle measure. Note that, in the discrete version we have developed, not only incident directions in the sense $\boldsymbol{s}_j \cdot \boldsymbol{n} > 0$ are used, but also critical angles are used as was shown schematically in Figure 3.2 as well as in Figure 3.9 for a bi-dimensional version. This process is exactly the same for the reflected radiative intensity.

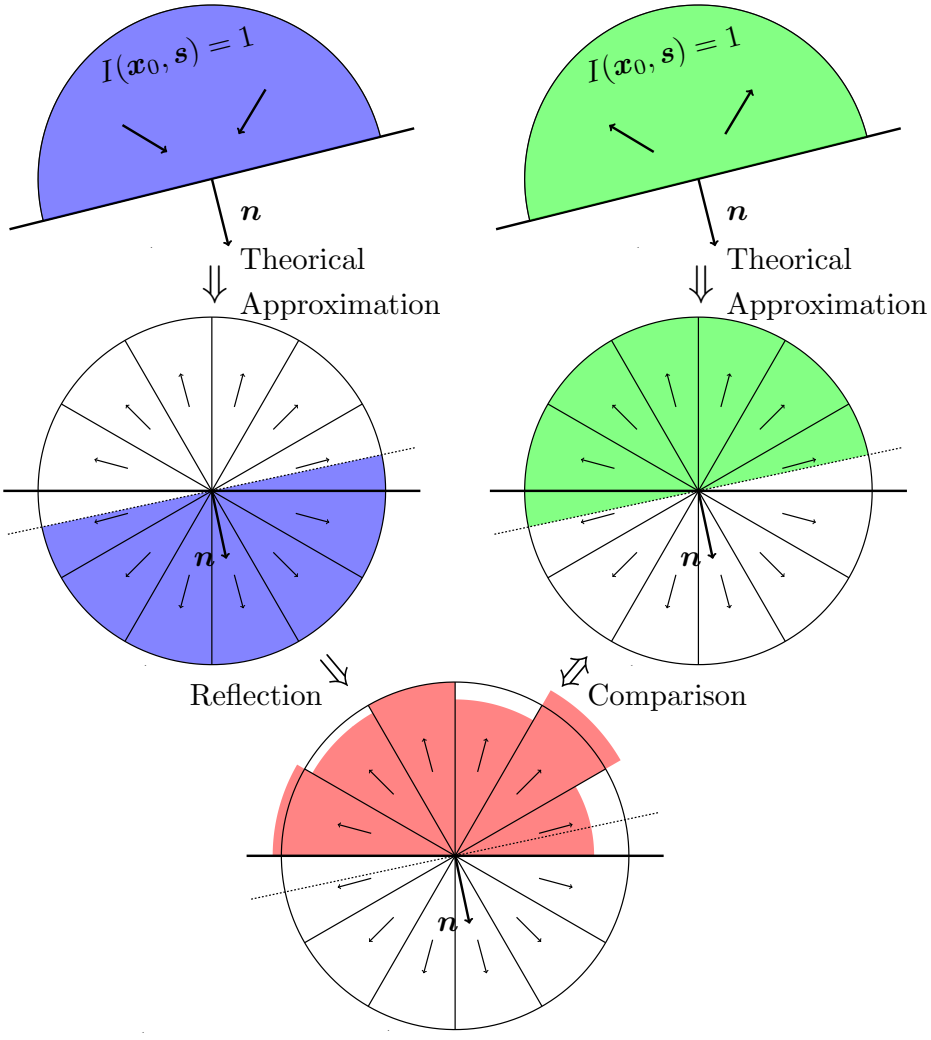

FIGURE 3.9 – Top : Incident radiative intensity (left) and theoretical reflected radiative intensity (right) – Middle : theoretical solution for the incident intensity (left) and the reflected intensity (right), along with angular discretization – Bottom : computed reflected intensity after reflection of the theoretical incident radiance.

The comparison between the theoretical solution $I_{\text{th}}(\boldsymbol{x}_0, \boldsymbol{s}_j)$ and the computed one $I(\boldsymbol{x}_0, \boldsymbol{s}_j)$ is performed for a large number of normal directions in $\mathcal{S}^2$. More specifically, the unit sphere is meshed. Each node of the mesh corresponds to a given normal direction. For the present case, 5994 nodes (directions) have been created on the surface, using Gmsh [70].

For each normal direction, the errors associated to the computed reflected intensity are given by :

$$E_1(\boldsymbol{n}) = \frac{2}{N_d} \sum_{\boldsymbol{s}_j \cdot \boldsymbol{n} < 0} |I_{\text{th}}(\boldsymbol{x}_0, \boldsymbol{s}_j) - I(\boldsymbol{x}_0, \boldsymbol{s}_j)| \tag{3.31}$$

$$E_2(\boldsymbol{n}) = \sqrt{\frac{2}{N_d} \sum_{\boldsymbol{s}_j \cdot \boldsymbol{n} < 0} \left(I_{\text{th}}(\boldsymbol{x}_0, \boldsymbol{s}_j) - I(\boldsymbol{x}_0, \boldsymbol{s}_j)\right)^2} \tag{3.32}$$

$$E_\infty(\boldsymbol{n}) = \max_{\boldsymbol{s}_j \cdot \boldsymbol{n} < 0} |I_{\text{th}}(\boldsymbol{x}_0, \boldsymbol{s}_j) - I(\boldsymbol{x}_0, \boldsymbol{s}_j)| \tag{3.33}$$

Such a test is performed for the partition method on one hand, and the two projection methods 1-DP and 3-DP defined above. Following angular discretizations have been tested : S_4, S_8, $SqT_{5,3}$ and $SqT_{8,3}$. These discretizations are presented in 3.9. Figures 3.10, 3.11 and 3.12 present errors $E_1(\boldsymbol{n})$, $E_2(\boldsymbol{n})$ and $E_\infty(\boldsymbol{n})$, respectively. For each figure, from top to bottom, following angular discretizations are dealt with : S_4, S_8, $SqT_{5,3}$ and $SqT_{8,3}$. Again, for each figure, the left column is for the 1-DP method, the one in the middle is for the 3-DP method, and the right column is for the PM partition method. For each row, the color scale is presented on the right hand side. Note that all symmetries can be well observed.

From the S_4 to the S_8 angular discretizations, the number of directions is almost multiplied by a factor 4, while the errors E_1 and E_2 are divided by almost the same factor (the error E_∞ being divided only by roughly a factor 2).

For the $SqT_{5,3}$ discretization, which is a discretization in which the ratio between two solid angles can be equal to two, it can be seen that errors associated to the 1-DP method is larger than that for the S_8 discretization, which is a rather uniform discretization (both S_8 and $SqT_{5,3}$ have approximately the same number of directions). But this is not verified at all for both the 3-DP method and the PM method.

To go further, for the $SqT_{8,3}$ discretization, which is a discretization in which the ratio between two solid angles reaches 6, it can be seen that errors associated to the 1-DP method is much larger than for the two other methods.

Also, from all Figures 3.10, 3.11 and 3.12, it is seen that errors E_1 and E_2 associated to the PM method are much less that errors associated to 1-DP and 3-DP methods. This is also the case for E_∞ errors, but less significantly.

To conclude, what appears from these three figures is that, whatever the chosen norm, and whatever the angular discretization, the associated error is much less for the PM method than for both 1-DP and 3-DP projection methods.

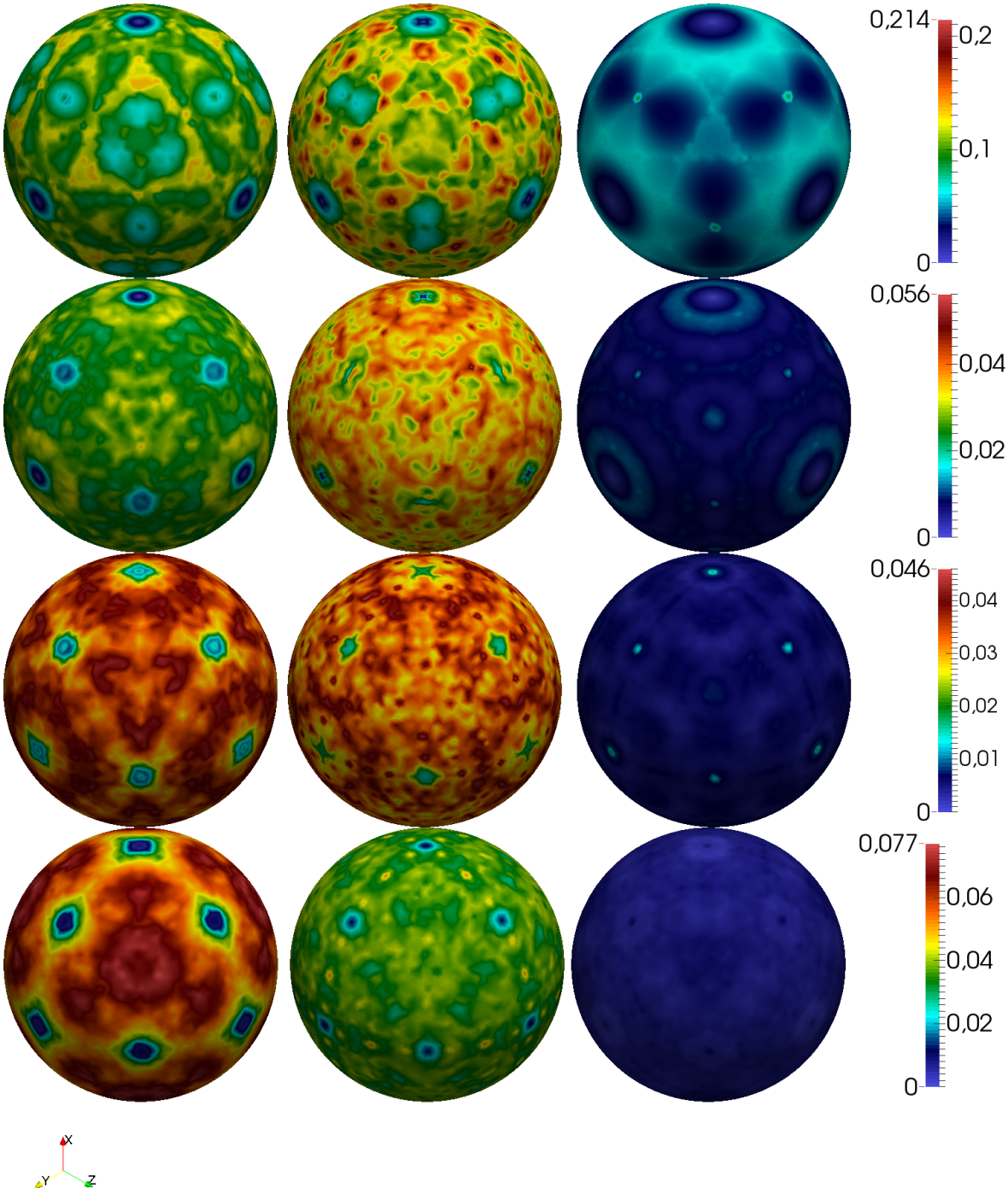

FIGURE 3.10 – Error $E_1(\boldsymbol{n})$. Left : 1-DP ; middle : 3-DP ; right : PM. First raw : S_4 discretization ; second raw : S_8 discretization ; third raw : $SqT_{5,3}$ discretization ; fourth raw : $SqT_{8,3}$ discretization.

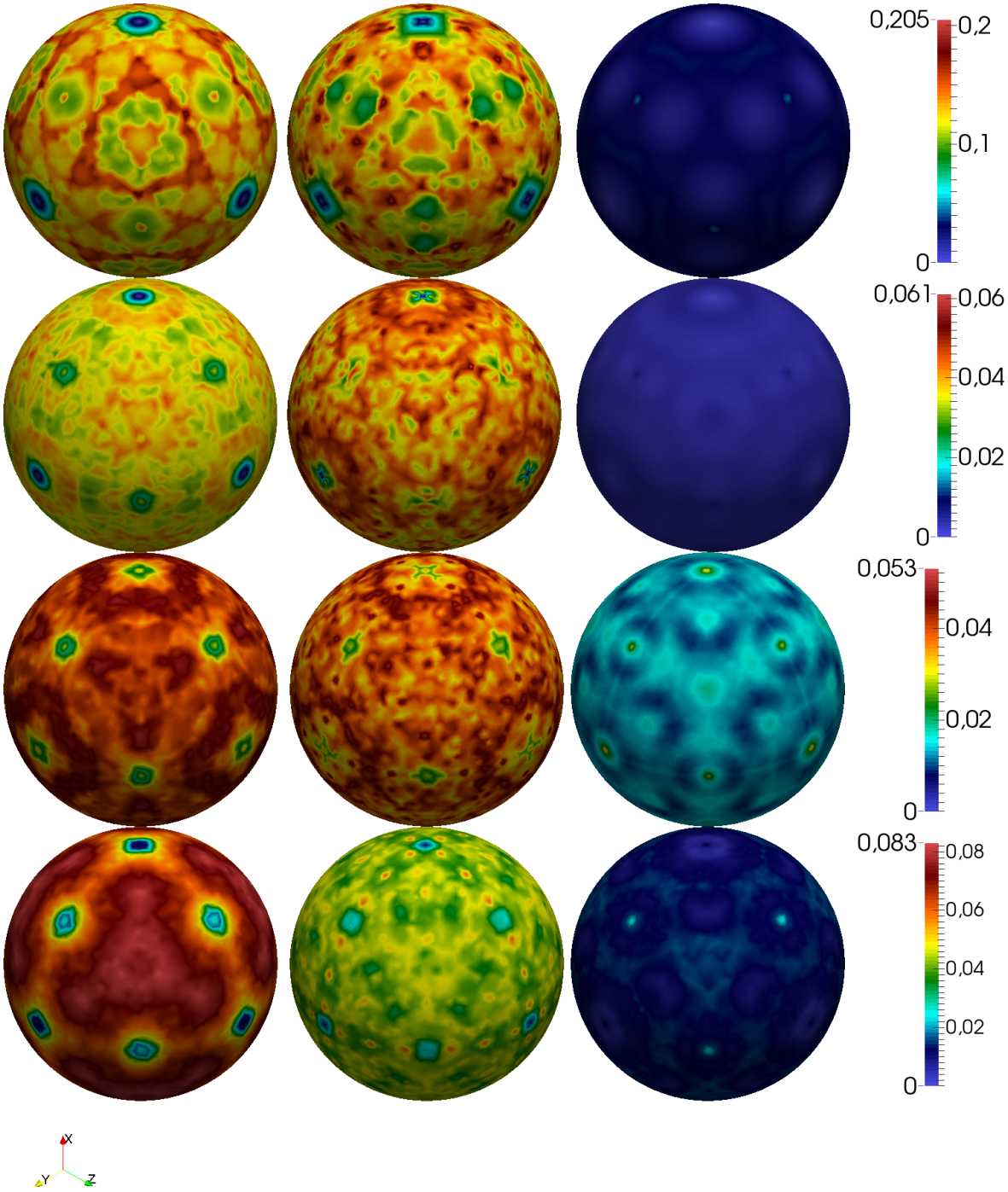

FIGURE 3.11 – Error $E_2(\boldsymbol{n})$. Left : 1-DP ; middle : 3-DP ; right : PM. First raw : S_4 discretization ; second raw : S_8 discretization ; third raw : $SqT_{5,3}$ discretization ; fourth raw : $SqT_{8,3}$ discretization.

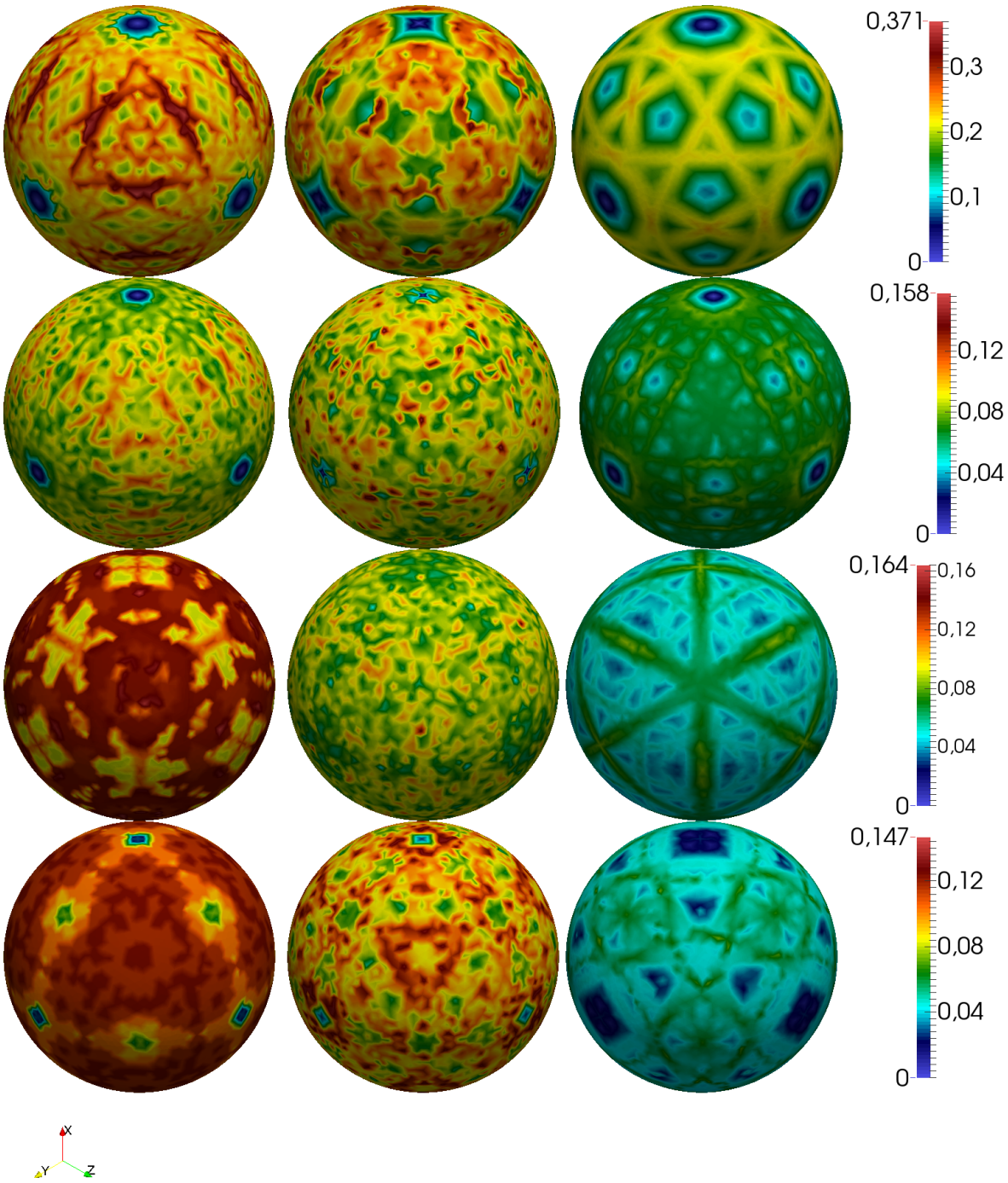

FIGURE 3.12 – Error $E_\infty(\boldsymbol{n})$. Left : 1-DP ; middle : 3-DP ; right : PM. First raw : S_4 discretization ; second raw : S_8 discretization ; third raw : $SqT_{5,3}$ discretization ; fourth raw : $SqT_{8,3}$ discretization.

2nd comparison : the pure collimated critical case

This test case is based on a hexahedron with a cubic base 1×1 m^2 and rectangular surfaces. The geometry of the medium depends on an angle denoted as θ, as schematically presented in Figure 3.13. The reflectivity is chosen to be $\rho = 0$ for all boundaries except for the surface (AB) where $\rho = \rho_0$ (represented in red color in Figure 3.13. Additional properties are $\kappa = 0.1$ m^{-1}, $\sigma = 0.0$ m^{-1} and $\alpha = 1$. An incident radiation beam is applied into the medium through the left surface towards the direction $\boldsymbol{s}_0 = (0, \eta, \xi)$. The incident beam is a collimated Gaussian beam such as $I(\boldsymbol{x} = (x, 0, z), \boldsymbol{s}_0) = e^{-20((x-0.5)^2+(z-0.5)^2)} \mathbb{1}_{(0.2<x,z<0.8)}$, in which $\mathbb{1}_{[\text{"bool"}]}$ is the indicator function that returns "one" is the boolean expression is true, and "zero" otherwise.

For such case, it can be found that the radiative intensity towards the $\boldsymbol{s}_0$ direction reads :

$$I(\boldsymbol{x}, \boldsymbol{s}_0) = e^{-20((x-0.5)^2+(z-\frac{\xi}{\eta}y-0.5)^2)} e^{-\kappa(\eta+\frac{\xi^2}{\eta})y} \mathbb{1}_{(0.2<x,z<0.8)} \mathbb{1}_{(0.2<z-\frac{\xi}{\eta}y<0.8)} \tag{3.34}$$

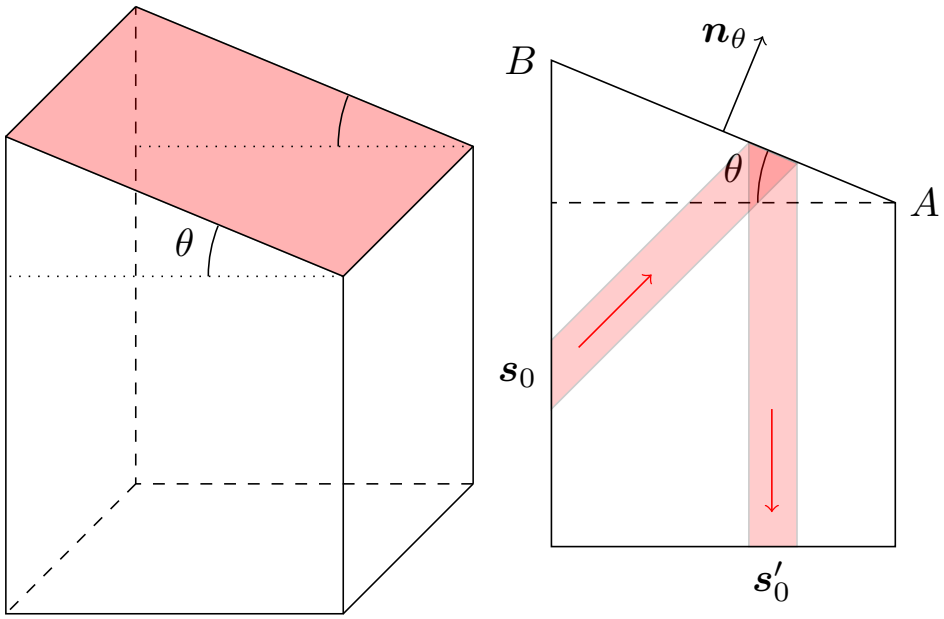

FIGURE 3.13 – Schematic representation of the hexahedron geometry

In order to derive the radiative intensity relative to the reflected beam towards the direction $\boldsymbol{s}'_0$, let $\boldsymbol{X}$ be the symmetric of $\boldsymbol{x}$ with respect to the (AB) surface :

$$\boldsymbol{X} = \begin{pmatrix} x \\ (2c^2-1)(y-1) - 2cs(z-1) + 1 \\ (2s^2-1)(z-1) - 2cs(y-1) + 1 \end{pmatrix} \tag{3.35}$$

with $c = \cos(\theta)$ and $s = \sin(\theta)$. The reflected beam into the direction $\boldsymbol{s}'_0$ is then $I(\boldsymbol{x}, \boldsymbol{s}'_0) = \rho_0 I(\boldsymbol{X}, \boldsymbol{s}_0)$.

For validation and comparisons, the SqT$_{p,n}$ developed discretization presented in 3.9 is used, with two sets $(p, n) = (3, 1)$ and $(p, n) = (5, 3)$. The former set yields to 26 directions, and the latter yields to 114 directions, respectively.

It is pointed out that the scattering coefficient has been chosen to be zero in order to exacerbate errors due to imperfect account of the reflection operation. Quadratic finite element space $\mathbb{P}_2$ is used. Also, the space mesh is chosen refined enough so that errors are mostly due to the reflection operation.

In the presented test case, the input direction of the collimated beam is chosen to be $\boldsymbol{s}_0 = (0, \frac{1}{\sqrt{2}}, \frac{1}{\sqrt{2}})$. Moreover, the angle θ is chosen to be varying from 0 (this gives a cube) to $\frac{3\pi}{8}$, using 28 equally stepped discrete angles.

In order to gauge the quality of numerical results, for the partitioning method and for the two projection methods, two quantitative criteria are used. The first is the $L_2(\mathcal{D})$-error, in terms of the radiation density $D(\boldsymbol{x}) = I(\boldsymbol{x}, \boldsymbol{s}_0) + I(\boldsymbol{x}, \boldsymbol{s}'_0)$. This error measures the deviation of the numerical solution from the analytical solution :

$$e(u) = \left(\int_{\mathcal{D}} (u - u_{ex})^2 \, \mathrm{d}\boldsymbol{x} \right)^{\frac{1}{2}} \tag{3.36}$$

Apart from that, the correlation factor $C_f \in [-1, 1]$ is also used to measure the linear correlation between the numerical and the analytical solution : a high value of C_f indicates a high conformity between both numerical and analytical solutions. Such tool is commonly used in the field of tomography, for example in [71, 72, 73]. This criterion, that uses value on nodes of a finite element mesh, is written as :

$$C_f(D) = \frac{\sum_{j=1}^{N} \left(D^j - \bar{D} \right) \left(D^j_{\mathrm{ex}} - \bar{D_{\mathrm{ex}}} \right)}{(N-1)\sigma_D \sigma_{D_{\mathrm{ex}}}} \tag{3.37}$$

where N is the number of vertices of the finite element mesh, D^j is the value of D on the j^{th} node, and $\bar{D}$ and $\bar{D_{\mathrm{ex}}}$ are mean values of D and D_{ex}. To add more, σ_D and $\sigma_{D_{\mathrm{ex}}}$ are standard deviations of numerical and exact solutions, respectively. These are given by :

$$\sigma_D = \sqrt{\frac{\sum_{j=1}^{N} \left(D^j - \bar{D} \right)^2}{N-1}} \quad \text{and} \quad \sigma_{D_{\mathrm{ex}}} = \sqrt{\frac{\sum_{j=1}^{N} \left(D^j_{\mathrm{ex}} - \bar{D_{\mathrm{ex}}} \right)^2}{N-1}} \tag{3.38}$$

Figure 3.14 summarizes the quality of numerical results, for the partitioning strategy and for the 1-DP and 3-DP strategies, in terms of quantitative L_2 errors and correlation factors, for two orders of angular discretization, namely $\mathrm{SqT}_{3,1}$ and $\mathrm{SqT}_{5,3}$. Figure 3.14 clearly shows that the error depends on the angle θ. Indeed, for some given angles θ, the direction of propagation of the reflected beam, $\boldsymbol{s}'_0$, corresponds exactly to a direction $\boldsymbol{s}_k$ of the angular discretization (this is for example the case for $\theta = 0$ and $\theta = \frac{\pi}{8}$). Such situation yields highly accurate numerical solution with tiny L_2-errors and correlation coefficients close to unity. Contrarily, there are angles for which the reflected direction $\boldsymbol{s}'_0$ is very far away from any other directions $\boldsymbol{s}_k$ of the angular discretization. This is for example the case when $\theta = \frac{13\pi}{72}$ (14^{th} discrete angle) with the coarse $\mathrm{SqT}_{3,1}$ angular discretization. In such case, the L_2-error is high, and the correlation coefficient is far from unity. The corresponding vertical cross section of radiative intensity D at $x = 0.5$ is plotted in Figure 3.15, along with errors, for the three strategies. It is seen for this extreme case that, since there is no scattering effect, the error is high on some discrete directions : towards the exact reflected direction $\boldsymbol{s}'_0$ (which does not correspond to any existing direction of the angular discretization), and towards discrete directions of the angular discretization $\boldsymbol{s}_m$ for which the coefficient $0 \ll \delta_{m,j} \leq 1$. It can also be noted

from Figure 3.15 that, locally close to the reflecting surface (AB), the dimension of the localization of the error is much larger for the projection method and the 3-DP method than that of the 1-DP method. Similar results can be observed for the finer angular discretization $\mathrm{SqT}_{5,3}$ on Figure 3.16. The main difference when compared to the coarser angular discretization is that width of error beams are less. Consequently, errors are less on specular reflected beams (exact and computed through one or the other method) as well as locally close to the reflecting boundary. Another critical case is presented in Figure 3.17. In this case, the coarser angular discretization is used and the plot is presented for the angle $\theta = \frac{\pi}{8}$. For this particular case, the computed reflected direction matches exactly the exact reflected direction $\boldsymbol{s}'_0$. For this case, the error is negligible for the projection methods, but this is not the case for the partition method. This comes from the fact that the reflected incident solid angle envelopes the solid angle categorized by the direction $\boldsymbol{s}'_0$. On other angles that are not so critical, errors are much less, hence it is not necessary to represent radiative intensity and associated errors.

To come back to Figure 3.14, globally, the 3-DP method yields more accurate results compared to the 1-DP method : this can be seen by lower errors $e(D)$ and greater correlation factors $C_f(D)$. The partition method is also, globally, very accurate, except for singular isolated discrete angles.

Conclusion of the specular validation

To conclude about the specular validation presented in this section, two very different tests have been performed to validate the PM partition method and gage its efficiency. Also, the partitioning method has been compared with respect to simpler 1-DP and 3-DP projection methods. For the first test, for which a uniform incoming radiative intensity was reflected on a boundary, the PM method was clearly much more accurate than both the 1-DP and the 3-DP methods. In the second case, which corresponds to a very critical case, in which a collimated beam was propagating within a non scattering medium and reflected specularly onto a surface, the PM solution is almost as efficient as the 3-DP method, for almost all the θ angles. Therefore, from all this, it can be concluded that the PM method is globally more efficient than the 3-DP method, and anyway much more efficient than the simple 1-DP method.

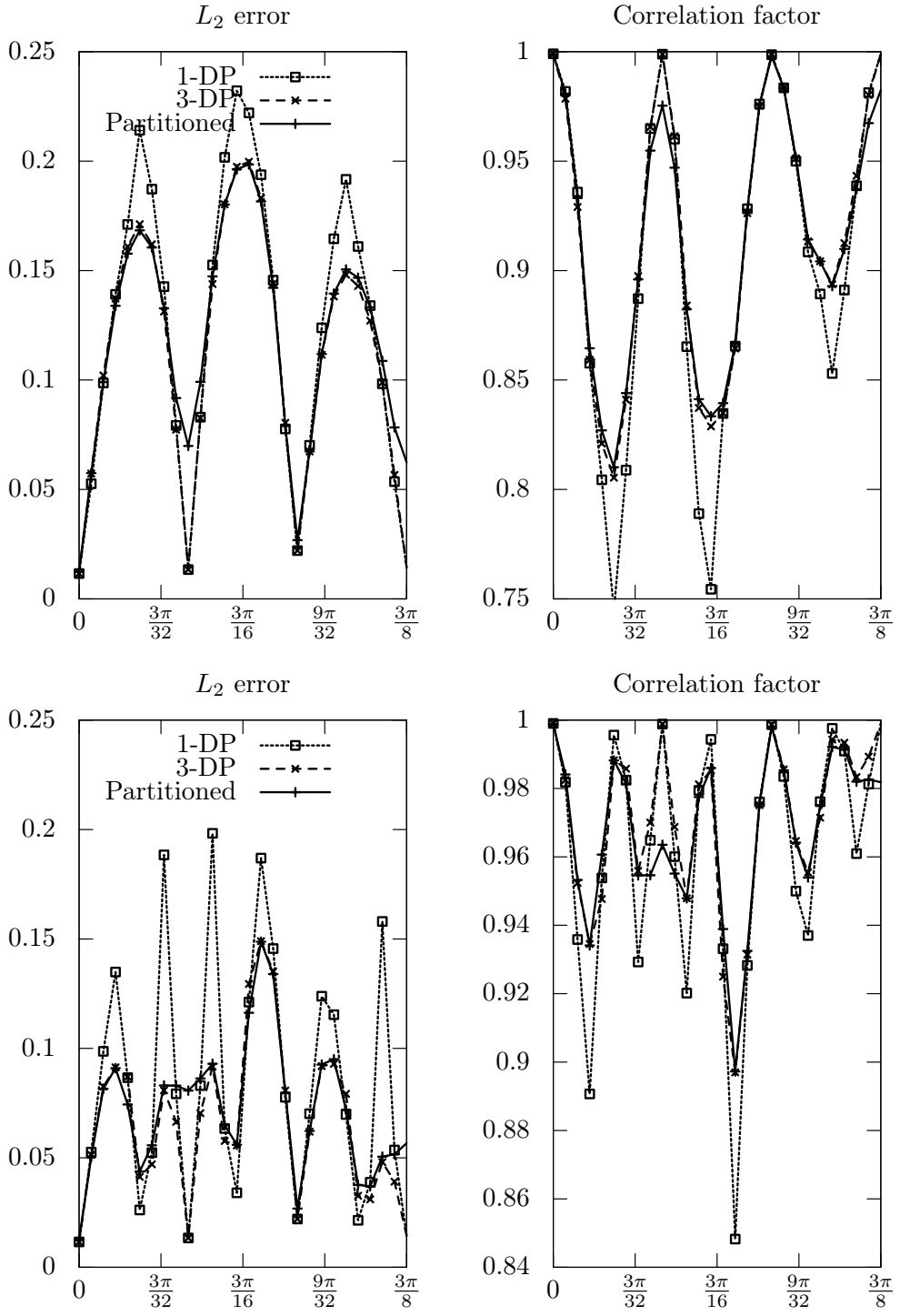

FIGURE 3.14 – Evolution of errors and correlation factors as functions of angle θ. Top figures concern coarse angular discretization $\mathrm{SqT}_{3,1}$. Bottom figures concern fine angular discretization $\mathrm{SqT}_{5,3}$. Left figures concern L_2-errors of radiative density, $e(D)$. Right figures concern correlation factor of radiative density, $C_f(D)$. Plain lines are for the partitioning method (PM), dotted lines are for the 1-DP method, and dashed lines are for the 3-DP method.

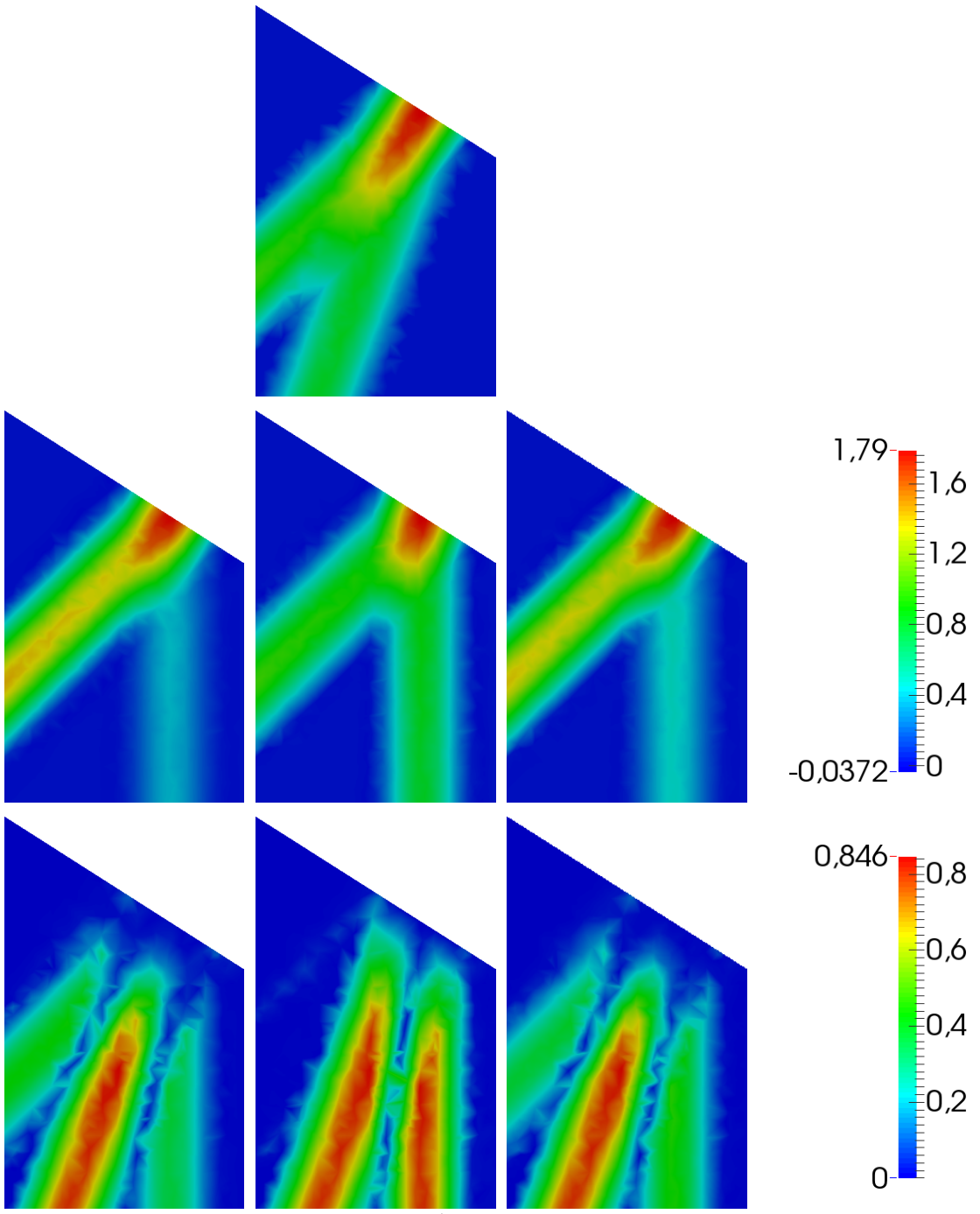

FIGURE 3.15 – $\theta = 13\pi/72$ and $\mathrm{SqT}_{3,1}$ angular discretization. Cross section at $x = 1/2$. Top : exact radiative density D. Middle : numerical radiative density D - with the PM partition method (left), with the 1-DP projection method (middle), and with the 3-DP projection method (right). Bottom : absolute errors of the radiative density $|D - D_{\mathrm{ex}}|$ - with the PM partition method (left), with the 1-DP projection method (middle), and with the 3-DP projection method (right).

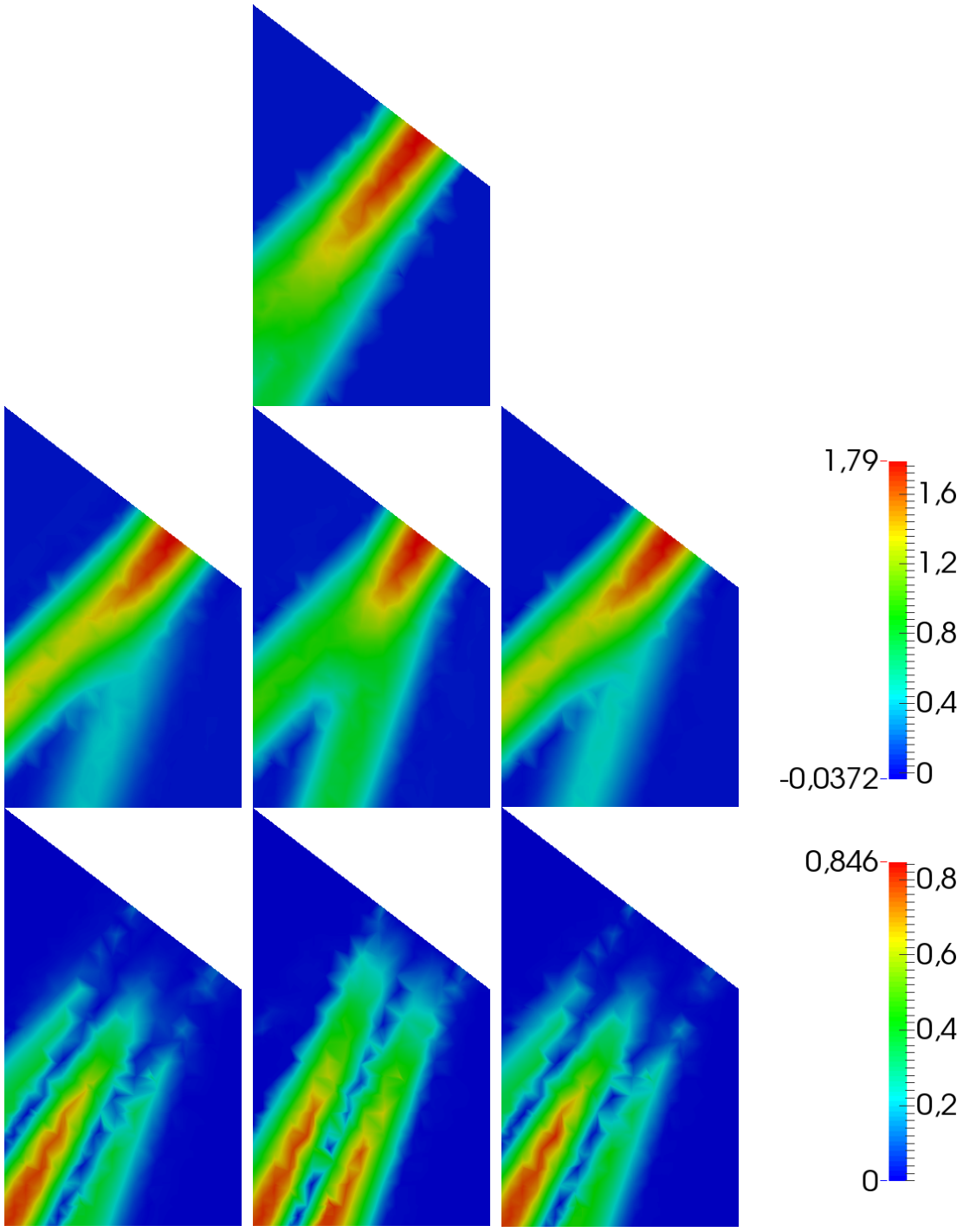

FIGURE 3.16 – $\theta = 15\pi/72$ and $\mathrm{SqT}_{5,3}$ angular discretization. Cross section at $x = 1/2$. Top : exact radiative density D. Middle : numerical radiative density D - with the PM partition method (left), with the 1-DP projection method (middle), and with the 3-DP projection method (right). Bottom : absolute errors of the radiative density $|D - D_{\mathrm{ex}}|$ - with the PM partition method (left), with the 1-DP projection method (middle), and with the 3-DP projection method (right).

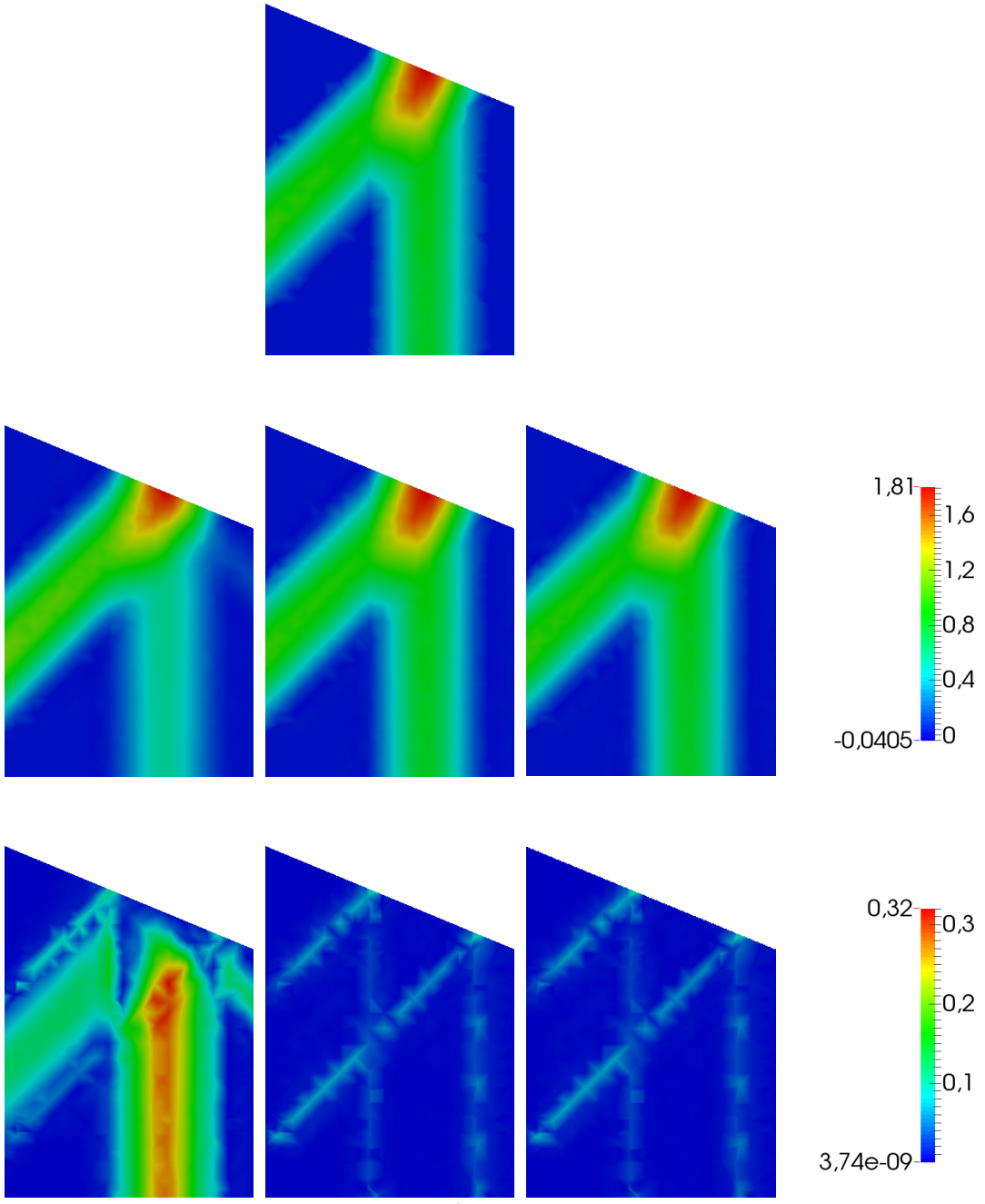

FIGURE 3.17 – $\theta = \pi/8$ and $\mathrm{SqT}_{3,1}$ angular discretization. Cross section at $x = 1/2$. Top : exact radiative density D. Middle : numerical radiative density D - with the PM partition method (left), with the 1-DP projection method (middle), and with the 3-DP projection method (right). Bottom : absolute errors of the radiative density $|D - D_{\mathrm{ex}}|$ - with the PM partition method (left), with the 1-DP projection method (middle), and with the 3-DP projection method (right).

3.5.2 Convergence study

A cylindrical isotropic medium close to the test case dealt with in [74] is considered here. The bases are disks with a radius $r = 1$ m. The length of the cylinder is $l = 2$ m. The specular reflectivity is $\rho = 1$ for the ruled surface and $\rho = 0$ for the two round bases. An incident radiation beam is applied into the medium through the disk surface represented in red in Figure 3.18 (where $\boldsymbol{x} = \boldsymbol{x}_{\mathrm{w}} = (0, y, z)$). The incident radiation is assumed to be collimated towards the normal direction with $\boldsymbol{s}_0 = (1, 0, 0)^t$ and $I(\boldsymbol{x}_w, \boldsymbol{s}_0) = 1$. The physical properties, for this medium, are $\kappa = 0.5$ m^{-1} and $\sigma_s = 4$ m^{-1}. As the medium is isotropic and supposedly cold, the Beer-Lambert law can be applied towards the $\boldsymbol{s}_0 = \boldsymbol{e}_x$ direction, so that the exact radiance $I_{\mathrm{ex}}(\boldsymbol{x}, \boldsymbol{s})$ is written as :

$$I_{\mathrm{ex}}(\boldsymbol{x}, \boldsymbol{s}) = e^{-\beta x} \times \mathbb{1}_{[\boldsymbol{s}=\boldsymbol{e}_x]} \tag{3.39}$$

in which $\beta = \kappa + \sigma$ is the extinction coefficient and $\mathbb{1}_{[\boldsymbol{s}=\boldsymbol{e}_x]}$ is an indicator function defined in previous section.

Four spatial meshes, $\mathcal{M}_i$, $i = 0, \cdots, 3$ are used, M_0 being the coarsest mesh, and M_3 being the most refined mesh, see Figure 3.19. Also, computations have been performed for three distinct angular discretizations, namely $\mathrm{SqT}_{3,1}$, $\mathrm{SqT}_{4,2}$ and $\mathrm{SqT}_{5,3}$. Note that these in-house discretizations have been developed on purpose for this particular test. 3.9 summarizes the main features of $\mathrm{SqT}_{p,n}$ angular discretization schemes. Figure 3.28 presents used quadratures $\mathrm{SqT}_{3,1}$, $\mathrm{SqT}_{4,2}$ and $\mathrm{SqT}_{5,3}$. To add more, computations have been performed for both $\mathbb{P}_1$ and $\mathbb{P}_2$ Lagrange functions.

In order to characterize errors, let h_i denotes the diameter of the cell $\mathcal{C}_i$, and let the mesh size be defined as the real number : $h = \max_{i=1,\cdots,N_e} h_i$. In the same way, let angle size ω being defined as the maximum solid angle of the angular triangulation, i.e. $\omega = \max_{i=1,\cdots,N_d} \omega_i$.

The $L_2(\mathcal{D})$-errors in terms of longitudinal radiative intensity plotted as a function of mesh size are given in Figure 3.20. It can be observed that errors decrease when mesh size decreases, when functional polynomial order increases, and also when angular discretization order increases. For illustration purposes, let errors be set as the sum of spatial and angular contributions :

$$e(I(\boldsymbol{x}, \boldsymbol{s}_0)) = e_h + e_\omega, \text{ with } e_h \propto h^p \text{ and } e_\omega \propto \omega^q \tag{3.40}$$

For the particular test case presented here, concerning space, convergence orders p have been found equal to 1.8 and 2.8 for the $\mathbb{P}_1$ and $\mathbb{P}_2$ Lagrange functionals, respectively. This means that the $\mathbb{P}_2$ gives more accurate solutions, which is classic to such configuration, but at the price of bigger linear systems to be solved due to higher number of degrees of freedom. Next, concerning the angular discretization, the convergence order has been found equal to 1.28. This can be realized in the Figure 3.20 where, for the fine enough spatial discretization, error e_h can be neglected in comparison to e_w.

The conclusion of this study is that one observes convergence of numerical results for both spatial and angular discretizations. Therefore, one could, in theory, obtain extremely accurate results if one could afford to solve extremely large linear systems. This study also confirms, somehow, that the whole process of stabilized finite elements

coupled with the computation of accurate partition ratio coefficients performed as pre-processing is exempt from any bias due to algorithmic errors.

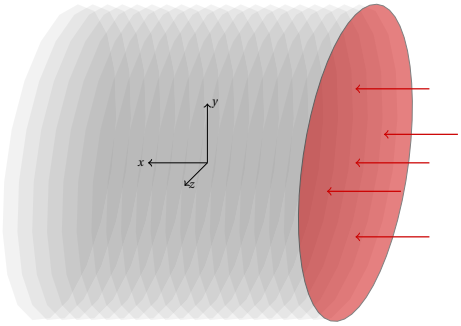

FIGURE 3.18 – Cylindrical medium. Incident radiative intensity is applied on one of the flat surface following the longitudinal direction.

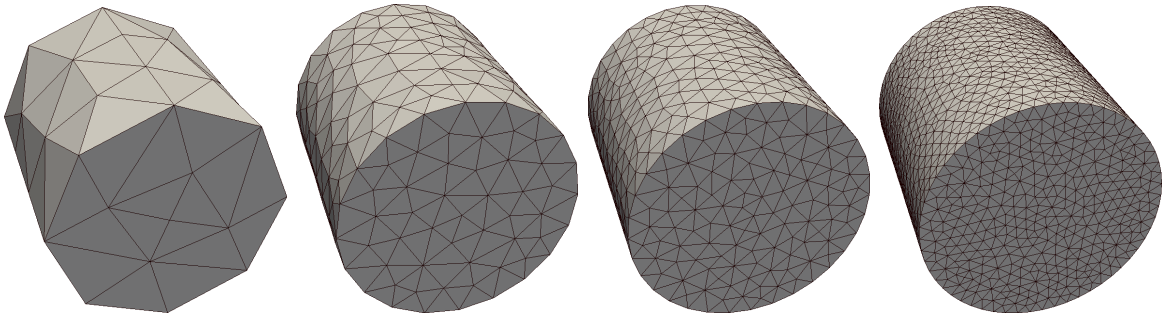

FIGURE 3.19 – Cylinder meshes. From left to right : $\mathcal{M}_0$, $\mathcal{M}_1$, $\mathcal{M}_2$ and $\mathcal{M}_3$.

3.6 Applications in complex geometries

The numerical treatment of the three-dimensional radiative transfer equation coupled with reflection has been precisely detailed in Sections 3.2, 3.3 and 3.4, and validation has been performed in Section 3.5. Such developments are interesting for academic problems but even more for industrial applications. Generally, for industrial cases, complex geometries are likely to be dealt with. One difficulty that arises while dealing with specular reflection with the radiative transfer equation comes from the fact that the number of normal directions may be very high. In fact, for each normal of the domain boundary, and for each pair of directions, the reflectivity coefficient (3.10) is to be calculated, and especially the partition ratio coefficients (3.20) using the whole strategy detailed in Section 3.3. Note that such computation is performed as a part of pre-processing only. To follow, two applications are considered, the first, in Section 3.6.1, concerns a parabolic concentrator and in Section 3.6.2, a berlingot-shaped geometry is dealt with.

3.6.1 Parabolic concentrator

The first application concerns radiative transfer within an absorbing and scattering medium with specular reflection on the curved parabolic surface with external incident

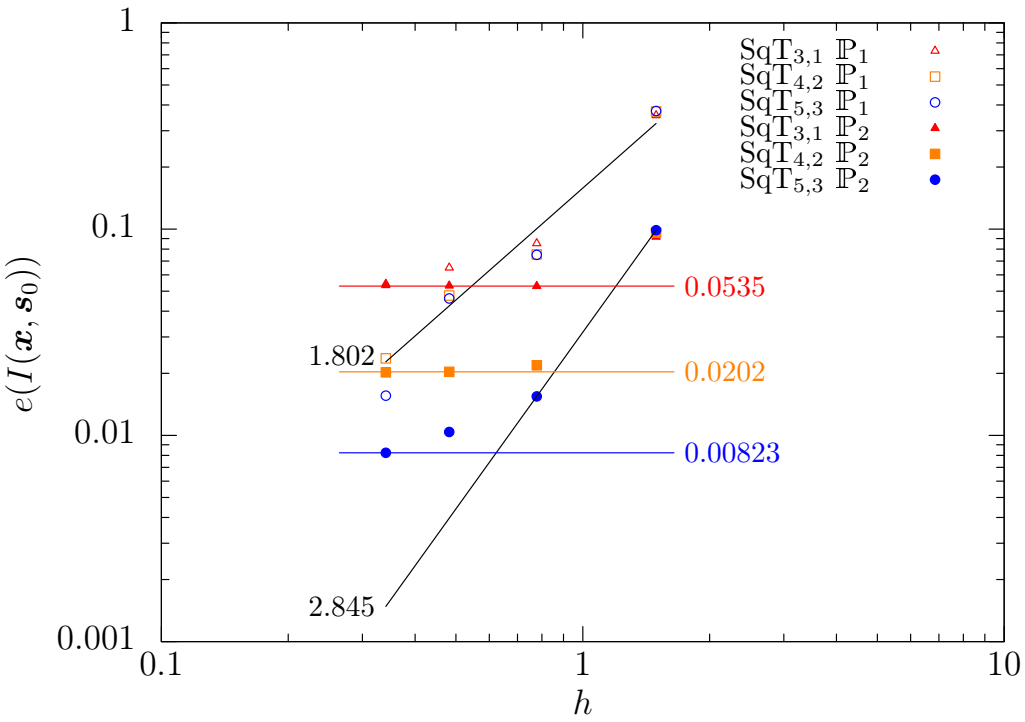

FIGURE 3.20 – Convergence study on the cylinder case. Evolution of the error $e(\cdot)$ of the longitudinal radiative intensity $I(\boldsymbol{x}, \boldsymbol{s}_0)$ with respect to mesh size h. Empty symbols are related to $\mathbb{P}_1$ Lagrange functions. Filled symbols are related to $\mathbb{P}_2$ Lagrange functions. Triangles are for the SqT$_{3,1}$ angular discretization, squares are for SqT$_{4,2}$ angular discretization, and circles are for SqT$_{5,3}$ angular discretization.

radiation on the top surface, as represented schematically in Figure 3.21. As stated in [32] (it is quoted exhaustively), "this problem is representative of collector-reactors systems in solar thermochemical applications, for example, for the synthesis of fuels from CO_2 and H_2O, methane reforming, or biomass pyrolysis using solar energy [75, 76, 77]."

Theoretically, for this case, the whole incoming beam, which enters the medium following the normal direction, converges to the focal point F after being reflected on the paraboloid surface. In order to catch this singular point F, the spatial and angular meshes both need to be fine enough, and algorithms used to deal with specular reflection need to be very precise. This case is indeed a challenging test previously proposed in [32] and re-used for the purpose of this paper.

The equation of the paraboloid surface is given by $z = \frac{1}{3}(x^2 + y^2)$ (note that dimensions are based on SI units, so meter is used). The position of the focal point is thus such that $|FO| = \frac{3}{4}$ m. Also, the point M which lies on the top surface is such that $|MO| = \frac{4}{3}$ m. These points are represented in Figure 3.21. These dimensions have been chosen so that the focal point is localized inside the medium.

The refraction index is chosen to be $n = 1$ for the top surface (in order to avoid reflection on this surface) and $n = 1.4$ for the curved surface. The absorption coefficient κ is chosen to be 0.01 and 0.2 m^{-1} for low and high absorbing media, respectively. The scattering coefficient σ_s is chosen to be 0.00 and 0.2 m^{-1} for no and high scattering media, respectively. The phase function $\Phi(\boldsymbol{s}, \boldsymbol{s}')$ is considered to be isotropic.

The mesh contains 2,678 boundary triangles with 1,462 different external normals, 8,381 tetrahedrons and 11,907 nodes, yielding a mesh size $h = 0.511$. The order $\mathbb{P}_2$ is used for the space discretization, so that one has 13,833 degrees of freedom for a single direction. The $SqT_{5,3}$ angular discretization is used with 114 discrete directions.

Figure 3.22 presents the radiative density $D(\boldsymbol{x}) = \sum_k I(\boldsymbol{x}, \boldsymbol{s}_k)$ for which the radiative intensity relative to the $-\boldsymbol{e}_z$ direction is subtracted. This is a truncated radiative density formally defined as

$$\hat{D}^{-\boldsymbol{e}_z}(\boldsymbol{x}) = D(\boldsymbol{x}) - I(\boldsymbol{x}, -\boldsymbol{e}_z) \tag{3.41}$$

Such a quantity is used to visualize whether or not the focal point exists numerically and if it is well localized. For each case, 4 sub-figures are presented. The first one represents a volumic solution with 3 orthogonal cross sections, centred on the focal point F. The other sub-figures are the standalone visualization of these orthogonal cross sections.

As in [32], qualitative remarks can be formulated. First, it is seen from the case with the low absorbing and no scattering medium (corresponding to the first row of Figure 3.22) that the focal point is well detected, with a small localization of the maximum truncated radiative density. Second, for the purely absorbing medium (third row of Figure 3.22), the highest value of the reflected density is much lowered, due to attenuation. An increase of absorption κ from 0.01 to 0.2 m^{-1} decreases the truncated radiative density from 1.32 to 0.776 $\mathrm{W/m^2}$. Finally, the second and fourth rows of Figure 3.22 present similar results but for the scattering media. In these cases, due to the scattering effect, the maximum truncated radiative density is lowered. For example, for $\kappa = 0.2$ m^{-1}, an increase of scattering σ from 0 to 0.2 m^{-1} decreases the truncated radiative density from 0.776 to 0.615 $\mathrm{W/m^2}$.

3.6.2 Berlingot

The second application is based on an absorbing and scattering berlingot-shaped medium with specular reflection on the boundary. This medium that has a non-convex border looks like a tetrahedron (See Figure 3.23). In fact, this medium can be assimilated to a cross section between two struts of open-cell foam used in concentrated solar power technologies [6].

The surface $P(t, \theta)$ of the medium is generated by the following parametric equations :

$$P(t,\theta) = \begin{cases} x = ba(1+t)\cos\theta \\ y = ba(1-t)\sin\theta \\ z = at \end{cases}, \; b, a \in \mathbb{R}, t \in [-1,1] \text{ and } \theta \in [0, 2\pi[\tag{3.42}$$

where a defines the height and b defines the width of the medium. For this particular case, we chose $a = b = 1$, so that the dimensions of the medium are 4 cm $\times$ 4 cm $\times$ 2 cm. Four cases are presented : two cases with the refraction index $n = 2$ and two cases without reflection. The absorption coefficient κ is chosen to be 0.1 cm^{-1}. The scattering

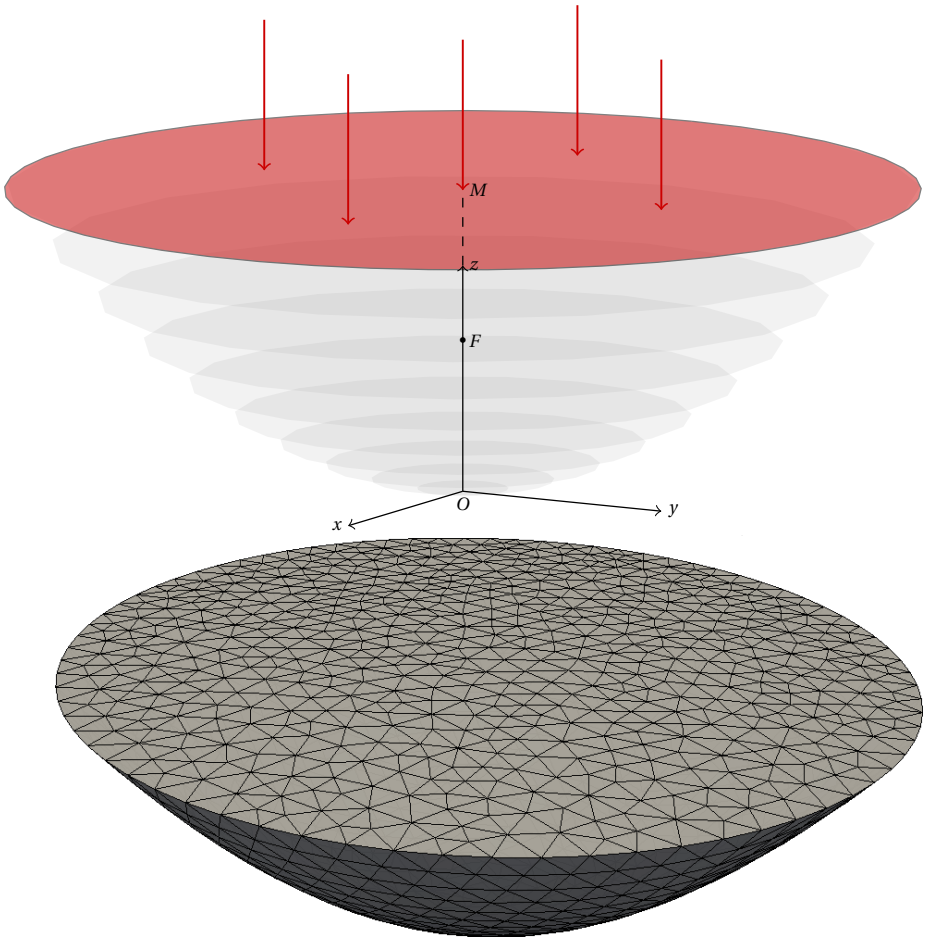

FIGURE 3.21 – Paraboloid medium. Top : the incident radiative intensity is applied uniformly on the top surface following the $-\boldsymbol{e}_z$ direction ; bottom : corresponding mesh.

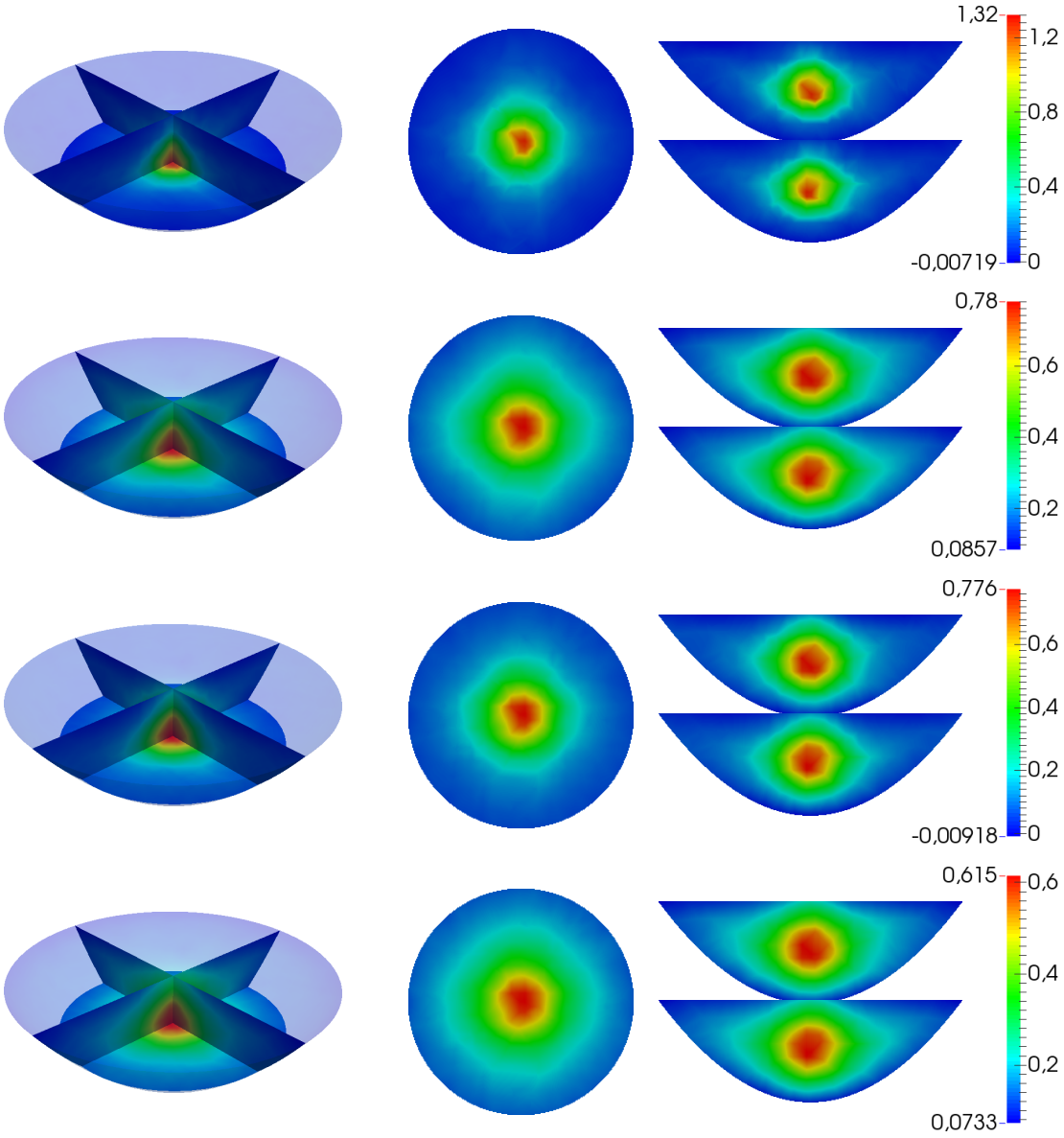

FIGURE 3.22 – Truncated radiative density $\hat{D}^{-\boldsymbol{e}_z}(\boldsymbol{x})$. First row : $\kappa = 0.01$ m^{-1} and $\sigma = 0$ m^{-1} ; second row : $\kappa = 0.01$ m^{-1} and $\sigma = 0.2$ m^{-1} ; third row : $\kappa = 0.2$ m^{-1} and $\sigma = 0$ m^{-1} ; Fourth row : $\kappa = 0.2$ m^{-1} and $\sigma = 0.2$ m^{-1}

coefficient σ_s is chosen to be 0.0 cm^{-1} for two cases and 1 cm^{-1} for the other two. For the two cases with $\sigma_s = 1$ cm^{-1}, the scattering is supposed to be isotropic.

A collimated beam enters the medium onto an approximately flat surface with external unit normals close to $(0, \frac{1}{\sqrt{2}}, \frac{1}{\sqrt{2}})$, and following the direction $\boldsymbol{s}_0 = (-\frac{1}{\sqrt{3}}, -\frac{1}{\sqrt{3}}, -\frac{1}{\sqrt{3}})$ The beam whose intensity is gaussian can be written as $e^{-3[(z-y)^2+(x+0.5-z)^2+(y-(x+0.5))^2]} \times \mathbb{1}_{[(z-y)^2+(x+0.5-z)^2+(y-(x+0.5))^2<0.75]} \times \mathbb{1}_{[\boldsymbol{s}=\boldsymbol{s}_0]}$. The beam hits the surface with an elliptical shape. For the 4 cases, the density $D(\boldsymbol{x}) = \sum_m I_m(\boldsymbol{x})$ is presented, in Figure 3.24 for non-scattering media, and in Figure 3.25 for scattering media. For each case, 4 subfigures are presented : one represents the density on the surface (top-right), one is a volumic representation with two orthogonal cross sections into the medium and with transparent boundary (top-left) and the other two represent the standalone visualization of the orthogonal cross sections mentioned above.

The mesh contains 6,080 boundary triangles with 5,602 different external normals, 27,118 tetrahedrons and 34,890 nodes, yielding a mesh size $h = 0.277$. The order $\mathbb{P}_2$ is used for the space discretization, so that one has 41,889 degrees of freedom for a single direction. The S_8 angular discretization is used with 80 discrete directions.

In Figure 3.24, the two cases without scattering are presented. The first test is the one that does not involve reflection while the second one involves specular reflection. In the first case, the beam just passes through the medium, but with attenuation due to absorption. In the second case, the beam is reflected on each near plan surface and makes a loop. Due to the nature of the geometry (not perfectly symmetrical), it can be observed that the intensity is not Gaussian on the entering surface. Most of the beam attenuation for this case is due to reflections, because the extinction coefficient is low.

In Figure 3.25, the two cases with isotropic scattering are presented. Again, the third test has no reflection while the fourth one has specular reflection. The radiative intensity for both tests are presented with the same scale in order to exacerbate the importance of reflection effects. The radiative density of the fourth case is higher than that of the third case because the beam travels in the medium with multiple internal reflections. Moreover, the radiative density $D(\boldsymbol{x})$ is focused on the entering boundary due to the scattering effect.

3.7 Conclusion

This paper presented numerical schemes based on finite elements for solving three-dimensional radiative transfer problems with absorption, scattering, emission and reflection. The specular reflection is taken into account accurately using a partition of the incident radiative intensity received on the border based on partition ratio coefficients calculated through solid angle intersection areas. The Streamline-Upwind Petrov–Galerkin formulation was used coupled with different angular discretization schemes.

Convergence studies with respect to both space and angle discretizations have been performed. Three specular strategies have been compared and validated numerically. The PM method was accurate for the two presented critical test cases. Numerical com-

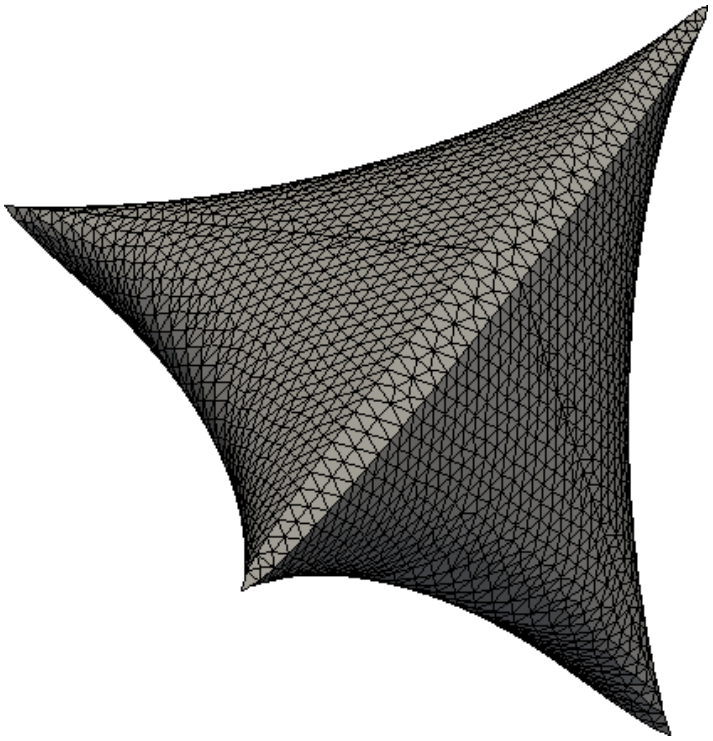

FIGURE 3.23 – Mesh of the berlingot

putations have been found to be accurate for a large range of coefficients of absorption and scattering and for a large range of index of refraction, ensuring robustness for all the developed schemes.

Two real-life applications for which the geometry of concern can be considered as complex have been considered. In the first, already treated in literature, a parabolic concentrator is dealt with, with several pairs of absorption-scattering coefficients. For this application, results presented in literature could be confirmed, qualitatively. In the second, a berlingot-shape geometry is used so that the medium could be assimilated to a single strut of a ceramic porous medium used for example in concentrated solar power technologies. Such a shape is interesting from a numerical point of view since it is close to a tetrahedron allowing multiple internal specular reflections.

Future work will concern the use of developed algorithms on highly complex geometries such as real struts of ceramic foam, the objective being radiative characterisation. For such cases, the geometry will be fully given by X-ray μ-tomography measurements, similarly as in [6]. Also, complex geometries leading to huge numbers of degree of freedom, we also plan to work on acceleration of numerical solution using, among other tools, domain decomposition techniques in space and/or in angles.

Acknowledgements

The authors thank the French Ministry of Higher Education and Research for funding this research. The authors would also like to thank developers of the gmsh [70] and paraview [78] environments which were both extensively used in this study. We

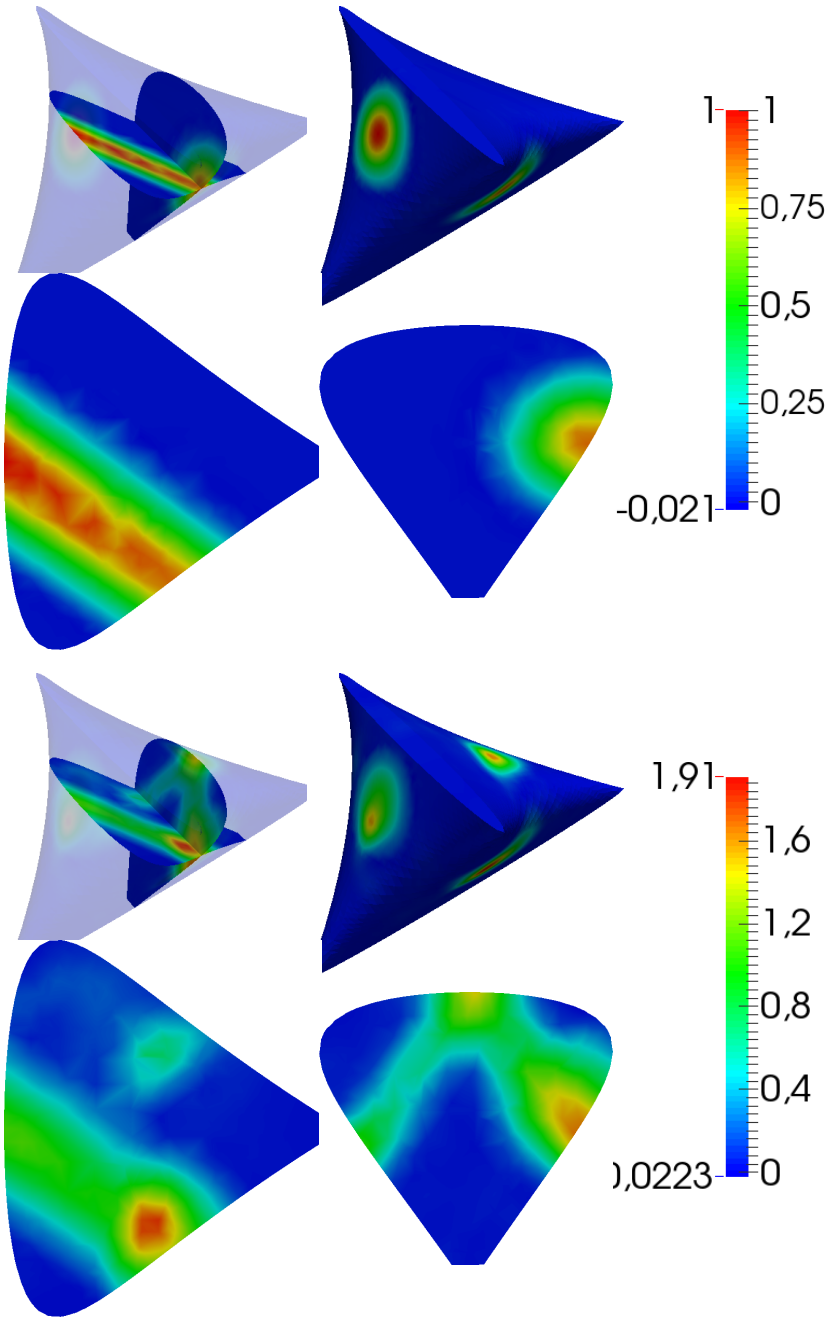

FIGURE 3.24 – Radiative density $D(\boldsymbol{x})$ for $\sigma = 0$ and $\kappa = 0.1$ cm^{-1}. Top : $n = 1$; bottom : $n = 2$

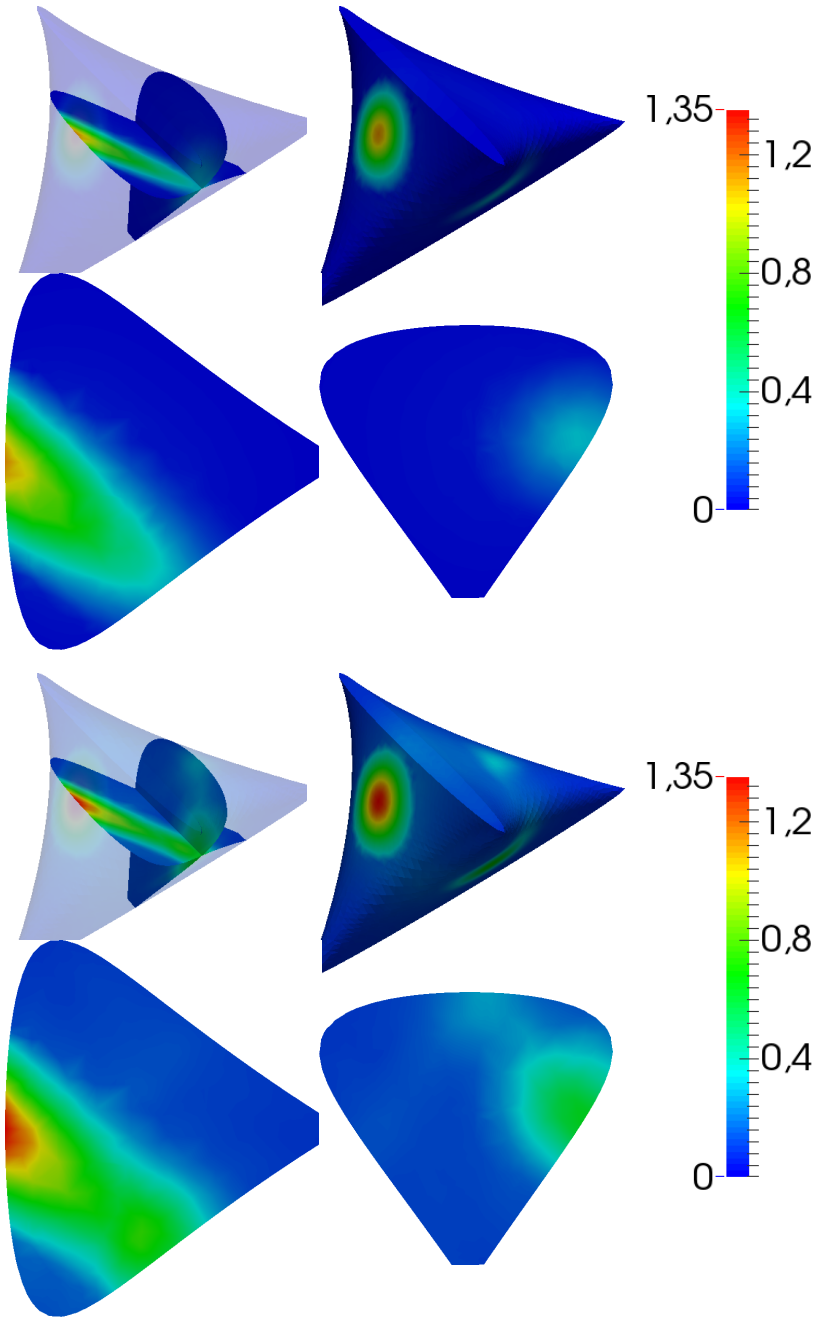

FIGURE 3.25 – Radiative density $D(\boldsymbol{x})$ for $\sigma = 1$ cm^{-1} and $\kappa = 0.1$ cm^{-1}. Top : $n = 1$; bottom : $n = 2$

sincerely thank the two reviewers for their highly constructive remarks that enabled us to improve drastically the quality of this paper. To add more, authors would like to thank members of the GDR CNRS ACCORT 3438 for fruitful and valuable discussions on the subject.

3.8 Appendix A : Algorithms

This Appendix presents some algorithms used to determine the reflected part of an incident triangular solid angle (Algo 1), and the cross section between two triangular solid angles (Algo 2, 3, 4 and 5). Several variables used in following algorithms are defined :

— `Positive` : number of directions $\boldsymbol{e}_i$ such as $\boldsymbol{e}_i \cdot \boldsymbol{n} > 0$

— `Only` : Position of the direction within the list such as it is the only direction that satisfies $\boldsymbol{e}_i \cdot \boldsymbol{n} > 0$ or not.

— `PosPosition` : integer to determine the position of the direction $\boldsymbol{e}_{\texttt{Only}}$ for each value of `Positive`

— `EdgeSolidAngle` : Edges of the reflected part of the incident solid angle. These edges are properly ordered.

— `M` : matrix such that it can be realized by combination of 3 row vectors $\boldsymbol{v}_1, \boldsymbol{v}_2$ and $\boldsymbol{v}_3$. This visualisation is used to simplify the equation of t_* in Algorithm 3.

— $\boldsymbol{e}_i^{(m)}$, $\boldsymbol{e}_i^{(j)}$, $\boldsymbol{e}_i^{(mj)}$: define the i^{th} edge of respectively the reflected solid angle of Ω_m, the solid angle Ω_j, and the cross section Ω_{mj}.

— $O\boldsymbol{e}_i$: define the list with ordered edges.

— `Position` : position of an edge $\boldsymbol{e}_i$ within the ordered list.

Algorithm 1: Determination of edges of the reflecting section of Ω_j

```
Positive = 0 ; PosPosition = 0 ; iter = 0;
for i = 1, 2, 3 do
    if e_i · n > 0 then
        Positive = Positive+1 ; PosPosition = PosPosition + 2i − 1;
    end
end
if Positive = 1 then
    Only = (PosPosition+1)/2;
    EdgeSolidAngle_1 = e_Only;
    for i = 1, 2, 3 ; i ≠ Only do
        t_* = −(e_i·n)/((e_Only−e_i)·n);
        EdgeSolidAngle_{2+iter} = C_{i,Only}(t_*);
        iter = iter + 1;
    end
end
else if Positive = 2 then
    Only = 4 − (PosPosition−2)/2;
    for i = 1, 2, 3 ; i ≠ Only do
        t_* = −(e_i·n)/((e_Only−e_i)·n);
        if iter = 0 then
            EdgeSolidAngle_1 = e_i ;
            EdgeSolidAngle_2 = C_{i,Only}(t_*);
            iter = 1;
        else
            EdgeSolidAngle_3 = C_{i,Only}(t_*);
            EdgeSolidAngle_4 = e_i ;
        end
    end
end
else if Positive = 3 then
    EdgeSolidAngle_i = e_i;
end
```

Algorithm 1 presents the determination of the reflected part of a triangular solid angle for a given normal vector $\boldsymbol{n}$. The fist step of this algorithm is to count the number `Positive` of reflected edges. 3 cases are taken into account :

— `Positive` $= 1$: 1 edge only is reflected, called $\boldsymbol{e}_{\texttt{only}}$. The reflected solid angle is still a triangle. The two other edges are determined by t_* and $\mathcal{C}_{i,\texttt{Only}}(t_*)$

— `Positive` $= 2$: 2 edges are reflected. The non-reflected one is called also $\boldsymbol{e}_{\texttt{only}}$. The reflected solid angle is rectangular.

— `Positive` $= 3$: All edges are reflected : the solid angle is not split.

All reflected edges are included within `EdgeSolidAngle`.

Algorithm 2: Check whether or not an edge lies within a solid angle

$\boldsymbol{e}_*$; $\mathtt{M}$;
$\boldsymbol{e}'_* = \mathtt{M} \cdot \boldsymbol{e}_*$;
if $\min \boldsymbol{e}'_* > 0$ **then**
    $\boldsymbol{e}^{(mj)}_{\mathtt{iter}} = \boldsymbol{e}_*$;
    $\mathtt{iter} = \mathtt{iter} + 1$
end

Algorithm 2 is a part of Algorithm 4. This algorithm checks whether or not the edge $\boldsymbol{e}_*$ is inside a given solid angle. The solid angle is defined by the matrix M equal to P_j^{-1} or P_m^{-1}. the index j defines the reflected solid angle and the index m represents a solid angle from the discretization.

Algorithm 3: Check whether or not an intersection exists between a side and a solid angle

$\boldsymbol{e}^{(1)}_*$; $\boldsymbol{e}^{(2)}_*$; $\mathtt{M} = [\boldsymbol{v}_1, \boldsymbol{v}_2, \boldsymbol{v}_3]^t$;
for $i = 1, 2, 3$ **do**
    $t_* = -\frac{\boldsymbol{e}^{(1)}_* \cdot \boldsymbol{v}_i}{(\boldsymbol{e}^{(2)}_* - \boldsymbol{e}^{(1)}_*) \cdot \boldsymbol{v}_i}$;
    if $t_* \in [0, 1]$ & $\min \boldsymbol{M} \cdot \mathcal{C}_{12}(t_*) = 0$ **then**
        $\boldsymbol{e}^{(mj)}_{\mathtt{iter}} = \mathcal{C}_{12}(t_*)$;
        $\mathtt{iter} = \mathtt{iter} + 1$
    end
end

Algorithm 3 is also a part of Algorithm 4. it determines the cross direction $\boldsymbol{e}_{\mathtt{iter}}(jm)$ between the side $(\boldsymbol{e}^{(1)}_* \boldsymbol{e}^{(2)}_*)$ from the reflected solid angle Ω_j and the ith side of the solid angle Ω_m. The cross section point is $\mathcal{C}_{12}(t_)$. The condition $t_* \in [0, 1]$ checks if the point $\mathcal{C}_{12}(t_)$ is on the side $(\boldsymbol{e}^{(1)}_* \boldsymbol{e}^{(2)}_*)$ of Ω_j. The second condition $\mathcal{C}_{12}(t_)$ checks if the point is

on the ith side of Ω_m.

Algorithm 4: Determination of edges $\boldsymbol{e}_i^{(mj)}$ of Ω_{mj}

```
M = P_j^{-1};
for i = 1, 2, 3 do
    e_* = e_i^{(m)};
    ⇒ Algorithm 2
end
M = P_m^{-1};
for i = 1, 2, 3 do
    e_* = e_i^{(j)};
    ⇒ Algorithm 2
end
M = P_m^{-1};
for i = 1, 2, 3 do
    e_*^{(1)} = e_i^{(j)};
    e_*^{(2)} = e_{i+1}^{(j)};
    ⇒ Algorithm 3
end
```

Algorithm 4 picks-up all edges of Ω_{mj}. The first two loops determine respectively the edges from Ω_m included in Ω_j and edges from Ω_j included in Ω_m. The third loop

determines the intersection edge between their sides.

Algorithm 5: Ordering the edge $\boldsymbol{e}_i$ of the solid angle $\Omega_{mj}(\boldsymbol{n})$

$\boldsymbol{e}'_i = P_m^{-1}\boldsymbol{e}_i$;
$\bar{\boldsymbol{e}}_i = \frac{\boldsymbol{e}'_i}{||\boldsymbol{e}'_i||_1}$;
$O\boldsymbol{e}_i = 0$; $O\bar{\boldsymbol{e}}_i = 0$;
$O\boldsymbol{e}_1 = \boldsymbol{e}_1$; $O\bar{\boldsymbol{e}}_1 = \bar{\boldsymbol{e}}_1$;
if $((\bar{\boldsymbol{e}}_2 - \bar{\boldsymbol{e}}_1) \wedge (\bar{\boldsymbol{e}}_3 - \bar{\boldsymbol{e}}_1))_x > 0$ **then**
  $O\bar{\boldsymbol{e}}_2 = \bar{\boldsymbol{e}}_2$; $O\boldsymbol{e}_2 = \boldsymbol{e}_2$;
  $O\bar{\boldsymbol{e}}_3 = \bar{\boldsymbol{e}}_3$; $O\boldsymbol{e}_3 = \boldsymbol{e}_3$;
else
  $O\bar{\boldsymbol{e}}_2 = \bar{\boldsymbol{e}}_3$; $O\boldsymbol{e}_2 = \boldsymbol{e}_3$;
  $O\bar{\boldsymbol{e}}_3 = \bar{\boldsymbol{e}}_2$; $O\boldsymbol{e}_3 = \boldsymbol{e}_2$;
end
for $i = 4, \cdots, Nb_e$ **do**
  `Change` $= 0$;
  for $j = 1, \cdots, i$ **do**
    if $((\bar{\boldsymbol{e}}_j - \bar{\boldsymbol{e}}_1) \wedge (\bar{\boldsymbol{e}}_i - \bar{\boldsymbol{e}}_1))_x < 0$ *and* *Change* $= 0$ **then**
      `Change` $= 1$;
      `Position` $= j$;
      `Break`;
    end
  end
  if *Change* $= 1$ **then**
    for $j = i - 1, \cdots,$ *Position* **do**
      $O\bar{\boldsymbol{e}}_{j+1} = O\bar{\boldsymbol{e}}_j$; $O\boldsymbol{e}_{j+1} = O\boldsymbol{e}_j$;
    end
    $O\bar{\boldsymbol{e}}_{\texttt{Position}} = \bar{\boldsymbol{e}}_i$; $O\boldsymbol{e}_{\texttt{Position}} = \boldsymbol{e}_i$;
  else
    $O\bar{\boldsymbol{e}}_{\texttt{i}} = \bar{\boldsymbol{e}}_i$; $O\boldsymbol{e}_{\texttt{i}} = \boldsymbol{e}_i$;
  end
end

Algorithm 5 orders intersection edges of Ω_{mj}. The first line changes the edge $\boldsymbol{e}_i$ on the edge $\boldsymbol{e}'_i$ by base change from the bases axe $(0xyz)$ to the bases $(0\boldsymbol{e}_1^{(m)}\boldsymbol{e}_2^{(m)}\boldsymbol{e}_3^{(m)})$. The second line projects the edge $\boldsymbol{e}'_i$ on $\bar{\boldsymbol{e}}_j$ into the triangular surface defined by edges $\boldsymbol{e}_1^{(m)}$, $\boldsymbol{e}_2^{(m)}$, and $\boldsymbol{e}_3^{(m)}$. The first step orders counterclockwisely the three first edges $\bar{\boldsymbol{e}}_i$ ((a) on Fig 3.26). This step is important to locate the position of the other edges. The second step checks where is the position of the next edge $\bar{\boldsymbol{e}}_j$ on the ordered edges $O\bar{\boldsymbol{e}}_i$ ((b) on Fig 3.26). The next step adds the edge $\boldsymbol{e}_j$ inside the ordering edge list at $O\boldsymbol{e}_{\texttt{Position}}$. Each ordering process for $\bar{\boldsymbol{e}}_i$ is done also for $\boldsymbol{e}_i$.

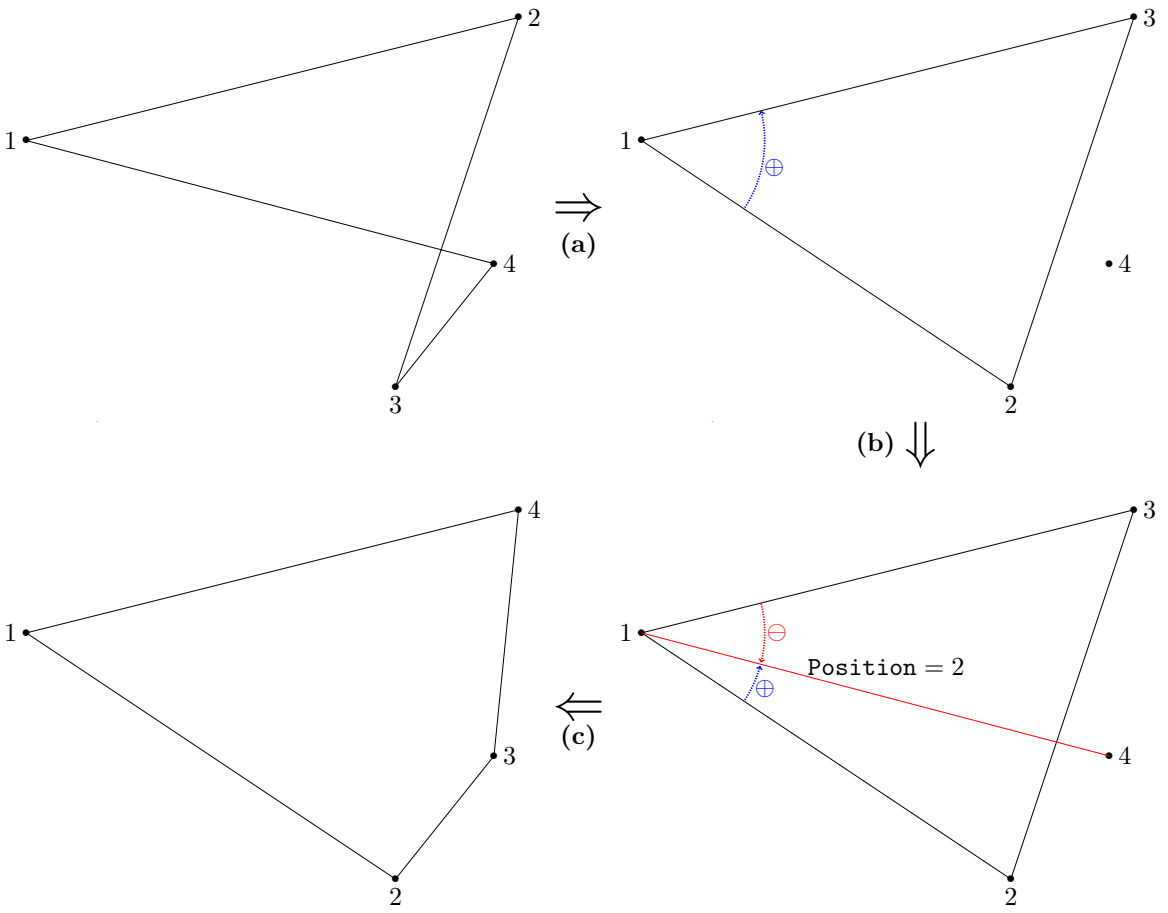

FIGURE 3.26 – Sketch of the ordering process of edges of Ω_{mj}

3.9 Appendix B : SqT$_n$ angular building and S$_n$ discretizations

This discretization is an extension of Thurgood discretization [34], since the structure on the SqT$_{p,n}$ discretization is based on the plan $x+y+z=1$. Two kinds of solid angles are built :

— rectangular solid angles such as the main directions $\boldsymbol{s}_m$ lie on the main orthogonal planes $(\boldsymbol{e}_x 0 \boldsymbol{e}_y)$, $(\boldsymbol{e}_x 0 \boldsymbol{e}_z)$ and $(\boldsymbol{e}_y 0 \boldsymbol{e}_z)$;

— triangular solid angles inside each truncated octant.

Let us define $\boldsymbol{e}_k$, a direction delimiting a solid angle, $\bar{\boldsymbol{e}}_k$ and $\bar{\boldsymbol{s}}_m$ the projections of $\boldsymbol{e}_k$ and $\boldsymbol{s}_m$ into the plan $x+y+z=1$. The calculation being the same for each orthogonal plane, the calculation for the rectangular solid angle is here presented only for the plane $z=0$. There are n projections $\bar{\boldsymbol{s}}_m$ on the line $x+y=1$ that can be calculated as (Fig 3.27) :

$$\bar{\boldsymbol{s}}_m = \left(1 - \frac{m-1}{n-1}, \frac{m-1}{n-1}, 0\right) \quad , \quad \forall m = 1, ..., n \tag{3.43}$$

To build the projections $\bar{\boldsymbol{e}}_k$, let us define the lines $C_k(t) = ((1-t)(1-\frac{k-0.5}{n-1}), (1-t)\frac{k-0.5}{n-1}, t)$, $k = 1, \cdots, n-1$ and $D(t) = (t, (1-\frac{0.5}{n-0.5}) - t, \frac{0.5}{n-0.5})$. The first lines $C_k(t)$ passes through $(1,0,0)$ and the middle of two succesive $\bar{\boldsymbol{s}}_m$. The last line $D(t)$ passes

through two intersection points between extreme $C_k(t)$ lines (Fig 3.27). The projection $\bar{\boldsymbol{e}}_k$ is the intersection point between $C_k(t)$ and $D(t)$ (Fig 3.27) :

$$\bar{\boldsymbol{e}}_k = \left(\frac{n-1}{n-0.5} \left(1 - \frac{k-0.5}{n-1} \right), \frac{n-1}{n-0.5} \frac{k-0.5}{n-1}, \frac{0.5}{n-0.5} \right), \forall k = 1, \cdots, n-1 \quad (3.44)$$

Using rotation, projections $\bar{\boldsymbol{s}}_m$ and $\bar{\boldsymbol{e}}_k$ can be calculated for other octants. The rotation gives a small triangle inside each octant (Fig 3.27). The triangle is defined by $\bar{\boldsymbol{e}}_1$ and its images by rotating.

The Thurgood discretization T_p is then performed inside the remaining triangle (Fig 3.27). If $p = n - 2$ the projections $\bar{\boldsymbol{e}}_k$ are on the boundary of the triangle.

Finally, the directions $\boldsymbol{s}_m$ and $\boldsymbol{e}_k$ can be easily calculated by projection of $\bar{\boldsymbol{s}}_m$ and $\bar{\boldsymbol{e}}_k$ onto the sphere (Fig 3.27) :

$$\boldsymbol{s}_m = \frac{\bar{\boldsymbol{s}}_m}{||\bar{\boldsymbol{s}}_m||_2} \quad , \quad \boldsymbol{e}_k = \frac{\bar{\boldsymbol{e}}_m}{||\bar{\boldsymbol{e}}_k||_2} \quad (3.45)$$

The $\mathrm{SqT}_{3,1}$, $\mathrm{SqT}_{4,2}$ and $\mathrm{SqT}_{5,3}$, used in the section 3.5, are presented in Figure 3.28.

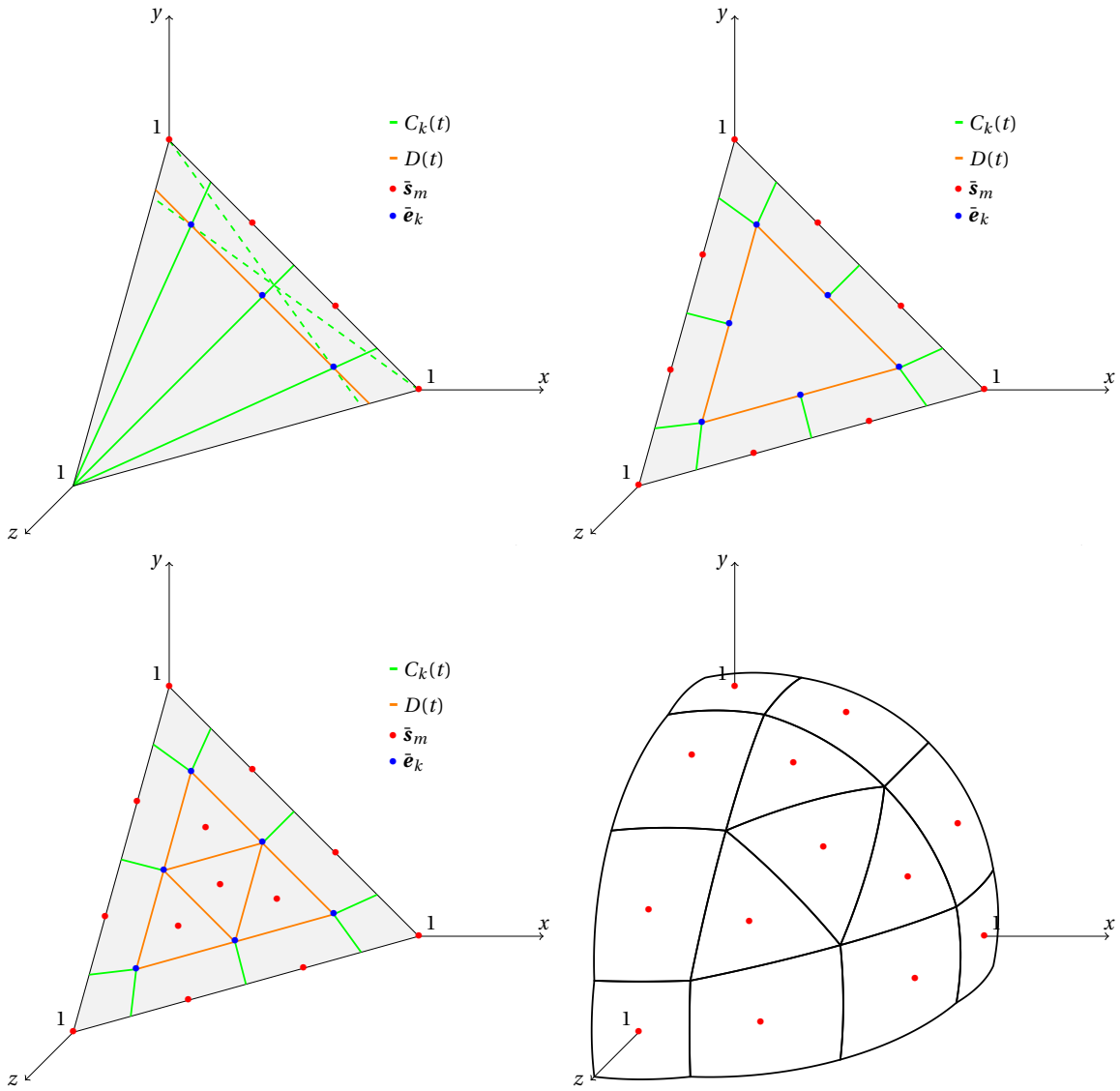

FIGURE 3.27 – Top left : calculation of $\bar{\boldsymbol{s}}_m$ and $\bar{\boldsymbol{e}}_k$ for the boundary solid angles ; top right : $\bar{\boldsymbol{s}}_m$ and $\bar{\boldsymbol{e}}_k$ of the boundary for all the first octant ; bottom left : Thurgood projection into the truncated octant ; bottom right : projection of all projections $\bar{\boldsymbol{s}}_m$ and $\bar{\boldsymbol{e}}_k$ onto the unit sphere.

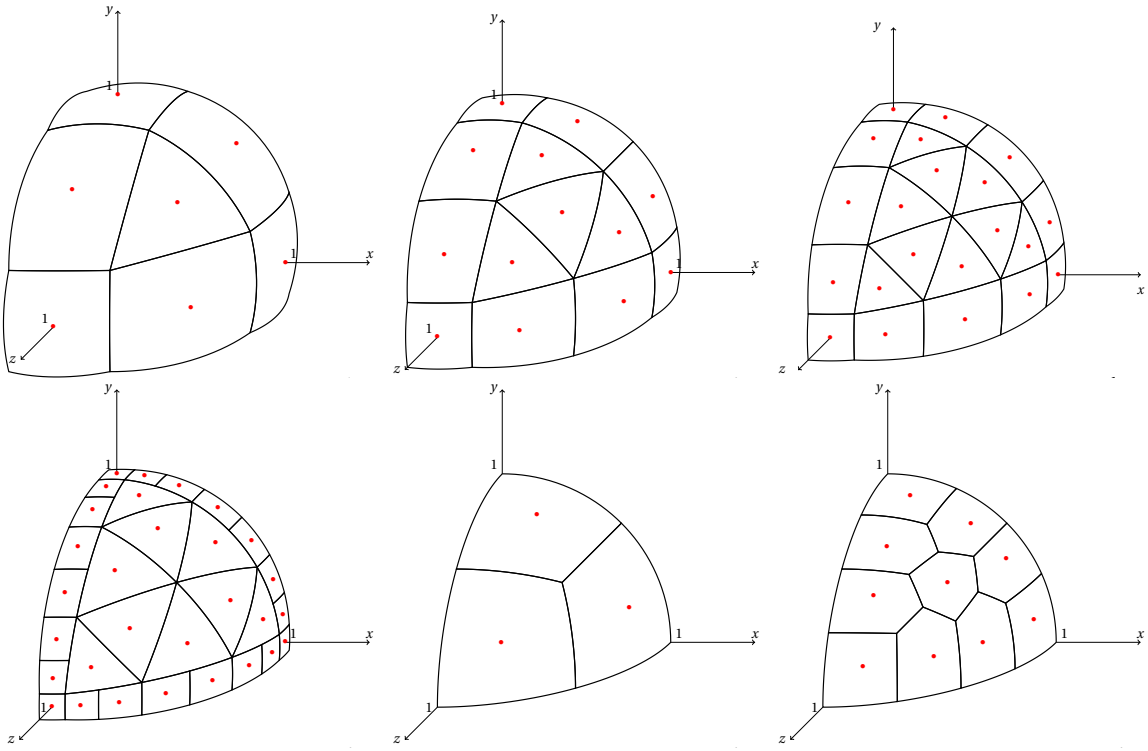

FIGURE 3.28 – Angular discretizations – Top : $SqT_{3,1}$, $SqT_{4,2}$ and $SqT_{5,3}$ – Bottom : $SqT_{8,3}$, S_4 and S_8

3.10 Discrétisations complémentaires

Cette section décrit les discrétisations S_n [33] et T_n [34], qui ont été respectivement utilisées pour les étapes de validation et pour construire la discrétisation $SqT_{p,n}$. De plus, la discrétisation uniforme à base icosaèdrale, utilisée lors de l'étude de la propagation d'un faisceau laser dans un brin de mousse, sera aussi décrite. Ces méthodes sont d'abord présentées d'un point de vue théorique. Les algorithmes permettant leur implémentations sont ensuite donnés.

3.10.1 Discrétisation S_n

La méthode S_n a été développée la première fois en 1961 sous forme d'une discrétisation angulaire [33]. Cette méthode est devenue populaire et a fait l'objet de modifications en pondérant les directions $\boldsymbol{s}_m$ par des poids de quadrature ω_m [63]. Ces poids de quadrature permettent de gagner en ordre lors de l'approximation de l'intégrale sur la sphère. Cependant, aucun angle solide n'est alors délimité par cette approche et la méthode de réflexion par partitionnement n'est pas applicable. La méthode de réflexion par partitionnement est seulement applicable à la discrétisation S_n de 1961.

Présentation théorique

Définissons tout d'abord les paramètres suivants :

$$\begin{cases} n : \text{ ordre de la discrétisation } (2, 4, 6, \cdots) \\ \mu_m : \text{cosinus directeur} \\ l : \text{niveau, } = 1, \cdots, n/2 \\ p_l : \text{somme des } \omega_m \text{ associés au niveau } l \\ \Delta : \text{paramètre dépendant de } n \text{ et } \mu_1 \end{cases}$$

La méthode S_n se déroule en 2 principales étapes : la détermination des directions portantes $\boldsymbol{s}_m$ et la détermination de l'angle solide associé à $\boldsymbol{s}_m$.

– **Détermination des directions portantes $\boldsymbol{s}_m$**

Soit n l'ordre de la discrétisation S_n. Le niveau l, parmi les $n/2$ niveaux, comporte $n/2 - l + 1$ directions par octant, comme présenté sur la figure 3.29. Il y a donc un total de $n(n+2)/8$ directions par octant.

La méthode S_n suppose que les directions sont symétriques par rotation de l'octant ainsi que par symétrie axiale. Pour toutes directions $\boldsymbol{s}_m = (\mu_i, \mu_j, \mu_k)$, les directions

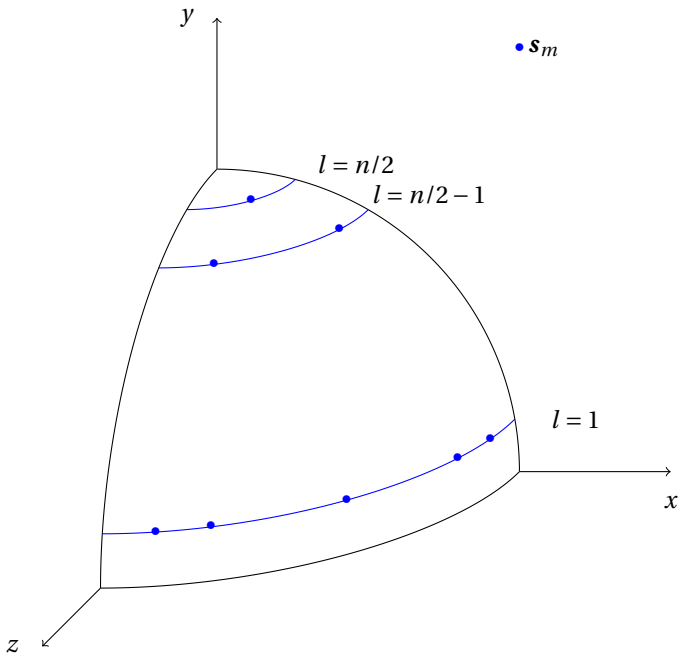

FIGURE 3.29 – Représentation des niveaux et des directions associées

suivantes font alors parti de la discrétisation :

$$\begin{cases} (\mu_i, \mu_j, \mu_k) \\ (\mu_i, \mu_k, \mu_j) \\ (\mu_j, \mu_i, \mu_k) \\ (\mu_j, \mu_k, \mu_i) \\ (\mu_k, \mu_i, \mu_j) \\ (\mu_k, \mu_j, \mu_i) \end{cases} \tag{3.46}$$

Pour situer la position de la direction $\boldsymbol{s}_m = (\mu_i, \mu_j, \mu_k)$, comme dans la figure 3.30, définissons les critères suivants :

— i représente le niveau par rapport à l'axe des x,

— j représente le niveau par rapport à l'axe des y,

— k représente le niveau par rapport à l'axe des z.

Pour mieux visualiser la position des directions $\boldsymbol{s}_m$ en fonction de leurs cosinus μ_i, définissons le symbole $\binom{j}{k\,i}$ représentant les différentes directions $\boldsymbol{s}_m$. La figure 3.31 représente les différentes directions $\boldsymbol{s}_m$ sous sa notation symbolique pour $n = 8$.

Par construction, on remarque que les indices i,j et k vérifient :

$$i + j + k = n/2 + 2 \tag{3.47}$$

Rappelons que chacune des directions $\boldsymbol{s}_m$ satisfait :

$$\mu_i^2 + \mu_j^2 + \mu_k^2 = 1 \tag{3.48}$$

Avec les égalités (3.47) et (3.48), et avec l'indice $k \in [1, n/2[$ fixé, on a les deux

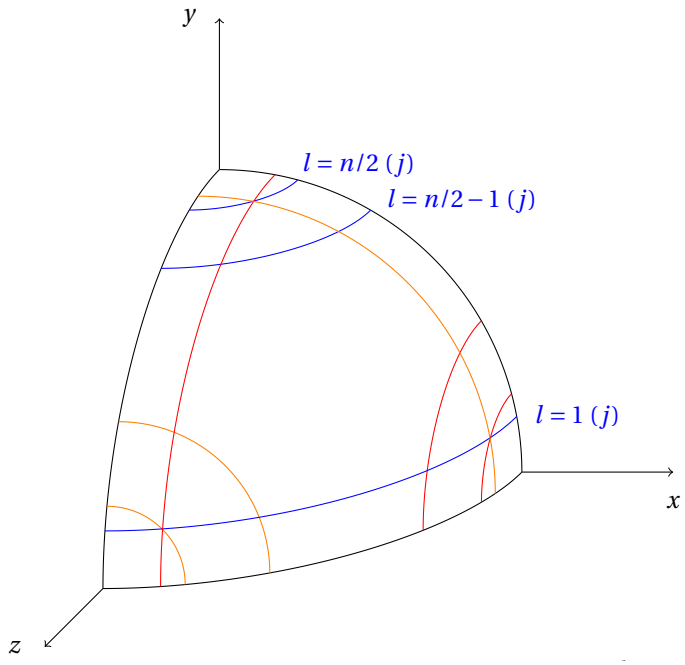

FIGURE 3.30 – Représentation des niveaux selon les 3 axes x, y et z.

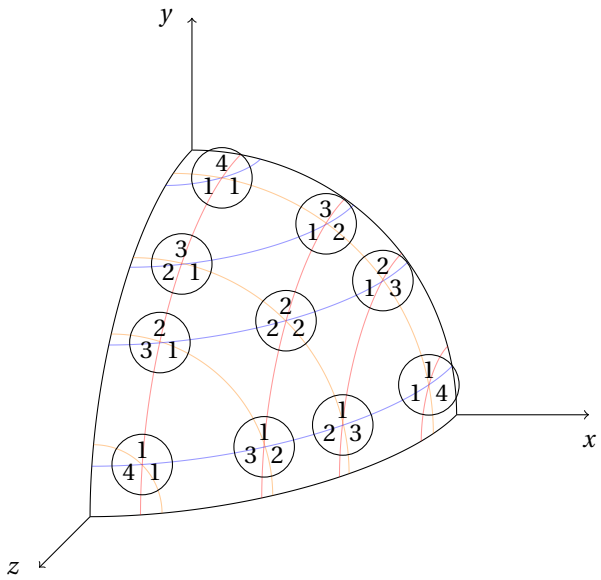

FIGURE 3.31 – Représentation symbolique des directions $\boldsymbol{s}_m$ pour S_8

égalités suivantes :

$$\begin{cases} \mu_i^2 + \mu_{j-1}^2 + \mu_{k+1}^2 = 1 \\ \mu_{i-1}^2 + \mu_j^2 + \mu_{k+1}^2 = 1 \end{cases} \tag{3.49}$$

En soustrayant ces 2 équations (3.49), on a pour tout i et j la relation d'invariance suivante :

$$\mu_i^2 - \mu_{i-1}^2 = \mu_j^2 - \mu_{j-1}^2 \tag{3.50}$$

L'égalité (3.50) est alors valable quelque soit $i, j \in \{1, \cdots, n/2\}$. Définissons le paramètre Δ comme étant l'écart entre le carré de deux cosinus consécutifs :

$$\Delta = \mu_{n/2}^2 - \mu_{n/2-1}^2 = \cdots = \mu_2^2 - \mu_1^2 \tag{3.51}$$

En sommant les $i-1$ dernières égalités de l'équation (3.51), on obtient une relation entre μ_1 et μ_i :

$$\mu_i^2 = \mu_1^2 + (i-1)\Delta \tag{3.52}$$

La forme analytique de Δ, en fonction de n et de μ_1, s'obtient avec les équations (3.47), (3.48) et (3.52) :

$$\Delta = \frac{2}{n-2}(1 - 3\mu_1^2) \tag{3.53}$$

La méthode S_n se génère en choisissant seulement n et μ_1. Par construction, le choix de μ_1 doit vérifier $\Delta > 0$. Ici le choix de μ_1 est :

$$\mu_1^2 \simeq \frac{1}{3(n-1)} \tag{3.54}$$

Avec les égalités (3.46), (3.47), (3.52) et (3.54), toutes les directions $\boldsymbol{s}_m$ sont déterminées et présentées dans la figure 3.32. Passons alors au calcul des angles solides associés pour calculer les poids ω_m.

– Détermination des angles solides et de leurs aires

Définissons tout d'abord les cosinus directeurs suivants :

$$\begin{cases} \bar{\mu}_i^2 = \mu_1^2 + \left(i - \dfrac{2}{3}\right)\Delta \\ \bar{\bar{\mu}}_i^2 = \mu_1^2 + \left(i - \dfrac{1}{3}\right)\Delta \end{cases} \tag{3.55}$$

qui définissent les directions suivantes :

$$\begin{cases} \bar{\boldsymbol{e}} = (\bar{\mu}_i, \bar{\mu}_j, \bar{\mu}_k) \\ \bar{\bar{\boldsymbol{e}}} = (\bar{\bar{\mu}}_i, \bar{\bar{\mu}}_j, \bar{\bar{\mu}}_k) \end{cases} \tag{3.56}$$

qui représentent une partie des sommets des angles solides. Par construction $\bar{\boldsymbol{e}}$ appartient à la sphère si et seulement si $i + j + k = n/2 + 1$. De la même façon, $\bar{\bar{\boldsymbol{e}}}$ appartient à la sphère si et seulement si $i + j + k = n/2$. Les directions $\boldsymbol{s}_m$ et les sommets $\bar{\boldsymbol{e}}$ et $\bar{\bar{\boldsymbol{e}}}$ sont représentés dans la figure 3.33 pour $n = 8$. Chacune de ces directions $\bar{\boldsymbol{e}}$ et $\bar{\bar{\boldsymbol{e}}}$

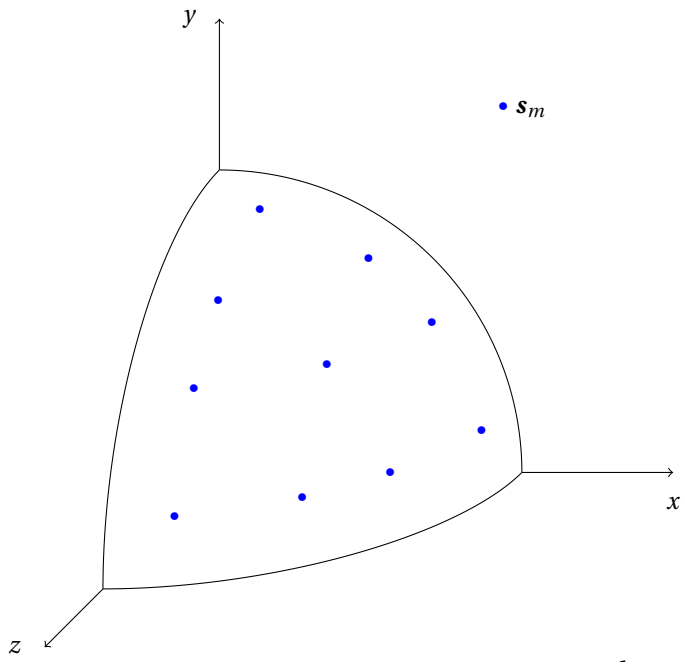

FIGURE 3.32 – Directions portantes pour $n = 8$

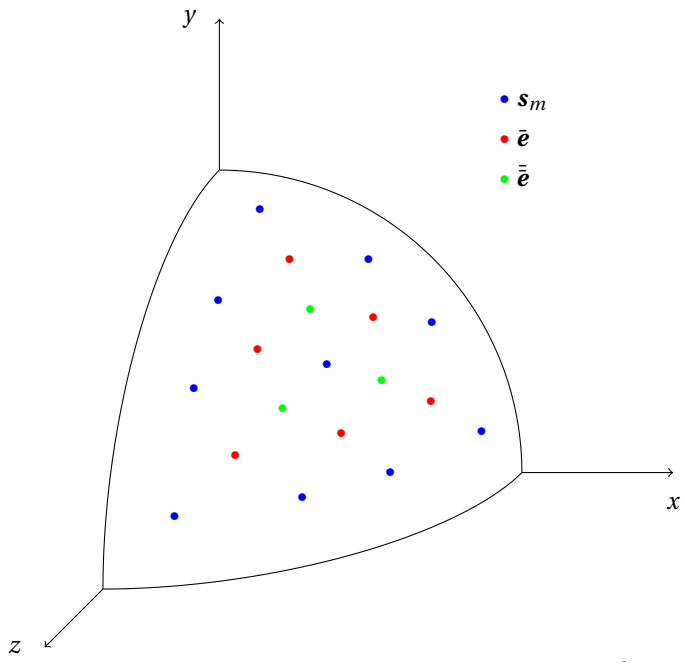

FIGURE 3.33 – Directions $\boldsymbol{s}_m$ et sommets $\bar{\boldsymbol{e}}$ et $\bar{\bar{\boldsymbol{e}}}$ pour $n = 8$

représente le centre d'un angle solide triangulaire, délimité par 3 directions $\boldsymbol{s}_m$.

Il ne manque plus que les directions sur les bords pour délimiter le contour des angles solides sur la frontière de l'octant. Appellons ces directions $\boldsymbol{e}_{\text{bord}}$. Ces directions sont les projections sphériques des $\bar{\boldsymbol{e}}$ situés au plus proche des bords de l'octant, comme présentés sur la figure 3.34. La relation entre les directions $\bar{\boldsymbol{e}}$ et $\boldsymbol{e}_{\text{bord}}$ est :

$$\boldsymbol{e}_{\text{bord}} = \left(\frac{\bar{\mu}_i}{\sqrt{\bar{\mu}_i^2 + \bar{\mu}_k^2}}, 0, \frac{\bar{\mu}_k}{\sqrt{\bar{\mu}_i^2 + \bar{\mu}_k^2}} \right) \tag{3.57}$$

Toutes les directions permettant de faire le contour des angles solides étant déterminées. La figure 3.35 montre les différents $\boldsymbol{e}_{bord}$ ainsi que les différents angles solides associés à $\boldsymbol{s}_m$. Les poids ω_m sont enfin calculés grâce au théorème de l'Huilier (3.11).

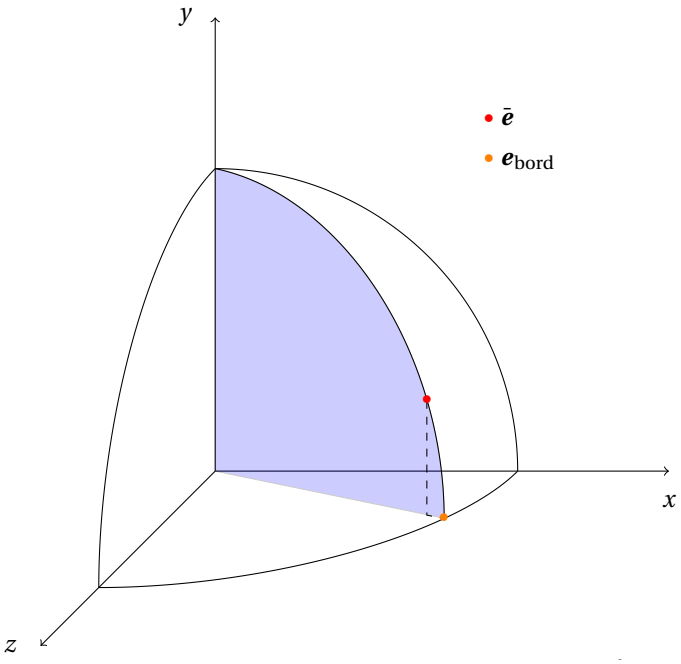

FIGURE 3.34 – Méthode de projection

Implémentation

Cette section vise à donner tous les éléments nécessaires à l'implémentation de la méthode S_n. Les algorithmes ainsi que les résultats intermédiaires sont présentés pour la discrétisation S_8. Le premier cosinus directeur μ_1 est calculé grâce à la relation (3.54). Les autres cosinus directeurs μ_i, $i > 1$ ainsi que $\bar{\mu}_i$ et $\bar{\bar{\mu}}_i$ sont calculés grâce aux équations (3.52) et (3.55). Les directions portantes $\boldsymbol{s}_m$ sont ordonnées selon l'algorithme 6. Le calcul des directions $\bar{\boldsymbol{e}}_i$ et des directions $\bar{\bar{\boldsymbol{e}}}_j$ est similaire au calcul des directions $\boldsymbol{s}_m$. Pour déterminer les directions $\bar{\boldsymbol{e}}_i$, il convient de remplacer les μ_i par les $\bar{\mu}_i$ et $n/2+2$ par $n/2+1$ dans l'algorithme 6. De même, pour déterminer les $\bar{\bar{\boldsymbol{e}}}_j$, il convient de remplacer les μ_i par les $\bar{\bar{\mu}}_j$ et $n/2+2$ par $n/2$. La figure 3.36 montre la numérotation des différentes directions $\boldsymbol{s}_m$ et des différents sommets $\bar{\boldsymbol{e}}_i$ et $\bar{\bar{\boldsymbol{e}}}_j$.

Pour créer la connexion entre les directions $\boldsymbol{s}_m$ et les sommets $\bar{\boldsymbol{e}}_i$ et $\bar{\bar{\boldsymbol{e}}}_i$, les sommets sont rassemblés et numérotés par l'algorithme 7. La figure 3.37 présente le résultat du

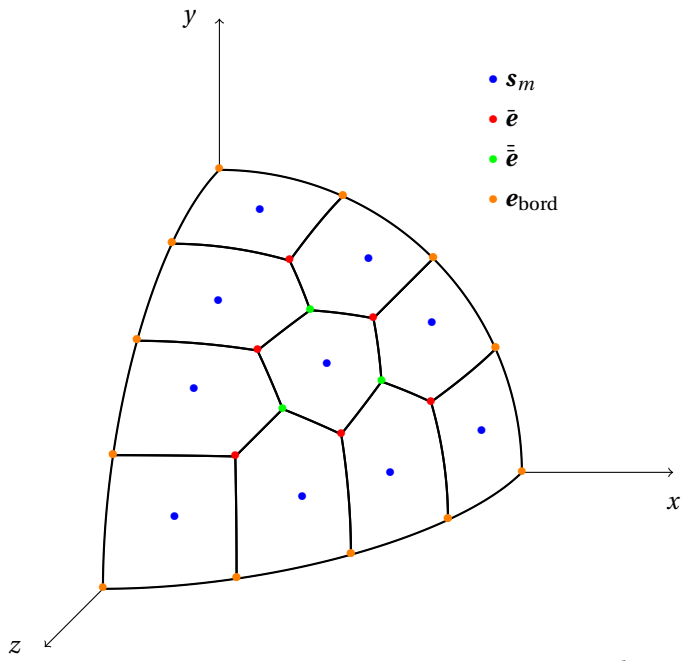

FIGURE 3.35 – Angles solides pour $n = 8$

Algorithm 6: Calcul des s_m

```
m=0;
for i = n/2, ··· , 1 do
    for j = n/2, ··· , 1 do
        for k = n/2, ··· , 1 do
            if i + j + k = n/2 + 2 then
                s_m = (μ_i, μ_j, μ_k);
                m = m + 1;
            end
        end
    end
end
```

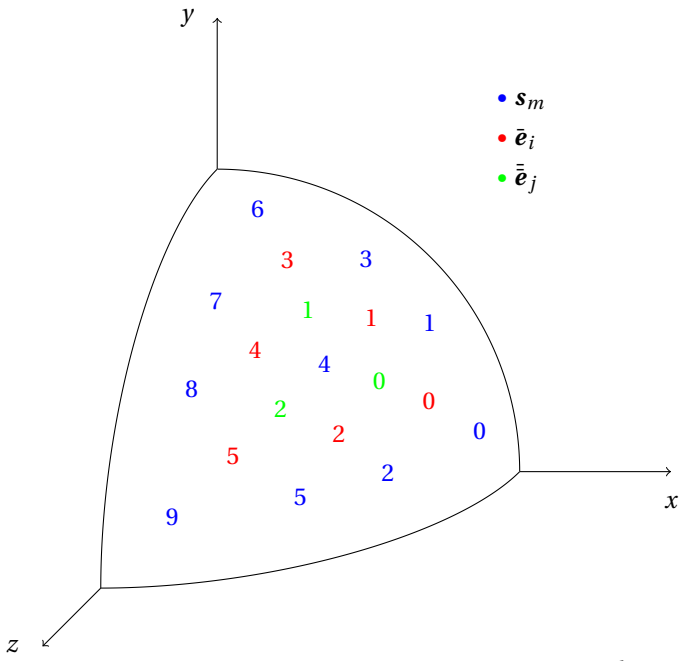

FIGURE 3.36 – Numérotation des directions $\boldsymbol{s}_m$, et des directions $\bar{e}_i$ et $\bar{\bar{e}}_j$ dans leur tableau respectif ($n = 8$)

rassemblement ainsi que la numérotation de chacun des sommets. Pour plus de clarté par la suite, on appelera $\boldsymbol{e}_k$ les différents sommets rassemblés.

De plus, on peut aussi remarquer sur la figure 3.37, que les directions $\boldsymbol{e}_k$ sont les centres des triangles engendrés pas les directions $\boldsymbol{s}_m$. Déterminer les sommets de ces triangles revient à déterminer l'appartenance du sommet $\boldsymbol{e}_k$ par rapport à tous les angles solides associés à $\boldsymbol{s}_m$. L'algorithme 8 permet de déterminer les angles solides associés à $\boldsymbol{s}_m$ auxquels appartient le sommet $\boldsymbol{e}_k$. Pour montrer le fonctionnement de l'algorithme 8, le tableau de connexion 3.1 est donné à titre d'exemple pour la quadrature S_8.

Une fois la connexion faite entre les sommets $\boldsymbol{e}_k$ et ses directions associées $\boldsymbol{s}_m$, la connexion inverse entre les directions $\boldsymbol{s}_m$ et ses sommets associés se fait facilement. L'algorithme 9 détaille ce processus de connexion. Définissons N_{bt}, le nombre de sommets $\boldsymbol{e}_k$ appartenant à l'angle solide $\boldsymbol{s}_m$. À cette étape, il y a trois sortes d'angles solides :

— N_{bt} =1 : il s'agit des 3 directions aux coins (numéros 0, 6 et 9 sur la figure 3.37),

— N_{bt} =3 : il s'agit des directions sur les bords excluant les coins (numéros 1, 2, 3, 5, 7 et 8),

— N_{bt} =6, il s'agit des directions au centre (numéro 4).

Le tableau 3.2 présente à titre d'exemple l'appartenance des différents sommets $\boldsymbol{e}_k$ à chaque angle solide Ω_m associé à la direction $\boldsymbol{s}_m$, déterminée par l'algorithme 9.

Il convient ensuite de déterminer les directions $\boldsymbol{e}_{bord}$ qui vont être répertoriées pour chacun des $\boldsymbol{s}_m$. trois cas sont à traiter :

— N_{bt} =1 : 3 directions $\boldsymbol{e}_{bord}$ doivent être rajoutées pour fermer le contour,

— N_{bt} =3 : 2 directions $\boldsymbol{e}_{bord}$ doivent être rajoutées pour fermer le contour,

— N_{bt} =6, aucune autre direction n'est à ajouter.

Algorithm 7: fusion des tableaux $\bar{\boldsymbol{e}}_i$ et $\bar{\bar{\boldsymbol{e}}}_j$ dans le tableau $\boldsymbol{e}_k$

```
1  i=0 ; j=0 ; m=0 ;
2  for k = 0, ··· , n/2 − 1 do
3  |   pair=0;
4  |   for l = 0, ··· , 2k + 1 do
5  |   |   if pair=0 then
6  |   |   |   e_{m+l} = ē_i;
7  |   |   |   i = i + 1;
8  |   |   |   pair=1;
9  |   |   else
10 |   |   |   e_{m+l} = ¯ē_j;
11 |   |   |   j = j + 1;
12 |   |   |   pair=0;
13 |   |   end
14 |   end
15 |   m = m + 2k + 1;
16 end
```

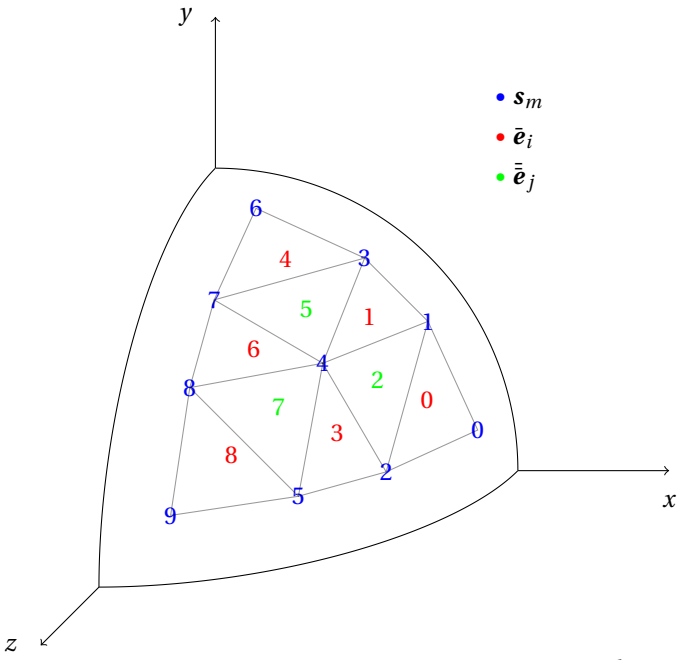

FIGURE 3.37 – Renumérotations des $\bar{\boldsymbol{e}}_i$ et $\bar{\bar{\boldsymbol{e}}}_j$

Algorithm 8: Numérotations des sommets des differents triangles

```
m = 0 ; k = 0;
for i = 0, ..., n/2 − 1 do
    Pair=0 ; Spair=0 ; Simpair=0;
    for j = 0, ..., 2i + 1 do
        if Pair=0 then
            SommetT(k + j, 1) = m+Spair;
            SommetT(k + j, 2) = m + i − 1+Spair;
            SommetT(k + j, 3) = m + iSpair;
            Spair=Spair+1;
            pair=1;
        else
            SommetT(k + j, 1) = m+Simpair;
            SommetT(k + j, 2) = m + 1+Simpair;
            SommetT(k + j, 3) = m + i + 1+Simpair;
            Simpair=Simpair+1;
            pair=0;
        end
    end
    k=k+2i+1;
    m=m+i+1;
end
```

$\boldsymbol{e}_k$			
0	0	1	2
1	1	3	4
2	1	2	4
3	2	4	5
4	3	6	7
5	3	4	7
6	4	7	8
7	4	5	8
8	5	8	9

Tableau 3.1 – Sommets des triangles, associés à $\boldsymbol{e}_k$, de la figure 3.37

Algorithm 9: Connexions entre $\boldsymbol{s}_m$ et $\boldsymbol{e}_k$

```
for i = 1, ··· , n(n + 2)/8 do
    N_bt(i − 1) = 0;
    l = 0;
    for k = 1, ··· , (n − 2)²/4 do
        if SommetT(k, 1) = i − 1 |
        SommetT(k, 2) = i − 1 |SommetT(k, 2) = i − 1 then
            l = l + 1;
            N_bt(i − 1) = N_bt(i − 1) + 1;
            NumD(i − 1, l) = k;
        end
    end
end
```

$\boldsymbol{s}_m$	N_{bt}						
0	1	0	×	×	×	×	×
1	3	0	1	2	×	×	×
2	3	0	2	3	×	×	×
3	3	1	3	4	×	×	×
4	6	1	2	3	5	6	7
5	3	3	7	8	×	×	×
6	1	4	×	×	×	×	×
7	3	4	5	6	×	×	×
8	3	6	7	8	×	×	×
9	1	8	×	×	×	×	×

TABLEAU 3.2 – Direction $\boldsymbol{e}_k$ pour chaque $\boldsymbol{s}_m$ pour la quadrature S_8

Si $N_{bt} = 1$, alors la direction portante est située proche d'un des coins de l'octant. L'angle solide associé ne possède qu'un seul sommet, noté $\boldsymbol{e}_{\text{in}}$, à l'intérieur de l'octant et 3 autres sommets sur la frontière. La particularité de $\boldsymbol{e}_{\text{in}}$ est qu'il possède deux composantes identiques dont une plus grande que les deux autres. On peut avoir trois cas possible pour $\boldsymbol{e}_{\text{in}}$:

$$\boldsymbol{e}_{\text{in}} = \begin{cases} (\alpha, \beta, \beta) \\ (\beta, \alpha, \beta) \\ (\beta, \beta, \alpha) \end{cases} \tag{3.58}$$

Pour le premier cas possible, les autres sommets se déterminent avec la formule de projection (3.57) :

$$\begin{cases} \left(\dfrac{\alpha}{\sqrt{\alpha^2 + \beta^2}}, 0, \dfrac{\beta}{\sqrt{\alpha^2 + \beta^2}} \right) \\ (1, 0, 0) \\ \left(\dfrac{\alpha}{\sqrt{\alpha^2 + \beta^2}}, \dfrac{\beta}{\sqrt{\alpha^2 + \beta^2}}, 0 \right) \end{cases} \tag{3.59}$$

Si $N_{bt} = 3$, alors il y a trois sommets à l'intérieur de l'octant, noté $\boldsymbol{e}_{\text{in}}^{(i)}$ et deux sur la même frontière. Dans ces trois sommets, il y a deux $\bar{\boldsymbol{e}}_i$ et un $\bar{\bar{\boldsymbol{e}}}_j$. On rappelle que les $\boldsymbol{e}_{\text{bord}}$ sont les projetés des $\bar{\boldsymbol{e}}_j$ (3.57) ; il faut donc les identifier. Comme les deux $\bar{\boldsymbol{e}}_i$ appartiennent à un même niveau, ils ont donc une composante en commun. Par construction des $\bar{\mu}_i$ et $\bar{\bar{\mu}}_j$ par les formules (3.55), $\bar{\bar{\boldsymbol{e}}}_j$ n'a aucune composante en commun avec les $\bar{\boldsymbol{e}}_i$. Pour construire les projetés, prenons l'exemple suivant :

$$\begin{cases} \boldsymbol{e}_{\text{in}}^{(1)} = (x_1, y_1, z_1) \\ \boldsymbol{e}_{\text{in}}^{(2)} = (\alpha, y_2, z_2) \\ \boldsymbol{e}_{\text{in}}^{(3)} = (\alpha, y_3, z_3) \end{cases} \tag{3.60}$$

Dans cet exemple là, $\boldsymbol{e}_{\text{in}}^{(2)}$ et $\boldsymbol{e}_{\text{in}}^{(3)}$ ont la première composante en commun et sont donc nos $\bar{\boldsymbol{e}}_i$. Les sommets $\boldsymbol{e}_{bord}$ pour cet exemple sont :

$$\begin{cases} \left(0, \dfrac{y_2}{\sqrt{{y_2}^2 + {z_2}^2}}, \dfrac{z_2}{\sqrt{{y_2}^2 + {z_2}^2}} \right) \\ \left(0, \dfrac{y_3}{\sqrt{{y_3}^2 + {z_3}^2}}, \dfrac{z_3}{\sqrt{{y_3}^2 + {z_3}^2}} \right) \end{cases} \tag{3.61}$$

Pour une meilleure organisation, chacun des projetés est mis à la suite des $\boldsymbol{e}_k$. Chaque projeté peut donc apparaître plusieurs fois dans cette liste. Les directions $\boldsymbol{e}_{\text{bord}}$ sont répertoriés par application de l'algorithme 10. Le tableau 3.2 est ensuite complété en prenant soin d'avoir les directions $\boldsymbol{e}_k$ bien orientées pour obtenir le tableau 3.3. Tous les sommets étant déterminés, les poids ω_m se déterminent avec la formule (3.11).

Remarque : pour la méthode S_4, le sommet $\boldsymbol{e} = (\frac{1}{\sqrt{3}}, \frac{1}{\sqrt{3}}, \frac{1}{\sqrt{3}})$ est unique. L'algorithme 10 ne fonctionne pas pour S_4.

Les figures 3.40 et 3.41 présentent respectivement les angles solides pour la discrétisation S_{40} et S_{200}. Dans chaque octant, la discrétisation S_{40} possède 210 angles

Algorithm 10: Ajout des sommets $\boldsymbol{e}_{bord}$ aux angles solides

$Nb = (n-2)^2/4$;
for $i = 1, \cdots, n(n+2)/2$ **do**
  if $N_{bt} = 1$ **then**
    $\min = \min(\boldsymbol{e}_{i,\text{in}}(1), \boldsymbol{e}_{i,\text{in}}(2))$;
    for $j = 1, 2, 3$ **do**
      if $\boldsymbol{e}_{i,in}(j) \neq \min$ **then**
        Projection par rapport à l'axe j;
        NumD$(i-1, 2) = Nb + 1$; NumD$(i-1, 3) = Nb + 2$;
        NumD$(i-1, 4) = Nb + 3$;
        $N_{bt}(i-1) = 4$;
        $Nb = Nb + 3$;
      end
    end
  end
  if $N_{bt} = 3$ **then**
    for $j = 1, 2, 3$ **do**
      for $k = j + 1, 3$ **do**
        for $l = 1, 2, 3$ **do**
          if $\boldsymbol{e}^{(j)}_{i,in}(l) = \boldsymbol{e}^{(k)}_{i,in}(l)$ **then**
            Projection de $\boldsymbol{e}^{(j)}_{i,\text{in}}$ et de $\boldsymbol{e}^{(k)}_{i,\text{in}}$ sur le plan normal à l'axe l;
            NumD$(i-1, 4) = Nb + 1$; NumD$(i-1, 5) = Nb + 2$;
            $N_{bt}(i-1) = 5$;
            $Nb = Nb + 2$;
          end
        end
      end
    end
  end
end

$\boldsymbol{s}_m$	N_{bt}						
0	4	0	10	9	11	×	×
1	5	0	2	1	13	12	×
2	5	0	2	3	15	14	×
3	5	1	5	4	17	16	×
4	6	1	2	3	7	6	5
5	5	7	3	8	19	18	×
6	4	4	21	20	22	×	×
7	5	4	5	6	24	23	×
8	5	6	7	8	26	25	×
9	4	8	28	27	29	×	×

TABLEAU 3.3 – Direction $\boldsymbol{e}_k$ pour chaque $\boldsymbol{s}_m$ pour la quadrature S_8

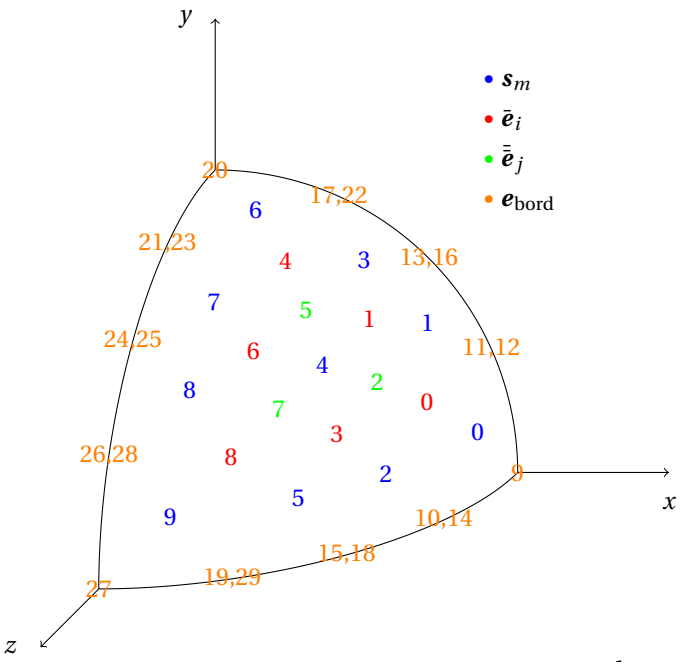

FIGURE 3.38 – Angles solide pour $n = 8$

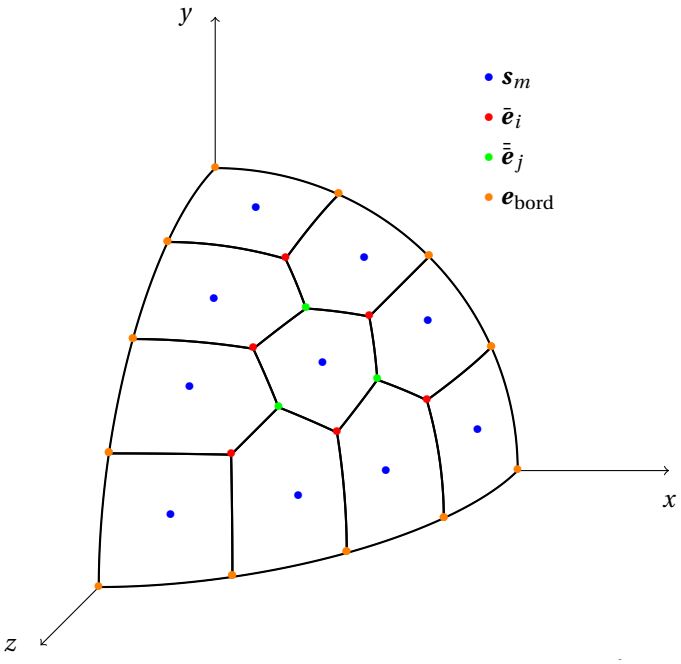

FIGURE 3.39 – Angles solides pour $n = 8$

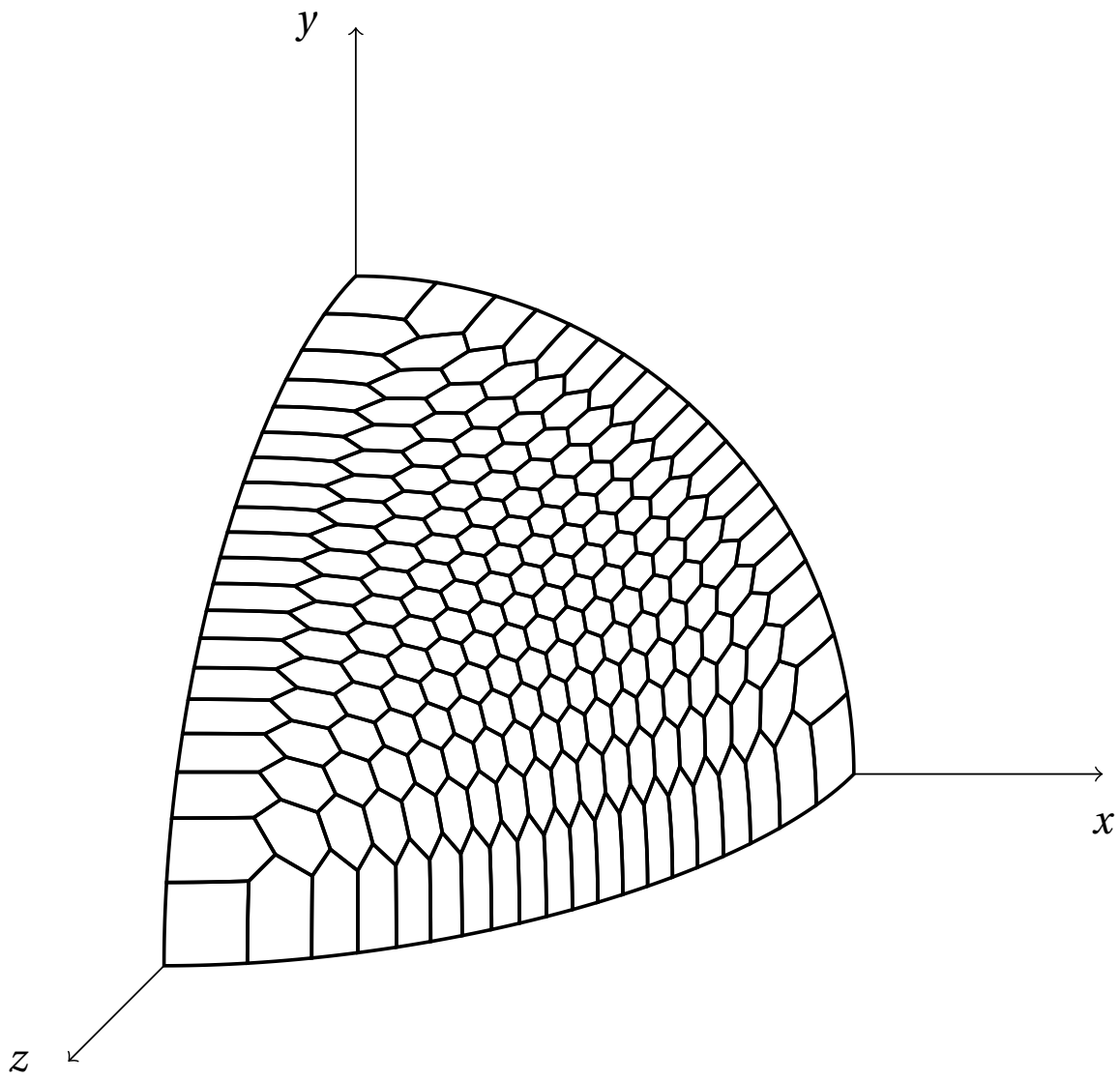

FIGURE 3.40 – Angles solides pour la discrétisation S_{40}

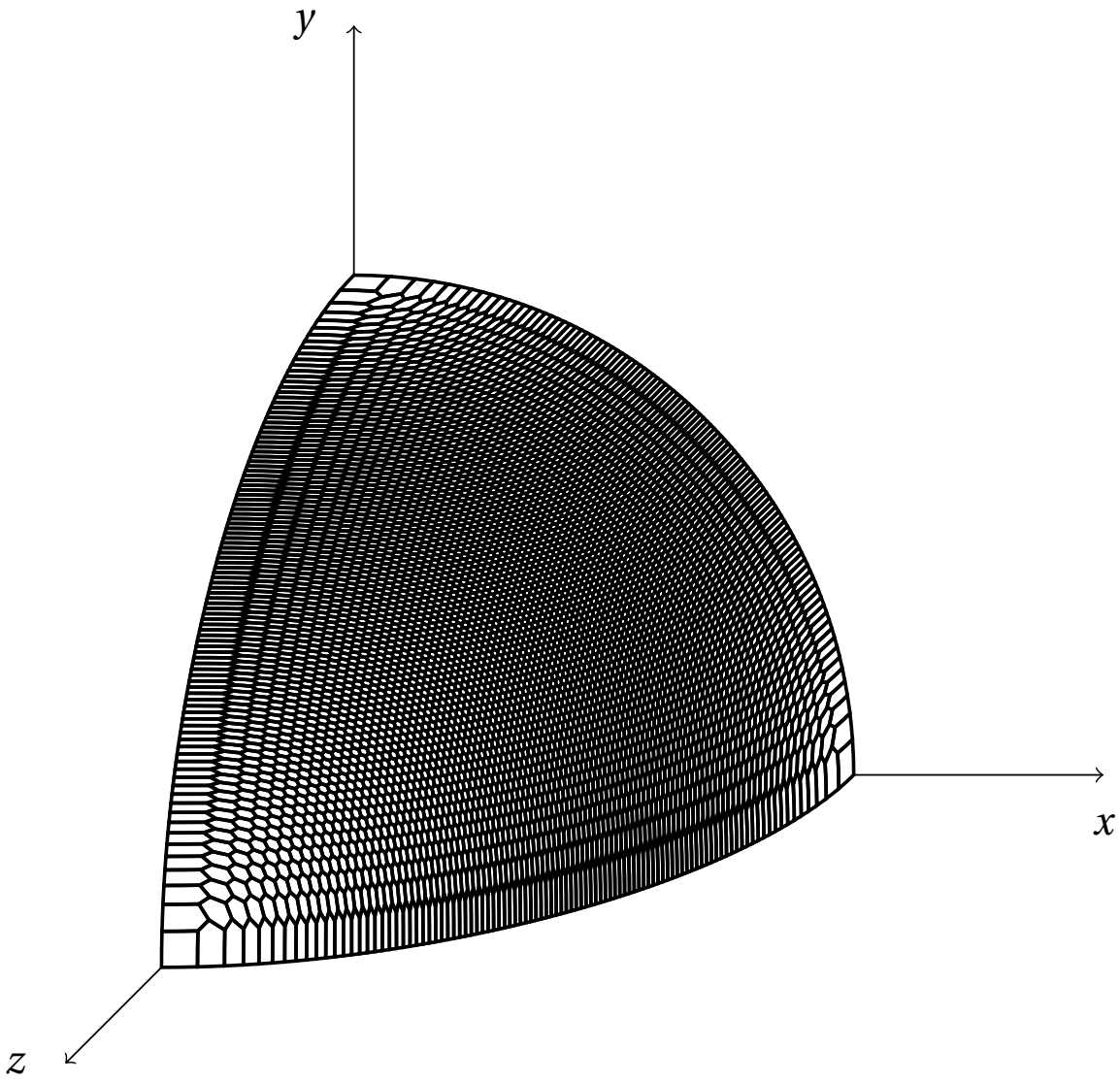

FIGURE 3.41 – Angles solides pour la discrétisation S_{200}

solide et la discrétisation S_{200} possède 5050 angles solides. On peut constater que la concentration d'angles solides est plus forte au centre, ce qui la rend fortement non uniforme.

3.10.2 Discrétisation T_n

Présentée par Thurgood en 1995 [34], la discrétisation T_n, comme la discrétisation S_n, possède une symétrie des angles solides par rotation. Elle ne possède que des angles sphériques triangulaires, ce qui la rend plus facile à comprendre et à implémenter que la méthode S_n.

Présentation théorique

Définissons tout d'abord les paramètres suivants :

$$\begin{cases} n : \text{ ordre de la discrétisation} (1, 2, 3, \cdots) \\ \boldsymbol{e}_k^p : \text{sommets des triangles plans} \\ \boldsymbol{c}_m : \text{centres de gravité des triangles plans} \\ L : \text{distance par axe entre deux sommets plans} \end{cases}$$

La méthode de Thurgood consiste à construire les directions $\boldsymbol{s}_m$ et les angles solides associés Ω_m en passant par la portion triangulaire du plan $x + y + z = 1$ délimitée par l'octant positif. Pour construire les angles solides, le triangle plan est subdivisé en n^2 sous-triangles, qui seront ensuite projetés sur la sphère. Notons $\boldsymbol{e}_k^p$ les $(n+2)(n+1)/2$ sommets de ces sous-triangles qui sont définis par :

$$\boldsymbol{e}_k^p = (1 - iL, jL, iL - jL) \ , \ \forall i = 0, \cdots, n \ , \ \forall j = 0, \cdots, i \tag{3.62}$$

Les centres de gravité $\boldsymbol{c}_m$ sont les moyennes des sommets pour chaque sous-triangle :

$$\boldsymbol{c}_m = \frac{\boldsymbol{e}_{m_1}^p + \boldsymbol{e}_{m_2}^p + \boldsymbol{e}_{m_3}^p}{3} \tag{3.63}$$

Les sommets $\boldsymbol{e}_k^p$ et les centres de gravité $\boldsymbol{c}_m$ sont présentés dans la figure 3.42 pour la discrétisation T_2.

Tous les points sur le triangle plan déterminés sont ensuite projetés sur la sphère. Par projection, les sommets des sous-triangles $\boldsymbol{e}_k^p$ deviennent les sommets des angles solides $\boldsymbol{e}_k$, et les centres de gravité $\boldsymbol{c}_m$ deviennent les directions $\boldsymbol{s}_m$. Les projections entre le plan et la sphère, présentées dans la figure 3.43 pour la quadrature T_2, sont :

$$\boldsymbol{s}_m = \frac{\boldsymbol{c}_m}{||\boldsymbol{c}_m||_2} \quad , \quad \boldsymbol{e}_k = \frac{\boldsymbol{e}_k^p}{||\boldsymbol{e}_k^p||_2} \tag{3.64}$$

Les directions $\boldsymbol{s}_m$ et les angles solides associés sont déterminés. Pour compléter la discrétisation T_n, les poids ω_m sont calculés avec la formule (3.11).

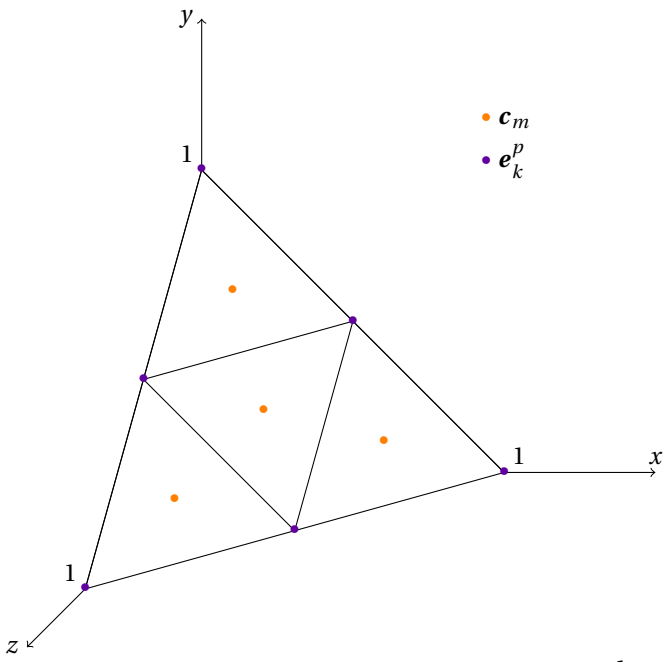

FIGURE 3.42 – Sous-triangles pour T_2

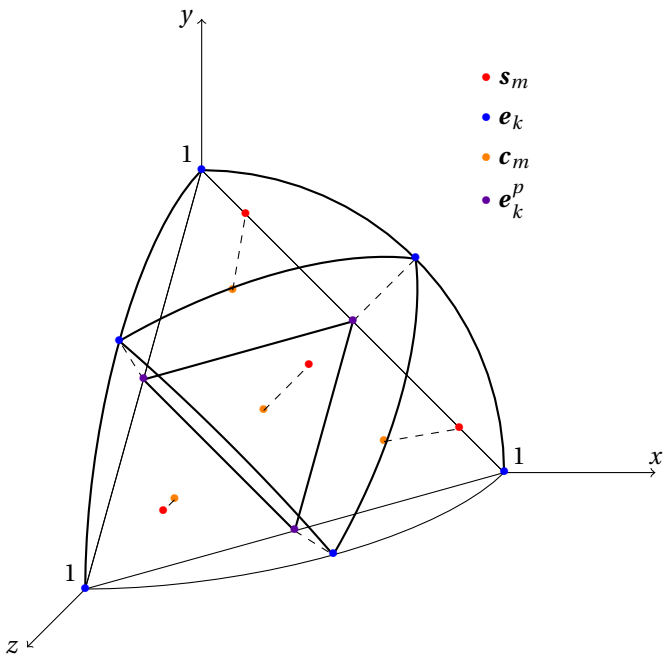

FIGURE 3.43 – Projection pour la discrétisation T_2

Implémentation

L'implémentation se déroule en trois étapes :

— la récupération des sommets $\boldsymbol{e}_k^p$ dans le plan,

— la détermination du centre de gravité $\boldsymbol{c}_m$,

— la projection sur la sphère des sommets et des centres de gravité.

Pour la première étape, les sommets plans $\boldsymbol{e}_k^p$ sont déterminés par l'algorithme 11. La figure 7 montre la numérotation des sommets déterminés par l'algorithme 11 pour la quadrature T_6.

Algorithm 11: Sommets plan $\boldsymbol{e}_k^p$

```
k=0;
for i = 0, ··· , n do
    for j = 0, ··· , i do
        e_k^p = (1 − iL, jL, iL − jL);
        k = k + 1;
    end
end
```

Ensuite, comme pour la méthode S_n, l'algorithme 8 détermine la connexion entre les sommets plan $\boldsymbol{e}_k^p$ et les centres de gravité $\boldsymbol{c}_m$. Une fois la connexion faite entre $\boldsymbol{e}_k^p$ et $\boldsymbol{c}_m$, les centres de gravité sont calculés par l'algorithme 12. La figure 3.45 montre la position et la numérotation de chaque centre de gravité $\boldsymbol{c}_m$.

Tous les sommets plans et tous les centres de gravité sont déterminés. Leur projection sur la sphère est calculée par les équations (3.64), formant ainsi tous les angles solides Ω_m et leur direction portante $\boldsymbol{s}_m$. Les poids ω_m sont déterminés par la formule (3.11).

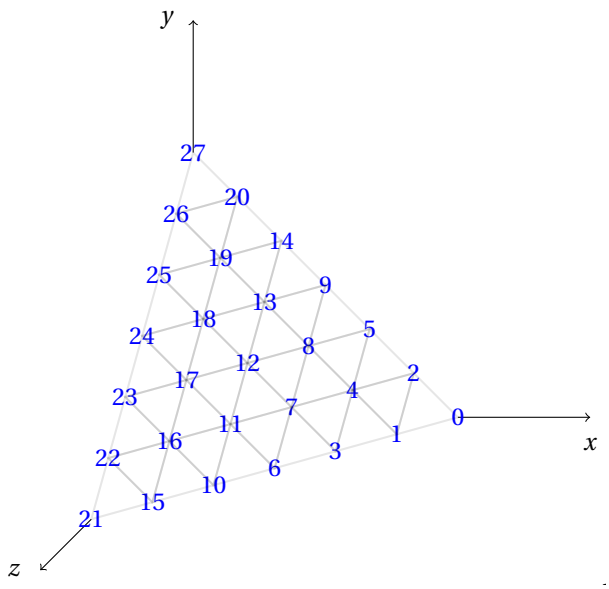

FIGURE 3.44 – Numérotation des sommets plans $\boldsymbol{e}_k^p$ pour la discrétisation T_6

Algorithm 12: Détermination des centres de gravité $\boldsymbol{c}_m$

1 **for** $m = 0, \cdots, n(n+1)/2$ **do**

2 $\quad bc_m = \dfrac{S_{\text{SommetT}(m,0)} + S_{\text{SommetT}(m,1)} + S_{\text{SommetT}(m,2)}}{3}$

3 **end**

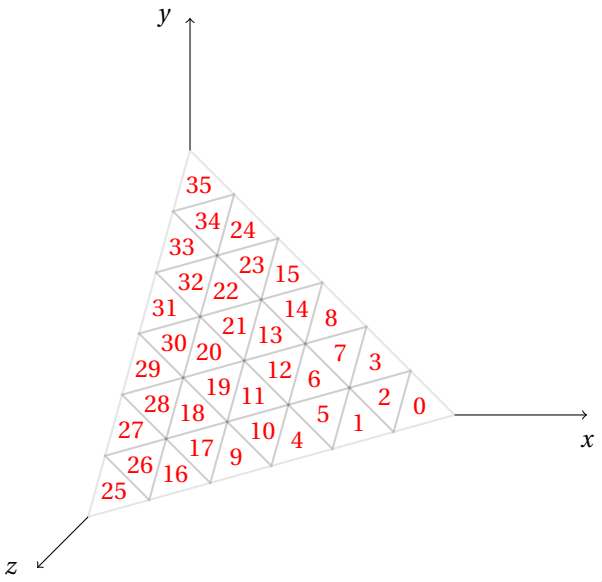

FIGURE 3.45 – Numérotation des centres de gravité $\boldsymbol{c}_m$ pour la discrétisation T_6

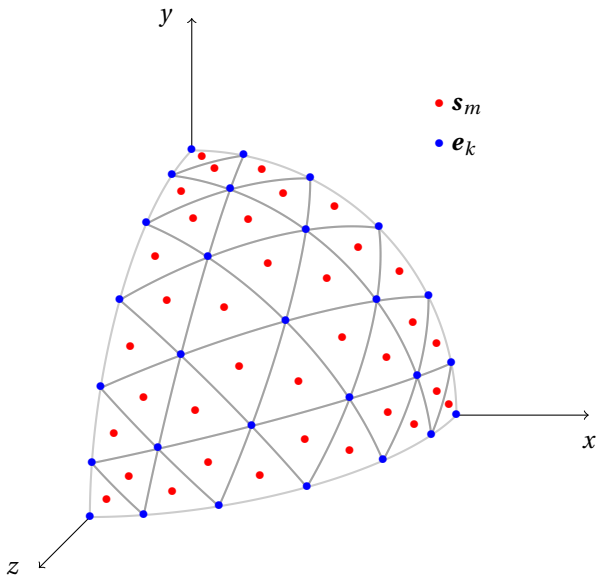

FIGURE 3.46 – discrétisation T_6

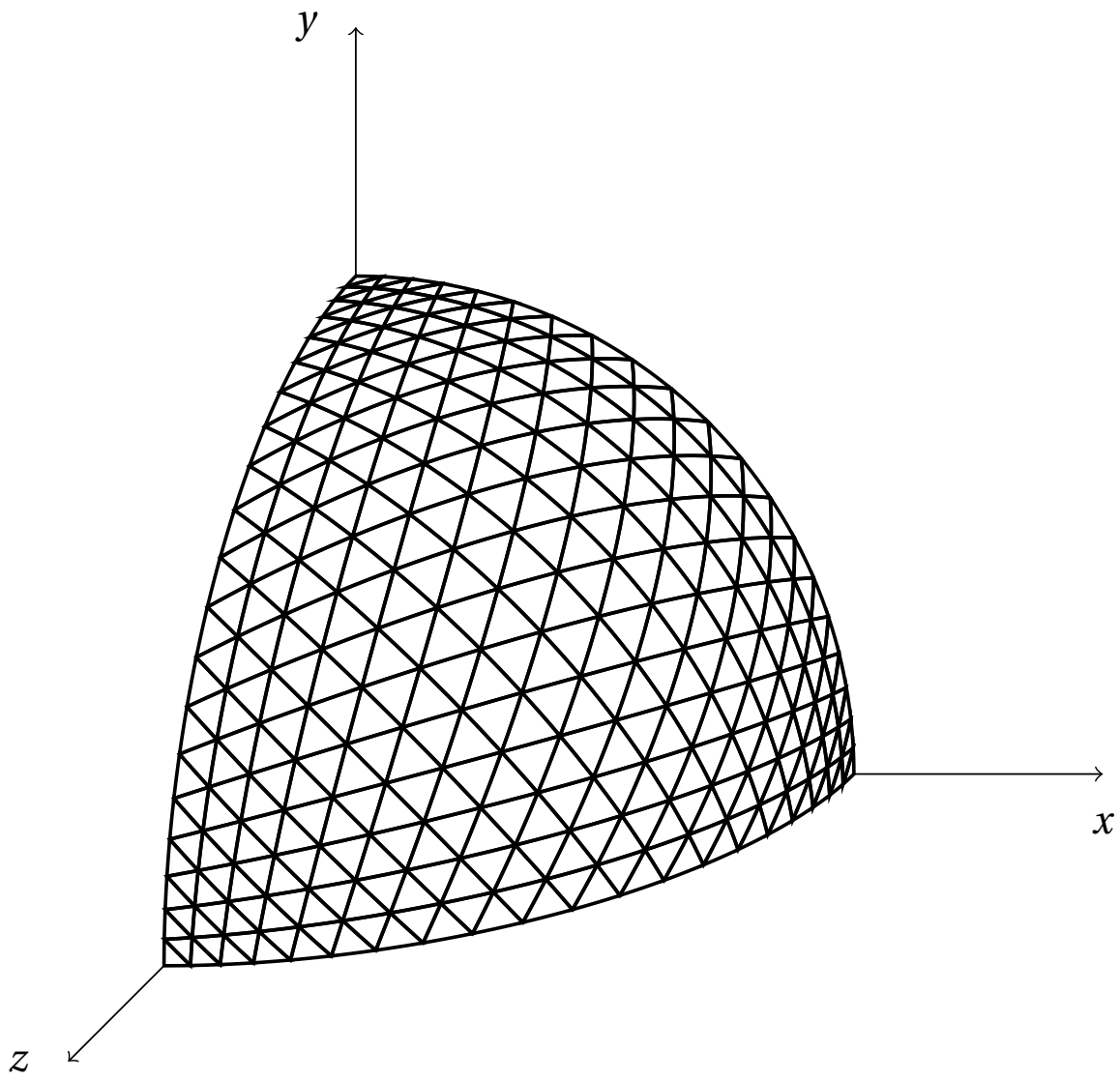

FIGURE 3.47 – Angles solides pour la discrétisation T_{20}

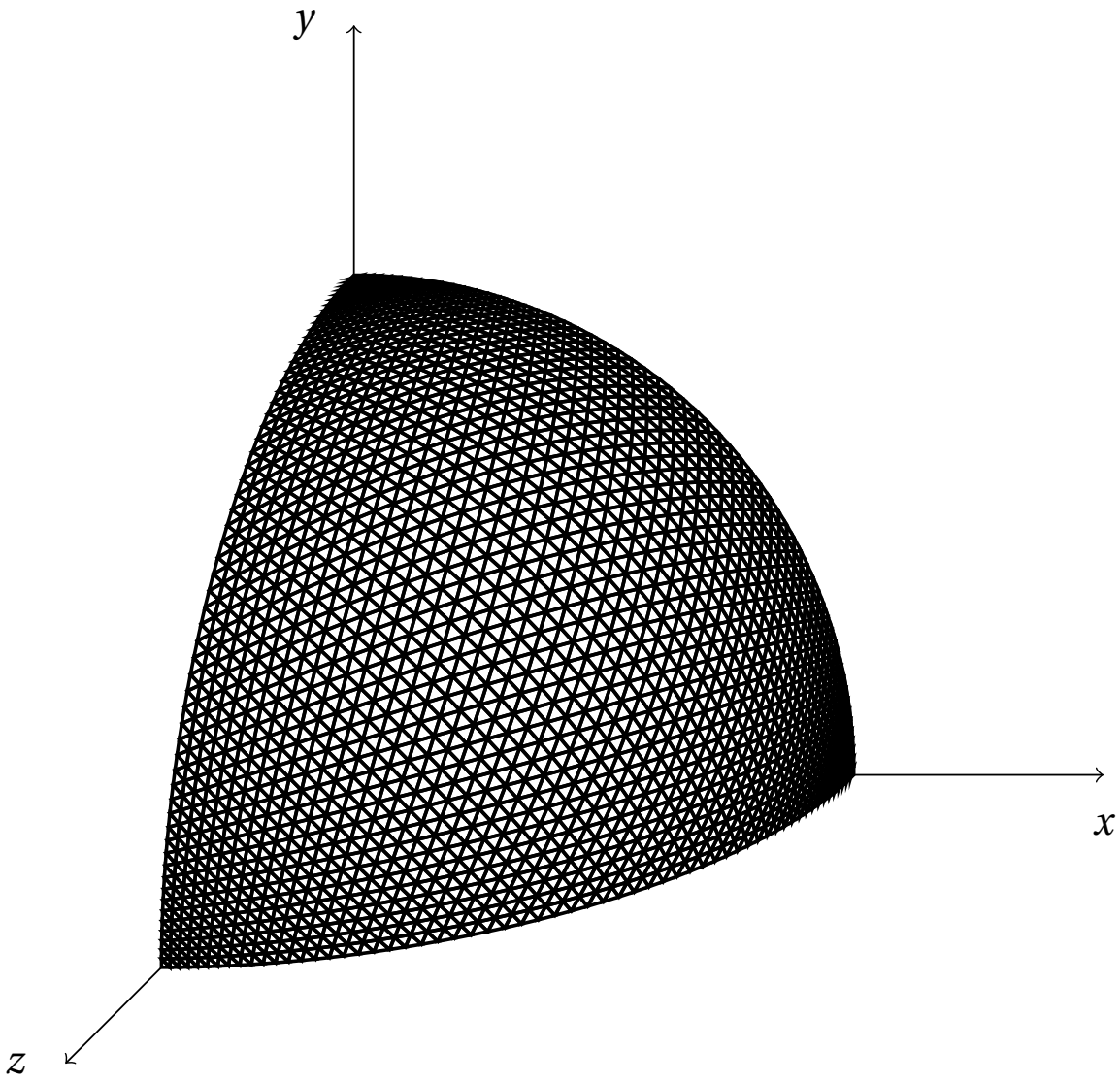

FIGURE 3.48 – Angles solides pour la discrétisation T_{60}

Les figures 3.47 et 3.48 présentent respectivement les angles solides pour la discrétisation T_{20} et T_{60}. Dans chaque octant, la discrétisation T_{20} possède 400 angles solides et la discrétisation T_{60} possède 3600 angles solides. On peut constater que la concentration d'angles solides est plus forte au niveau des coins, à l'opposé de la discrétisation S_n. La discrétisation T_n est aussi fortement non-uniforme.

3.10.3 Discrétisation uniforme : icosaèdre régulier

Contrairement aux discrétisations S_n,T_n et $SqT_{p,n}$, la discrétisation à base icosaédrique ne construit pas ses angles solides sur un octant. Cette discrétisation permet des angles solides uniformes.

Présentation théorique

La discrétisation uniforme est basée sur un icosaèdre régulier. Chaque sommet d'icosaèdre représente un sommet d'angle solide, $\boldsymbol{e}_k$. Les centres de gravité $\boldsymbol{c}_m$, des triangles formés pas les sommets $\boldsymbol{e}_k$, sont déterminés puis projetés sur la sphère pour construire les directions $\boldsymbol{s}_m$.

La construction de cette discrétisation se base sur le squelette de l'icosaèdre régulier, présenté dans la figure 3.49. L'icosaèdre régulier possède 12 sommets $\boldsymbol{e}_k$ et 20 surfaces triangulaires. L'ordre 0 de cette discrétisation possède alors 20 directions.

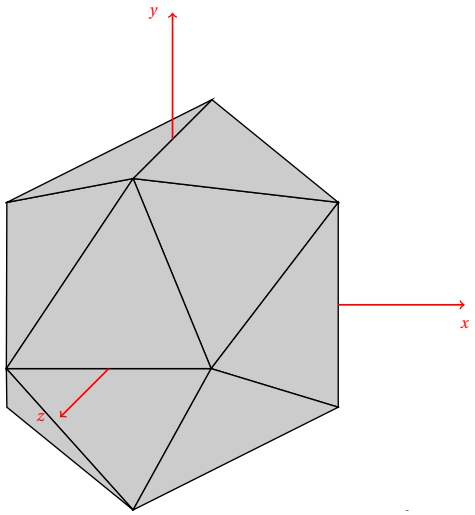

FIGURE 3.49 – Icosaèdre régulier

Pour monter en ordre, chaque triangle est divisé en quatre sous-triangles, avec leurs sommets sur la sphère unité. La figure 3.50 présente le passage de l'ordre 1 à l'ordre 2. À chaque augmentation d'ordre, le nombre de directions est multiplié par 4. Par conséquent, il y a 20×4^n directions pour l'ordre n avec des poids ω_m uniformes, égaux à $4\pi/(20 \times 4^n)$.

Les centres de gravités $\boldsymbol{c}_m$ sont calculés avec la formule (3.63). Les directions $\boldsymbol{s}_m$

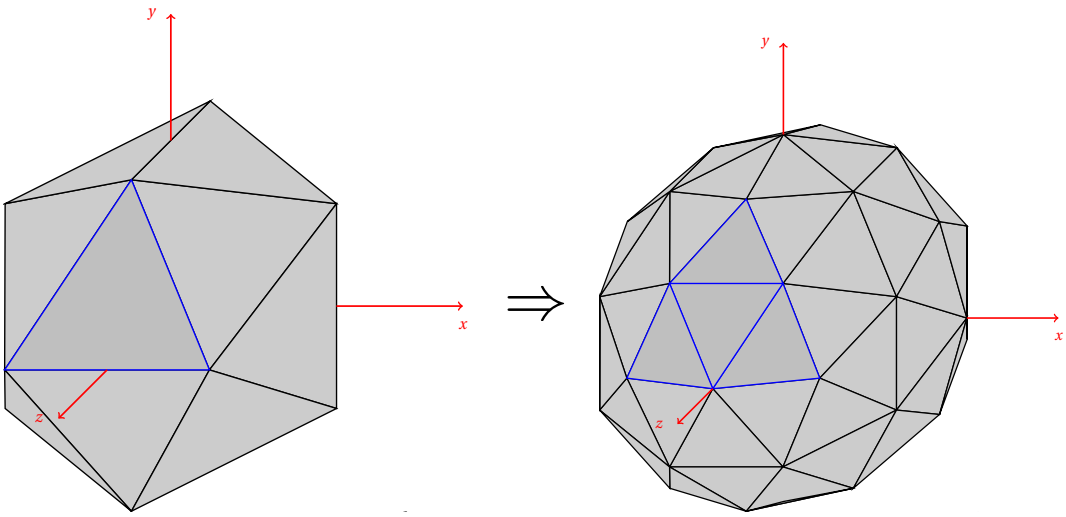

FIGURE 3.50 – Passage de l'ordre 0 à l'ordre 1

sont déterminées par projection sur la sphère des centres de gravités $\boldsymbol{c}_m$ avec la formule (3.64)

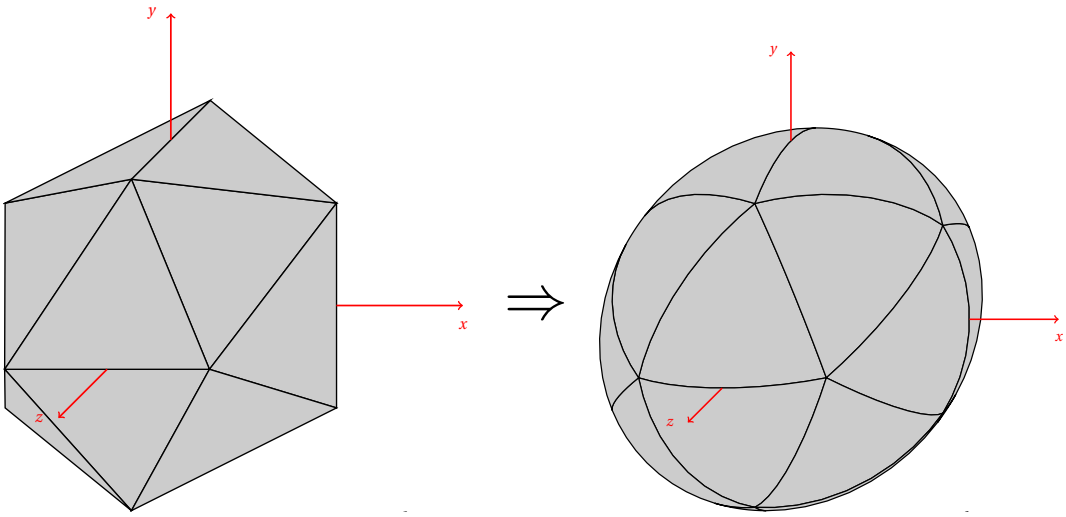

FIGURE 3.51 – Projection pour l'ordre 0

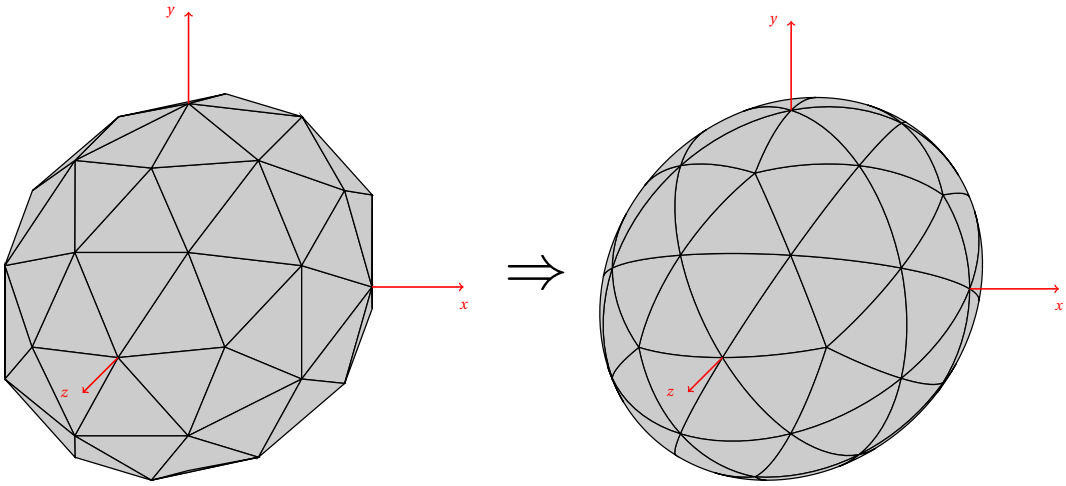

FIGURE 3.52 – Projection pour l'ordre 1

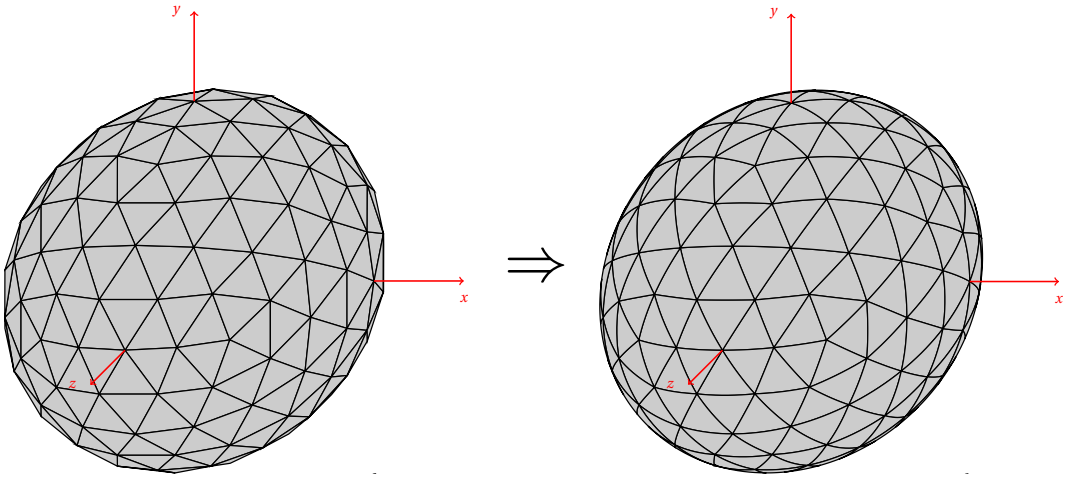

FIGURE 3.53 – Projection pour l'ordre 2

Implémentation

Pour construire la discrétisation à base icosaédrique, définissons les variables suivantes :

$$\begin{cases} n : \text{ ordre de la discrétisation } (0, 1, 2, \cdots) \\ N_d^{(n)} : \text{ nombre de directions à l'ordre } n \\ N_k^{(n)} : \text{ nombre des sommets à l'ordre } n \\ \boldsymbol{e}_k^{(n)} : \text{ liste des sommets à l'ordre } n. \text{ Le tableau 3.4 représente } \boldsymbol{e}_k^0. \\ C^{(n)}(m,l) : \text{ indice du } l^{ieme} \text{ sommet du triangle } m \text{ à l'ordre } n \text{ dans le tableau } \boldsymbol{e}_k^{(n)}. \text{ Le tableau 3.5 représente le tableau d'indices } C^{(0)}(m,l). \\ \boldsymbol{e}_{i,j} : \text{sommet à l'ordre } n \text{ situé entre les sommets } \boldsymbol{e}_{C^{(n-1)}(m,i)}^{(n-1)} \text{ et } \boldsymbol{e}_{C^{(n-1)}(m,j)}^{(n-1)} \\ k_{i,j} : \text{ indice du sommet } \boldsymbol{e}_{i,j} \text{ dans le tableau } \boldsymbol{e}_k^{(n)} \\ Del : \text{ permet de savoir si les directions } e_{i,j} \text{ existent déjà dans le tableau } \boldsymbol{e}_k^{(n)} \text{ ou non} \\ N_{old} : \text{ nombre de directions } \boldsymbol{e}_{i,j} \text{ déjà existantes dans } \boldsymbol{e}_k^{(n)} \\ \phi_g = \dfrac{1+\sqrt{5}}{2} \text{ nombre d'or} \end{cases}$$

La construction de cette discrétisation se base sur le squelette de l'icosaèdre régulier. Une construction manuelle est alors à faire pour l'ordre 0. Définissons le coefficient de normalisation $\alpha = \frac{1}{1+\phi_g^2}$. Les données formant le squelette de l'icosaèdre sont :

- les sommets de l'icosaèdre $\boldsymbol{e}_k$, rangés dans le tableau 3.4,
- la connexion entre les centres de gravités $\boldsymbol{c}_m$ et les sommets $\boldsymbol{e}_k^{(0)}$ détaillée dans le tableau 3.5

Les centres $\boldsymbol{c}_m$ se déterminent avec le tableau 3.5 et la formule (3.63). Ensuite, les directions $\boldsymbol{s}_m$ sont calculées par projection sur la sphère des centre $\boldsymbol{c}_m$, avec la normalisation (3.64). Les angles solides étant uniformes, les poids associés aux directions $\boldsymbol{s}_m$ valent $\omega_m = \frac{4\pi}{20\times 4^n}$.

Algorithm 13: Détermination des nouveaux sommets $\boldsymbol{e}_{0,1}$, $\boldsymbol{e}_{0,2}$ et $\boldsymbol{e}_{1,2}$ par subdivision d'un triangle avec les sommets $\boldsymbol{e}_k^{(n-1)}$

$\boldsymbol{e}_{0,1}$, $\boldsymbol{e}_{0,2}$, $\boldsymbol{e}_{1,2}$;

$\boldsymbol{e}_{0,1} = (\boldsymbol{e}_{C^{(n-1)}(m,0)}^{(n-1)} + \boldsymbol{e}_{C^{(n-1)}(m,1)}^{(n-1)})/||\boldsymbol{e}_{C^{(n-1)}(m,0)}^{(n-1)} + \boldsymbol{e}_{C^{(n-1)}(m,1)}^{(n-1)}||_2$;

$\boldsymbol{e}_{0,2} = (\boldsymbol{e}_{C^{(n-1)}(m,0)}^{(n-1)} + \boldsymbol{e}_{C^{(n-1)}(m,2)}^{(n-1)})/||\boldsymbol{e}_{C^{(n-1)}(m,0)}^{(n-1)} + \boldsymbol{e}_{C^{(n-1)}(m,2)}^{(n-1)}||_2$;

$\boldsymbol{e}_{1,2} = (\boldsymbol{e}_{C^{(n-1)}(m,1)}^{(n-1)} + \boldsymbol{e}_{C^{(n-1)}(m,2)}^{(n-1)})/||\boldsymbol{e}_{C^{(n-1)}(m,1)}^{(n-1)} + \boldsymbol{e}_{C^{(n-1)}(m,2)}^{(n-1)}||_2$;

k	x	y	z
0	$-\alpha$	0	$\phi_g\alpha$
1	$-\alpha$	0	$-\phi_g\alpha$
2	α	0	$\phi_g\alpha$
3	α	0	$-\phi_g\alpha$
4	0	$\phi_g\alpha$	α
5	0	$\phi_g\alpha$	$-\alpha$
6	0	$-\phi_g\alpha$	α
7	0	$-\phi_g\alpha$	$-\alpha$
8	$\phi_g\alpha$	α	0
9	$\phi_g\alpha$	$-\alpha$	0
10	$-\phi_g\alpha$	α	0
11	$-\phi_g\alpha$	$-\alpha$	0

TABLEAU 3.4 – Sommets de l'icosaèdre 3.49

m	m_1	m_2	m_3
0	1	4	0
1	4	9	0
2	4	5	9
3	8	5	4
4	1	8	4
5	1	10	8
6	10	3	8
7	8	3	5
8	3	2	5
9	3	7	2
10	3	10	7
11	10	6	7
12	6	11	7
13	6	0	11
14	6	1	0
15	10	1	6
16	11	0	9
17	2	11	9
18	5	2	9
19	11	2	7

TABLEAU 3.5 – Connexion entre les directions $\boldsymbol{s}_m$ et les sommets $\boldsymbol{e}_k$ pour l'icosaèdre 3.49

Algorithm 14: Verifie si les sommets $\boldsymbol{e}_{0,1}$, $\boldsymbol{e}_{0,2}$ et $\boldsymbol{e}_{1,2}$ existent déjà dans la nouvelle liste

$k_{0,1}$, $k_{0,2}$, $k_{1,2}$, $Del = [0,0,0]$, $N_{old} = 0$;
for $k = N_k^{(n-1)}; k < N_k^{(n)}; k++$ **do**
    if $\boldsymbol{e}_{0,1} = \boldsymbol{e}_k$ **then**
        $k_{0,1} = k$;$Del[0] = 1$; $N_{old}++$;
    end
    if $\boldsymbol{e}_{0,2} = \boldsymbol{e}_k$ **then**
        $k_{0,2} = k$;$Del[1] = 1$; $N_{old}++$;
    end
    if $\boldsymbol{e}_{1,2} = \boldsymbol{e}_k$ **then**
        $k_{1,2} = k$;$Del[2] = 1$; $N_{old}++$;
    end
end

Algorithm 15: Construction de la discrétisation à l'ordre n à l'aide de la discrétisation à l'ordre $n-1$

for $m = 0; m < N_d^{(n-1)}; m++$ **do**
  $Iter = 0$;
  Algo 13 $\rightarrow$ $\boldsymbol{e}_{0,1}$, $\boldsymbol{e}_{0,2}$, $\boldsymbol{e}_{1,2}$;
  Algo 14 $\rightarrow$ $k_{0,1}$, $k_{0,2}$, $k_{1,2}$, Del, N_{old} ;
  if *Del[0]==0* **then**
    $k_{0,1} = N_k^{(n)}$; $Iter++$;
  end
  if *Del[1]==0* **then**
    $k_{0,2} = N_k^{(n)} + Iter$; $Iter++$;
  end
  if *Del[2]==0* **then**
    $k_{1,2} = N_k^{(n)} + Iter$;
  end
  $C^{(n)}(m,0) = k_{0,1}$; $C^{(n)}(m,1) = k_{0,2}$; $C^{(n)}(m,2) = k_{1,2}$;
  $C^{(n)}(N_d^{(n-1)} + 3m, 0) = C^{(n-1)}(m,0)$;
  $C^{(n)}(N_d^{(n-1)} + 3m, 1) = k_{0,1}$;
  $C^{(n)}(N_d^{(n-1)} + 3m, 2) = k_{0,2}$;
  $C^{(n)}(N_d^{(n-1)} + 3m + 1, 0) = k_{0,1}$;
  $C^{(n)}(N_d^{(n-1)} + 3m + 1, 1) = C^{(n-1)}(m,1)$;
  $C^{(n)}(N_d^{(n-1)} + 3m + 1, 2) = k_{1,2}$;
  $C^{(n)}(N_d^{(n-1)} + 3m + 2, 0) = k_{0,2}$;
  $C^{(n)}(N_d^{(n-1)} + 3m + 2, 1) = k_{1,2}$;
  $C^{(n)}(N_d^{(n-1)} + 3m + 2, 2) = C^{(n-1)}(m,2)$;
  $\boldsymbol{e}_{k_{0,1}}^{(n)} = e_{0,1}$;
  $\boldsymbol{e}_{k_{0,2}}^{(n)} = e_{0,2}$;
  $\boldsymbol{e}_{k_{1,2}}^{(n)} = e_{1,2}$;
  $N_k^{(n)} += 3 - N_{old}$;
end

Algorithm 16: Construction des directions $\boldsymbol{s}_m$ pour l'ordre n

for $m = 0; m < N_d^{(n)}; m++$ **do**
  $\boldsymbol{s}_m = \boldsymbol{e}_{C^{(n)}(m,0)}^{(n)} + \boldsymbol{e}_{C^{(n)}(m,1)}^{(n)} + \boldsymbol{e}_{C^{(n)}(m,2)}^{(n)}$;
  $\boldsymbol{s}_m = \boldsymbol{s}_m / ||\boldsymbol{s}_m||_2$;
end

Références

[1] E. Lewis, W. Miller, Computational methods of neutron transport, John Wiley and Sons, Inc., New York, NY, 1984. 63

[2] J. Howell, R. Siegel, M. Mengüç, Thermal Radiation Heat Transfer, CRC press, 2011. 63, 66, 70

[3] M. Modest, Radiative heat transfer, 3rd Edition, Academic press, New York, 2013. 63, 66, 71

[4] L. Wang, H.-i. Wu, Biomedical optics : principles and imaging, John Wiley & Sons, 2012. 63

[5] C.-J. Winter, R. Sizmann, L. Vant-Hull, Solar power plants : fundamentals, technology, systems, economics, Springer Science & Business Media, 2012. 63

[6] S. Guévelou, B. Rousseau, G. Domingues, J. Vicente, C. Caliot, Representative elementary volumes required to characterize the normal spectral emittance of silicon carbide foams used as volumetric solar absorbers, International Journal of Heat and Mass Transfer 93 (2016) 118–129. 63, 94, 98

[7] J. Spanier, E. Gelbard, Monte Carlo principles and neutron transport problems, Reading, Mass., USA. 64

[8] J. Howell, The Monte Carlo method in radiative heat transfer, Journal of Heat Transfer 120 (3) (1998) 547–560. 64

[9] M. Cherkaoui, J.-L. Dufresne, R. Fournier, J.-Y. Grandpeix, A. Lahellec, Monte Carlo simulation of radiation in gases with a narrow-band model and a net-exchange formulation, Journal of Heat Transfer 118 (2) (1996) 401–407. 64

[10] J. Dauchet, S. Blanco, J.-F. Cornet, M. El Hafi, V. Eymet, R. Fournier, The practice of recent radiative transfer Monte Carlo advances and its contribution to the field of microorganisms cultivation in photobioreactors, Journal of Quantitative Spectroscopy and Radiative Transfer 128 (2013) 52–59. 64

[11] M. Roger, C. Caliot, N. Crouseilles, P. Coelho, A hybrid transport-diffusion model for radiative transfer in absorbing and scattering media, Journal of Computational Physics 275 (2014) 346–362. 64

[12] J. Willert, H. Park, Residual Monte Carlo high-order solver for Moment-Based Accelerated Thermal Radiative Transfer equations, Journal of Computational Physics 276 (2014) 405–421. 64

[13] J. Densmore, K. Thompson, T. Urbatsch, A hybrid transport-diffusion Monte Carlo method for frequency-dependent radiative-transfer simulations, Journal of Computational Physics 231 (20) (2012) 6924–6934. 64

[14] T. Yamamoto, H. Sakamoto, Frequency domain optical tomography using a Monte Carlo perturbation method, Optics Communications 364 (2016) 165–176. 64

[15] J. Briesmeister, et al., MCNPTM – a general Monte Carlo N-Particle transport code, Version 4C, LA-13709-M, Los Alamos National Laboratory. 64

[16] J. Leppänen, SERPENT –a continuous-energy Monte Carlo reactor physics burnup calculation code, VTT Technical Research Centre of Finland 4. 64

[17] J. Wagner, D. Peplow, S. Mosher, FW-CADIS method for global and regional variance reduction of Monte Carlo radiation transport calculations, Nuclear Science and Engineering 176 (1) (2014) 37–57. 64

[18] W. Fiveland, Discrete-ordinates solutions of the radiative transport equation for rectangular enclosures, Journal of Heat Transfer 106 (4) (1984) 699–706. 64, 66

[19] J. Chai, H. Lee, S. Patankar, Finite volume method for radiation heat transfer, Journal of Thermophysics and Heat Transfer 8 (3) (1994) 419–425. 64

[20] P. Coelho, A hybrid finite volume/finite element discretization method for the solution of the radiative heat transfer equation, Journal of Quantitative Spectroscopy and Radiative Transfer 93 (1) (2005) 89–101. 64

[21] M. Charest, C. Groth, Ö. Gülder, Solution of the equation of radiative transfer using a Newton–Krylov approach and adaptive mesh refinement, Journal of Computational Physics 231 (8) (2012) 3023–3040. 64

[22] P. Coelho, Advances in the discrete ordinates and finite volume methods for the solution of radiative heat transfer problems in participating media, Journal of Quantitative Spectroscopy and Radiative Transfer 145 (2014) 121–146. 64

[23] F. Hecht, New development in FreeFem++, Journal of Numerical Mathematics 20 (3-4) (2012) 251–266. 64

[24] O. Balima, Y. Favennec, J. Boulanger, A. Charette, Optical tomography with the discontinuous galerkin formulation of the radiative transfer equation in frequency domain, Journal of Quantitative Spectroscopy and Radiative Transfer 113 (10) (2012) 805–814. 64

[25] O. Balima, Y. Favennec, D. Rousse, Optical tomography reconstruction algorithm with the finite element method : An optimal approach with regularization tools, Journal of Computational Physics 25 (1) (2013) 461–479. 64

[26] D. Le Hardy, Y. Favennec, B. Rousseau, Solution of the 2-D steady-state radiative transfer equation in participating media with specular reflections using SUPG and DG finite elements, Journal of Quantitative Spectroscopy and Radiative Transfer 179 (2016) 149–164. 64, 66, 69

[27] H. Gao, H. Zhao, A fast-forward solver of radiative transfer equation, Transport Theory and Statistical Physics 38 (3) (2009) 149–192. 64, 69

[28] H. Gao, H. Zhao, Analysis of a numerical solver for radiative transport equation, Mathematics of Computation 82 (281) (2013) 153–172. 64

[29] X. He, E. Lee, L. Wilcox, R. Munipalli, L. Pilon, A High-Order-Accurate GPU-Based Radiative Transfer Equation Solver for Combustion and Propulsion Applications, Numerical Heat Transfer, Part B : Fundamentals 63 (6) (2013) 457–484. 64

[30] O. Lehtikangas, T. Tarvainen, A. Kim, S. Arridge, Finite element approximation of the radiative transport equation in a medium with piece-wise constant refractive index, Journal of Computational Physics 282 (2015) 345–359. 64

[31] A. Buchan, A. Candy, S. Merton, C. Pain, J. Hadi, M. Eaton, A. Goddard, R. Smedley-Stevenson, G. Pearce, The inner-element subgrid scale finite element method for the Boltzmann transport equation, Nuclear Science and Engineering 164 (2) (2010) 105–121. 64, 66

[32] R. Castro, J. Trelles, Spatial and angular finite element method for radiative transfer in participating media, Journal of Quantitative Spectroscopy and Radiative Transfer 157 (2015) 81–105. 65, 66, 93, 94

[33] C. Lee, The discrete Sn approximation to transport theory, Tech. rep., Los Alamos Scientific Lab., N. Mex. (1961). 66, 67, 110, XIV

[34] C. Thurgood, A. Pollard, H. Becker, The TN quadrature set for the discrete ordinates method, Journal of heat transfer 117 (4) (1995) 1068–1070. 66, 67, 106, 110, 126, XIV

[35] V. Lebedev, Quadratures on a sphere, USSR Computational Mathematics and Mathematical Physics 16 (2) (1976) 10–24. 66

[36] W. Fiveland, Three-dimensional radiative heat-transfer solutions by the discrete-ordinates method, Journal of Thermophysics and Heat Transfer 2 (4) (1988) 309–316. 66

[37] V. Fiveland, J. Jessee, Acceleration schemes for the discrete ordinates method, Journal of Thermophysics and Heat Transfer 10 (3) (1996) 445–451. 66

[38] H. Fujii, S. Okawa, Y. Yamada, Y. Hoshi, Hybrid model of light propagation in random media based on the time-dependent radiative transfer and diffusion equations, Journal of Quantitative Spectroscopy and Radiative Transfer 147 (2014) 145–154. 66

[39] T. Tarvainen, M. Vauhkonen, V. Kolehmainen, J. Kaipio, Finite element model for the coupled radiative transfer equation and diffusion approximation, International Journal for Numerical Methods in Engineering 65 (3) (2006) 383–405. 66

[40] J. Zhao, L. Liu, Second-order radiative transfer equation and its properties of numerical solution using the finite-element method, Numerical Heat Transfer, Part B : Fundamentals 51 (4) (2007) 391–409. 66

[41] O. Balima, T. Pierre, A. Charette, D. Marceau, A least square finite element formulation of the collimated irradiation in frequency domain for optical tomography applications, Journal of Quantitative Spectroscopy and Radiative Transfer 111 (2) (2010) 280–286. 66

[42] Y. Zhang, H.-L. Yi, H.-P. Tan, Least-squares natural element method for radiative heat transfer in graded index medium with semitransparent surfaces, International Journal of Heat and Mass Transfer 66 (2013) 349–354. 66

[43] A. Pulkkinen, T. Tarvainen, Truncated Fourier-series approximation of the time-domain radiative transfer equation using finite elements, Optical Society of America A 30 (3) (2013) 470–478. 66

[44] R. Becker, R. Koch, H.-J. Bauer, M. Modest, A finite element treatment of the angular dependency of the even-parity equation of radiative transfer, Journal of Heat Transfer 132 (2) (2010) 023404. 66

[45] J. Morel, J. McGhee, A self-adjoint angular flux equation, Nuclear Science and Engineering 132 (3) (1999) 312–325. 66

[46] J. Morel, B. Adams, T. Noh, J. McGhee, T. Evans, T. Urbatsch, Spatial discretizations for self-adjoint forms of the radiative transfer equations, Journal of Computational Physics 214 (1) (2006) 12–40. 66

[47] J. Hansen, J. Peterson, J. Morel, J. Ragusa, Y. Wang, A Least-Squares Transport Equation Compatible with Voids, Journal of Computational and Theoretical Transport 43 (1-7) (2014) 374–401. 66

[48] Y. Wang, F. Gleicher, Revisit boundary conditions for the self-adjoint angular flux formulation. 66, 77

[49] V. Laboure, R. McClarren, Y. Wang, Globally Conservative, Hybrid Self-Adjoint Angular Flux and Least-Squares Method Compatible with Void, Nuclear Science and Engineering. 66, 77

[50] J. Zhao, J. Tan, L. Liu, A second order radiative transfer equation and its solution by meshless method with application to strongly inhomogeneous media, Journal of Computational Physics 232 (1) (2013) 431–455. 66, 67

[51] H. Sadat, C.-A. Wang, V. Le Dez, Meshless method for solving coupled radiative and conductive heat transfer in complex multi-dimensional geometries, Applied Mathematics and Computation 218 (20) (2012) 10211–10225. 66

[52] P. Coelho, N. Crouseilles, P. Pereira, M. Roger, Multi-scale methods for the solution of the radiative transfer equation, Journal of Quantitative Spectroscopy and Radiative Transfer 172 (2016) 36–49. 66

[53] D. Balsara, Fast and accurate discrete ordinates methods for multidimensional radiative transfer. part i, basic methods, Journal of Quantitative Spectroscopy and Radiative Transfer 69 (6) (2001) 671–707. 66

[54] P. Boulet, A. Collin, J. Consalvi, On the finite volume method and the discrete ordinates method regarding radiative heat transfer in acute forward anisotropic scattering media, Journal of Quantitative Spectroscopy and Radiative Transfer 104 (3) (2007) 460–473. 66

[55] M. Gazdallah, V. Feldheim, K. Claramunt, C. Hirsch, Finite volume method for radiative heat transfer in an unstructured flow solver for emitting, absorbing and scattering media, in : Journal of Physics : Conference Series, Vol. 369, IOP Publishing, 2012, p. 012020. 66

[56] H. Grissa, F. Askri, M. Salah, S. Nasrallah, Three-dimensional radiative transfer modeling using the control volume finite element method, Journal of Quantitative Spectroscopy and Radiative Transfer 105 (3) (2007) 388–404. 66

[57] B. Ramamoorthy, G. Cheng, R. Koomullil, R. Rahmani, Finite volume method for non-equilibrium radiative heat transfer, International Journal of Heat and Mass Transfer 65 (2013) 670–681. 66

[58] F. Asllanaj, A. Addoum, S. Contassot-Vivier, Detection of tumor-like inclusions embedded within human liver tissue using a short-pulsed near-infrared laser beam : Parallel simulations with radiative transfer equation, Journal of Quantitative Spectroscopy and Radiative Transfer 165 (2015) 1–11. 66

[59] M. Marin, F. Asllanaj, D. Maillet, Sensitivity analysis to optical properties of biological tissues subjected to a short-pulsed laser using the time-dependent radiative transfer equation, Journal of Quantitative Spectroscopy and Radiative Transfer 133 (2014) 117–127. 66

[60] K. Ren, G. Abdoulaev, G. Bal, A. Hielscher, Algorithm for solving the equation of radiative transfer in the frequency domain, Optics letters 29 (6) (2004) 578–580. 66

[61] K. Ren, G. Bal, A. Hielscher, Frequency domain optical tomography based on the equation of radiative transfer, SIAM Journal on Scientific Computing 28 (4) (2006) 1463–1489. 66

[62] M. Adams, E. Larsen, Fast iterative methods for discrete-ordinates particle transport calculations, Progress in Nuclear Energy 40 (1) (2002) 3–159. 66

[63] W. Fiveland, The selection of discrete ordinate quadrature sets for anisotropic scattering, Fundamentals of Radiation Heat Transfer 160 (1991) 89–96. 66, 110

[64] J. Truelove, Three-dimensional radiation in absorbing-emitting-scattering media using the discrete-ordinates approximation, Journal of Quantitative Spectroscopy and Radiative Transfer 39 (1) (1988) 27–31. 66

[65] J. Zhao, J. Tan, L. Liu, A deficiency problem of the least squares finite element method for solving radiative transfer in strongly inhomogeneous media, Journal of Quantitative Spectroscopy and Radiative Transfer 113 (12) (2012) 1488–1502. 67

[66] T. Yin, J.-P. Gastellu-Etchegorry, N. Lauret, E. Grau, J. Rubio, A new approach of direction discretization and oversampling for 3D anisotropic radiative transfer modeling, Remote Sensing of Environment 135 (2013) 213–223. 69

[67] P. Bochev, M. Gunzburger, J. Shadid, Stability of the SUPG finite element method for transient advection–diffusion problems, Computer Methods in Applied Mechanics and Engineering 193 (23) (2004) 2301–2323. 76

[68] G. Kanschat, E. Meinköhn, R. Rannacher, R. Wehrse, Numerical methods in multidimensional radiative transfer, Springer, 2009. 77

[69] L. Léger, L. Chevallier, F. Paletou, Fast 2D non–LTE radiative modelling of prominences-numerical methods and benchmark results, Astronomy & Astrophysics 470 (1) (2007) 1–9. 77

[70] C. Geuzaine, J.-F. Remacle, Gmsh : A 3-D finite element mesh generator with built-in pre-and post-processing facilities, International Journal for Numerical Methods in Engineering 79 (11) (2009) 1309–1331. 80, 98

[71] A. Klose, A. Hielscher, Quasi-Newton methods in optical tomographic image reconstruction, Inverse Problems 19 (2) (2003) 387. 85

[72] F. Dubot, Y. Favennec, B. Rousseau, D. Rousse, A wavelet multi-scale method for the inverse problem of diffuse optical tomography, Journal of Computational and Applied Mathematics 289 (2015) 267–281. 85

[73] Y. Favennec, F. Dubot, D. Le Hardy, B. Rousseau, D. Rousse, Space-Dependent Sobolev Gradients as a Regularization for Inverse Radiative Transfer Problems, Mathematical Problems in Engineering 2016. 85

[74] V. Le Dez, H. Sadat, On the radiative heat transfer in a semi-transparent medium enclosed in a cylindrical annulus of infinite length with specularly reflecting lateral surfaces, Applied Mathematical Modelling 40 (1) (2016) 150–168. 91

[75] T. Kodama, High-temperature solar chemistry for converting solar heat to chemical fuels, Progress in Energy and Combustion Science 29 (6) (2003) 567–597. 93

[76] S. Lorentzou, G. Karagiannakis, C. Pagkoura, A. Zygogianni, A. Konstandopoulos, Thermochemical CO_2 and CO_2/H_2O splitting over $NiFe_2O_4$ for solar fuels synthesis, Energy Procedia 49 (2014) 1999–2008. 93

[77] C. Agrafiotis, H. von Storch, M. Roeb, C. Sattler, Solar thermal reforming of methane feedstocks for hydrogen and syngas production — a review, Renewable and Sustainable Energy Reviews 29 (2014) 656–682. 93

[78] J. Ahrens, B. Geveci, C. Law, C. Hansen, C. Johnson, Paraview : An End-User Tool for Large-Data Visualization (2005). 98

Chapitre 4

Exploitation : Géometries complexes et Couplage

Sommaire

Avant-propos

Les deux chapitres précédents ont permis de construire un outil numérique capable de résoudre l'ETR dans des matériaux à géométrie complexe.

Dans ce chapitre, trois études plus expérimentales ont été faites :

— La première étude est une comparaison des transmittances normales- hémisphériques et des réflectances normales-hémisphériques avec deux autres méthodes numériques : une méthode Monte-Carlo [1] et la méthode à deux flux modifiée [2], toutes deux étudiées lors de deux stages de Master 2 [1] que j'ai partiellement encadré. Cette étude a pour but de montrer la robustesse de notre outil numérique en se basant sur la référence Monte-Carlo.

— La deuxième étude est un article étendu de la conférence "Theoretical and Computational Physic" à Xi'an, publié dans "Journal of Applied Mathematics and Physics" en août 2016. Il traite le couplage conducto-radiatif dans une géométrie parabolique en 3 dimensions en espace. Cette étude a été faite pour mettre en évidence l'importance de la prise en compte des conditions aux limites en surface.

— La dernière étude est un article, accepté le 2 mars 2017 dans "Journal of Quantitative Spectroscopy and Radiative Transfer". Il traite sur l'effet des propriétés radiatifs sur l'évolution du rayonnement dans un ligament de mousses à pores ouverts (porosité=80%). Cette étude montre, aussi, l'importance de l'effet de la géométrie du ligament

1. International Master Degrees, Thermalscience and Energy ,Polytech'Nantes

4.1 Comparaisons avec une méthode Monte-Carlo et une méthode à deux-flux, en terme de transmittances et réflectances

Pour déterminer des transmittances et réflectances, la méthode de Monte-Carlo est souvent la méthode de référence. Cependant, les méthodes d'ordonnées discrètes peuvent aussi être appliquées. Dans cette section, la méthode SUPG sera comparée à une méthode Monte-Carlo [1] et à une méthode à deux-flux modifiée [2]. Ces travaux ont été réalisés dans le cadre de deux stages, que j'ai encadrés partiellement. Le premier stage s'est déroulé en 2015 avec l'étudiante de master 2 Mme Ketaki Mishra. Ce stage portait sur la construction d'un code Monte-Carlo dans un cube avec des conditions spéculaires aux surfaces. Le deuxième stage, réalisé par l'étudiant en master 2 Mr Akshansh Kataria en 2016, portait sur l'étude de la méthode à deux-flux modifiée [2]. Ces deux méthodes sont détaillées en Annexes A et B.

Dans cette section, le calcul des transmittances normales-hémisphériques et des réflectances normales-hémisphériques est expliqué pour les trois méthodes étudiées. Ensuite, la méthode Monte-Carlo et la méthode à deux flux sont comparées à l'échelle 1D. Enfin, la méthode SUPG et la méthode à deux flux sont comparées à la méthode Monte-Carlo, à l'échelle 3D, pour montrer d'une part l'efficacité de la méthode SUPG, et d'autre part la limite de la méthode à deux flux.

4.1.1 Transmittances et réflectances

Les transmittances et réflectances sont des rapports entre les flux transmis/réfléchis et les flux entrants. En supposant que le flux incident entre dans la direction $\boldsymbol{s}_0$ sur une surface Γ_0 de normales $\boldsymbol{n}_0$, et que le flux transmis sort par une surface Γ_1 de normale $\boldsymbol{n}_1$, les transmittances et réflectances normales-hémisphériques R_{NH} et T_{NH} sont déterminées par :

$$\begin{cases} R_{\text{NH}} = \dfrac{\displaystyle\int_{\Gamma_0} Q^-(\boldsymbol{x})\ \mathrm{d}\boldsymbol{x}}{\displaystyle\int_{\Gamma_0} E(\boldsymbol{x})\ \mathrm{d}\boldsymbol{x}} + \rho_s(\boldsymbol{s}_0 \cdot \boldsymbol{n}_0) \\ T_{\text{NH}} = \dfrac{\displaystyle\int_{\Gamma_1} Q^-(\boldsymbol{x})\ \mathrm{d}\boldsymbol{x}}{\displaystyle\int_{\Gamma_0} E(\boldsymbol{x})\ \mathrm{d}\boldsymbol{x}} \end{cases} \tag{4.1}$$

où $E(\boldsymbol{x})$ est l'éclairement (1.15) et $Q^-(\boldsymbol{x})$ est le flux sortant (1.14).

Pour la méthode Monte-Carlo, la réflectance R_{NH} se détermine par :

$$R_{\text{NH}}^{\text{MC}} = \frac{\text{Nombre de photons réfléchis et sortants par } \Gamma_0}{\text{Nombre de photons total } N_p} \tag{4.2}$$

De manière analogue, la transmittance $T_{\text{NH}}^{\text{MC}}$ est le rapport entre le nombre de photons traversant Γ_1 et le nombre de photons total N_p.

Pour les méthodes de discrétisations spatiales combinées aux ordonnées discrètes, la réflectance R_{NH} est approchée par :

$$R_{\mathrm{NH}}^{\mathrm{DOM}} = \frac{\sum\limits_{\boldsymbol{s}_m \cdot \boldsymbol{n}_0 > 0} \omega_m \int_{\Gamma_0} I_m(\boldsymbol{x}) \boldsymbol{s}_m \cdot \boldsymbol{n}_0 \, \mathrm{d}\boldsymbol{x}}{|\boldsymbol{s}_0 \cdot \boldsymbol{n}_0| \int_{\Gamma_0} \tilde{I}_0(\boldsymbol{x}) \, \mathrm{d}\boldsymbol{x}} + \rho_s(\boldsymbol{s}_0 \cdot \boldsymbol{n}_0) \tag{4.3}$$

La transmittance T_{NH} est déterminée de manière analogue :

$$T_{\mathrm{NH}}^{\mathrm{DOM}} = \frac{\sum\limits_{\boldsymbol{s}_m \cdot \boldsymbol{n}_1 > 0} \omega_m \int_{\Gamma_1} I_m(\boldsymbol{x}) \boldsymbol{s}_m \cdot \boldsymbol{n}_1 \, \mathrm{d}\boldsymbol{x}}{|\boldsymbol{s}_0 \cdot \boldsymbol{n}_0| \int_{\Gamma_0} \tilde{I}_0(\boldsymbol{x}) \, \mathrm{d}\boldsymbol{x}} \tag{4.4}$$

D'autre part, la méthode à deux-flux modifiée donne une approximation analytique des transmittances et réflectances normales-hémisphériques. Celles-ci sont divisées en deux parties : la partie collimaté et la partie diffuse :

$$\begin{cases} T_{\mathrm{NH}}^{\mathrm{2F}} = T_{\mathrm{NH}}^{c} + T_{\mathrm{NH}}^{d} \\ R_{\mathrm{NH}}^{\mathrm{2F}} = R_{\mathrm{NH}}^{c} + R_{\mathrm{NH}}^{d} \end{cases} \tag{4.5}$$

qui sont détaillées dans l'annexe B.

4.1.2 Comparaisons 1D

Pour une comparaison 1D, le domaine d'étude est composé d'une couche mince isotrope d'épaisseur $x_0 = 1\mathrm{cm}$ et de longueur et hauteur infinies. Le milieu est supposé isotrope. Deux comparaisons sont faites : la première où T_{NH} et R_{NH} s'expriment en fonction du coefficient de diffusion σ_s, avec κ et n fixés ; et la deuxième où T_{NH} et R_{NH} s'expriment en fonction de l'indice de réfraction n, avec κ et σ_s fixés.

T_{NH} et R_{NH} en fonction de σ_s

Dans le premier cas test, on suppose que $\kappa = 0{,}5\ \mathrm{cm}^{-1}$, $\sigma_s \in [0, 2]\ \mathrm{cm}^{-1}$ et $n = 1{,}4$. La figure 4.1 présente l'évolution de T_{NH} et R_{NH} en fonction du coefficient de diffusion σ_s, pour la méthode Monte-Carlo ainsi que la méthode à deux-flux.

Quand σ_s augmente, une plus grande proportion de photons est déviée avant d'atteindre la surface opposée. Par conséquent la transmittance décroît lorsque le coefficient de diffusion σ_s augmente. La figure 4.1 montre bien la diminution de T_{NH} en fonction de σ_s.

De plus, quand le coefficient de diffusion augmente, les photons ont plus tendance à être déviés à proximité de la paroi d'entrée. Il y a donc en moyenne plus de photons diffusés vers l'arrière, ce qui contribue à l'augmentation de R_{NH}. La figure 4.1 montre

l'augmentation de la réflectance R_{NH} en fonction de σ_s, autant pour la méthode Monte-Carlo que pour la méthode à deux-flux.

La figure 4.1 présente l'ensemble des résultats, pour les transmittances et réflectances, pour les deux méthodes, pour $\sigma_s \in [0, 2]$ cm^{-1}. On voit que les deux méthodes donnent des résultats très proches, avec un écart qui augmente cependant légèrement avec σ_s.

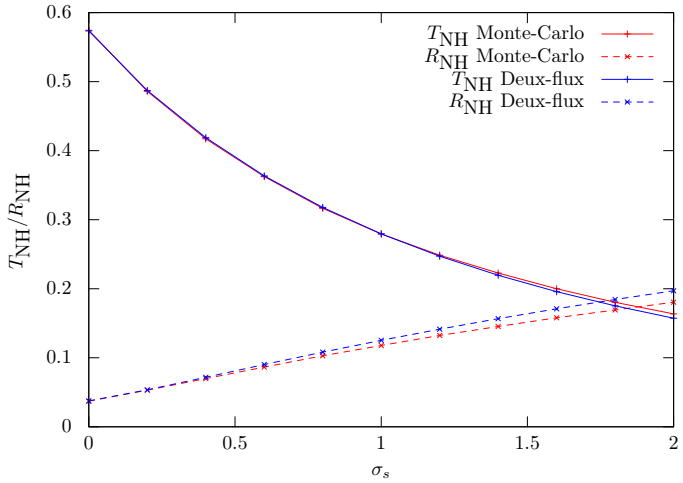

FIGURE 4.1 – Comparaison 1D : T_{NH} et R_{NH} en fonction de σ_s en 1 dimension. $x_0 = 1$ cm, $\kappa = 0{,}5$ cm^{-1} et $n = 1{,}4$.

T_{NH} et R_{NH} en fonction de n

Dans le deuxième cas test, on suppose que $\kappa = 0{,}5$ cm^{-1}, $\sigma_s = 1$ cm^{-1} et $n \in [1, 2]$. La figure 4.2 montre l'évolution de T_{NH} et R_{NH} en fonction de l'indice de réfraction n, pour la méthode Monte-Carlo ainsi que pour la méthode à deux-flux.

Lorsque l'indice de réfraction augmente, les photons sont de plus en plus réfléchis sur la surface d'impact. Par conséquent la réflectance R_{NH} est censée augmenter en même temps que l'indice de réfraction. Cependant, peut-être dû à l'effet de la diffusion, la réflectance décroît pour les indices de réfraction $n \in [1, 1.5]$ puis augmente ensuite. De plus, comme il y a plus de photons réfléchis à l'entrée, alors moins de photons sont réfractés. Par conséquent la transmittance T_{NH} décroît quand l'indice de réfraction augmente, avec ou sans diffusion.

Entre la méthode à deux-flux et la méthode Monte-Carlo, l'écart le plus important se situe au niveau des indices de réfraction faibles $n \in [1, 1.5]$. Pour des indices n plus grands, l'écart se réduit. La réduction de l'écart pourrait être dû aux parties collimatées T^c_{NH} et R^c_{NH} de la méthode à deux flux, qui sont exactes et qui prennent plus d'importance que les parties diffuses T^d_{NH} et R^d_{NH} pour le calcul de T^{2F}_{NH} et R^{2F}_{NH}.

Comparée à la méthode Monte-Carlo, la méthode à deux flux est efficace pour une couche mince. Cependant, pour des études en 3 dimensions, cette méthode devient limitée, comme nous allons le voir dans les tests suivants.

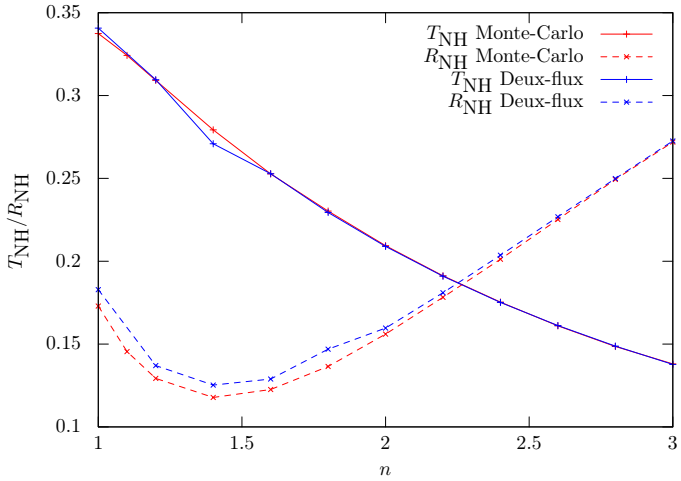

FIGURE 4.2 – Comparaison 1D : T_{NH} et R_{NH} en fonction de n. $x_0 = 1$ cm, $\kappa = 0{,}5$ cm^{-1} et $\sigma_s = 1$ cm^{-1}.

4.1.3 Comparaisons 3D

Pour les études 3D, le domaine est un cube de cotés $x_0 = 1$ cm, supposant une diffusion isotrope. Un faisceau lumineux homogène et collimaté impacte la globalité d'une des surfaces. La méthode à deux-flux, la méthode SUPG et la méthode Monte-Carlo sont comparées autour de différent tests.

T_{NH} et R_{NH} en fonction de σ_s

Dans le premier test, T_{NH} et R_{NH} sont exprimées en fonction du coefficient de diffusion σ_s pour $\kappa = 0{,}5$ cm^{-1} et $n = 1{,}4$. La figure 4.3 montre leurs évolutions pour chacune des méthodes en fonction de $\sigma_s \in [0, 1]$.

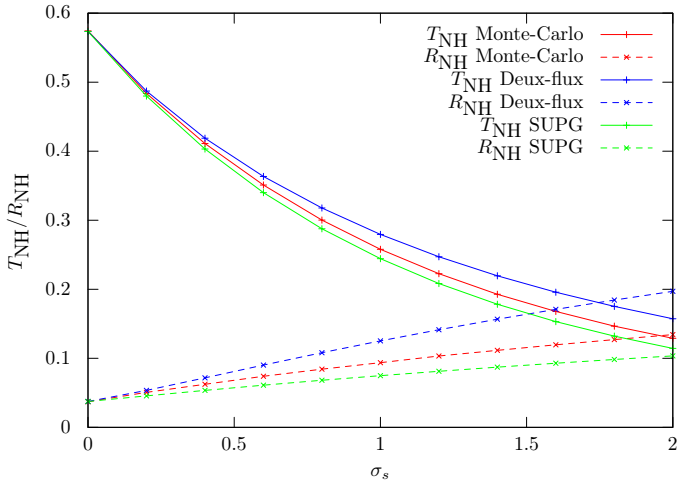

FIGURE 4.3 – Comparaison 3D : T_{NH} et R_{NH} en fonction de σ_s pour $\kappa = 0{,}5$ cm^{-1} et $n = 1{,}4$.

Sans terme de diffusion, la méthode à deux flux est exacte car seule sa partie collimatée, déterminée analytiquement, est prise en compte. Par contre, lorsque σ_s augmente, les transmittances et réflectances de la méthode à deux-flux sont plus grandes que pour

les deux autres méthodes. La valeur des transmittances et des réflectances entre l'étude 1D et l'étude 3D baisse à cause des transmittances au niveau des parois latérales. La solution de la méthode SUPG est plus faible que la solution de la méthode Monte-Carlo, et l'écart grandit lorsque σ_s augmente. L'erreur reste cependant raisonnable : pour $\sigma_s = 2$ cm^{-1}, on a une différence entre les deux solutions de 0,015 pour T_{NH} et de 0,031 pour R_{NH}.

T_{NH} et R_{NH} en fonction de n

Le deuxième test étudie un matériau cubique ayant comme propriétés radiatives $\kappa = 0{,}5$ cm^{-1} et $\sigma_s = 1$ cm^{-1}, et comme propriété optique $n \in [1, 3]$. La figure 4.4 décrit l'évolution de T_{NH} et R_{NH} en fonction de l'indice de réfraction n.

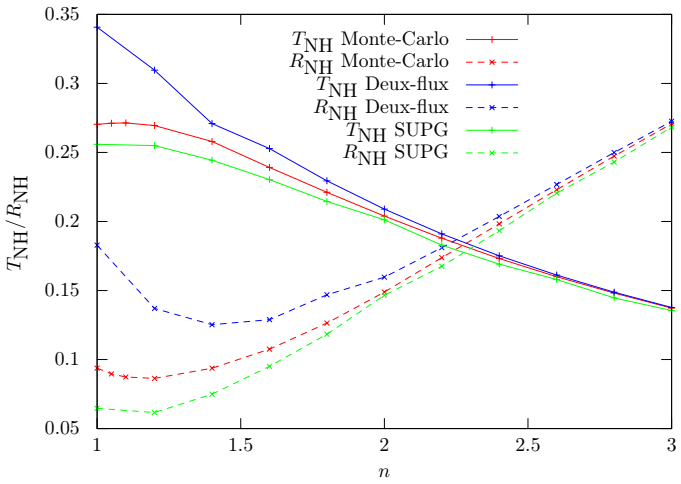

FIGURE 4.4 – Comparaison 3D : T_{NH} et R_{NH} en fonction de n pour $\kappa = 0{,}5$ cm^{-1} et $\sigma_s = 1$ cm^{-1}.

La méthode à deux-flux fournit des résultats nettement différents de ceux provenance de la méthode Monte-Carlo de la méthode SUPG. Plus l'indice de réfraction est faible, moins la méthode à deux-flux est pertinente dû aux transmittances latérales. Par contre, on peut observer que pour des forts indices de réfraction ($n > 2$) les trois méthodes se rejoignent. En effet, plus l'indice est élevé, moins il y a de pertes latérales. Donc, pour le cas spéculaire, les solutions de l'étude 3D tendent vers les solutions de l'étude 1D. Aussi pour ce test, la solution SUPG est plus faible que la solution de la méthode Monte-Carlo : pour $n = 1$, on a une différence de 0,015 pour T_{NH} et un différence de 0,029 pour R_{NH} entre les deux solutions. Toutefois l'écart entre la méthode SUPG et la méthode Monte-Carlo reste modéré. La différence pourrait provenir du code Monte-Carlo, code maison relativement basique, ou peut-être encore de la partie "post-processing" de la méthode SUPG, pour le calcul de T_{NH} et de R_{NH}.

4.2 Article 3 : "3D radiative transfer equation coupled with heat conduction equation with realistic boundary conditions applied on complex geometries" (*publié en août 2016 dans JAMP*)

D. Le Hardy , Y. Favennec , G. Domingues, B. Rousseau

LTN UMR CNRS 6607, Université de Nantes, France

Abstract

This paper presents the solution of coupled radiative transfer equation with heat conduction equation in complex three-dimensional geometries. Due to very different time scales for both physics, the radiative problem is considered steady-state but solved at each time iteration of the transient conduction problem. The discrete ordinate method along with the decentered stream- line-upwind Petrov-Galerkin method is developed. Since specular reflection is considered on bor- ders, a very accurate algorithm has been developed for calculation of partition ratio coefficients of incident solid angles to the several reflected solid angles. The developed algorithms are tested on a paraboloid-shaped geometry used for example on concentrated solar power technologies.

Keywords : Radiative transfer equation, Heat conduction equation, Finite element methods, SUPG, DOM, specular reflection, complex geometry

4.2.1 Introduction

The study of the thermal and radiative heat transfer in semitransparent media plays an important role for industrial applications such as thermal insulation [3], photothermal therapy [4], glass forming [5, 6] , porous media [7] and many others [8]. The steady thermal equation is commonly used to give a global and sometimes sufficient solution [9, 10] but, in some applications [4, 5], the knowledge of the evolution of the thermal heat transfer is necessary.

The coupling takes into account of the steady-state radiative transfer equation (RTE), as well as the transient heat conduction equation (HCE). Such a transient coupling is well derived in [11, 12]. The RTE is an integro-differential equation that contains an advection term and also an angular integral term corresponding to a gain by scattering. Deterministic and statistical methods are both popular in the radiative transfer community to solve the RTE. For the determinist methods, the most well-known angular discretization methods are the dis- crete ordinate methods [11, 13, 14] and the P N methods [4, 12, 15] . The RTE being a hyperbolic equation, the finite volume methods (FVM) are widely used for such kind of equation, for the spatial discretization [16, 17]. To add more, Finite Element Methods (FEM) are useful for complex

geometries. In FEM, the classical Galerkin FEM in its original version, is not suited for the RTE, due to first order differential [18]. In such case, the Streamline-Upwind Petrov-Galerkin (SUPG) stabilizes the solution by adding artificial diffusion [13, 19] . Other methods have been developed in the past [11, 12, 20, 21, 22, 23, 24, 25] . For the statistical methods, the Monte Carlo [25, 26] and Ray Tracing [27] model the transport of photons using samples and randoms. The statistical methods are easy to handle for simple geometries and consume low memory. Moreover, to calculate an exchange between two surfaces/volumes, the methods are fast. However, when the geometries are complex, when the solution is to be found in a whole enclosure, and when the radiative properties are heterogeneous, then the statistical methods are difficult to handle and the CPU time needed to obtain an accurate solution may become extremely high.

Due to the second-order diffusion operator, the Galerkin finite element methods are efficient to solve the HCE as long as the nonlinear part from the blackbody radiance is properly dealt with. Lattice Boltzmann [9] and meshless methods [10] may also be good alternative to finite elements for this rather simple physics. Recently, Monte Carlo methods have been developed specifically for coupled conduction, convection and radiative trans fers [28].

The paper is organized as follow. In section 2, the physical models are presented : in one hand the radiative transfer equation along with mixed diffuse / specular boundary conditions, and, in the other hand, the transient heat conduction equation along with its specific boundary conditions. The section 3 deals with the numerical methods which are used to solve the coupling RTE-HCE. A discrete ordinate method for angular discretization, combined with SUPG, a decentered finite element scheme for space discretization, allow the solution of the RTE. For the HCE, Euler implicit scheme combined with a Galerkin finite element method are used to solve the energy problem. Section 4 finally deals with numerical results. A three-dimensional paraboloid is considered. Numerical results are given for several refractive index coefficients yielding to model on some cases highly reflecting materials as well as, on other cases, non-reflecting boundary reflections. According to cases, the temperature evolution inside the medium of concern greatly changes.

4.2.2 Mathematical models

Two models are presented : the radiative transfer equation and the heat transfer equation, both with their respec- tive boundary conditions. The speed of the light being much higher than the conduction time constant, the steady solution of the radiative transfer equation is considered for all given conduction time steps. The radiative transfer equation is written as follow :

$$\boldsymbol{s} \cdot \nabla I(\boldsymbol{x}, \boldsymbol{s}) + \beta I(\boldsymbol{x}, \boldsymbol{s}) = \sigma_s \int_{4\pi} \Phi(\boldsymbol{s}, \boldsymbol{s}') I(\boldsymbol{x}, \boldsymbol{s}') \, \mathrm{d}\Omega(\boldsymbol{s}') + \kappa I_b(T) \tag{4.6}$$

where I is the radiative intensity for a monochromatic wavelength in $\mathrm{Wm}^{-2}\mu\mathrm{m}^{-1}\mathrm{sr}^{-1}$, solution of the radiative transfer equation which is to be solved for all direction s in the unit sphere and for all x into the open bounded domain $\mathcal{D}$. σ_s is the scattering coefficient, κ is the absorption coefficient and $\beta = \kappa + \sigma_s$ is the so-called ex tinction

coefficient in m^{-1} , Φ is the scattering phase function and $I_b(T)$ is the given Planck function defined for a given wavelength in vacuum λ_0 [11] :

$$I_b(T(t,\boldsymbol{x})) = C_1 n^3 \lambda_0^{-5} \left(e^{\frac{C_2}{\lambda_0 T}} - 1 \right)^{-1} \text{ in } \mathrm{Wm}^{-2}\mu\mathrm{m}^{-1} \tag{4.7}$$

where $C_1 = 1.191 \times 10^{-16}$ Wm^2, $C_2 = 1.4388 \times 10^{-2}$ Km. Moreover, the behavior of the radiative intensity on borders is important to be well taken into account in order to simulate a physics close to the reality. For a smooth media, specular reflection is considered :

$$I(\boldsymbol{x},\boldsymbol{s}) = \tilde{I}(\boldsymbol{x},\boldsymbol{s}) + \rho(\boldsymbol{s}\cdot\boldsymbol{n}) I(\boldsymbol{x},[\boldsymbol{s} - 2(\boldsymbol{s}\cdot\boldsymbol{n})\boldsymbol{n}]) \text{ on } \partial\mathcal{D} \text{ and } \forall \boldsymbol{s} \text{ such as } \boldsymbol{s}\cdot\boldsymbol{n} < 0 \tag{4.8}$$

The first term in the right-hand-side of the equality sign is the Dirichlet contribution which may explain external sources for example. The other term is the gain by specular reflection from the incident direction $\boldsymbol{s} - 2(\boldsymbol{s}\cdot\boldsymbol{n})\boldsymbol{n}$. $\rho(\boldsymbol{s}\cdot\boldsymbol{n}) \in [0,1]$ is the reflection coefficient based on the Fresnel formulation and the Snell-Descartes law. The reflectivity coefficient depends of the scalar product $\boldsymbol{s}\cdot\boldsymbol{n} = \cos\theta_i$ and the index of refraction $\tilde{n}$.

The blackbody emissivity $I_b(T)$ depends explicitly of the temperature $T(t,\boldsymbol{x})$ supposed unknown. The tem- perature is the solution of the following unsteady-conduction equation :

$$\frac{\partial T}{\partial t}(t,\boldsymbol{x}) = D_T \Delta T(t,\boldsymbol{x}) - \nabla \cdot q_r(t,\boldsymbol{x}) \tag{4.9}$$

where $D_T = \frac{k}{\rho c_p}$ is the thermal diffusivity coefficient, k the thermal conductivity (WK^{-1} m^{-1}), ρ is the density (kg^{-3}) and c_p is the specific heat capacity ($\mathrm{Jkg}^{-1}\mathrm{K}^{-1}$). The divergence of the radiative flux $\nabla \cdot q_r(t,\boldsymbol{x}) = \kappa I_b - \kappa \int_{4\pi} I(\boldsymbol{x},\boldsymbol{s})\ \mathrm{d}\boldsymbol{s}$ depends on the radiative intensity and the temperature. The temperature at $t = 0$ is supposed known $T(0,\boldsymbol{x}) = T_0(\boldsymbol{x})$. Also, Robin boundary conditions are applied on borders to simulate convective transfers with an external fluid at temperature T_{ext} : $\frac{\partial T}{\partial \boldsymbol{n}}(t,\boldsymbol{x}) = h(T_{\text{ext}}(\boldsymbol{x}) - T(t,\boldsymbol{x}))$ on $\partial\mathcal{D}$, where h is the exchange coefficient.

4.2.3 Mathematical approximations

In the general case, the RTE and the HCE cannot be solved analytically. Some numerical tools need to be developed to get an approximation of the continuous solution. The discretization of the RTE and the HCE are respectively presented.

To cut off the integral problem into the radiative transfer equation, the unit sphere is discretized into N_d solid angles with a main direction $\boldsymbol{s}_m$. The radiative transfer equation becomes a system of N_d equations with N_d unknowns, noted $I_m(\boldsymbol{x})$ each being continuous in space. As the number of directions is limited, the specular condition is also discretized accordingly :

$$\boldsymbol{s}_m \cdot \nabla I(\boldsymbol{x}) = \sigma_s \sum_{j=1}^{N_d} \omega \Phi_{m,j} I_j(\boldsymbol{x}) + \kappa I_b(T)\ ,\ \forall = 1, \cdots, N_d \tag{4.10}$$

$$I_m(\boldsymbol{x}) = \tilde{I}_m(\boldsymbol{x}) + \rho(\boldsymbol{s}_m \cdot \boldsymbol{n}) \sum_{\boldsymbol{s}_j \cdot \boldsymbol{n} > 0} \delta_{m,j}(\boldsymbol{n}) I_j(\boldsymbol{x}) \tag{4.11}$$

where ω_j corresponds to the weight associated to the direction $\boldsymbol{s}_j$, and $\delta_{m,j}(\boldsymbol{n})$ is the partition ratio coefficient representing the proportion of the radiative intensity I_j which is reflected towards the direction $\boldsymbol{s}_m$, taking into account of the weight $\rho(\boldsymbol{s}_m \cdot \boldsymbol{n})$ according to Fresnel law.

The Galerkin finite element method being as well known unstable for the radiative transfer equation due to the advection term $\boldsymbol{s}_m \cdot \nabla I_m$, the streamline-upwind Petrov-Galerkin method uses an additional term to the test function v to throw off the scheme and to get stability. To obtain the weak formulation, the m th equation of the global system is multiplied by the test function $v + \gamma \boldsymbol{s}_m \cdot \nabla v$, it is then integrated on the full domain $\mathcal{D}$, and the Green theorem is finally used to express the boundary conditions. To add stability, $\gamma = 0.3 h_{\mathcal{D}}$, with $h_{\mathcal{D}}$ depend of the mesh refinement of $\mathcal{D}$ [19]. The variational formulation reads, with $\tilde{\beta}_m = \kappa + \sigma_s(1 - \omega_m \Phi_{m,m})$:

$$\begin{aligned}
&\int_{\mathcal{D}} (\gamma \boldsymbol{s}_m \cdot \nabla I_m - I_m)(\boldsymbol{s}_m \cdot \nabla v) + \tilde{\beta}_m I_m (v + \gamma \boldsymbol{s}_m \cdot \nabla v) \, \mathrm{d}\boldsymbol{x} \\
&\quad + \int_{\boldsymbol{s}_m \cdot \boldsymbol{n} > 0} I_m v \boldsymbol{s}_m \cdot \boldsymbol{n} \, \mathrm{d}\Gamma + \sum_{j=1}^{N_d} \Big[- \int_{\mathcal{D}} \sigma_s \omega_j \Phi_{m,j} I_j (v + \gamma \boldsymbol{s}_m \cdot \nabla v) \, \mathrm{d}\boldsymbol{x} \\
&\quad\quad + \int_{\boldsymbol{s}_m \cdot \boldsymbol{n} < 0 \cap \boldsymbol{s}_j \cdot \boldsymbol{n} > 0} \rho(\boldsymbol{s}_m, \boldsymbol{n}) \delta_{m,j}(\boldsymbol{n}) I_j(\boldsymbol{x}) v \boldsymbol{s}_m \cdot \boldsymbol{n} \, \mathrm{d}\Gamma \Big] \\
&\quad\quad = - \int_{\boldsymbol{s}_m \cdot \boldsymbol{n} < 0} \tilde{I}_m v \boldsymbol{s}_m \cdot \boldsymbol{n} \, \mathrm{d}\Gamma + \int_{\mathcal{D}} I_b (v + \gamma \boldsymbol{s}_m \cdot \nabla v) \, \mathrm{d}\boldsymbol{x}
\end{aligned} \tag{4.12}$$

To cut off the temporal derivative, the first order implicit Euler scheme is used. Moreover, at a given time step, the divergence of the flux q_r is calculated at the previous time step to remove the nonlinearity due to the blackbody term $I_b(T)$. The weak formulation of the conduction problem reads :

$$\begin{aligned}
\int_{\mathcal{D}} \frac{T^{N+1}}{\delta t} + D_T \nabla T^{N+1} \cdot \nabla v \, \mathrm{d}\boldsymbol{x} + \int_{\partial \mathcal{D}} \frac{D_h}{k} T^{N+1} v \, \mathrm{d}\Gamma = \int_{\mathcal{D}} \frac{T^N}{\delta t} v - \nabla \cdot q_r^N v \, \mathrm{d}\boldsymbol{x} \\
+ \int_{\partial \mathcal{D}} \frac{D_h}{k} T_{\mathrm{ext}} v \, \mathrm{d}\Gamma
\end{aligned} \tag{4.13}$$

4.2.4 Numerical solution

The set of the varatiational formulation (4.12)-(4.13) gives us steady-state solutions of radiative intensities along with the transient solution of the temperature in the whole domain. The geometry of concern is a paraboloid with a height of 4/3 m and a diameter of 4 m. The equation of the paraboloid surface is given by $z = 0.333(x^2 + y^2)$. The physical properties are the following. The absorption coefficient is $\kappa = 0.4$ m^{-1} , the isotropic scattering coefficient is $\sigma_s = 0.1$ m^{-1} . Next, the thermal conductivity is $k = 1$Wm^{-1} K^{-1} , the density is $\rho = 2$ kgm $^{-3}$, the heat capacity is $c_p = 5$ Jkg^{-1} K^{-1} , and the convective exchange coefficient is $h = 5$ m^{-2} . At $t = 0$ s, the tem- perature is $T_0(\boldsymbol{x}) = 300$ K. A collimated beam is entering to the medium on the full plan surface such as $I(\boldsymbol{x}, \boldsymbol{s}_0) = 10^3$ Wm$^{-2}\mu$m^{-1}sr^{-1}. Solutions are presented below for three values

of refractive index. The first case, with $n = 1$, considers the border is transparent, there is no reflection. Another case, with $n = 1.8$, considers that the reflected part is very important. The last case stands in between, with $n = 1.4$.

Figure 4.5 presents the evolutions of the radiative intensity and of temperature at $t = 0.5$ s along the longitudinal axis, and Figure 4.6 presents the same data in cross-sections. It can be observed that the maximum radiative intensity increases with the refraction index. Henceworth, the temperature inside the medium also greatly increases with the refraction index. As an example an increase of the index factor from 1 to 1.4 increases the maximum temperature difference from 164 to 220 K. In the same manner, an increase of the index factor from 1.4 to 1.8 increases the maximum temperature difference from 220 to 551 K. This confirms that the design of materials for such systems is highly important.

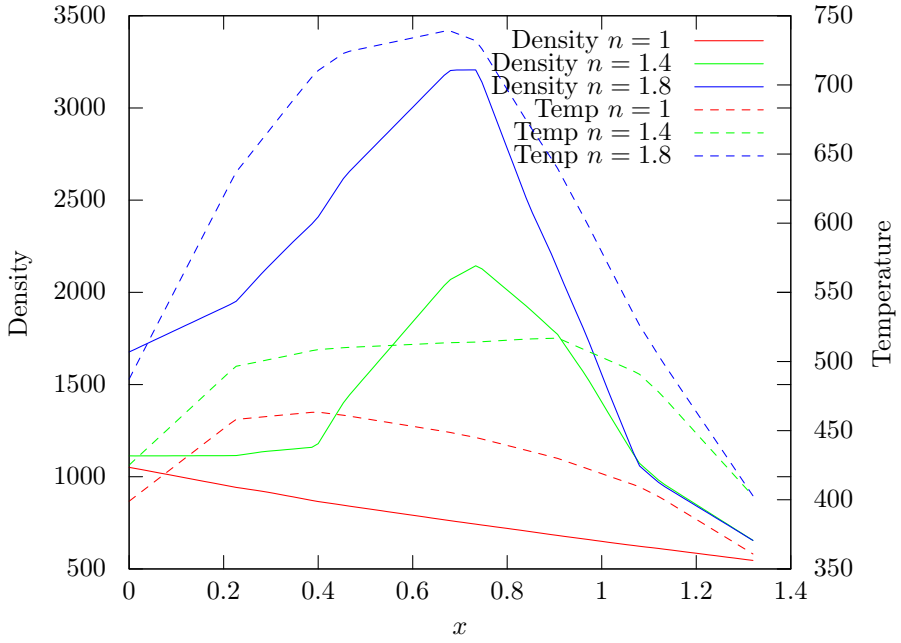

FIGURE 4.5 – Evolution of the radiative intensity and of temperature at $t = 0.5$ s along the longitudinal axis.

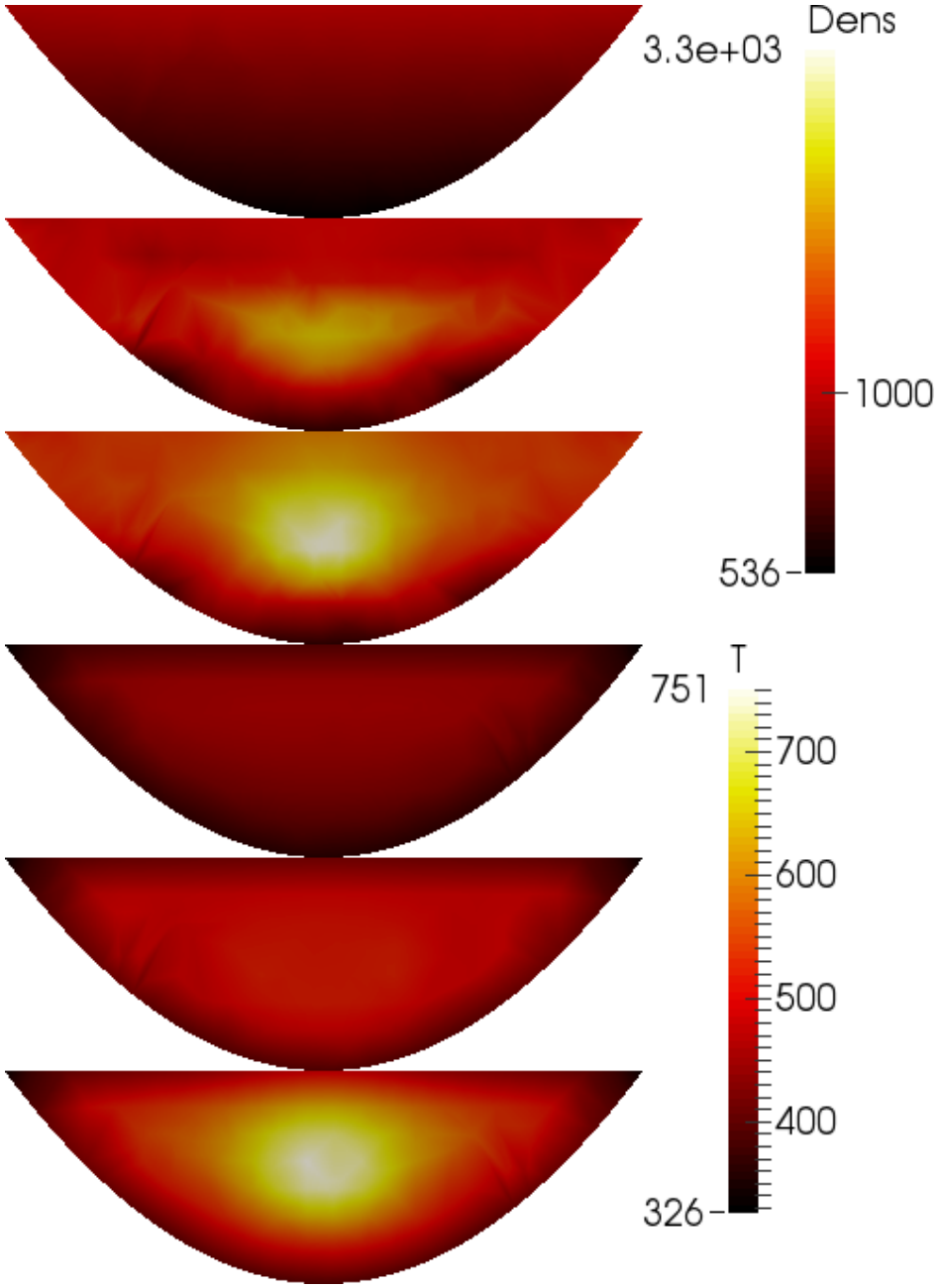

FIGURE 4.6 – Top : radiative intensity ; bottom : temperature at $t = 0.5$ s. For each, the first is for $n = 1$, the second is for $n = 1.4$, the third is for $n = 1.8$

4.3 Article 4 : "3D numerical modelling of the propagation of radiative intensity through a real X-ray tomographied ligament" (*Accepté dans JQSRT, en publication*)

D. Le Hardy , MA Badri, B. Rousseau, S. Chupin, D. Rochais, Y. Favennec

1 : CNRS, Laboratoire de Thermocinétique de Nantes, UMR 6607, Université de Nantes, Rue Christian Pauc, 44306 Nantes Cedex 3,France 1 :Institut de Recherche Technologique Jules Verne, Chemin du Chaffault, 44340 Bouguenais, France 3 :Commissariat à l'Energie Atomique et aux Energies Alternatives (CEA)/Le Ripault, BP 16, 37260 Monts, France

Abstract

In order to explain the macroscopic radiative behaviour of an open-cell ceramic foam, knowledge of its solid phase distribution in space and the radiative contributions by this solid phase is required. The solid phase in these open-cell ceramic foams is arranged as a porous skeleton, which is itself composed of an interconnected network of ligament. Typically, ligaments being based on the assembly of grains more or less compacted, exhibit an anisotropic geometry with a concave cross section having a lateral size of one hundred microns. Therefore, ligaments are likely to emit, absorb and scatter thermal radiation. This framework explains why experimental investigations at this scale must be developed to extract accurate homogenized radiative properties regardless the shape and size of ligaments. To support this development, a 3D numerical investigation of the radiative intensity propagation through a real world ligament, beforehand scanned by X-Ray micro-tomography, is presented in this paper. The Radiative Transfer Equation (RTE), applied to the resulting meshed volume, is solved by combining Discrete Ordinate Method (DOM) and Streamline upwind Petrov-Garlekin (SUPG) numerical scheme. A particular attention is paid to propose an improved discretization procedure (spatial and angular) based on ordinate parallelization with the aim to reach fast convergence. Towards the end of this article, we present the effects played by the local radiative properties of three ceramic materials (silicon carbide, alumina and zirconia), which are often used for designing open-cell refractory ceramic foams.

Keywords : Radiative Transport, Ligament, Alumina, Ziconia, Silicon Carbide, Discrete Ordinate Method, Galerkin Method, SUPG, Specular Reflection, Complex Geometry

4.3.1 Introduction

Refractory ceramic open-cell foams offer versatile possibilities for developing high temperature systems ($T \approx 1000$ °C) in which fluid flow and heat transfers may occur simultaneously. Typical applications are porous gas burners [29], volumetric solar receivers [30] or heat exchangers for recovering sensible heat [31]. A key challenge to increase the thermal efficiency of these energy conversion systems is to integrate pro-

perly the contribution of the thermal radiation for establishing an appropriate thermal balance. Dealing accurately with the radiative exchanges involves, firstly robust solving of the radiative transfer equation for these refractory open-cell foams which by nature are generally considered as semi-transparent materials [32] in reason of their high porosity, p, with $p \in [0.7 - 0.95]$. Secondly, the spectral radiative properties such as the absorption coefficient κ_ν, the scattering coefficient $\sigma_{s\nu}$, the scattering phase function Φ_ν and the complex refractive index $\tilde{n}(\nu, T)$ must be exactly known for the spectral range $[\nu_{min}, \nu_{max}]$, that corresponds here to wave numbers,ν where the Planck's law takes significant values at the considered temperature. Here T stands for the temperature. This set of parameters is governed by the materials used to manufacture the ceramic open-cell foams. Popular manufacturing materials involved are, silicon carbide [30, 33] a typically opaque material for sample thickness higher than few microns and alumina, [34] mullite [35] or zirconia [36] which are rather semi-transparent materials by nature. Being able to work with compact expressions that govern the radiative properties from simple chemical and textural [37] parameters relevant to the foams are useful when global heat and fluid transfers are treated simultaneously for energy optimization [30, 33].

However, ceramic open-cell foams are complex materials, from a topological viewpoint, since they are composed from a solid network of ligaments [38] which posses confined macropores most often filled with air. Further, adding to the complications is the multi-scale length organization of open-cell foams, where each element of matter contributes to the global radiative behaviours [39]. To detail these lengths, there exist : (i) the crystalline structure of the solid grains at nanometric scale, which is itself imposed by the chemical composition of the foams, (ii) the grains and the micropores constituting the ligaments at micronic scale, (iii) the ligaments and the macropores at millimetric scale that define the architecture of the foams and (iv) the final shape and volume of the foams at centimetric scale when they are used in industrial systems. Adding more to the complexities is the elaboration process used to elaborate the foams [40]. Indeed, the process tends to form solid ligaments that are more or less dense or really hollow [29] and often exhibit, based on the replication methods, a concave shape where the cross sectional area remains nearly constant over the central half of the ligament but increases on its extremities [41]. It has been recently underlined that the ligament geometries influence the determination of the extinction coefficient of metallic foams since computed values can evolve around 10 % [42, 43]. Let us notify that in the latter case, ligaments are considered as optically thick media. On the other hand, in the case of mullite foam possessing semi-transparent ligaments, authors have successfully extracted the solid phase radiative properties on an available dense ceramic of mullite to compute afterwards the bi-directional reflectance of the foam through a Monte Carlo code [44]. This two-step process proves to be delicate since it requires to find a centimetric sample with a similar textural feature than the one present in the ligaments. However, from an elaboration viewpoint, it is well known that the texture of a ligament can not be strictly the same than in a dense sintered ceramic composed of the same material [29].

This description indicates that the direct investigation of the radiative properties of ligaments at the local scale either for semi-transparent compounds or for opaque compounds constitutes a new domain of development for researchers involved in the design of foam with controlled macroscopic radiative properties. Recently, Guevelou

et al. performed infrared microscopy reflectivity measurement on the ligaments of a silicon carbide open-cell foam foam with the aim to determine their effective complex index of refraction [33]. The authors developed an analytical methodology based on an effective medium law in order to avoid treating directly the effect played by the rough surface of the ligaments. Rochais et al., measured, until 900 °C, through a microscopic photothermal set-up, the thermal diffusivity of mullite foams and developed a meticulous sample preparation for dealing with the semitransparency of the observed lumps [45]. The sample preparation consisted to optically polished a mullite foam, which has been impregnated with a glue ceramic (stable until 900 °C) and to deposit an opaque coating on the surfaces of the lumps. These two experimental works are restricted on microscopic pieces of matter being opaque and the theoretical modeling of the reflected spectra requires to bear on some assumptions. This is why the knowledge of the transport of thermal radiation within the ligament, either opaque or semitransparent, can provide critical information for developing high-quality experimental developments.

This framework shows that investigating the radiative behaviour of the ligaments regardless of their shapes and optical thicknesses, $\tau_\nu = \beta_\nu d$, are today of crucial importance. Let us recall here d is the typical length of the ligament cross-section and β_ν is the extinction coefficient. To go one step further, one proposes to model the 3D radiative transport within a ligament, beforehand 3D imaged by X-ray micro-tomography, and endowed with a set of gradual radiative properties (κ_ν, $\sigma_{s\nu}$, Φ_ν, $\tilde{n}_\nu$) that confers to its opacity or semi transparency. The 3D image is entirely meshed within its all volume. To follow the volumetric propagation of the radiative intensity within the ligament which is exposed to a collimated beam of radiation, the radiative transfer equation (RTE) is solved by combining the discrete ordinate method (DOM) and the Streamline upwind Petrov-Galerkin methods (SUPG). The treatment of reflection of radiative intensive on borders is also performed very accurately, following [46]. Such a numerical methodology allows to deal with the specular reflective behaviour of the ligaments. The paper is organized as follows. Part 4.3.2 exposes the mathematical models used in this work. Part 4.3.3 details the numerical methodologies used to solve the RTE. Then, Part 4.4 gives the results which are further discussed.

4.3.2 Physical model

The steady-state radiative transfer equation (RTE) governs the radiative intensity $I_\nu(\boldsymbol{x}, \boldsymbol{s})$ through a 5 dimensional integro-differential equation that reads [11, 12] :

$$\boldsymbol{s} \cdot \nabla I_\nu(\boldsymbol{x}, \boldsymbol{s}) + \beta_\nu I_\nu(\boldsymbol{x}, \boldsymbol{s}) = \sigma_{s\nu} \oint_{\mathcal{S}^{n-1}} \Phi(\boldsymbol{s}' \to \boldsymbol{s}) I_\nu(\boldsymbol{x}, \boldsymbol{s}') \, \mathrm{d}\boldsymbol{s}' + \kappa_\nu I_b(T, \nu) \qquad (4.14)$$

in which $\boldsymbol{x} \in \mathcal{D} \subset \mathbb{R}^3$ represents the space coordinate, $\boldsymbol{s}$ is the unit direction within the sphere (2D) and I_b is the Plancks function dependent on the wavelength as well as on temperature. To model carefully the evolution of the radiative intensity, appropriate intensity attenuations due to reflection effect on the boundaries is to be taken into account. The boundary condition on the borders can be expressed as follows, for $\boldsymbol{x} \in \partial\mathcal{D}^- = \partial\mathcal{D} | \boldsymbol{s} \cdot \boldsymbol{n} < 0$:

$$I_w(\boldsymbol{x}, \boldsymbol{s}) = (1 - \alpha) I_\nu^{\Cup}(\boldsymbol{x}, \boldsymbol{s}) + \alpha I_\nu^{\Cap}(\boldsymbol{x}, \boldsymbol{s}) \qquad (4.15)$$

The first term in the right-hand-side of (4.15) is the diffusion contribution of reflection, and the second term represents the specular contribution. The partition ratio coefficient $\alpha \in [0, 1]$, also called "parameter of specularity" [47] yields a linear interpolation between diffuse and specular contributions while dealing with mixed boundary conditions. To add more, the entering beam $\tilde{I}_\nu(\boldsymbol{x}, \boldsymbol{s}_0)$ towards the direction $\boldsymbol{s}_0$ also yields both diffuse and specular refractions. Reflections and refractions brought together for diffuse and specular parts are finally given by, $\forall \boldsymbol{x} \in \partial\mathcal{D}^-$:

$$I^{\Cup}(\boldsymbol{x}, \boldsymbol{s}) = -\boldsymbol{s}_0 \cdot \boldsymbol{n} \frac{1 - \rho_d}{\pi} \tilde{I}(\boldsymbol{x}, \boldsymbol{s}_0) + \frac{\rho_d}{\pi} \int_{\partial\mathcal{D}^+} I(\boldsymbol{x}, \boldsymbol{s}') \boldsymbol{s}' \cdot \boldsymbol{n} \, \mathrm{d}\boldsymbol{s}' \tag{4.16}$$

$$I^{\Vee}(\boldsymbol{x}, \boldsymbol{s}) = (1 - \rho_s(\boldsymbol{s}_0 \cdot \boldsymbol{n}))\tilde{I}(\boldsymbol{x}, \boldsymbol{s}_0) + \rho_s(\boldsymbol{s} \cdot \boldsymbol{n}) I(\boldsymbol{x}, \xi(\boldsymbol{s})) \tag{4.17}$$

where $\rho_s(\cdot)$ and ρ_d are respectively the specular and diffuse reflectivity. $\xi(\boldsymbol{s}) = \boldsymbol{s} - 2(\boldsymbol{s} \cdot \boldsymbol{n})\boldsymbol{n}$ is the incident radiation of the reflected direction $\boldsymbol{s}$. The first terms in right hand sides of (4.16) and (4.17) actually come from the Dirichlet conditions, while the second terms represent internal reflections. To add more, in (4.16), $\tilde{\omega}$ denotes the solid angle characterizing the direction $\boldsymbol{s}_0$ of the entering beam. Note that the subscript ν has been dropped here and so forth for readability considerations. Also, the reflectivity ρ_s is a function of the cosine angle between the direction $\boldsymbol{s}$ and the outward normal $\boldsymbol{n}$.

4.3.3 Numerical development

To solve the radiative transfer problem involving (4.14) and (4.15), numerical methods have to be used. Two major kinds of numerical methods are available to solve such problem : the statistical methods and the deterministic methods. For the statistical approach, the Monte-Carlo [48, 49, 50, 51] and Ray-Tracing methods [52, 53] are the most popular. These methods are fast, efficient and use little memory to get an exchange between two surfaces, at least for simple geometries and homogeneous media. However, on the other hand, we have the deterministic approach based on discretizations, as it is presented in this paper. For Deterministic methods, the P_N method [54, 55, 56] and the DOM method [57, 58, 59, 60] are the most commonly-used methods concerning the angular discretizations of the integro-differential equation (RTE). The DOM methods are very popular in the radiative community because boundary conditions are easy to handle. To approximate the solution in space of the RTE, when coupled with the (DOM), the finite volume methods (FVM), the Discontinuous Galerkin (DG) and the Streamline upwind Petrov-Galerkin methods (SUPG) are the most popular methods. Besides FVM methods [61, 62, 63], SUPG methods are Galerkin methods that use a stability parameter to add numerical diffusion and smooth the solution for advection equations. In the area of solving radiative transport equation, this scheme has been introduced by Kanschat in 1998 [64]. It has then been reused afterwards as, for example, in [65, 66, 67]. When the added numerical diffusion parameter is equal to β_ν, the SUPG method is sometimes called the Least-Square method [68]. Further, DG method is an hybrid between FVM and classical finite element methods (FEM) [69, 70, 71]. A comparison between DG and SUPG is done for 2D geometries [13]. This comparison shows the SUPG method outruns the DG method for certain cases of interest. For the presented work DOM combined with the SUPG method is used to solve the radiative problem, which concerns equations (4.14) and (4.15). Such a numerical treatment is dealt with in this section.

Volumic mesh of the ligament

The study is based on the 3D digitalized image of ligament coming from a real ceramic foam, elaborated with the replication method [29]. A polymeric template was coated with a slurry composed of micronic grains and burned after. It led to the formation of the solid skeleton. Then, the image was obtained as follows. X-ray tomography experiment was performed on a cylindrical silicon carbide open-cell foam (diameter = 10 mm, thickness = 10 mm) at the European Synchrotron Radiation Facilities (Grenoble, France) on the ID19 beamline. The spatial resolution was 5.06 micron per edge of a cubic voxel. The reconstructed volume had a size of 2048 per 2048 per 2048 $voxels^3$. A sub volume of 50 per 50 per 100 $voxels^3$ was then extracted from the native image. A Markov field algorithm [72] was applied to convert the original 256 grey level image into a 2 grey level image. A gaussian blur is applied to this image to obtain a smooth ligament surface. Then, a marching cube algorithm [73] helps to obtain the external surface mesh of the ligament. Finally, the ligament is represented by a volumetric mesh with 27,432 vertices, 131,618 tetrahedrons and 27,916 triangles on the surface, built with the open-source software Gmsh [74]. The ligament length is twice the size of its lateral dimensions. The image of the ligament is depicted in Figure 4.7.

FIGURE 4.7 – Mesh of the fiber – left : surface mesh – right : volumetric mesh.

Discrete Ordinate Methods by isocahedron discretization

The RTE equation (4.14) is an integro-differential equation. Combined with the boundary conditions (4.15), the RTE cannot be solved analytically, henceforth the need of numerical method in order to solve it. To facilitate the numerical solution, the angular sphere $\mathcal{S}^{n-1}$ (angular discretization) and the space domain $\mathcal{D}$ (spatial discretization) are divided into subdomains (mesh). In this study, the Discrete Ordinate Method (DOM) concerns discretizing the unit sphere $\mathcal{S}^{n-1}$ into N_d solid angles Ω_m, each being associated to its main direction $\boldsymbol{s}_m$. The integral in the RTE is then approximated by $\oint u(\boldsymbol{s})\ \mathrm{d}\boldsymbol{s} \approx \sum_{j=1}^{N_d} \omega_j u_j$, with $u_j = u(\boldsymbol{s}_j)$, in which the weight ω_j is equal to the area of the solid angle of the spherical triangle surrounding the direction $\boldsymbol{s}_j$. Such area is calculated using L'Huilier's Theorem explained below. The discretisation of the angular

sphere is based on icosahedra, as suggested in [66]. As schematically presented in Fig. 4.8, each triangle of a icosahedron represents a solid angle with the barycentre as the main direction. This yields a quasi-uniform angular discretization. This discretization being almost uniform, the weight for each direction $\boldsymbol{s}_m$ is $\omega_m \approx 4\pi/N_d$. More precisely, defining $\alpha_m^{ik} = \arccos(\boldsymbol{e}_m^i \cdot \boldsymbol{e}_m^k)$ the angle between edges $\boldsymbol{e}_m^i$ and $\boldsymbol{e}_m^k$ of the spherical angle Ω_m surrounding the direction $\boldsymbol{s}_m$, the area $\omega_m = \text{meas}(\Omega_m)$ is calculated using L'Huilier theorem :

$$\omega_m = 4 \arctan \left[\sqrt{\tan \frac{p_m}{2} \tan \frac{p_m - \alpha_m^{12}}{2} \tan \frac{p_m - \alpha_m^{13}}{2} \tan \frac{p_m - \alpha_m^{23}}{2}} \right] \tag{4.18}$$

where $p_m = \frac{1}{2}(\alpha_m^{12} + \alpha_m^{13} + \alpha_m^{23})$ is the half perimeter.

The generic function given above, $u(\boldsymbol{s})$, is applied on the product of the radiative intensity with the phase function in the scattering integral term. The DOM then consists in rewriting the RTE in all directions $\boldsymbol{s}_j$, $j = 1, \ldots, N_d$ of the angular discretization. This transforms the RTE (4.14) into a semi-discretised differential system that contains N_d equations, such that the m^{th} one explains the transport of the radiative intensity towards the $\boldsymbol{s}_m$ direction. At this stage, the system has N_d unknown $I_j(\boldsymbol{x})$, each being still continuous in space. In the following, the space variable $\boldsymbol{x}$ as well as the temperature variable T are omitted for clarity. The semi-discrete RTE reads, for the m^{th} direction :

$$\boldsymbol{s}_m \cdot \nabla I_m + \beta I_m = \sigma_s \sum_{j=1}^{N_d} \omega_j \Phi_{m,j} I_j + \kappa I_b \tag{4.19}$$

Note that the equation (4.19) is written down for the single direction m, but all directions $m = 1, \ldots, N_d$ are to be taken into account. Also, in practice, the well-known Henyey–Greenstein phase function is used [75] :

$$\Phi_{i,j} = \frac{1}{4\pi} \frac{1 - g^2}{(1 + g^2 - 2g\boldsymbol{s}_i \cdot \boldsymbol{s}_j)^{\frac{3}{2}}} \tag{4.20}$$

Note this scattering function depends on the mean cosine of the scattering function, $-1 < g < 1$. The discrete version of this function is to be normalized such that the approximation of the integral over the whole unit sphere is unity :

$$\Phi_{i,j} = \frac{\Phi_{i,j}}{\sum_{k=1}^{N_d} \omega_k \Phi_{i,k}} \tag{4.21}$$

DOM applied on boundary conditions

Due to angular discretization, the number of directions is limited, and so is the number of partial differential equations to be solved. In the same manner, continuous boundary conditions (4.15) are also to be discretized. For the diffuse boundary condition (4.16), all discrete radiative fluxes are gathered together. That yields, for m such that $\boldsymbol{s}_m \cdot \boldsymbol{n} < 0$:

$$I_m^{\uplus} = -\boldsymbol{s}_0 \cdot \boldsymbol{n} \, (1 - \rho_d) \frac{\omega_{\boldsymbol{s}_0}}{\pi} \tilde{I} + \frac{\rho_d}{\pi} \sum_{j | \boldsymbol{s}_j \cdot \boldsymbol{n} > 0} \omega_j \boldsymbol{s}_j \cdot \boldsymbol{n} I_j \tag{4.22}$$

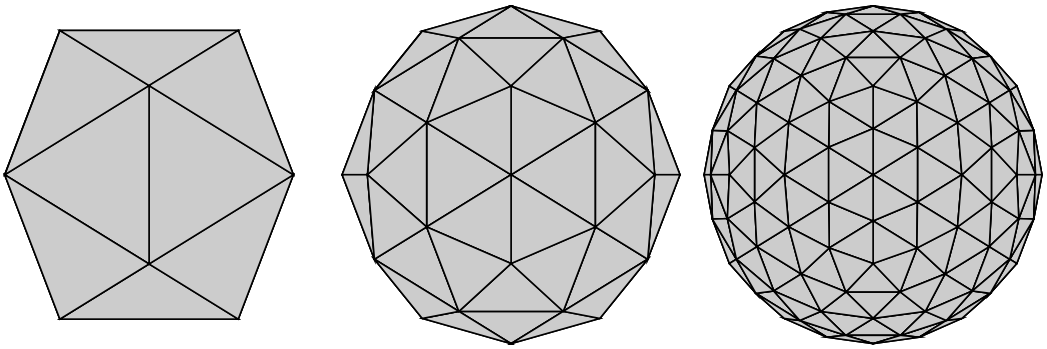

FIGURE 4.8 – Three icosahedra with, from the left to the right, 20 triangles, 80 triangles, and 320 triangles

In this relationship, the solid angle $\omega_{\boldsymbol{s}_0}$ is the weight associated to the prescribed direction $\boldsymbol{s}_0$. For the specular contribution, the incident solid angle Ω_j associated to the main direction $\boldsymbol{s}_j$ is shared. For the collimated solid angle, the entering flux is shared with its neighbouring directions. For the internal reflection, the incident solid angle Ω_j is shared into all other solid angles Ω_m. The partition ratio coefficient $\tilde{\delta}_m(\boldsymbol{n})$ is introduced to express the amount of intensity towards the m^{th} direction, from the direction $\boldsymbol{s}_0$. It is a function of space because it depends on the cosine between the direction $\boldsymbol{s}_0$ and the outward normal $\boldsymbol{n}$. Also, for reflection, the partition ratio coefficient $\delta_{m,j}(\boldsymbol{n})$ is the part of the incident solid angle Ω_j into the reflected solid angle Ω_m. This way, the discrete version of (4.17) reads, for m such that $\boldsymbol{s}_m \cdot \boldsymbol{n} < 0$:

$$I_m^{\vee} = (1 - \rho_s(\boldsymbol{s}_0 \cdot \boldsymbol{n}))\tilde{\delta}_m(\boldsymbol{n})\frac{\boldsymbol{s}_0 \cdot \boldsymbol{n}}{\boldsymbol{s}_m \cdot \boldsymbol{n}}\tilde{I} + \rho_s(\boldsymbol{s}_m \cdot \boldsymbol{n})\sum_j \delta_{m,j}(\boldsymbol{n})I_j \tag{4.23}$$

Fig. 4.9 schematically presents how the incident solid angle is shared after reflection, and Fig. 4.10 schematically presents the reflection of a given incident solid angle, and how this intersects with existing solid angles. The treatment of reflection of radiative intensive on borders is this way performed very accurately. Note that all numerical schemes have been tested and validated very thoroughly, in a previous study, see [46]. As suggested in this paper, the calculation of partition ratio coefficients is performed in three main steps summarized as :

1. a solid angle, say Ω_j is reflected on a border to yield Ω'_j. This means that all vertices $\boldsymbol{e}_i$ characterizing the incident solid angle are reflected to $\boldsymbol{e}'_i$, using $\boldsymbol{e}'_i = \boldsymbol{e}_i - 2(\boldsymbol{e}_i \cdot \boldsymbol{n})\boldsymbol{n}$;

2. the area of the intersection of the reflected solid angle Ω'_j with all other solid angles Ω_m of the discretization is then calculated. This process consists in computing intersection points of polygons edges. The process then re-ordinates all reflected edges, thanks to basis changes, projections, and the use of the convex envelop algorithm ;

3. the partition ratio coefficient $\delta_{m,j}$ is then set as the ratio $\text{mes}(\Omega_m \cap \Omega_j)/\text{mes}(\Omega_j)$. A normalization is also performed, for energy conservation.

More technical details along with algorithms are given in [46]. The computation of partition ratio coefficients is performed as a pre-process. These coefficients are then to be introduced in the variational formulation, presented in Section 4.3.3.

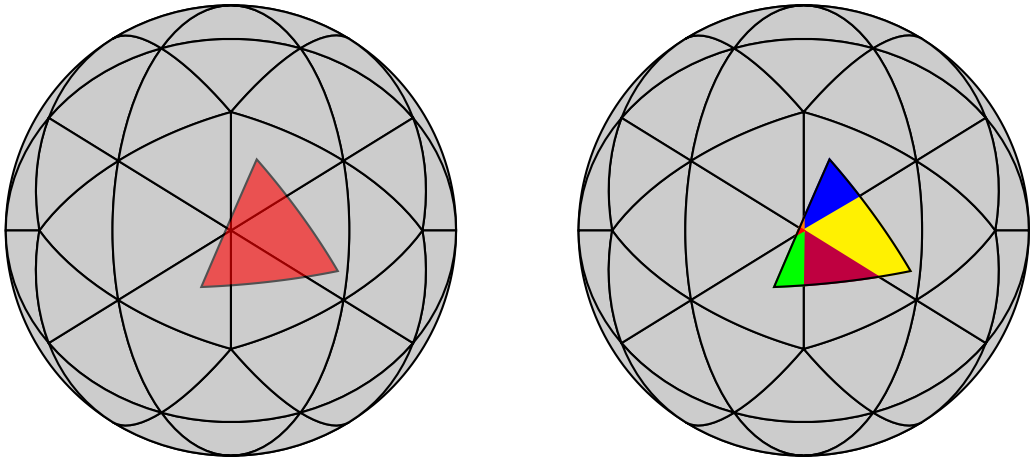

FIGURE 4.9 – Left : reflected solid angle – right : share of area of the reflected solid angle between the existing solid angles of the discretization

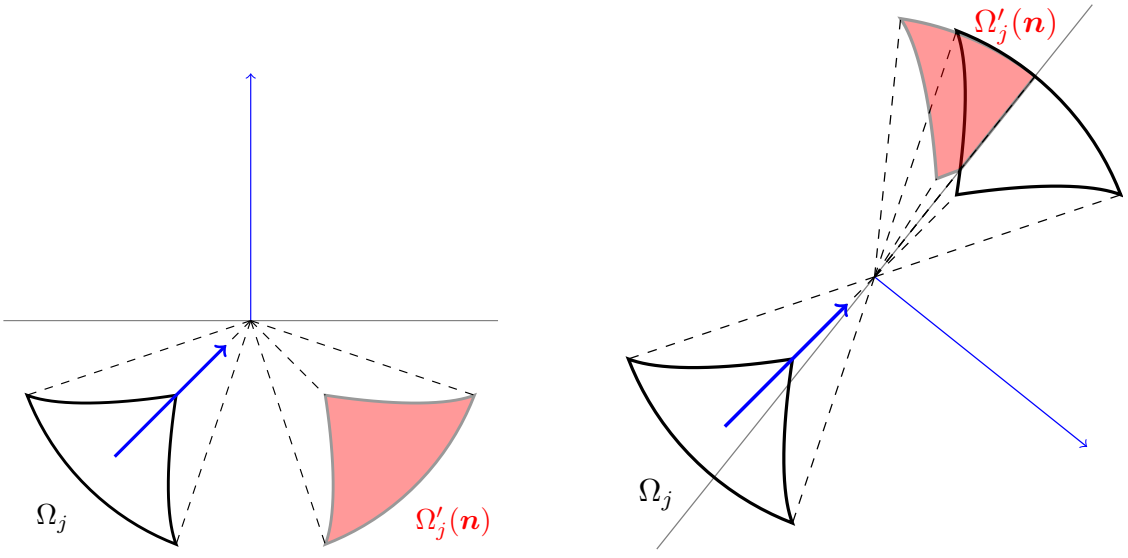

FIGURE 4.10 – Reflection of a solid angle – left : the reflection of the solid angle is total – right : only a part of the solid angle is reflected

Main direction of propagation

The incident beam impacts a curved surface. Let us define $\{\boldsymbol{n}_i\}_{1,\cdots,N_n}$ the different external normals of the surface of the domain $\mathcal{D}$. In the general case, the refracted beam is split into several directions that do not correspond to the existing directions of the discretization. To get less error on the dirichlet boundary condition, let us define $\bar{\boldsymbol{n}}$ the mathematical average of normals $\boldsymbol{n}_i$, and further let us define $\bar{\boldsymbol{s}}_r$ the refracted direction from the $\boldsymbol{s}_0$ dirichlet direction. To get the direction $\bar{\boldsymbol{s}}_r$ on the angular discretization, all the directions and all the edges are rotated such that the first direction $\boldsymbol{s}_1$ fits with $\bar{\boldsymbol{s}}_r$. The rotational operator $R(c, \boldsymbol{u})$ depends on the cosine c and sine s, as well as on a normal axis $\boldsymbol{u}$:

$$R(c,\boldsymbol{u}) = \begin{pmatrix} (\boldsymbol{u})_x^2(1-c)+c & (\boldsymbol{u})_x(\boldsymbol{u})_y(1-c)-(\boldsymbol{u})_z s & (\boldsymbol{u})_x(\boldsymbol{u})_z(1-c)+(\boldsymbol{u})_y s \\ (\boldsymbol{u})_x(\boldsymbol{u})_y(1-c)+(\boldsymbol{u})_z s & (\boldsymbol{u})_y^2(1-c)+c & (\boldsymbol{u})_y(\boldsymbol{u})_z(1-c)-(\boldsymbol{u})_x s \\ (\boldsymbol{u})_x(\boldsymbol{u})_z(1-c)-(\boldsymbol{u})_y s & (\boldsymbol{u})_y(\boldsymbol{u})_z(1-c)+(\boldsymbol{u})_x s & (\boldsymbol{u})_z^2(1-c)+c \end{pmatrix} \tag{4.24}$$

The operator R_{1r} to transform $\boldsymbol{s}_1$ to $\bar{\boldsymbol{s}}_r = R_{1r}\boldsymbol{s}_1$ is :

$$R_{1r} = R\left(\boldsymbol{s}_1 \cdot \bar{\boldsymbol{s}}_r,\ \frac{\boldsymbol{s}_1 \wedge \bar{\boldsymbol{s}}_r}{||\boldsymbol{s}_1 \wedge \bar{\boldsymbol{s}}_r||_2}\right) \tag{4.25}$$

The other directions $\boldsymbol{s}_j$ and edges of the solid angles $\boldsymbol{e}_k$ are also transformed by the rotation operator R_{1r}.

SUPG weak formulation

Developed by Hughes and Brooks [76], the SUPG method has then be used in the context of radiative transfer equation by Kanschat [64]. The SUPG method consists in multiplying all equations of the system (2.11), i.e. $\forall m = 1, \ldots, N_d$, by the corresponding test function $v + \gamma \boldsymbol{s}_m \cdot \nabla v$, and integrate over the whole domain $\mathcal{D}$. This yields, for the specific direction m :

$$\int_{\mathcal{D}} (\boldsymbol{s}_m \cdot \nabla I_m + \beta I_m)\,(v + \gamma \boldsymbol{s}_m \cdot \nabla v)\ \mathrm{d}\boldsymbol{x} = \int_{\mathcal{D}} \left(\sigma_s \sum_{j=1}^{N_d} \omega_j \Phi_{m,j} I_j + \kappa I_b\right)(v + \gamma \boldsymbol{s}_m \cdot \nabla v)\ \mathrm{d}\boldsymbol{x} \tag{4.26}$$

The Green theorem is then applied on advection terms of the kind $\boldsymbol{s}_m \cdot \nabla I_m\ v$, following the rule :

$$\int_{\mathcal{D}} \boldsymbol{s}_m \cdot \nabla I_m\ v\ \mathrm{d}\boldsymbol{x} = -\int_{\mathcal{D}} I_m\ \boldsymbol{s}_m \cdot \nabla v\ \mathrm{d}\boldsymbol{x} + \int_{\partial\mathcal{D}} I_m v\ \boldsymbol{s}_m \cdot \boldsymbol{n}\ \mathrm{d}\Gamma \tag{4.27}$$

In order to express the boundary conditions (4.22) and (4.23), the integral over the border $\partial\mathcal{D}$ is split into 2 integrals : over the boundary $\partial\mathcal{D}^{m+}$ that satisfies $\boldsymbol{s}_m \cdot \boldsymbol{n} > 0$, and over the boundary $\partial\mathcal{D}^{m-}$ that satisfies $\boldsymbol{s}_m \cdot \boldsymbol{n} < 0$. The former integral remains unchanged, and the latter is used to express the condition $I_m = I_w(\boldsymbol{s}_m)$:

$$\int_{\partial\mathcal{D}} I_m v\ \boldsymbol{s}_m \cdot \boldsymbol{n}\ \mathrm{d}\Gamma = \int_{\partial\mathcal{D}^{m+}} I_m v\ \boldsymbol{s}_m \cdot \boldsymbol{n}\ \mathrm{d}\Gamma + \int_{\partial\mathcal{D}^{m-}} I_w(\boldsymbol{s}_m) v\ \boldsymbol{s}_m \cdot \boldsymbol{n}\ \mathrm{d}\Gamma \tag{4.28}$$

The weak formulation is built gathering equations (4.26), (4.27) and (4.28) all in one. The weak formulation can be written as follows :

$$\sum_{j=1}^{N_d} a_{m,j}(I_j, v) = l_m(v) \tag{4.29}$$

with

$$\begin{aligned}
a_{m,m}(I_m, v) &= \int_{\mathcal{D}} \left(-I_m + \gamma \boldsymbol{s}_m \cdot \nabla I_m\right)\ \boldsymbol{s}_m \cdot \nabla v \ \mathrm{d}\boldsymbol{x} \\
&\quad + \int_{\mathcal{D}} \tilde{\beta}_m I_m\ \left(v + \gamma \boldsymbol{s}_m \cdot \nabla v\right)\ \mathrm{d}\boldsymbol{x} \\
&\quad + \int_{\partial\mathcal{D}^{m+}} I_m\ v\ \boldsymbol{s}_m \cdot \boldsymbol{n}\ \mathrm{d}\Gamma \\
a_{m,j}(I_j, v) &= \int_{\mathcal{D}} \sigma_s \omega_j \Phi_{m,j} I_j\ \left(v + \gamma \boldsymbol{s}_m \cdot \nabla v\right)\ \mathrm{d}\boldsymbol{x} \\
&\quad + \alpha \int_{\partial\mathcal{D}^{m-}} \rho_s \delta_{m,j}(\boldsymbol{n}) I_j v\ \boldsymbol{s}_m \cdot \boldsymbol{n}\ \mathrm{d}\Gamma \\
&\quad + (1-\alpha) \int_{\partial\mathcal{D}^{m-}} \frac{\rho_d}{\pi} \omega_j (\boldsymbol{s}_j \cdot \boldsymbol{n}) I_j v\ \boldsymbol{s}_m \cdot \boldsymbol{n}\ \mathrm{d}\Gamma \\
l_m(v) &= \int_{\mathcal{D}} \kappa I_b \left(v + \gamma\ \boldsymbol{s}_m \cdot \nabla v\right)\ \mathrm{d}\boldsymbol{x} \\
&\quad + \alpha \int_{\partial\mathcal{D}^{m-}} (1 - \rho_{s0}) \tilde{\delta}_m(\boldsymbol{n}) \tilde{I} v \boldsymbol{s}_0 \cdot \boldsymbol{n}\ \mathrm{d}\Gamma \\
&\quad - (1-\alpha) \int_{\partial\mathcal{D}^{m-}} \boldsymbol{s}_0 \cdot \boldsymbol{n}\ \frac{1-\rho_d}{\pi} \tilde{I} v\ \boldsymbol{s}_m \cdot \boldsymbol{n}\ \mathrm{d}\Gamma
\end{aligned} \tag{4.30}$$

To solve the weak formulation (4.29), the space is discretized. One introduces $\mathcal{M}_h$ the mesh approximation of the domain $\mathcal{D}$ where the index h represents the mesh fineness. Based on this mesh, the P1 linear finite element basis is used, yielding to N_{dof} degrees of freedom for a single direction. This basis allows to get a linear system of equations of the kind $A\boldsymbol{X} = b$, in which A is a matrix of size $(N_d \times N_{dof})^2$ built with the bilinear parts $a_{m,j}$, and $\boldsymbol{X}$ is the unknown vector of dimension $N_d \times N_{dof}$ that concatenates all the discrete radiative intensities I_j expressed on the finite element basis. The finest refinement of angular discretization (DOM with $N_d = 320$) leads to a massive linear system $A\boldsymbol{X} = b$ containing over 9 million unknown. To built the linear system, we apply ordinate parallelization (angular decomposition) via Message Passing Interface (MPI), combined with the open-source library FreeFem++ [77], which facilitates parallel matrix building on a parallel architecture machine. From there, the decomposed matrix is solved using parallel GMRES algorithm. In computations presented in the next section, the number of processors have been chosen equal to the number of discrete directions (20 processors when N_d =20, and 320 processors when N_d =320).

4.4 Numerical experiment

Numerical description of the virtual optical bench

In the following, one tracks the volumetric propagation of a collimated beam which impinges the ligament on one of its lateral side with the direction $s_0 = (0, 1, 0)$ as we can see in Fig. 4.11. It is worth notifying that the side-to-side distance propagation is

135 μm. The beamsize is of $r = 25$ μm radius and has a gaussian shape, defined by :

$$\tilde{I}(\boldsymbol{x}, \boldsymbol{s}_0) = \tilde{I}_0 e^{-10^{9.5}\left[(x-x_0)^2+(z-z_0)^2\right]} \mathbb{1}_{[(x-x_0)^2+(z-z_0)^2<r^2]} \tag{4.31}$$

where $x_0 = 187.5$ μm and $z_0 = 200$ μm represent the position of the center of the beam, relative to the mesh, and $\mathbb{1}_{[bool]}$ is the Heaviside function such as $\mathbb{1}_{[bool]} = 1$ if $bool = true$ or $\mathbb{1}_{[bool]} = 0$ if $bool = false$. Also, $\tilde{I}_0$ denotes the amplitude of the incident beam radiative intensity, which has been chosen equal to 500 W/m^2 sr in following simulations (D_0=500 W/m^2). Figure 4.11 represents the spatial repartition of the radiative intensity (normalized with D_0) when the ligament is illuminated with the incoming beam.

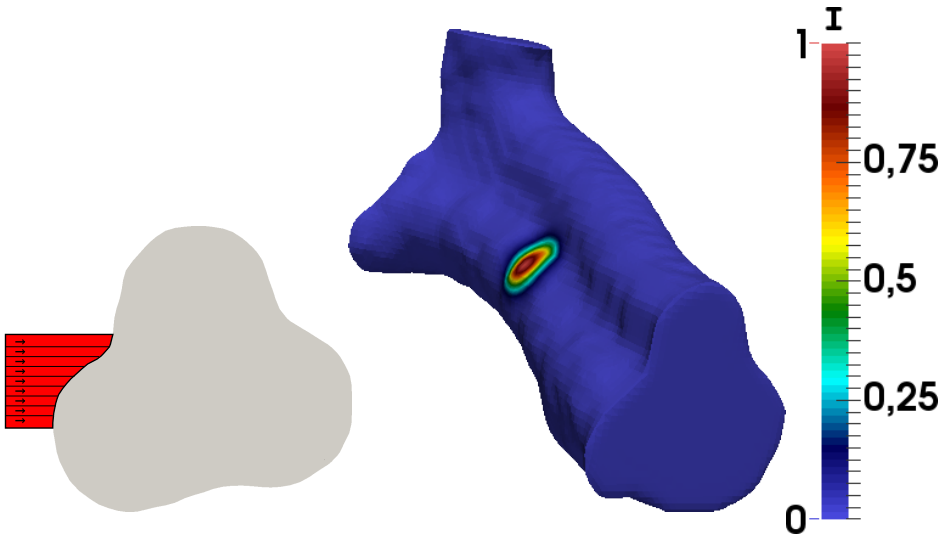

FIGURE 4.11 – Normalized incoming collimated beam with the direction $\boldsymbol{s}_0 = (0, 1, 0)$ hitting the ligament. The left part of the figure shows the decomposition of the beam on the triangular facets of the mesh.

The associated wavelengths are lying in the thermal radiation spectral range. The described optical experience is not strictly representative of the conventional optical configuration available on commercial infrared microscopes. Indeed, in most of the cases, convergent dual incident beams hit the mid part of thin samples either according to the combination of Cassegrain objectives [78] or of Schwarzchild objectives [79]. However, bench deriving from high brightness infrared beamlines on advanced synchrotrons allow to handle, through a judicious association of optical elements, quasi collimated incident beam with micronic size [80]. In the following, one makes the choice to propose numerical experiments which can be surely developed in synchrotron environment. For the collection of the reflected and transmitted radiation intensity, once the interaction of radiation within the ligament is finished, one can numerically compute the ratios $\hat{R}_{DH}$ and $\hat{T}_{DH}$ between the entering flux F_{in} and respectively the backward outgoing flux F^-_{out} and the forward outgoing flux F^+_{out} according to the following ex-

pressions :

$$\begin{cases} \hat{R}_{DH} = \dfrac{F_{out}^{-}}{F_{in}} \quad ; \quad \hat{T}_{DH} = \dfrac{F_{out}^{+}}{F_{in}} \\ \\ F_{in} = \displaystyle\int_{\partial\mathcal{D}_0} (1-\rho_s)\omega_{\boldsymbol{s}_0}\tilde{I}(\boldsymbol{x},\boldsymbol{s}_0)|\boldsymbol{s}_0\cdot\boldsymbol{n}|\ \mathrm{d}\Gamma \\ F_{out}^{-} = \displaystyle\sum_{m=1}^{N_d}\int_{\partial\mathcal{D}^{m+}} (1-\rho_s)\omega_m I_m(\boldsymbol{x},\boldsymbol{s}_0)|\boldsymbol{s}_m\cdot\boldsymbol{n}|\mathbb{1}_{[\boldsymbol{s}_m\cdot\boldsymbol{e}_y<0]}\ \mathrm{d}\Gamma \\ F_{out}^{+} = \displaystyle\sum_{m=1}^{N_d}\int_{\partial\mathcal{D}^{m+}} (1-\rho_s)\omega_m I_m(\boldsymbol{x},\boldsymbol{s}_0)|\boldsymbol{s}_m\cdot\boldsymbol{n}|\mathbb{1}_{[\boldsymbol{s}_m\cdot\boldsymbol{e}_y>0]}\ \mathrm{d}\Gamma \end{cases} \tag{4.32}$$

Let us precise that the subscript DH stands for directional hemispherical. Furthermore, one assumes that the reflective behavior of the struts is dominated by specular reflections that is plausible for ligaments composed of micronic grains.

Material properties

Once the geometry of the ligament is known, it is assigned the volumetric radiative properties of three representative ceramic materials often used for engineering devices where thermal radiation dominates the heat transport. A particular attention is paid to select chemical composition being able to illustrate either a semitransparent behaviour or an opaque one for the same thickness of propagation within the ligament. One uses the work of Makino et al. [81], who determined the volumetric radiative properties of low porous refractory ceramics 2-3 percent for wavelengths ranging from 0.4 to 33.3 μm and at temperatures going from 290 to 700 K. Table 1 presents the properties recorded for a wavelength of 2 μm. They were obtained with an identification procedure where experimental reflectance and transmittance spectra where reproduced through a four-flux model, assuming moreover an isotropic scattering for the scattering phase function. For these cases, the choice of an isotropic scattering phase function was justified by the authors because, although the samples consisted of a small micron size pore population, they were composed of a high density of micronic grains, almost randomly arranged, which acted as high multiple scattering centers. This assumption was later reused by Zeghondy et al.[44] to characterize, trough an adding-doubling technique, the radiative properties of a dense mullite ceramic which were used, afterwards, to identify the macroscopic radiative properties of an open-cell mullite foam. Eldrige et al. [82] also used a similar hypothesis for interpreting the radiative properties of plasma-sprayed yttria-stabilized ziconia ceramic applied for the design thermal barrier coatings. However the texture of the specimens had to be different (mean grain size must be higher), which perhaps makes the hypothesis of isotropy for the scattering phase function less valuable. Dombrovsky et al.[83] found for porous zirconia ceramics (porosity about 16 percent) a asymmetry factor of scattering of 0.5 gives more importance to the forward scattering but the studied texture was different from those of the samples of Makino et al.. Even if certain ceramics can be characterized by an anisotropic scattering phase functions [84], one considers that the isotropic scattering behaviours proposed by Makino et al. is sufficient to model afterwards the radiative transport within ceramic ligaments obtained through the replica method as it is the case in this work. The replica method, based on sintering ceramic process [29], allows

the obtaining ligaments composed of grains and pores with micronic sizes. Let us now give some comments on the absorption and the scattering coefficients provided in table 1. For the opaque silicon carbide ceramic, $\kappa = 250$ cm^{-1} and the scattering albedo, $\omega = \sigma_s/(\sigma_s + \kappa)$ is smaller than 0.1. It means that the diffuse light backscattering contribution is likely to be rather negligible : the length of propagation is found to be 185 μm for across travel thickness of 135 μm. On the contrary, absorption coefficient for alumina and zirconia permit a travel of the light on higher distances (respectively 495 μm and 306 μm). The computed albedo properties are in good agreement with other identification works where the semi-transparent features are underlined (respectively $\omega \approx 0.97$ and $\omega \approx 0.99$). Indeed,, by using also a four-flux model, Eldrige et al. [82] found for plasma-sprayed zirconia layers previously discussed, a value of 650 cm^{-1} for σ_s and less than 1 cm^{-1} for κ . Zeghondy et al. [44] determined for a dense ceramic of mullite that $\omega = 0.993$, $\sigma_s \approx 1040$ cm^{-1} , $\kappa \approx 10$ cm^{-1}. For all the three compositions, the real part of the complex refractive indices are higher than 1.7. Let us now describe the propagation of the thermal radiation within the ligament, thanks to the numerical study, in order to get a more quantitative appraisal.

Sample	κ (cm^{-}1)	σ_s (cm^{-}1)	Φ	$\mathcal{R}(\tilde{n})$
alumina	3	90	isotropic	1.7
zirconia	0.09	150	isotropic	2.2
silicon carbide	250	25	none	2.4

TABLEAU 4.1 – Volumetric radative properties (absorption and scattering coefficients, scattering phase function) and real part of the refractive indices for alumina, zirconia and silicon carbide ceramics.

Angular discretization

At first, the choice of the angular mesh fineness is essential to obtain a stabilized solution. The research is done for the ligament of alumina, i.e. $\kappa = 3$ cm^{-1}, $\sigma_s = 90$ cm^{-1} and $n = 1.7$, for the three discretizations represented in Fig. 4.8. The ligament of alumina presents the highest length of extinction with a high albedo so that the weight of the scattering is predominant in the transport of radiation. Figures 4.12 to 4.15 represent the computed radiative density $D(\boldsymbol{x})$ that is transported within the ligament, this quantity being computed by :

$$D(\boldsymbol{x}) = \sum_{m=1}^{N_d} \omega_m I_m(\boldsymbol{x}) \tag{4.33}$$

Firstly, Figure 4.12 presents all in one, the three orthogonal cross-section representations of radiative density within the ligament. Figures 4.13, 4.14 and 4.15 then present the cross-sections orthogonal to $\boldsymbol{e}_x$, $\boldsymbol{e}_y$ and $\boldsymbol{e}_z$, respectively. Note that the point $\boldsymbol{x}_0 = (18.75\ \mu\text{m}, 17.28\ \mu\text{m}, 18.38\ \mu\text{m})$ is the intersection point between the three cross-sections. As previously mentioned, 20 directions are used for the figures layed out on the left hand side, 80 directions are used for the figures layed out in the middle, and 320 directions are used for the figures layed out on the right hand side.

The solution computed with 20 directions is clearly different from those obtained with more directions. Indeed, the extraction of the main direction of propagation within the ligament shows a deviation of approximately 5° when compared with the ones

computed with 80 and 320 directions. This is realized essentially through Fig. 4.13 because the direction of propagation is almost orthogonal to $\boldsymbol{e}_x$. Obviously, the choice of 20 directions in the angular discretization may lead to an underestimation of the deviation angle of the radiation transport within the ligament. Let us recall that the deviation of the propagation (respectively to $\boldsymbol{e}_y$) is due to the refraction phenomenon, according to the Snell-Descartes law. Moreover, the choice of 20 directions also underestimates the area of propagation as can be seen on the cross-section views of Figure 4.13. By defining the area of propagation as the spatial domain where the radiation density is higher than 250, the choice of 20 directions for the computation divides this area by a factor of roughly 2 as can be realized by this figure. Figures 4.14 and 4.15 also show the ray effect appearing when using too few directions [85].

The numerical results obtained with 80 directions tend towards those obtained with 320 directions, even though some differences remain. At first, one can realize that the main propagation direction has converged. However, the radiative density amplitude is smaller with 80 directions than with 320 directions. The difference may come from the scattering effect, on one hand, and from the reflection effect on the other hand, that are much better approximated with 320 directions than with 80 directions.

Note that for a simple cubic geometry, the S_8 quadrature is often used [86]. This quadrature, that yields 80 directions in total, is most of the time enough because of all symmetries. Elsewhere, in 1D and 2D geometries, some tests have been performed using many directions, but with no scattering [87]. However, few people use more than 80 directions, even for complex geometries, mainly because the size of the finite element matrices becomes huge [14].

It has been realized by this study, because of the very complicated geometry, and also because of the coupled involved phenomena, that 80 directions only give approximate results ; the use of 320 directions is indeed necessary to obtain accurate converged solutions.

Finally, let us say that it would have been interesting to perform computations at the next level of sphere discretization through icosahedra (i.e. with 1280 directions), but this would imply huge matrix systems, that are not solvable yet at this stage of research.

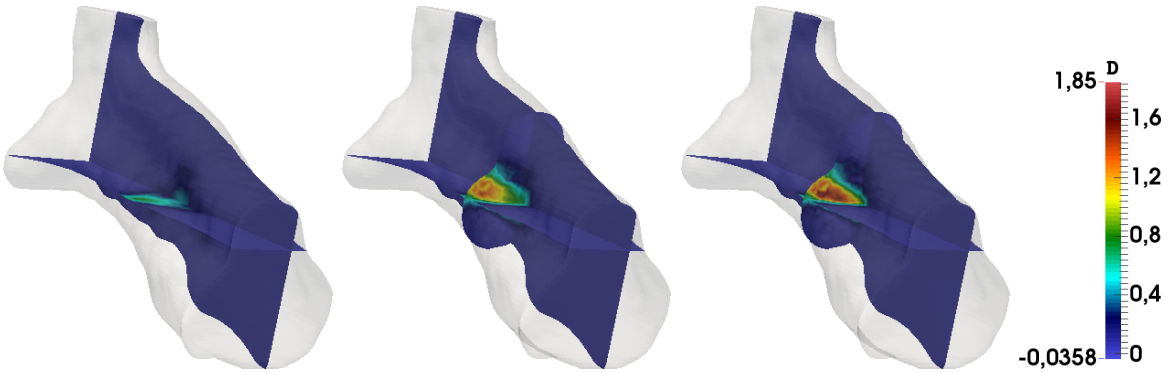

FIGURE 4.12 – Volumic representation of the normalized radiative density for the ligament of alumina with, from left to right, 20, 80, and 320 directions.

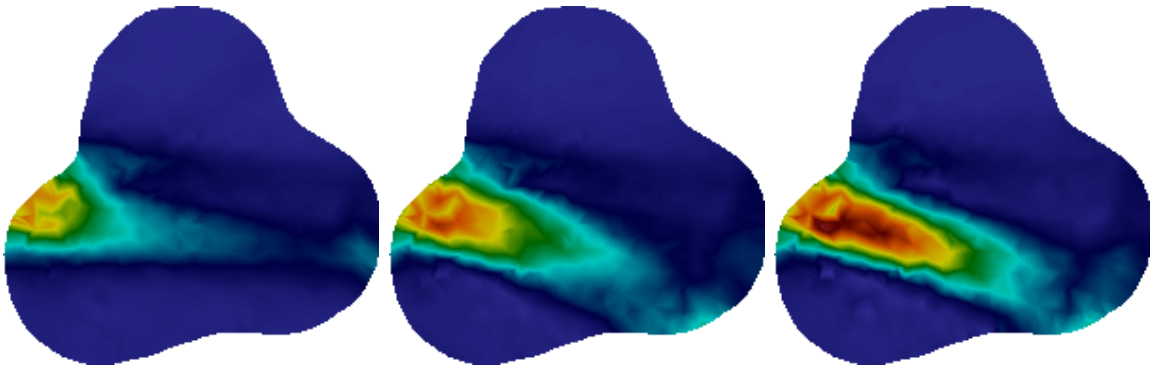

FIGURE 4.13 – Cross-section (normal to $\boldsymbol{e}_x$ and passing by $\boldsymbol{x}_0$) representation of the normalized radiative density for the ligament of alumina with, from left to right, 20, 80, and 320 directions.

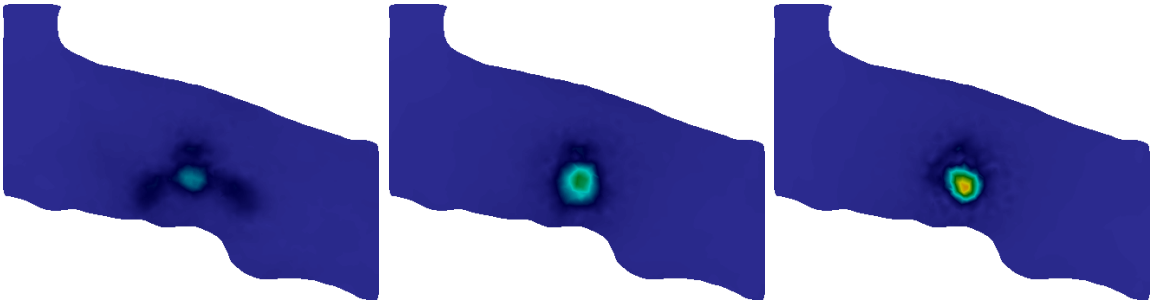

FIGURE 4.14 – Cross-section (normal to $\boldsymbol{e}_y$ and passing by $\boldsymbol{x}_0$) representation of the normalized radiative density for the ligament of alumina with, from left to right, 20, 80, and 320 directions.

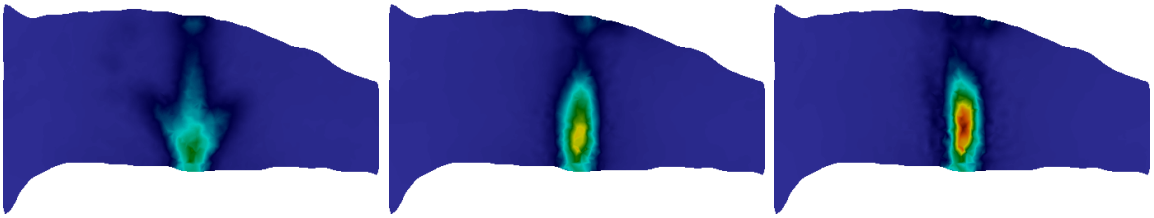

FIGURE 4.15 – Cross-section (normal to $\boldsymbol{e}_z$ and passing by $\boldsymbol{x}_0$) representation of the normalized radiative density for the ligament of alumina with, from left to right, 20, 80, and 320 directions.

Effect of the volumetric radiative properties

According to volumetric radiative properties of the selected material, the volumetric propagation of the radiative intensity exhibit different behaviours.

For the whole set of compound, the refractive index is high ($n \in [1.7, 2.4]$). This is the reason why the main direction of propagation $\bar{\boldsymbol{s}}_r$, defined in Section 4.3.3, deviates from $\boldsymbol{e}_y$, according to the Snell-Descartes laws. The computed mean angle of deviation along with the main direction of propagation of the beam are given in Table 4.2. Such deviation of the main propagation of the beam can also be realized in Figure 4.16 which presents cross-section orthogonal to $\boldsymbol{e}_x$ of the radiative density $D(\boldsymbol{x})$ within the ligament composed of alumina, zirconia and silicon carbide, respectively.

From Figure 4.16, it is also seen that the radiative density for the silicon carbide is more localized in the vicinity of the illuminated boundary, when compared to the two other materials. This is explained by the fact that the silicon carbide is more absorbing than the two other materials. To add more, the maximum of the radiative density for the silicon carbide is almost half than that for the alumina and the zirconia.

Moreover, because the alumina ligament is more absorbing and less scattering than the zirconia ligament, as shown in Table 4.1, then the beam travels further within the material. This can also be realized thanks to Figure 4.16, pointing out that the extinction coefficient of the alimina is 1.6 times less than that of the zirconia.

Sample	direction of propagation $\bar{\boldsymbol{s}}_r$	deviation angle
alumina	(0.0327, 0.992, -0.119)	7.25°
zirconia	(0.0433, 0.987, -0.153)	9.25°
silicon carbide	(0.0464, 0.986, -0.163)	9.60°

TABLEAU 4.2 – Main direction of propagation of the beam, $\bar{\boldsymbol{s}}_r$, and its deviation with respect to $\boldsymbol{s}_0$.

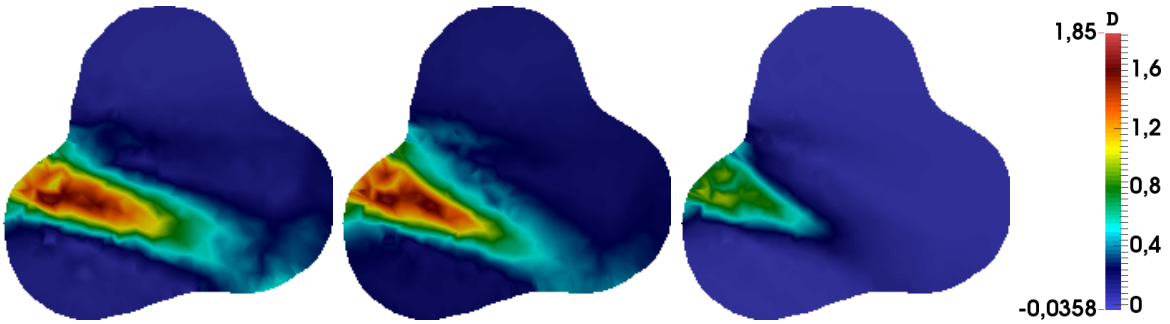

FIGURE 4.16 – Cross-section (normal to $\boldsymbol{e}_z$ and passing by $\boldsymbol{x}_0$) representation of the normalized radiative density for alumina, zirconia and silicon carbide with 320 directions.

To go one step further in the analysis, let us define the so-called propagating volume, V^ℓ, equal to the volume truncated to the condition that the normalized radiative density $\bar{D}(\boldsymbol{x}) = D(\boldsymbol{x})/D_0$ is greater than the level ℓ, i.e. $V^\ell = V_{[\bar{D}(\boldsymbol{x})>\ell]}$. Figure 4.17 depicts different contours of the propagating volume function V^ℓ for alumina, zirconia and silicon carbide ligaments, respectively. The blue contour presents the propagating

volume for the density level ℓ equals to 0.12, the green contour presents the propagating volume for $\ell = 0.2$, and the red one presents the propagating volume for $\ell = 0.4$.

To interpret the visualization of the the propagating volumes depicted in Figure 4.17, one can associate a secondary reading based on the computations of their respective values which are exposed in Table 4.3. First, let us notify that all the volumes for alumina and zirconia present a nearly central symmetry, as is can be expected since both materials have an isotropic scattering phase function. Furthermore, one can see that the volumetric propagation of the beam is less broadened for the alumina sample than for the zirconia sample. Indeed, the scattering volume $V^{0.12}$ for the zirconia sample is 1.64 times bigger than the one for the alumina sample : in Figure 4.17 it can be realized that the radiative density propagating within the zirconia is spread more than the one propagating within alumina. The extent of the spread is characterized by its larger area for the corresponding low radiative density values. The size of the envelop can be explained by the absorbing properties of the ceramic, smaller sizes of envelop mean stronger influence of absorbing coefficient. In our case, the absorbing coefficient of zirconia is 33 times weaker than the one of alumina. On the other hand, the propagating volume $V^{0.4}$ for the alumina sample, that represents the highest presented radiative density value, is 1.23 times bigger than the one relative to the ziconia. This may be due to the highest scattering coefficient of zirconia which limits more the extension of the radiation intensity in comparison with the case of alumina. Our results suggest that for semitransparent media, two competitive phenomena between absorption and scattering may be underlined. In the contrary, for a more opaque compound such as the ligament of silicon carbide, the beam is efficiently absorbed in the vicinity of its entrance and is therefore much less scattered. This is the reason why, V^{ℓ}, with $\ell = 0.12$ is nearly equal to V^{ℓ}, with $\ell = 0.2$ as the propagation is stopped.

Sample	$V^{0.12}$	$V^{0.2}$	$V^{0.4}$
alumina	4.68×10^5 μm^3	2.53×10^5 μm^3	9.14×10^4 μm^3
zirconia	7.67×10^5 μm^3	2.40×10^5 μm^3	7.42×10^4 μm^3
silicon carbide	7.92×10^4 μm^3	5.09×10^4 μm^3	2.23×10^4 μm^3

TABLEAU 4.3 – Propagating volumes V^{ℓ}, for $\ell = 0.12$, 0.2 and 0.4, respectively, according to Figure 4.17.

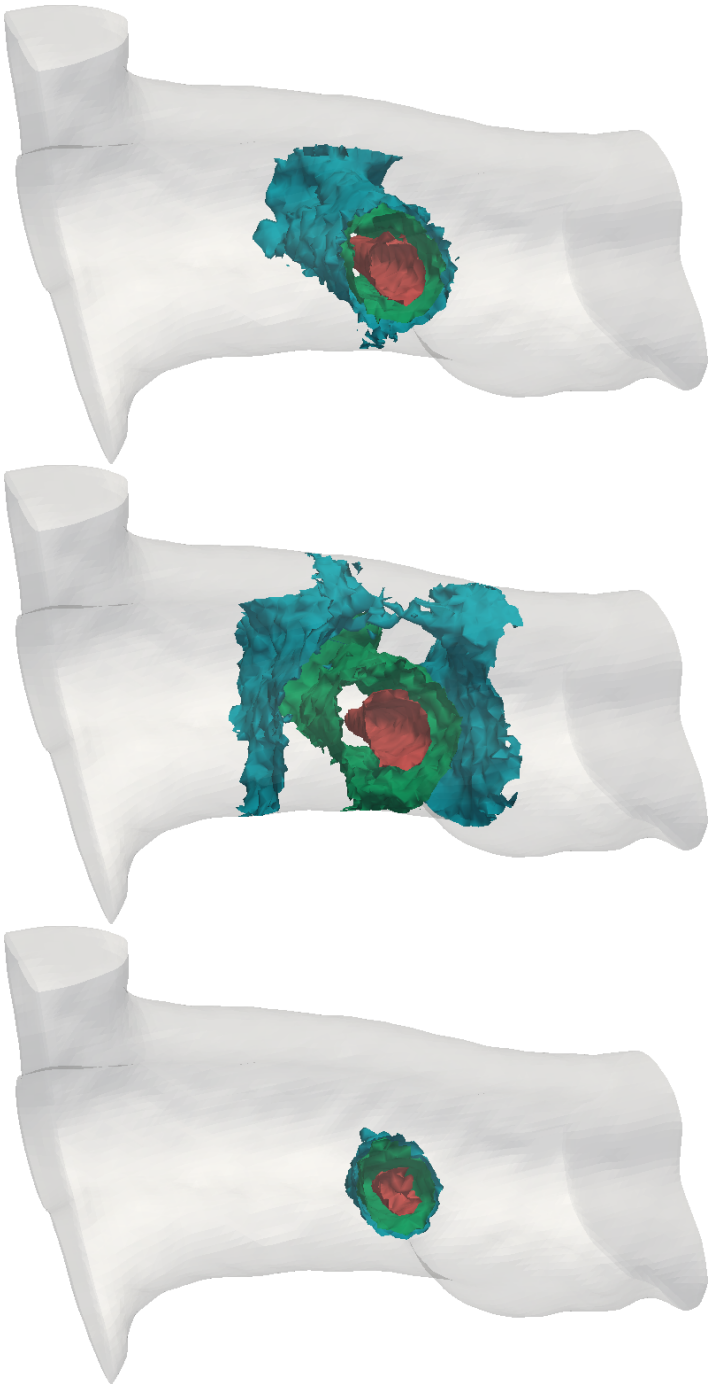

FIGURE 4.17 – Scattering volumes V^{ℓ} for $\ell = 0.12$ (blue), $\ell = 0.2$ (green), and $\ell = 0.4$ (red). Top : Alumina – middle : Zirconia – bottom : Silicon carbide

Backward and forward radiative flux

From the collection of the radiative intensity in the upper and lower hemispheres around the ligament, one can plan to compute the directional hemispherical reflectance and directional hemispherical transmittance, similarly as it can be done with an experimental integrating sphere [33]. To calculate these two quantities, it is necessary to determine the backward flux $Q^-(\boldsymbol{x})$, as well as the forward flux $Q^+(\boldsymbol{x})$, both being calculated within the whole domain. These two quantities are defined by :

$$\begin{cases} Q^-(\boldsymbol{x}) = \sum\limits_{\boldsymbol{s}_m \cdot \boldsymbol{s}_0 < 0} \omega_m I_m(\boldsymbol{x}) |\boldsymbol{s}_m \cdot \boldsymbol{s}_0| \\ Q^+(\boldsymbol{x}) = \sum\limits_{\boldsymbol{s}_m \cdot \boldsymbol{s}_0 > 0} \omega_m I_m(\boldsymbol{x}) |\boldsymbol{s}_m \cdot \boldsymbol{s}_0| \end{cases} \tag{4.34}$$

where $\boldsymbol{s}_0$ is the prescribed direction of the beam.

Figure 4.18 presents the backward flux $Q^-(\boldsymbol{x})$ within the media, for the three studied materials. Note that the related forward flux is not represented, for the sake of conciseness. For each material, a cross-section containing the propagation direction is presented, as well as values of the backward flux on the front border of impingement. To add more, the contour of the impingement surface is also represented. All these views have been chosen in order to point out the effect of scattering and reflections on the map of backward flux.

Firstly, the effect of specular reflection can be clearly seen at the rear border of the ligament for both the alumina and the zirconia (see Figure 4.18 top-left and Figure 4.18 middle-left). When compared to the backward flux for the alumina, the backward flux propagating within the zirconia is more spread out due to its higher refractive index, as can be realized by these figures. The other reason why the backward flux is more spread out for the zirconia than that for the alumina is of course because of its inherent scattering coefficient which is almost twice as much. Moreover, the silicon carbide being highly absorbing and less scattering, the backward flux becomes very small, at least when compared to the two other materials.

Secondly, the backward flux is spread out for both the alumina and the zirconia, and this is to be compared to the size of impingement of the incoming beam. Therefore, from an experimenter point of view, it means that in these two cases, capturing the back-scattered radiant intensity requires to adapt the optical system of collection with an aperture with a size higher than the one defined by the diameter of the incident beam. However when the medium presents a strong absorption behaviour as it is the case for the silicon carbide, the size of the aperture can be reduced, and the optical system of collection may be not adapted. However, for all cases, the backward flux is not null on the rear border, so that one can expect to be able to measure transmitted outgoing flux.

Table 4.4 gives the relative transmittance $\hat{T}_{DH}$ and relative reflectance $\hat{R}_{DH}$ defined previously in equation (4.32), as well as the relative directional absorptance $\hat{A}_b = 1 - \hat{T}_{DH} - \hat{R}_{DH}$. These three quantities are given for the three studied materials : alumina, zirconia and silicon carbide.

For silicon carbide ligament, the value of $\hat{R}_{DH}$ is very low ; this is due to the high

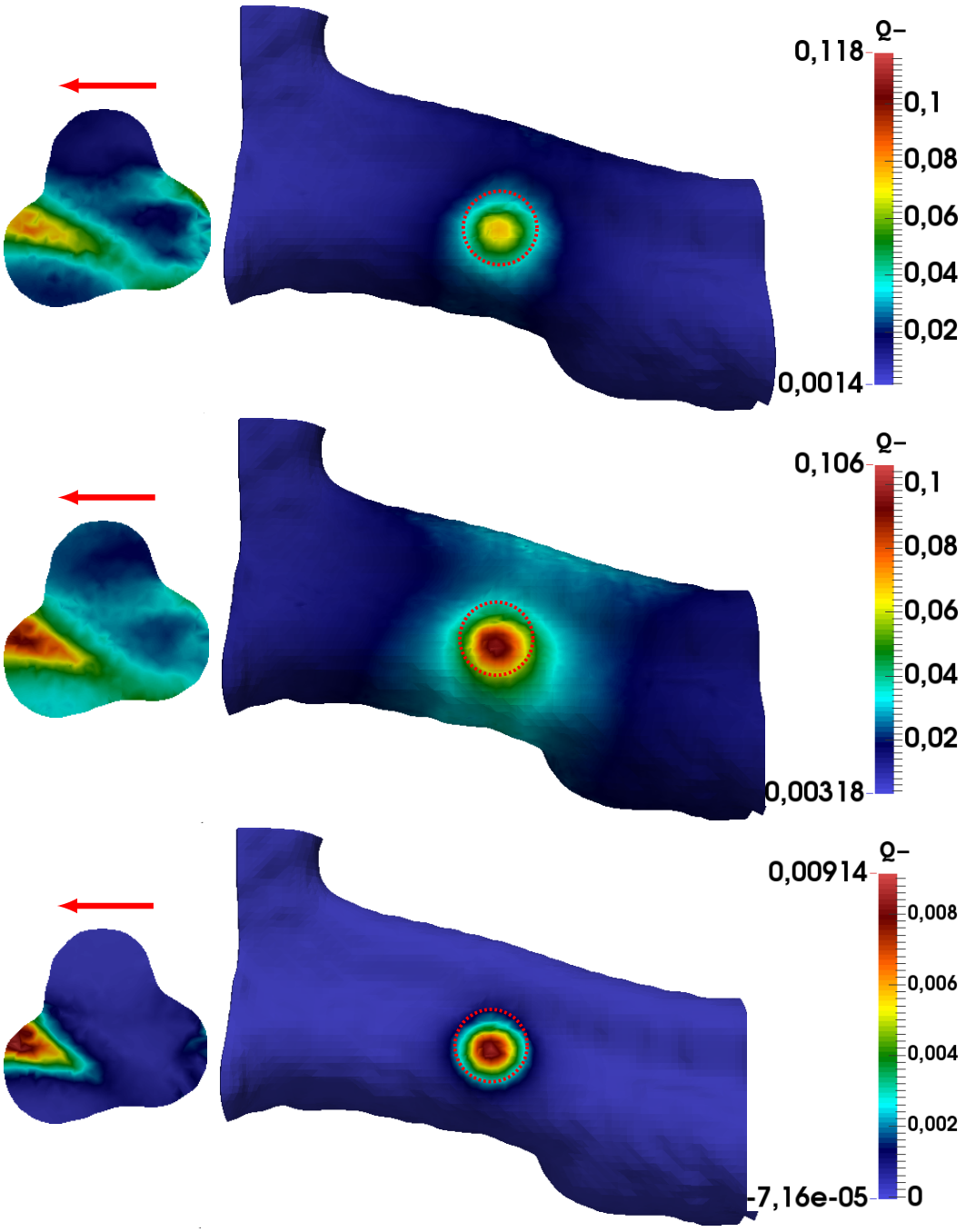

FIGURE 4.18 – Backward flux Q^- as defined by (4.34). Top : alumina, middle : zirconia, bottom : silicon carbide. Left : cross-section normal to $\boldsymbol{e}_x$ and passing by $\boldsymbol{x}_0$. Right : outgoing flux Q^- on the front border and representation of the impingement surface contour.

absorbing power of this material. Contrarily, $\hat{R}_{DH}$ is almost hundred times bigger for both alumina and zirconia ligaments. This is explained because these two materials are much less absorbing, even though they are more scattering.

Moreover, the value of $\hat{T}_{DH}$ for the silicon carbide is also the lowest. This is due to its inherent high extinction coefficient $\beta = 275$ cm^{-1}, which is 1.8 times bigger than the ziconia's extinction coefficient and 3.0 times bigger than the alumia's extinction coefficient. Also, its albedo ($\omega = 0.09$) is the lowest between the three materials.

According to the size of the extinction coefficient, the value $\hat{T}_{DH}$ relative to the alumina is 1.3 times greater than that relative to the zirconia. This is because the scattering coefficient σ_s and the refractive index n of the zirconia are higher than for the alumina. In particular, it had been demonstrated for semitransparent millimetric composands that when the refractive index increases, the hemispherical transmittance decreases [88]. So, our results are consistent with previous work. This balance point may explain the similarity between the $\hat{R}_{DH}$ of the alumina and the zirconia. Consequently, the silicon carbide ligament is close to be fully absorbing as expected for an optically thick medium ; the zirconia, appears quite absorbing, partly due to its high refractive index ; and the alumina is less absorbing, due to its low extinction coefficient and its low refractive index. However, let us precise that these results can not constitute a quantitative and definitive analysis since the contribution of the specular reflection is not integrated in the definition of $\hat{R}_{DH}$. Indeed, one can see roughly that ρ_s for zirconia is 0.14 for the normal incident whereas it is 0.06 for alumina.

Sample	$\hat{T}_{DH}$	$\hat{R}_{DH}$	$\hat{T}_{DH} + \hat{R}_{DH}$	$\hat{A}_b$
alumina	0.539	0.371	0.910	0.090
zirconia	0.425	0.354	0.778	0.222
silicon carbide	0.00554	0.00283	0.00837	0.99163

TABLEAU 4.4 – Relative transmittance $\hat{T}_{DH}$, relative reflectance $\hat{R}_{DH}$ and relative absortance $\hat{A}_b$ for alumina, zirconia and silicon carbide.

4.4.1 Conclusion

A three-dimensional modelling of the propagation of radiative intensity within a real X-ray tomographied ligament has been performed. From a numerical point of view, developments are based on a discrete ordinate method (DOM) coupled with stabilized finite elements (SUPG), the GMRES solver and the MPI library. Particular attention has been paid on the accurate treatment of specular conditions on borders. Such numerical developments enabled us to predict the volumetric transport of radiation in such a complex geometry, and perform a parametric study of global energetic quantities such as relative reflectance, transmittance and absorptance with respect to several volumetric radiative properties such as absorption and scattering phase function and and optical properties such as the refractive index. The latter properties allow to change the radiative behaviour of the ligament from a semi-transparent one to an opaque one. This paper introduces a first study on the radiative transfer into a submillimetric ligament. Next studies will concern the modelling on different geometries in order to point out the effects of ligament shapes on radiative heat transfer, complementarily to [43]. The main

highlight of this work is that it constitutes as a preliminary step for the investigation of the thermal radiative properties of a ligament of a small open-cell foam with complex geometry at microscale. Also, from a numerical point of view, due to the choice of discrete ordinates – which is in this special case equivalent to $\mathcal{P}_0$ Lagrange functions in a finite element context – the number of needed directions is very high to get accurate results due to the great complexity of the geometry. The use of higher-order Lagrange functions would certainly reduce the number of needed directions. Future numerical developments will also deal with a more accurate treatment of the incoming beam for which multiple external reflections may occur.

Références

[1] S. Prahl, M. Keijzer, S. Jacques, A. Welch, A Monte Carlo model of light propagation in tissue, Dosimetry of laser radiation in medicine and biology 5 (1989) 102–111. 146, 147

[2] L. Dombrovsky, J. Randrianalisoa, D. Baillis, Modified two-flux approximation for identification of radiative properties of absorbing and scattering media from directional-hemispherical measurements, Optical Society of America A 23 (1) (2006) 91–98. 146, 147

[3] F. Asllanaj, G. Jeandel, J. Roche, Numerical solution of radiative transfer equation coupled with nonlinear heat conduction equation, International Journal of Numerical Methods for Heat & Fluid Flow 11 (5) (2001) 449–473. 153

[4] A. Bruno, A. Maurente, B. Lamien, H. Orlande, Numerical simulation of nanoparticles assisted laser photothermal therapy : a comparison of the P1-approximation and discrete ordinate methods, Journal of the Brazilian Society of Mechanical Sciences and Engineering (2016) 1–10. 153

[5] D. Lacroix, G. Parent, F. Asllanaj, G. Jeandel, Coupled radiative and conductive heat transfer in a non-grey absorbing and emitting semitransparent media under collimated radiation, Journal of Quantitative Spectroscopy and Radiative Transfer 75 (5) (2002) 589–609. 153

[6] D. Lacroix, N. Berour, P. Boulet, G. Jeandel, Transient radiative and conductive heat transfer in non-gray semitransparent two-dimensional media with mixed boundary conditions, Heat and Mass Transfer 42 (4) (2006) 322–337. 153

[7] G.-J. Li, J. Ma, B.-W. Li, Collocation Spectral Method for the Transient Conduction–Radiation Heat Transfer With Variable Thermal Conductivity in Two-Dimensional Rectangular Enclosure, Journal of Heat Transfer 137 (3) (2015) 032701. 153

[8] X.-H. Luo, B.-W. Li, J.-K. Zhang, Z.-M. Hu, Simulation of thermal radiation effects on MHD free convection in a square cavity using the Chebyshev collocation spectral method, Numerical Heat Transfer, Part A : Applications 66 (7) (2014) 792–815. 153

[9] J. Sun, H.-L. Yi, H.-P. Tan, Local RBF meshless scheme for coupled radiative and conductive heat transfer, Numerical Heat Transfer, Part A : Applications (2016) 1–15. 153, 154

[10] C.-A. Wang, H. Sadat, J.-Y. Tan, Meshless method for solving coupled radiative and conductive heat transfer in refractive index medium, in : Journal of Physics : Conference Series, Vol. 676, IOP Publishing, 2016, p. 012024. 153, 154

[11] J. Howell, R. Siegel, M. Mengüç, Thermal Radiation Heat Transfer, CRC press, 2011. 153, 154, 155, 161

[12] M. Modest, Radiative Heat Transfer, 3rd Edition, Academic press, New York, 2013. 153, 154, 161

[13] D. Le Hardy, Y. Favennec, B. Rousseau, Solution of the 2-D steady-state radiative transfer equation in participating media with specular reflections using SUPG and DG finite elements, Journal of Quantitative Spectroscopy and Radiative Transfer 179 (2016) 149–164. 153, 154, 162

[14] R. Castro, J. Trelles, Spatial and angular finite element method for radiative transfer in participating media, Journal of Quantitative Spectroscopy and Radiative Transfer 157 (2015) 81–105. 153, 172

[15] E. Hachem, H. Digonnet, E. Massoni, T. Coupez, Immersed volume method for solving natural convection, conduction and radiation of a hat-shaped disk inside a 3D enclosure, International Journal of Numerical Methods for Heat & Fluid Flow 22 (6) (2012) 718–741. 153

[16] P. Boulet, A. Collin, J. Consalvi, On the finite volume method and the discrete ordinates method regarding radiative heat transfer in acute forward anisotropic scattering media, Journal of Quantitative Spectroscopy and Radiative Transfer 104 (3) (2007) 460–473. 153

[17] P. Coelho, Advances in the discrete ordinates and finite volume methods for the solution of radiative heat transfer problems in participating media, Journal of Quantitative Spectroscopy and Radiative Transfer 145 (2014) 121–146. 153

[18] L. Zhang, J. Zhao, L. Liu, Finite element method for modeling radiative transfer in semitransparent graded index cylindrical medium, Journal of Quantitative Spectroscopy and Radiative Transfer 110 (13) (2009) 1085–1096. 154

[19] G. Kanschat, E. Meinköhn, R. Rannacher, R. Wehrse, Numerical methods in multidimensional radiative transfer, Springer, 2009. 154, 156

[20] Y.-S. Sun, B.-W. Li, Spectral collocation method for transient conduction-radiation heat transfer, Journal of Thermophysics and Heat Transfer 24 (4) (2010) 823–832. 154

[21] Y. Sun, X. Zhang, Analysis of transient conduction and radiation problems using lattice Boltzmann and finite volume methods, International Journal of Heat and Mass Transfer 97 (2016) 611–617. 154

[22] J. Zmywaczyk, P. Koniorczyk, Numerical Solution of Inverse Radiative–Conductive Transient Heat Transfer Problem in a Grey Participating Medium, International Journal of Thermophysics 30 (4) (2009) 1438–1451. 154

[23] A. Sakurai, S. Mishra, S. Maruyama, Radiation element method coupled with the lattice Boltzmann method applied to the analysis of transient conduction and radiation heat transfer problem with heat generation in a participating medium, Numerical Heat Transfer, Part A : Applications 57 (5) (2010) 346–368. 154

[24] J. Tencer, J. Howell, Coupling radiative heat transfer in participating media with other heat transfer modes, Journal of the Brazilian Society of Mechanical Sciences and Engineering 38 (5) (2016) 1473–1487. 154

[25] J. Grandpeix, A. Lahellec, Monte Carlo simulation of radiation in gases with a narrow-band model and a net-exchange formulation, Journal of Heat Transfer 118 (1996) 401. 154

[26] J. Delatorre, G. Baud, J. Bézian, S. Blanco, C. Caliot, J. Cornet, C. Coustet, J. Dauchet, M. El Hafi, V. Eymet, et al., Monte Carlo advances and concentrated solar applications, Solar Energy 103 (2014) 653–681. 154

[27] J. Kajiya, B. Von Herzen, Ray tracing volume densities 18 (3) (1984) 165–174. 154

[28] R. Fournier, S. Blanco, V. Eymet, M. El Hafi, C. Spiesser, Radiative, conductive and convective heat-transfers in a single Monte Carlo algorithm 676 (1) (2016) 012007. 154

[29] A. Füssel, D. Böttge, J. Adler, F. Marschallek, A. Michaelis, Cellular ceramics in combustion environments, Advanced Enginnerring Materials 13 (2011) 1008–1014. 159, 160, 163, 170

[30] A. Kribus, Y. Gray, M. Grijnevich, G. Mittelmanand, S. Mey-Cloutier, C. Caliot, The promise and challenge of solar volumetric absorbers, Solar Energy 110 (2014) 463–481. 159, 160

[31] A. Banerjee, R. Chandran, J. Davidson, Experimental investigation of a reticulated porous alumina heat exchanger for high temperature gas heat recovery, Applied Thermal Engineering 75 (2015) 889–895. 159

[32] D. Baillis, J. Sacadura, Thermal radiation properties of dispersed media : theoretical prediction and experimental characterization, Journal of Quantitative Spectroscopy and Radiative Transfer 67 (2000) 327–363. 160

[33] S. Guévelou, B. Rousseau, G. Domingues, J. Vicente, C. Caliot, Representative elementary volumes required to characterize the normal spectral emittance of silicon carbide foams used as volumetric solar absorbers, International Journal of Heat and Mass Transfer 93 (2016) 118–129. 160, 161, 177

[34] B. Dietrichk, T. Fischedick, S. Heissler, P. Weidler, C. Wöll, M. Kind, Optical parameters for characterization of thermal radiation in ceramic sponges-experimental results and correlation, International Journal of Heat and Mass Transfer 79 (2014) 655–665. 160

[35] B. Zeghondy, E. Iacona, , J. Taine, Determination of the anisotropic radiative properties of a porous material by radiative distribution function identification (RDFI), International Journal of Heat and Mass Transfer 49 (2006) 2810–2819. 160

[36] T. Hendricks, J. Howell, Absorption/scattering coefficients and scattering phase functions in reticulated porous ceramics, Journal of Heat Transfer 118 (1996) 79–87. 160

[37] B. Rousseau, D. De Sousa Meneses, P. Echegut, J. Thovert, Textural parameters influencing the radiative properties of a semitransparent porous media, International Journal of Thermal Sciences 50 (2011) 178–186. 160

[38] V. Deshpande, M. Ashby, N. Fleck, Foam topology : bending versus stretching dominated architectures, Acta Materialia 49 (2001) 1035–1040. 160

[39] S. Guévelou, B. Rousseau, G. Domingues, J. Vicente, A simple expression for the normal spectral emittance of open-cell foams composed of optically thick and smooth struts, Journal of Quantitative Spectroscopy and Radiative Transfer 189 (2017) 329–338. 160

[40] M. Scheffler, P. Colombo, Cellular ceramics : structure manufacturing properties and applications, John Wiley & Sons, 2006. 160

[41] J. Randrianalisoa, D. Baillis, C. Martin, R. Dendievel, Microstructure effects on thermal conductivity of open-cell foams generated from the Laguerre–Voronoï tessellation method, International Journal of Thermal Sciences 98 (2015) 277–286. 160

[42] S. Cunsolo, M. Oliviero, W. Harris, A. Andreozzi, N. Bianco, W. Chiu, V. Naso, Monte carlo determination of radiative properties of metal foams : Comparison between idealized and real cell structures, International Journal of Thermal Sciences 87 (2015) 94–102. 160

[43] B. Šarler, N. Massarotti, P. Nithiarasu, S. Cunsolo, N. Baillis, D.and Bianco, V. Naso, M. Oliviero, Effects of ligaments shape on radiative heat transfer in metal foams, International Journal of Numerical Methods for Heat & Fluid Flow 26 (2) (2016) 477–488. 160, 179

[44] B. Zeghondy, E. Iacona, J. Taine, Experimental and rdfi calculated radiative properties of a mullite foam, International Journal of Heat and Mass Transfer 49 (19) (2006) 3702–3707. 160, 170, 171

[45] D. Rochais, R. Coquard, D. Baillis, Microscopic thermal diffusivity measurements of ceramic and metallic foams lumps in temperature, International Journal of Thermal Sciences 92 (2015) 179–187. 161

[46] D. Le Hardy, Y. Favennec, F. Hecht, B. Rousseau, Specular reflection treatment for the 3D radiative transfer equation solved with the discrete ordinates method, (submitted). 161, 165

[47] M. Loretz, R. Coquard, D. Baillis, E. Maire, Metallic foams : Radiative properties/comparison between different models, Journal of Quantitative Spectroscopy and Radiative Transfer 109 (1) (2008) 16–27. 162

[48] J. Spanier, E. Gelbard, Monte Carlo principles and neutron transport problems, Reading, Mass., USA. 162

[49] J. Howell, The Monte Carlo method in radiative heat transfer, Journal of Heat Transfer 120 (3) (1998) 547–560. 162

[50] P. Zhai, G. Kattawar, P. Yang, Impulse response solution to the three-dimensional vector radiative transfer equation in atmosphere-ocean systems. I. Monte Carlo method, Applied Optics 47 (8) (2008) 1037–1047. 162

[51] M. Modest, Backward Monte Carlo simulations in radiative heat transfer, Journal of Heat Transfer 125 (1) (2003) 57–62. 162

[52] S. Guévelou, B. Rousseau, G. Domingues, J. Vicente, C. Caliot, Representative elementary volumes required to characterize the normal spectral emittance of silicon carbide foams used as volumetric solar absorbers, International Journal of Heat and Mass Transfer 93 (2016) 118–129. 162

[53] C. Chan, D. Psaltis, F. Özel, GRay : A massively parallel GPU-based code for ray tracing in relativistic spacetimes, The Astrophysical Journal 777 (1) (2013) 13. 162

[54] J. Jeans, The equations of radiative transfer of energy, Monthly Notices of the Royal Astronomical Society 78 (1) (1917) 28–36. 162

[55] W. Ge, M. Modest, S. Roy, Development of high-order P N models for radiative heat transfer in special geometries and boundary conditions, Journal of Quantitative Spectroscopy and Radiative Transfer 172 (2016) 98–109. 162

[56] C. Sandoval, A. Kim, Extending generalized Kubelka–Munk to three-dimensional radiative transfer, Applied Optics 54 (23) (2015) 7045–7053. 162

[57] S. Chandrasekhar, Radiative Transfer, Courier Corporation, 2013. 162

[58] W. Fiveland, The selection of discrete ordinate quadrature sets for anisotropic scattering, Fundamentals of Radiation Heat Transfer 160 (1991) 89–96. 162

[59] Z. Lin, W. Li, C. Gatebe, R. Poudyal, K. Stamnes, Radiative transfer simulations of the two-dimensional ocean glint reflectance and determination of the sea surface roughness, Applied Optics 55 (6) (2016) 1206–1215. 162

[60] Z. Jin, K. Stamnes, Radiative transfer in nonuniformly refracting layered media : atmosphere–ocean system, Applied Optics 33 (3) (1994) 431–442. 162

[61] J. Chai, H. S. Lee, S. Patankar, Finite volume method for radiation heat transfer, Journal of Thermophysics and Heat Transfer 8 (3) (1994) 419–425. 162

[62] P. Coelho, Advances in the discrete ordinates and finite volume methods for the solution of radiative heat transfer problems in participating media, Journal of Quantitative Spectroscopy and Radiative Transfer 145 (2014) 121–146. 162

[63] M. Charest, C. Groth, Ö. Gülder, Solution of the equation of radiative transfer using a Newton–Krylov approach and adaptive mesh refinement, Journal of Computational Physics 231 (8) (2012) 3023–3040. 162

[64] G. Kanschat, A robust finite element discretization for radiative transfer problems with scattering, Citeseer, 1998. 162, 167

[65] P. Bochev, M. Gunzburger, J. Shadid, Stability of the SUPG finite element method for transient advection–diffusion problems, Computer Methods in Applied Mechanics and Engineering 193 (23) (2004) 2301–2323. 162

[66] G. Kanschat, E. Meinköhn, R. Rannacher, R. Wehrse, Numerical methods in multidimensional radiative transfer, Springer, 2009. 162, 164

[67] L. Zhang, J. Zhao, L. Liu, Finite element method for modeling radiative transfer in semitransparent graded index cylindrical medium, Journal of Quantitative Spectroscopy and Radiative Transfer 110 (13) (2009) 1085–1096. 162

[68] J. Pontaza, J. Reddy, Least-squares finite element formulations for one-dimensional radiative transfer, Journal of Quantitative Spectroscopy and Radiative Transfer 95 (3) (2005) 387–406. 162

[69] H. Gao, H. Zhao, A fast-forward solver of radiative transfer equation, Transport Theory and Statistical Physics 38 (3) (2009) 149–192. 162

[70] H. Gao, H. Zhao, Analysis of a numerical solver for radiative transport equation, Mathematics of Computation 82 (281) (2013) 153–172. 162

[71] X. He, E. Lee, L. Wilcox, R. Munipalli, L. Pilon, A high-order-accurate GPU-based radiative transfer equation solver for combustion and propulsion applications, Numerical Heat Transfer, Part B : Fundamentals 63 (6) (2013) 457–484. 162

[72] A. Walbron, S. Chupin, D. Rochais, R. Abraham, M. Bergounioux, 3d image segmentation and cylinder recognition for composite materials (2014) 47–52. 163

[73] W. Lorensen, H. Cline, Marching cubes : A high resolution 3D surface construction algorithm 21 (4) (1987) 163–169. 163

[74] C. Geuzaine, J.-F. Remacle, Gmsh : A 3-D finite element mesh generator with built-in pre-and post-processing facilities, International Journal for Numerical Methods in Engineering 79 (11) (2009) 1309–1331. 163

[75] L. G. Henyey, J. L. Greenstein, Diffuse radiation in the galaxy, The Astrophysical Journal 93 (1941) 70–83. 164

[76] A. N. Brooks, T. J. Hughes, Streamline upwind/petrov-galerkin formulations for convection dominated flows with particular emphasis on the incompressible navier-stokes equations, Computer methods in applied mechanics and engineering 32 (1-3) (1982) 199–259. 167

[77] F. Hecht, New development in FreeFem++, Journal of Numerical Mathematics 20 (3-4) (2012) 251–266. 168

[78] P. Griffiths, Infrared and raman instrumentation for mapping and imaging, Infrared and Raman spectroscopic imaging (2009) 3–64. 169

[79] G. Carr, Resolution limits for infrared microspectroscopy explored with synchrotron radiation, Review of Scientific Instruments 72 (3) (2001) 1613–1619. 169

[80] I. Yousef, S. Lefrançois, T. Moreno, H. Hoorani, F. Makahleh, A. Nadji, P. Dumas, Simulation and design of an infrared beamline for SESAME (Synchrotron-Light for Experimental Science and Applications in the Middle East), Nuclear Instruments and Methods in Physics Research Section A : Accelerators, Spectrometers, Detectors and Associated Equipment 673 (2012) 73–81. 169

[81] T. Makino, T.and Kunitomo, I. Sakai, H. Kinoshita, Thermal radiation properties of ceramic materials, Heat Transfer-Japanese Research 13 (1984) 33–50. 170

[82] J. Eldridge, C. Spuckler, J. Markham, Determination of scattering and absorption coefficients for plasma sprayed yttria stabilized zirconia thermal barrier coatings at elevated temperatures, Journal of the American Ceramic Society 92 (2009) 2276–2285. 170, 171

[83] L. A. Dombrovsky, H. K. Tagne, D. Baillis, L. Gremillard, Near-infrared radiative properties of porous zirconia ceramics, Infrared Physics & Technology 51 (1) (2007) 44–53. 170

[84] L. A. Dombrovsky, J. H. Randrianalisoa, W. Lipiński, D. Baillis, Approximate analytical solution to normal emittance of semi-transparent layer of an absorbing, scattering, and refracting medium, Journal of Quantitative Spectroscopy and Radiative Transfer 112 (12) (2011) 1987–1994. 170

[85] J. Chai, H. Lee, S. Patankar, Ray effect and false scattering in the discrete ordinates method, Numerical Heat Transfer, Part B Fundamentals 24 (4) (1993) 373–389. 172

[86] W. Fiveland, A. Jamaluddin, Three-dimensional spectral radiative heat transfer solutions by the discrete-ordinates method, Journal of Thermophysics and Heat Transfer 5 (3) (1991) 335–339. 172

[87] M. Ramankutty, A. Crosbie, Modified discrete ordinates solution of radiative transfer in two-dimensional rectangular enclosures, Journal of Quantitative Spectroscopy and Radiative Transfer 57 (1) (1997) 107–140. 172

[88] O. Rozenbaum, D. De Sousa Meneses, P. Echegut, P. Levitz, Influence of the texture on the radiative properties of semitransparent materials. comparison between model and experiment, High Temperatures—High Pressures 32 (2000) 61–66. 179

Conclusions et perspectives

Nous nous sommes intéressés dans cette thèse au développement d'outils numériques pour la résolution de l'Équation du Transfert Radiatif (ETR) appliquée à des matériaux semi-transparents à géométrie complexe, avec prise en compte de la spécularité aux bords, Les principaux outils développés sont :

- la méthode dite de Galerkin discontinue ainsi que la méthode des éléments finis stabilisés de type SUPG pour l'approximation de l'espace de l'ETR ;
- la méthode des ordonnées discrètes basée sur la discrétisation angulaire pour approcher le terme intégrale ;
- plusieurs discrétisations angulaires : la méthode originelle de Lee pour S_n, la méthode de Thurgood T_n, une méthode de conception maison nommée $SqT_{p,n}$ ainsi que la discrétisation par icosaèdres ;
- une méthode de partitionnement de flux réfléchi spéculairement qui s'est avérée très précise, par rapport à d'autres méthodes plus simples d'ailleurs également envisagées ;
- des solveur itératifs de type Gauss-Siedel pour les premières études, puis GMRES pour les dernières impliquant un grand nombre de degrés de liberté, et couplage avec la librairie MPI.

Ces développements ont permis de modéliser la propagation de la luminance dans des géométries tri-dimensionnelles à complexité graduelle comme, entre autres :

- un capteur solaire parabolique ;
- un berlingot, dont la forme dérive d'un tétraèdrique, et qui est une sucrerie typiquement nantaise ;
- un brin de mousse céramique sub-millimétrique provenant d'un image de micro-tomographie X.

Chaque configuration a permis de montrer la flexibilité du code SUPG. Plus particulièrement la dernière étude sur le brin micro-tomographié nous a incité, au vu du grand nombre de degrés de liberté, à revoir nos stratégies de construction de système linéaire et de résolution.

Ces développement laissent, à ce stade, entrevoir de nombreuses perspectives :

- l'ajout de conditions de réfraction entre deux phases solides sucessives permettrait de résoudre l'ETR dans des matériaux hétérogènes polyphasiques, comme par exemple les matériaux composites ou encore des mousses céramiques et/ou métalliques fonctionnalisées avec des revêtements semi-transparents. Cela permettrait d'avoir à disposition un outil numérique plus complet permettant de modéliser des conditions aux limites combinant à la fois réflexion et réfraction ;

— pour aller encore plus loin dans ce sens, une meilleure prise en compte des conditions de bord mixtes, situées entre les conditions de réflexions diffuses et spéculaires, permettrait d'obtenir les fameuses "poires de diffusion", bien connues au niveau des surfaces opaques rugueuses. Ceci pourrait être fait en "pré-processing", en se basant sur l'article de Bergström [1] et son site web [2].

— L'étude de la luminance dans le brin de mousse céramique ouvre des pistes d'investigation novatrices. Une prolongation de ce premier travail sera dans un premier temps de mieux tirer profit du potentiel offert par la microscopie infrarouge afin d'extraire les propriétés radiatives volumiques en décorrélant les effets de forme. Dans un second temps, il permettra ensuite d'affiner les approches basées sur des mesures Flash à micro-échelle afin de déterminer des diffusivités thermiques en tenant compte du couplage conducto-radiatif. Une étude sur une famille de brin à indice de forme graduel pourrait aussi être faite afin de générer, par la suite, des mousses à géométrie optimisées, fonction du mode de transport de masse et/ou de la chaleur à priviligier.

— Le couplage de l'ETR avec les équations de la mécanique des fluides pourrait aussi être très intéressant, notamment pour la modélisation du chauffage de gaz en géométrie complexe. Ce type de couplage pourrait s'avérer ainsi utile dans plusieurs domaines d'étude, comme par exemple la production de rayonnement infrarouge par combustion de gaz dans une mousse céramique ou pour l'optimisation da géométrie de chambres de chauffage.

— Grâce aux outils de parallélisation, le code étant maintenant suffisamment rapide en 3 dimensions, les méthodes inverses, développées dans notre laboratoire [3], pourraient être utilisées sur l'ETR 3D afin de caractériser certaines propriétés radiatives de matériaux semi-transparents. La connaissance précise de la configuration optique du banc de mesures des grandeurs radiatives, disponible au laboratoire, permettra de mener à bien ce développement.

— Un couplage avec une méthode Monte-Carlo pourrait permettre une meilleure prise en compte de l'impact d'un faisceau incident sur une surface concave impliquant de multiples réflexions du faisceau incident.

— Une étude sur l'adaptation de maillages, autant pour la partie spatiale que angulaire pourrait être faite, afin de limiter le nombre de degrés de liberté, et par conséquent diminuer le temps de résolution.

— Le calcul haute performance (HPC), qui fait partie du sujet de thèse d'un autre doctorant de l'équipe, devrait permettre d'étudier des objets comprenant plus de degrés de liberté, tout en gardant une même vitesse de résolution.

Références

[1] D. Bergström, J. Powell, A. Kaplan, A ray-tracing analysis of the absorption of light by smooth and rough metal surfaces, Journal of Applied Physics 101 (11) (2007) 113504. 188

[2] http://www.mysimlabs.com/. 188

[3] Y. Favennec, F. Dubot, D. Le Hardy, B. Rousseau, D. Rousse, Space-Dependent Sobolev Gradients as a Regularization for Inverse Radiative Transfer Problems, Mathematical Problems in Engineering 2016. 188

Annexes

Annexe A

Monte-Carlo

Cette partie décrit tous les tirages aléatoires pour la description de chacun des phénomènes physiques impliqués dans l'ETR. Les différents phénomènes seront décrits dans cet ordre :

— calcul d'une distance aléatoire d ;

— comportement lors d'une extinction ;

— détermination d'une direction lors d'une diffusion ;

— tirage aléatoire au niveau d'une surface.

On rappellera que pour toute fonction de répartition $Y = F(X)$, son inverse $F^{-1}(Y)$ suit une loi uniforme entre zéro et un. Notons $\xi \in [0, 1]$ le réel déterminé par tirage aléatoire de la loi uniforme $\mathcal{U}[0, 1]$.

A.1 Calcul d'une distance aléatoire d

Le long de la direction $\boldsymbol{s}$, l'extinction des photons décrit une loi exponentielle. Sa fonction de répartition est :

$$\xi = F(d) = 1 - e^{-\beta d} \ , \ d \in [0, \infty[\tag{A.1}$$

La distance d peut donc être exprimée en fonction du coefficient d'extinction β et du réel aléatoire ξ :

$$d = -\frac{\ln \xi}{\beta} \tag{A.2}$$

Une fois cette distance d parcouru dans la direction $\boldsymbol{s}$, un phénomène de diffusion ou d'absorption a lieu.

A.2 Extinction : Diffusion ou absorption

Lors d'une extinction, deux cas sont possibles : soit le photon est diffusé, soit le photon est absorbé. La probabilité que le photon soit diffusé suit alors une loi de

Bernoulli de paramètre $\alpha = \frac{\sigma}{\beta}$. La fonction de répartition est :

$$\xi = F(X) = \begin{cases} 0 \text{ si } x < 0 \\ \alpha \text{ si } x \in [0, \alpha] \\ 1 \text{ sinon} \end{cases} \tag{A.3}$$

La variable aléatoire $\xi \in [0, 1]$ détermine si l'événement est une diffusion ou une absorption :

$$\begin{cases} \text{si } \xi \leq \alpha : \text{Diffusion} \\ \text{si } \xi > \alpha : \text{Absorption} \end{cases} \tag{A.4}$$

Dans le cas où le photon est absorbé, on étudie un autre photon. Dans le cas où le photon est diffusé, le photon change de direction aléatoirement.

A.3 Changement de direction : Diffusion

Cette section se découpe en deux partie : le cas où la diffusion est isotrope, et le cas où la diffusion est anisotrope selon la fonction de phase d'Henyey-Greenstein.

A.3.1 Diffusion isotrope

Le tirage aléatoire sur une sphère dépend de deux paramètres aléatoires ξ_θ, $\xi_\varphi \in [0, 1]$ qui dépendent respectivement de l'angle azimutal θ et zénithal φ :

$$\begin{cases} \cos\theta = 2\xi_\theta - 1 \\ \varphi = 2\pi\xi_\varphi \end{cases} \tag{A.5}$$

La nouvelle direction $\boldsymbol{s}^{(1)}$ est :

$$\begin{cases} (\boldsymbol{s}^{(1)})_x = \sin\theta\cos\varphi \\ (\boldsymbol{s}^{(1)})_y = \sin\theta\sin\varphi \\ (\boldsymbol{s}^{(1)})_z = \cos\theta \end{cases} \tag{A.6}$$

A.3.2 Diffusion anisotrope

On rappelle la fonction de phase d'HG :

$$\phi(\theta, g) = \frac{1}{4\pi} \frac{1 - g^2}{(1 - 2g\cos\theta + g^2)^{3/2}} \tag{A.7}$$

Pour $g \neq 0$ on admet la relation entre l'angle azimutal θ en fonction du paramètre d'anisotropie g et le paramètre aléatoire ξ_θ. L'angle zénithal se détermine comme pour la diffusion isotrope :

$$\begin{cases} \cos\theta = \dfrac{1}{2g}\left[1 - g^2 - \left(\dfrac{1-g^2}{1-g+2g\xi_\theta}\right)^2\right] \\ \varphi = 2\pi\xi_\varphi \end{cases} \tag{A.8}$$

La nouvelle direction $\boldsymbol{s}^{(1)}$ est calculée comme ci-dessous :

$$\begin{cases} (\boldsymbol{s}^{(1)})_x = \dfrac{\sin\theta}{\sqrt{1-(\boldsymbol{s})_z^2}}\left[(\boldsymbol{s})_x(\boldsymbol{s})_z\cos\varphi - (\boldsymbol{s})_y\sin\varphi\right] + (\boldsymbol{s})_x\cos\theta \\ (\boldsymbol{s}^{(1)})_y = \dfrac{\sin\theta}{\sqrt{1-(\boldsymbol{s})_z^2}}\left[(\boldsymbol{s})_y(\boldsymbol{s})_z\cos\varphi + (\boldsymbol{s})_x\sin\varphi\right] + (\boldsymbol{s})_y\cos\theta \\ (\boldsymbol{s}^{(1)})_z = -\sin\theta\cos\varphi\sqrt{1-(\boldsymbol{s})_z^2} + (\boldsymbol{s})_z\cos\theta \end{cases} \tag{A.9}$$

Si $|(\boldsymbol{s})_z| > 0.99999$, on peut approcher la direction $\boldsymbol{s}^{(1)}$ par :

$$\begin{cases} (\boldsymbol{s}^{(1)})_x = \sin\theta\cos\varphi \\ (\boldsymbol{s}^{(1)})_y = \sin\theta\sin\varphi \\ (\boldsymbol{s}^{(1)})_z = \dfrac{(\boldsymbol{s})_z}{|(\boldsymbol{s})_z|}\cos\theta \end{cases} \tag{A.10}$$

A.4 Traitement spéculaire aux surfaces

Deux cas se présentent au niveau d'une surface :

— les photons provenant de l'extérieur du domaine

— les photons provenant de l'intérieur du domaine

Les deux cas sont différenciés. Le cas où le photon provient de l'extérieur étant plus simple, celui-ci sera présenté dans un premier temps. Ensuite, le cas où le photon provient de l'intérieur est présenté.

A.4.1 Photons entrants

Les photons entrants impactent une surface Γ_0, munie de sa normale $\boldsymbol{n}_0$, dans la direction $\boldsymbol{s}_0$.

Le coefficient $\rho_s(\boldsymbol{s}_0, \boldsymbol{n}_0)$ est déterminé par la loi de Fresnel (1.21). La probabilité que le photon soit réfléchi suit une loi de Bernoulli de paramètre $\rho_s(\boldsymbol{s}_0, \boldsymbol{n}_0)$. Par conséquent :

$$\begin{cases} \text{si } \xi \leq \rho_s(\boldsymbol{s}_0, \boldsymbol{n}_0) : \text{Photon réfléchi} \\ \text{si } \xi > \rho_s(\boldsymbol{s}_0, \boldsymbol{n}_0) : \text{Photon réfracté} \end{cases} \tag{A.11}$$

Si le photon est réfléchi, alors le photon contribue au calcul de la réflectance R_{NH}. Si le photon est réfracté, alors le photon se propage dans la direction $\boldsymbol{s}_0''$ d'une distance aléatoire d.

A.4.2 Photons sortants

Après plusieurs diffusions, un photon, situé à l'intérieur du domaine $\mathcal{D}$, peut impacter, dans la direction $\boldsymbol{s}$, la surface Γ_i , munie de sa normale $\boldsymbol{n}_i$. Comme le photon entrant, la probabilité que le photon soit réfléchi suit la loi de Bernoulli (A.11).

Si le photon est réfracté, alors le photon contribue au calcul de R_{NH}, si $i = 0$, ou de T_{NH} si $i = 1$. Si le photon est réfléchi, alors $\boldsymbol{s}'$ devient sa nouvelle direction de propagation et sa position est modifiée. Supposons $\boldsymbol{x}_i$ le point d'impact du photon sur Γ_i, alors la nouvelle position $f(\boldsymbol{x})$ du photon est déterminée par :

$$f(\boldsymbol{x}) = \boldsymbol{x} - 2\left((\boldsymbol{x} - \boldsymbol{x}_i) \cdot \boldsymbol{n}_i\right)\boldsymbol{n}_i \tag{A.12}$$

A.5 Schéma global pour la méthode Monte-Carlo utilisée

Maintenant que tous les comportements possibles du photons sont modélisés, le comportement du photon peut être généralisé par le schéma suivant :

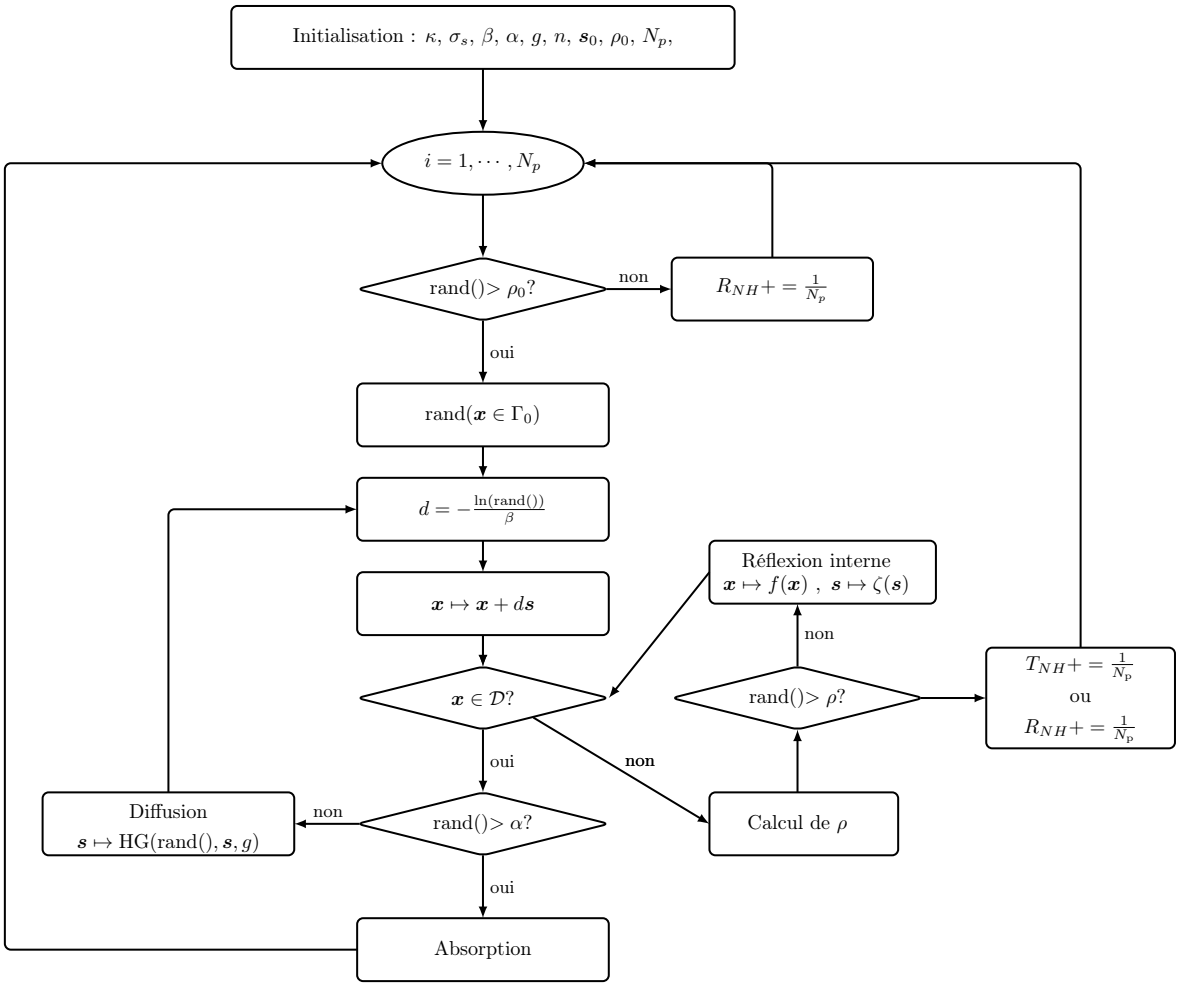

FIGURE A.1 – Schéma de la méthode Monte-Carlo utilisée

Annexe B

Méthode à deux-flux modifiée

Cette méthode est basée sur les travaux de L. Dombrovsky de 2006. La méthode à deux flux permet d'approcher, par réduction de modèle, la transmittance T_{NH} et la réflectance R_{NH} par une solution analytique. Elle a été étudiée lors d'un stage de master 2 par Mr Akshansh Kataria en 2016, stage encadré par Y. Favennec et moi-même.

Cette annexe montre les étapes clés de la méthode à deux flux modifiée. Elle se divise en plusieurs étapes :

— adimensionnalisation de l'ETR 1D et normalisation du terme source ;

— splitting de l'équation et décomposition de la luminance en une composante diffuse et une composante collimatée ;

— détermination d'une équation du second ordre, et résolution de celle-ci ;

— détermination de T_{NH} et R_{NH}.

B.1 Réduction de modèle et normalisation

Rappelons tout d'abord l'ETR 3D en stationnaire, sans l'émission du corps noir :

$$\boldsymbol{s}\cdot\nabla I(\boldsymbol{x},\boldsymbol{s})+\beta I(\boldsymbol{x},\boldsymbol{s})=\sigma_s\oint_{\mathcal{S}^{n-1}}\Phi(\boldsymbol{s}'\cdot\boldsymbol{s})I(\boldsymbol{x},\boldsymbol{s}')\,\mathrm{d}\Omega(\boldsymbol{s}') \tag{B.1}$$

La méthode suppose l'étude 1D d'une couche mince d'un matériau absorbant, diffusant et réfléchissant, de longueur x_0. De plus on supposera ici que la diffusion est isotrope et invariante selon l'angle azimutal :

$$\mu\frac{\mathrm{d}I}{\mathrm{d}x}(x,\mu)+\beta I(x,\mu)=\frac{\sigma_s}{2}\int_{-1}^{1}I(x,\mu')\,\mathrm{d}\mu' \tag{B.2}$$

Définissons l'épaisseur optique $\tau=\beta x$. En divisant l'équation (B.2) par β et en faisant le changement de variable $\tau=\beta x$, l'équation (B.2) devient une équation adimentionnalisée :

$$\mu\frac{\mathrm{d}I}{\mathrm{d}\tau}(\tau,\mu)+I(\tau,\mu)=\frac{\alpha}{2}\int_{-1}^{1}I(\tau,\mu')\,\mathrm{d}\mu' \tag{B.3}$$

où α est l'albédo. Pour compléter le modèle, on suppose qu'un faisceau d'intensité $\tilde{I}$ entre normal à la surface, c'est à dire $\tilde{I}(0,1) = 1$. Le matériau est optiquement lisse, par conséquent, la partie du faisceau entrant vérifie $I(0,1) = 1 - \rho_s$. En comprenant les réflexions internes, les conditions aux limites peuvent s'écrire :

$$\begin{cases} I(0,\mu) = \rho_s(\mu) I(0,-\mu) + (1-\rho_s(\mu))\mathbb{1}_{[\mu=1]} \\ I(\tau_0,-\mu) = \rho_s(\mu) I(\tau_0,\mu) \end{cases} \tag{B.4}$$

B.2 Décomposition de la luminance et splitting

Le modèle se réduit à nouveau en supposant que la luminance en un point peut se séparer en deux parties : la partie collimaté I_c, comprenant le terme source, et la partie diffuse I_d :

$$I(\tau,\mu) = I_c(\tau,\mu) + I_d(\tau,\mu) \tag{B.5}$$

On décompose l'équation (B.3) ainsi que les conditions aux limites (B.4). Cela donne deux équations accompagnées de leurs conditions aux limites respectives :

$$\begin{cases} \mu \dfrac{\mathrm{d}I_c}{\mathrm{d}\tau}(\tau,\mu) + I_c(\tau,\mu) = 0 \\ I_c(0,\mu) = \rho_s(\mu) I_c(0,-\mu) + (1-\rho_s(\mu))\mathbb{1}_{[\mu=1]} \\ I_c(\tau_0,-\mu) = \rho_s(\mu) I_c(\tau_0,\mu) \end{cases} \tag{B.6}$$

$$\begin{cases} \mu \dfrac{\mathrm{d}I_d}{\mathrm{d}\tau}(\tau,\mu) + I_d(\tau,\mu) = \dfrac{\alpha}{2}\displaystyle\int_{-1}^{1} I_d(\tau,\mu')\,\mathrm{d}\mu' + \dfrac{\alpha}{2}\int_{-1}^{1} I_c(\tau,\mu')\,\mathrm{d}\mu' \\ I_d(0,\mu) = \rho_s(\mu) I_d(0,-\mu) \\ I_d(\tau_0,-\mu) = \rho_s(\mu) I_d(\tau_0,\mu) \end{cases} \tag{B.7}$$

La luminance collimatée I_c se détermine analytiquement en utilisant la loi de Beer-Lambert :

$$I_c(\tau,\mu) = \frac{1-\rho_{s1}}{1-\rho_{s1}C}\left(e^{-\tau}\mathbb{1}_{\mu=1} + Ce^{\tau}\mathbb{1}_{\mu=-1}\right) \tag{B.8}$$

avec $\rho_{s1} = \rho_s(1) = (1-n)^2/(1+n)^2$ et $C = \rho_{s1}e^{-2\tau_0}$.

La partie diffuse I_d est quant à elle plus difficile à déterminer.

B.3 Approximation de I_d et résolution d'une équation du second ordre

Définissons le cosinus μ_c, le cosinus de l'angle critique θ_c. Supposons que la partie diffuse est divisée en 3 parties constantes. La luminance diffuse I_d est alors définie par :

$$I_d(\tau,\mu) = \begin{cases} \varphi^-(\tau) \text{ si } -1 < \mu < -\mu_c \\ \psi(\tau) \quad \text{si } -\mu_c < \mu < \mu_c \\ \varphi^+(\tau) \text{ si } \mu_c < \mu < 1 \end{cases} \tag{B.9}$$

Supposons que les flux associés à I_d se propagent dans les 3 directions $\frac{1+\mu_c}{2} = \tilde{\mu}$, 0 et $-\frac{1+\mu_c}{2} = -\tilde{\mu}$. Dans ce cas, l'équation (B.7) se transforme en un système à 3 equations à 3 inconnues, continues en espace :

$$\begin{cases} \tilde{\mu}\dfrac{\mathrm{d}\phi^+}{\mathrm{d}\tau} + \phi^+ = \dfrac{\alpha}{2}\left[(1-\mu_c)g + 2\mu_c\psi + \dfrac{1-\rho_{s1}}{1-\rho_{s1}C}\left(e^{-\tau} + Ce^{\tau}\right)\right] \\ -\tilde{\mu}\dfrac{\mathrm{d}\phi^-}{\mathrm{d}\tau} + \phi^- = \dfrac{\alpha}{2}\left[(1-\mu_c)g + 2\mu_c\psi + \dfrac{1-\rho_{s1}}{1-\rho_{s1}C}\left(e^{-\tau} + Ce^{\tau}\right)\right] \\ \psi = \dfrac{\alpha}{2}\left[(1-\mu_c)g + 2\mu_c\psi + \dfrac{1-\rho_{s1}}{1-\rho_{s1}C}\left(e^{-\tau} + Ce^{\tau}\right)\right] \end{cases} \tag{B.10}$$

où $g = \phi^- + \phi^+$. Pour des raisons de clarté, la dépendance en τ est omise.

En additionnant les deux premières, en soustrayant les deux premières équations et en isolant ψ dans la dernière équation du système (B.10), celui-ci devient :

$$\begin{cases} \tilde{\mu}\dfrac{\mathrm{d}(\phi^+ - \phi^-)}{\mathrm{d}\tau} + g = \alpha\left[(1-\mu_c)g + 2\mu_c\psi + \dfrac{1-\rho_{s1}}{1-\rho_{s1}C}\left(e^{-\tau} + Ce^{\tau}\right)\right] \\ \phi^+ - \phi^- = -\tilde{\mu}\dfrac{\mathrm{d}g}{\mathrm{d}\tau} \\ \psi = \dfrac{\alpha}{2(1-\alpha\mu_c)}\left[(1-\mu_c)g + \dfrac{1-\rho_{s1}}{1-\rho_{s1}C}\left(e^{-\tau} + Ce^{\tau}\right)\right] \end{cases} \tag{B.11}$$

En remplaçant $\phi^+ - \phi^-$ et ψ de la première équation par la seconde équation et la troisième équation du système (B.11), on obtient une équation du second ordre d'inconnu g :

$$\frac{\mathrm{d}^2 g}{\mathrm{d}\tau^2} + \varsigma^2 g = \varsigma^2 \varpi\left[e^{-\tau} + Ce^{\tau}\right] \tag{B.12}$$

où

$$\varsigma = \frac{1}{\tilde{\mu}^2}\frac{1-\alpha}{1-\alpha\mu_c} \quad , \quad \varpi = \frac{\alpha}{1-\alpha}\frac{1-\rho_{s1}}{1-\rho_{s1}C} \tag{B.13}$$

Maintenant que l'équation du second ordre (B.12) est déterminée, il faut déterminer les conditions aux limites de g. en choisissant $\mu = \tilde{\mu}$, les conditions aux limites du système (B.7) deviennent :

$$\begin{cases} \phi^+(0) = \rho_s(\tilde{\mu})\phi^-(0) \\ \phi^-(\tau_0) = \rho_s(\tilde{\mu})\phi^+(\tau_0) \end{cases} \tag{B.14}$$

On additionne respectivement $\phi^-(0)$ et $\phi^+(\tau_0)$ aux équations (B.14) :

$$\begin{cases} g(0) = (1+\rho_s(\tilde{\mu}))\phi^-(0) \\ g(\tau_0) = (1+\rho_s(\tilde{\mu}))\phi^+(\tau_0) \end{cases} \tag{B.15}$$

En s'aidant de la deuxième équation du système (B.11) et des deux systèmes (B.14) et (B.15), les conditions aux limites de g sont :

$$\begin{cases} \tilde{\mu}\dfrac{\mathrm{d}g}{\mathrm{d}\tau}(0) = \gamma g(0) \\ \tilde{\mu}\dfrac{\mathrm{d}g}{\mathrm{d}\tau}(\tau_0) = -\gamma g(\tau_0) \end{cases} \tag{B.16}$$

où $\gamma = (1 - \rho_s(\tilde{\mu}))/(1 + \rho_s(\tilde{\mu}))$

Les équations (B.12) et (B.16) permettent de déterminer g. Divisons $g = g_h + g_p$ où g_p est une solution particulière de (B.12) et g_h et la solution homogène :

$$\begin{cases} g_p(\tau) = \dfrac{\varsigma^2 \varpi}{1 - \varsigma^2} \left[e^{-\tau} - C e^{\tau} \right] \\ g_h(\tau) = A e^{-\varsigma \tau} + B e^{\varsigma \tau} \end{cases} \tag{B.17}$$

où A et B se déterminent avec les conditions aux limites (B.12)

$$\begin{cases} A = \dfrac{\varsigma^2 \varpi}{\varsigma^2 - 1} \dfrac{e^{\varsigma \tau_0}(\varsigma + \gamma/\tilde{\mu}) k_2 + (\varsigma - \gamma/\tilde{\mu}) k_1}{2\varsigma^2 [(1 + \varepsilon^2) s_h + 2\varepsilon c_h]} \\ B = \dfrac{\varsigma^2 \varpi}{\varsigma^2 - 1} \dfrac{e^{-\varsigma \tau_0}(\varsigma - \gamma/\tilde{\mu}) k_2 + (\varsigma + \gamma/\tilde{\mu}) k_1}{2\varsigma^2 [(1 + \varepsilon^2) s_h + 2\varepsilon c_h]} \end{cases} \tag{B.18}$$

avec

$$\begin{cases} k_1 = e^{-\tau_0} \left[(1 - \gamma/\tilde{\mu}) - (1 + \gamma/\tilde{\mu}) \rho_s(\tilde{\mu}) \right] \\ k_2 = (1 - \gamma/\tilde{\mu}) C - (1 + \gamma/\tilde{\mu}) \\ \varepsilon = \dfrac{\gamma}{\varsigma \tilde{\mu}} \\ c_h = \cosh(\varsigma \tau_0) \\ s_h = \sinh(\varsigma \tau_0) \end{cases} \tag{B.19}$$

g étant déterminé, la transmittance T_{NH} et la réfléctance R_{NH} peuvent être approchées analytiquement.

Remarque : la constante ς peut, en théorie, être égale à 1, mais il s'agit d'un cas vraiment trop particulier. L'étude pour $\varsigma = 1$ n'est donc pas présentée ici. De plus, si l'albédo $\alpha = 0$, une solution asymptotique existe.

B.4 Détermination de T_{NH} et R_{NH}

Définissons T^c_{NH} et R^c_{NH} la transmittance et la réfléctance de la luminance collimatée I_c, et T^d_{NH} et R^d_{NH} la transmittance et la réfléctance de la luminance diffuse I_d. Par construction on a :

$$\begin{cases} T_{\text{NH}} = T^c_{\text{NH}} + T^d_{\text{NH}} \\ R_{\text{NH}} = R^c_{\text{NH}} + R^d_{\text{NH}} \end{cases} \tag{B.20}$$

Connaissant analytiquement I_c (B.8), T^c_{NH} et R^c_{NH} se déterminent immédiatement :

$$\begin{cases} T^c_{\text{NH}} = (1 - \rho_{s1}) I_c(\tau_0, 1) = \dfrac{(1 - \rho_{s1})^2}{1 - \rho_{s1} C} e^{-\tau_0} \\ R^c_{\text{NH}} = \rho_{s1} + (1 - \rho_{s1}) I_c(0, -1) = \rho_{s1} + \dfrac{(1 - \rho_{s1})^2 C}{1 - \rho_{s1} C} \end{cases} \tag{B.21}$$

En supposant que le flux diffus soit concentré dans la direction $\tilde{\mu}$, T^d_{NH} et R^d_{NH} valent :

$$\begin{cases} T^d_{\mathrm{NH}} = (1 - \rho_s(\tilde{\mu})) \int_0^1 I_d(\tau_0, \mu)\mu \, \mathrm{d}\mu \\ R^d_{\mathrm{NH}} = (1 - \rho_s(\tilde{\mu})) \int_0^1 I_d(0, -\mu)\mu \, \mathrm{d}\mu \end{cases} \tag{B.22}$$

Pour tout flux dont la direction μ dépasse la direction critique μ_c, celui-ci est théoriquement totalement réfléchi. Les vecteurs flux dans les directions $\mu \in [-\mu_c, \mu_c]$ ne sont donc pas réfractés. Par conséquent, T^d_{NH} et R^d_{NH} peuvent s'exprimer en fonction de ϕ^+ et ϕ^- :

$$\begin{cases} T^d_{\mathrm{NH}} = (1 - \rho_s(\tilde{\mu}))\phi^+(\tau_0)\dfrac{1 - \mu_c^2}{2} \\ R^d_{\mathrm{NH}} = (1 - \rho_s(\tilde{\mu}))\phi^-(0)\dfrac{1 - \mu_c^2}{2} \end{cases} \tag{B.23}$$

Avec les conditions aux limites (B.14) et la deuxième équation de (B.11), on obtient une relation de T^d_{NH}, R^d_{NH} en fonction de la dérivé de g :

$$\begin{cases} T^d_{\mathrm{NH}} = -\tilde{\mu}\dfrac{\mathrm{d}g}{\mathrm{d}\tau}(\tau_0)\dfrac{1 - \mu_c^2}{2} \\ R^d_{\mathrm{NH}} = \tilde{\mu}\dfrac{\mathrm{d}g}{\mathrm{d}\tau}(0)\dfrac{1 - \mu_c^2}{2} \end{cases} \tag{B.24}$$

Avec les conditions aux limites sur g (B.16), on obtient la relation de T^d_{NH}, R^d_{NH} en fonction de g :

$$\begin{cases} T^d_{\mathrm{NH}} = \gamma\dfrac{1 - \mu_c^2}{2}g(\tau_0) \\ R^d_{\mathrm{NH}} = \gamma\dfrac{1 - \mu_c^2}{2}g(0) \end{cases} \tag{B.25}$$

Les équations (B.20), (B.21) et (B.25) permettent de déterminer explicitement la transmittance T_{NH} et la réfléctance R_{NH}.

Liste des figures

Liste des tableaux

Liste des algorithmes

l'université nantes angers le mans

PÔLE DE RECHERCHE ET D'ENSEIGNEMENT SUPÉRIEUR

UNIVERSITÉ DE NANTES

Thèse de Doctorat

David LE HARDY

Traitement des conditions aux limites spéculaires pour l'étude du transport radiatif dans des matériaux à géométrie complexe

Specular boundary conditions treatement for the study of the radiative transport into materials with complex geometry

Résumé :

Dans le cadre de cette thèse, des outils numériques ont été développés, ayant pour objectif la résolution de l'équation du transfert radiatif pour des matériaux à géométrie complexe, avec prise en compte des conditions aux limites spéculaires. Les développements s'articulent autour de la méthode des ordonnées discrètes combinée aux éléments finis stabilisés de type SUPG. Une méthode de partionnement a été spécialement conçue pour un traitement fin de la spécularité en surface. Par ailleurs, des solveurs parallèles du type Gauss-Seidel puis GMRES ont été utilisés afin de traiter des problèmes de grande taille, provenant d'une discrétisation fine en espace et en angulaire, toutes deux nécessaires au vu de la complexité géométrique. Les outils développés ont finalement été utilisés sur un brin de mousse céramique réel, au préalable micro-tomographié.

Mot Clés: Méthodes Éléments Finis, Galerkin, Méthodes des Ordonnées Discrètes, Géometries complexes, Conditions aux limites spéculaires, Matériaux semi-transparents

Abstract :

This dissertation considers the development of numerical tools for the solution of the radiative transfer equation within three-dimensional media with complex geometries, combined with the accurate treatment of specular boundary conditions. Numerical developments rely on the Discrete Ordinate Method, combined with SUPG-type stabilized Finite Elements. A very novel partitioning method has been developped for accurate treatment of specularity on borders. Also, some Gauss–Seidel type and GMRES parallel solvers have been used to deal with huge size matrix systems, due to fine discretization in both space and angles, needed for such considered geometrical complexity. Finally, all developped numerical tools have been tested for the modelling of radiative transport within a micro-tomographied ceramic ligament, extracted from a real open-cell foam.

Keywords: Finite Element Methods, Galerkin, Discrete Ordinate Methods, Complex geometries, Specular Boundary Conditions, Semi-transparent materials